1-1-2014

First Measurements of the Differential Cross Sections of Higgs Boson Production and Decay in the Four Lepton Final State

Jonathan Mark Stahlman
University of Pennsylvania, stahlman@sas.upenn.edu

First Measurements of the Differential Cross Sections of Higgs Boson Production and Decay in the Four Lepton Final State

Abstract
The discovery of a new scalar particle in the search for the Higgs boson at the Large Hadron Collider (LHC) was a great success for the ATLAS and CMS collaborations. Additional measurements of this new particle present opportunities to both test the Standard Model (SM) predictions for the Higgs boson and to search for non-SM properties of this new particle. This thesis presents measurements of the mass, signal strength, and production cross sections of the Higgs boson in the H -> ZZ* -> lll'l' (l,l'=e,μ) decay channel. The cross section measurements are performed using 20.3 fb^-1 of *pp* collisions at center of mass energy sqrt(s) = 8 TeV collected by the ATLAS detector and the mass and signal strength measurements are performed using an additional 4.5 fb^-1 of *pp* collisions at sqrt(s) = 7 TeV. From the data in the H -> 4l channel, the best estimate of the mass is 124.51 ± 0.52 (stat) ± 0.06 (syst) GeV. The signal strength (the ratio of observed signal events to expected events from a Standard Model Higgs boson) is measured to be 1.64 ± 0.38 (stat) ± 0.18 (syst). An inclusive cross section time branching ratio measurement is performed within a fiducial volume and found to be $2.11^{+0.53}_{-0.47}$ (stat) $^{+0.08}_{-0.08}$(syst) fb. Differential cross section measurements are performed for six observables which are sensitive to properties of the Higgs boson production and decay. An unfolding procedure is used to correct for detector effects in the differential measurements and comparisons are made to several theoretical calculations. No significant deviations from the SM predictions are observed.

Degree Type
Dissertation

Degree Name
Doctor of Philosophy (PhD)

Graduate Group
Physics & Astronomy

First Advisor
Hugh H. Williams

Subject Categories
Elementary Particles and Fields and String Theory

First Measurements of the Differential Cross Sections of Higgs Boson Production and Decay in the Four Lepton Final State

Jonathan M. Stahlman

A DISSERTATION
in
Physics and Astronomy

Presented to the Faculties of The University of Pennsylvania
in Partial Fulfillment of the Requirements for the Degree of Doctor of Philosophy
2014

Hugh H. Williams, Professor, Physics
Supervisor of Dissertation

Marija Drndic, Professor, Physics
Graduate Group Chairperson

Dissertation Committee
Elliot Lipeles, Associate Professor, Physics
Evelyn Thomson, Associate Professor, Physics
Justin Khoury, Associate Professor, Physics
Mark Devlin, Professor, Physics
Hugh H. Williams, Professor, Physics

First Measurements of the Differential Cross Sections of Higgs Boson Production and Decay in the Four Lepton Final State

Acknowledgements

Completion of this dissertation is by no means a singular effort on my part; there is a multitude of people to whom I am grateful for help and support during my graduate studies. I would like to acknowledge those people here. I have tried to recall everyone, but inevitably, I will miss someone, so please know that I appreciate all those who have helped me during the past six years even if your name is not listed here specifically.

First and foremost, I would like to acknowledge my parents Paul and Linda Stahlman because without their constant support and encouragement to further my education and broaden my knowledge, I would not have made it to this point. I also want to thank my brothers Matthew and Ryan and sisters-in-law Lisa and Somayeh for the many times that they hosted me over the years. I fondly remember all the good memories we created together during these trips!

In Philadelphia, there are a number of graduate students and others with whom I worked late nights on problem sets, explored Philadelphia, and generally had a great time. Thank you to Mitch Lerner, Austin Joyce, Matthew Gratale, Kim Venta, Cristi Resczenski, Elio Angilè, Doug Robl, Stephanie Majkut, Sarah Clark, Matthew Lohr, Jim Halverson, and Paul Rubin.

The TRT electronics group at Penn has been a pleasure to work in. Thanks go to Rick Van Berg, Mitch Newcomer, Mike O'Reilly, Ben LeGeyt, and Paul Keener for sharing their

extensive expertise in the TRT electronics and DAQ system with me. I could always depend on them to come up with a hypothesis to test which, more often than not, was the key to debugging issues in the DAQ. I must also thank Michael Hance, Dominick Olivito and Peter Wagner for teaching me the ways of the TRT Champion. Together, we commissioned and maintained the TRT readout electronics successfully during Run 1, albeit with a few middle of the night calls from time to time. I would like to thank Sarah Heim, Ximo Poveda, and Jamie Saxon because they quickly mastered the TRT DAQ system, allowing me to move on and complete this analysis after the end of Run 1.

I also want to thank my other TRT collaborators. I owe much gratitude to Christoph Rembser, Anatoli Romaniouk, and Andrey Loginov for their strong leadership of the TRT collaboration. I want to thank Zbyszek Hajduk, Elzbieta Banas, and Jolanta Olszowska for their support of the TRT DCS; they were always extremely helpful and a pleasure to work with. I also want to thank those who worked with me on the TRT software in the early days of data-taking, including Saša Fratina, James Degenhardt, Jahred Adelman and Fred Luehring, who taught me much about particle tracking.

Of course, I must acknowledge the entire ATLAS collaboration in general. The scope and complexity of this experiment still amazes me daily and the expertise among my collaborators is vast. In particular, Anthony Morley and Pawel Bruckman de Renstrom were extremely helpful in my studies of the ID alignment. I also want to thank the conveners of the $H \to 4\ell$ analysis group for their leadership both leading up to the discovery of the Higgs boson and the first measurements afterwards, including the results of this dissertation. The conveners, including Konstantinos Nikolopoulos, Christos Anastopoulos, Stefano Rosati, Fabien Tarrade, and Rosy Nikolaidou, were fantastic in coordinating the group to produce the high quality results of Run 1.

A number of people deserve special mention due to their direct contributions to the differ-

ential cross section measurements. I would like to thank the analysis editorial board, including Jianming Qian, Alex Read, Anna Sfyrla, and Bernd Stelzer, who helped to refine our results for publication. The analysis editors, Sarah Heim and Fabio Cerutti, consistently made excellent recommendations for the analysis and were essential throughout the preparation of the analysis. Finally, I highly value the direct contributions of others to the analysis, including Kate Whalen, Gabriella Pasztor, Giada Mancini, Eleonora Benhar, and Kurt Brendlinger. This collaboration made the results of this dissertation possible.

I want to give recognition to my fellow graduate students at Penn and CERN, who have taught me both about HEP research and the joys of living in Europe. I will never forget Friday night TRT BBQs with Dominick Olivito, John Alison, and John Penwell, whose resolve for having a good time is unquestionable. During my first summer at CERN, I spent many hours soldering and installing TRT patch panels with Josh Kunkle, Liz Hines, and Brett Jackson and have cherished their collaboration ever since. I enjoyed many intense conversations over Penn Dinner with Ryan Reece, Rami Vanguri, Doug Schaefer, and Jamie Saxon. Finally, I want to thank Chris Lester for always being there as a friend, both in the highs and lows of graduate school.

A number of people at Penn also deserve acknowledgments. I want to thank Jean O'Boyle, as she has always been extremely patient and helpful even when I have not been so organized. I also want to thank the professors in the HEP group, including Joe Kroll, Elliot Lipeles, and Evelyn Thomson, for their collaboration and help. They have always challenged me intellectually and I have learned much from them. Of course, I couldn't have finished this dissertation without my adviser Brig Williams, who has mentored me in my research and given me just the right amount of guidance to keep me moving through graduate school. Brig has taught me so much and I am forever grateful for his mentorship.

Finally, I want to thank my girlfriend Susan Johnson. She has stuck with me through (in

spite of?) all the stressful times of finishing my analysis, moving across the ocean, and writing this dissertation. She has kept me sane and I often wonder how I could have done it without her. Susan, I love you!

ABSTRACT

First Measurements of the Differential Cross Sections of Higgs Boson Production and Decay in the Four Lepton Final State

Jonathan M. Stahlman

H.H. Williams

The discovery of a new scalar particle in the search for the Higgs boson at the Large Hadron Collider (LHC) was a great success for the ATLAS and CMS collaborations. Additional measurements of this new particle present opportunities to both test the Standard Model (SM) predictions for the Higgs boson and to search for non-SM properties of this new particle. This thesis presents measurements of the mass, signal strength, and production cross sections of the Higgs boson in the $H \to ZZ^{(*)} \to \ell\ell\ell'\ell'(\ell, \ell' = e, \mu)$ decay channel. The cross section measurements are performed using 20.3 fb^{-1}of pp collisions at center of mass energy $\sqrt{s} = 8$ TeV collected by the ATLAS detector and the mass and signal strength measurements are performed using an additional 4.5 fb^{-1}of pp collisions at $\sqrt{s} = 7$ TeV. From the data in the $H \to 4\ell$ channel, the best estimate of the mass is 124.51 $\pm$ 0.52 (stat) $\pm$ 0.06 (syst) GeV. The signal strength (the ratio of observed signal events to expected events from a Standard Model Higgs boson) is measured to be 1.64 $\pm$ 0.38 (stat) $\pm$ 0.18 (syst). An inclusive cross section time branching ratio measurement is performed within a fiducial volume and found to be $2.11^{+0.53}_{-0.47}$ (stat)$^{+0.08}_{-0.08}$ (syst) fb. Differential cross section measurements are performed

for six observables which are sensitive to properties of the Higgs boson production and decay. An unfolding procedure is used to correct for detector effects in the differential measurements and comparisons are made to several theoretical calculations. No significant deviations from the SM predictions are observed.

Contents

List of Tables

List of Figures

Preface

The past six years has turned out to be one of the most exciting and productive times for particle physics in recent history as the Large Hadron Collider (LHC) and its associated experiments have been commissioned and proceeded to collect data which led to the discovery of a new particle which, in all respects, looks very much like the Higgs boson of the Standard Model. I consider myself extremely fortunate to have been able to participate in these activities, having started my graduate studies in 2008 just as the experiments were preparing to collect first data. Of course, an accident in the LHC tunnel in the fall of 2008 delayed the start of data-taking and caused me a bit of stress over graduation timelines, but I continued working in the U. Penn ATLAS group and am now finishing my Ph.D. after the end of a very fruitful first LHC run.

During the first several years, my focus was on commissioning and maintenance of the data acquisition (DAQ) electronics for the Transition Radiation Tracker (TRT), a sub-detector of ATLAS in which the Penn HEP group is heavily involved, having designed and built much of the front-end electronics. One of my first contributions was the development of a graphical user interface (GUI) known as the "Cobra Panel" which provided experts an immediate overview of the TRT electronics status. Simultaneously, I began studies of tracking in minimum bias events in the Inner Detector (ID) with the goal of detecting and minimizing misalignments in the TRT, resulting in improvements to the track position resolution within the TRT.

After moving to CERN full-time in 2010, TRT operations and maintenance occupied much of my time as data-taking continued in earnest. In 2012, I took over as DAQ electronics coordinator for the TRT. The push to higher luminosity by the LHC and higher trigger rates by ATLAS lead to interesting challenges for the TRT DAQ. During the same time, the tracking studies matured as the knowledge of the ID alignment improved, leading to studies of subtle detector misalignment effects. The data-driven measurements of momentum biases using the quickly growing dataset of $Z \to \mu^+\mu^-$ events was essential in improving the knowledge of the resolution and scale systematic uncertainties in the ID tracking. This included studies of weak modes and time-dependent alignment effects which could have significantly degraded the momentum scale and resolution performance.

Towards the end of the 2011, I joined the ATLAS HSG2 group, which is responsible for the search for and measurements of the Higgs boson in the four lepton final state, making contributions based on my experience in ID tracking performance. At the time (and to a lesser extent still today), there was some tension between the $H \to 4\ell$ and $H \to \gamma\gamma$ mass measurements which required much scrutiny before the results could be released. My studies of the momentum scale in the ID tracking helped to confirm that the tension was not due to underestimated systematic uncertainties in the mass scale.

In July of 2012, the ATLAS and CMS experiments acquired enough data to announce the 5σ observation of a new particle with a mass of approximately 125 GeV primarily based on observations in the diphoton and four lepton final states, with smaller contributions from the $H \to WW$ search. After the discovery, work began on measurements of this new particle using the full Run 1 dataset from the LHC, which is the focus of this thesis. My main contribution to this effort has been the development and implementation of the differential cross section measurements in the $H \to 4\ell$ channel, which were recently published in arXiv:1408.3226. I also made auxiliary contributions to the background estimates and mass and signal strength

measurements.

Working on an experiment with the scale of ATLAS necessarily requires one to rely on the work of many others. As such, this thesis presents results of both my work and others. I have attempted to write the results in my own words in cases where the original text is not my own. For reference, Chapters 6, 7, 9, and 10 are based on ATL-COM-PHYS-2013-1599, Chapters 8 and 12 are based on ATL-COM-PHYS-2014-056, and Chapter 11 is based on ATL-COM-PHYS-2014-056.

Jonathan Stahlman

Washington D.C., May 2014

Chapter 1

Introduction

The discovery of a new scalar particle in the search for the Higgs boson at the Large Hadron Collider (LHC) was a great success for the ATLAS and CMS collaborations. Additional measurements of this new particle present opportunities to both test the Standard Model (SM) predictions of the Higgs boson and to search for non-SM properties of this new particle. This thesis presents updated measurements of the Higgs mass and signal strength and first measurements of the differential cross sections of the Higgs boson in the $H \to ZZ^{(*)} \to \ell\ell\ell\ell$ ($\ell = e, \mu$) decay channel.

The $H \to 4\ell$ decay channel is often referred to as the "golden channel" for Higgs boson discovery and measurements because of the striking signature of the four relatively high momentum leptons in the final state. This final state allows full reconstruction of the Higgs kinematics while simultaneously having relatively small backgrounds. However, it will be seen that the sensitivity of this channel with the current dataset is almost entirely limited by the statistical uncertainties, which are relatively large compared to other Higgs decay channels due to the small branching ratios of the $H \to 4\ell$ decay.

The cross section measurements are performed using 20.3 fb^{-1}of pp collisions at $\sqrt{s} = 8$ TeV collected by the ATLAS detector and the mass and couplings measurements are performed using an additional 4.5 fb^{-1}of pp collisions at $\sqrt{s} = 7$ TeV. An inclusive cross section

measurement is carried out within a fiducial volume and differential cross section measurements are performed for six observables which are sensitive to properties of the Higgs boson production and decay. An unfolding procedure is used to correct for detector effects in the differential measurements and comparisons are made to several theoretical calculations.

This thesis is organized as follows: Chapter 2 provides theoretical motivations for the search for and measurements of the Higgs boson. Chapter 3 gives a description of the experimental apparatus, the ATLAS detector and a study of the detector alignment and tracking performance is presented in Chapter 4. An overview of the measurements performed in the $H \to 4\ell$ analysis is given in Chapter 5. Chapter 6 describes the data and simulation samples and Chapter 7 explains the event selection and final observables used in the $H \to 4\ell$ channel. Chapter 8 defines and presents studies of the fiducial detector volume used for the fiducial cross section measurements. The background estimation methods and results are shown in Chapter 9. Studies of the systematic uncertainties are presented in Chapter 10. Chapter 11 describes the methods and results of the mass and signal strength measurements and Chapter 12 presents the methods and results of the differential cross section measurements. Conclusions are given in Chapter 13.

Chapter 2

Theoretical Motivations

The Standard Model of particle physics has been extremely successful in precisely describing many of the interactions of the fundamental particles observed in nature over a wide range of energy scales. The discovery in 2012 at the Large Hadron Collider (LHC) of a scalar particle with characteristics closely resembling those of the predicted Higgs boson is yet another step in confirming the predictions of this theory. This chapter begins with a brief description of the Standard Model and electroweak symmetry breaking, continues with a discussion of particle physics at hadron colliders and the discovery of the Higgs boson at the LHC, and finishes with a discussion of the shortcomings and possible extensions of the Standard Model.

2.1 The Standard Model

The Standard Model (SM) of particle physics is a theoretical framework conceived to describe the interactions of the fundamental particles of nature. It has been developed incrementally over the course of many years based on empirical observation and advances in quantum field theory. It currently contains the known matter fields, the leptons and quarks, and describes three of the four known fundamental interactions: electromagnetism, the weak interaction, and the strong interaction. Only gravity has yet to be incorporated into the SM. A thorough

description of the Standard Model is beyond the scope of this thesis and many texts will give a much better treatment of the subject - see Reference [1] for example. Instead, a summary of the main features of the SM, especially those related to electroweak symmetry breaking, will be discussed here.

The SM is a quantum field theory in which quarks and leptons (known as fermions) are represented by a set of spin 1/2 Dirac fields interacting via the fundamental forces. A Lagrangian specifies the dynamics of these interactions which in the SM is invariant under a set of local space-time transformations specified by the Lie group $SU(3)_{\mathrm{C}} \times SU(2)_{\mathrm{L}} \times U(1)_{\mathrm{Y}}$. This invariance is known as a "gauge symmetry" and is required in order for a theory to be renormalizable. Gauge symmetry is required in the SM because non-renormalizable theories contain uncontrolled divergences which result in non-predictive models. All terms that preserve this gauge symmetry are present in the SM Lagrangian.

Preservation of the gauge symmetry necessitates a set of additional "gauge fields" with corresponding "gauge bosons". The fundamental forces are represented by these gauge fields with the gauge bosons acting as the force carriers. The SM has eight gauge bosons corresponding to the generators of $SU(3)$, three gauge bosons associated with $SU(2)$ and one gauge boson from $U(1)$, all of which are spin 1 particles.

As described, this theory is perfectly self-consistent as a theory of massless fields interacting via electroweak and strong interactions. However, experimentally both massive fermions and massive electroweak gauge bosons have been observed so mass terms must be generated in order for the SM to be a meaningful theory. However, the addition of standard mass terms in the Lagrangian for the electroweak gauge fields would break the gauge invariance and thus are forbidden. A similar issue exists for fermions because the introduction of mass terms for the fermions would mix the left and right handed sectors of the fermions, breaking gauge invariance.

A method of introducing mass terms into the Lagrangian without breaking the gauge invariance within a relativistic theory was first proposed in the 1960's by several groups of theorists including Robert Brout and Francois Englert [2], Peter Higgs [3, 4], and Gerald Guralnik, Carl R. Hagen, and Tom Kibble [5] and is now commonly known as the Brout-Englert-Higgs (BEH) mechanism. The BEH mechanism introduces an additional complex scalar field, known as the Higgs field, for which the zero-point of the field potential is not the ground state of the field. The Higgs field preserves the gauge invariance of the Lagrangian but the gauge symmetry will be "spontaneously" broken when the Higgs field assumes its ground state value.

The structure of the electroweak gauge symmetry in the SM was originally proposed by Glashow[6], Weinberg[7] and Salam [8, 9, 10]. In this model, the Higgs field is an $SU(2)$ doublet field, which couples to the electroweak $SU(2)_{\rm L}\times U(1)_{\rm Y}$ gauge fields. After spontaneous symmetry breaking, only the $U(1)_{\rm EM}$ symmetry remains. The $W^{\pm}$ and Z bosons result from the the mixing of the $SU(2)$ fields and the photon remains as the massless propagator of the $U(1)_{\rm EM}$ group.

The fact that the Higgs field acquires a non-zero vacuum expectation value (a "vev") through spontaneous symmetry breaking dynamically generates mass terms for the weak gauge bosons while the photon remains massless. The masses of the $W^{\pm}$ and Z bosons are set by the vev of the Higgs field. Gauge invariant fermion mass terms must still be added using so called "Yukawa" coupling terms, which couple the Higgs field to the fermions with arbitrary coupling parameters. This means that the fermion masses are not predicted by the SM but are instead inputs to the theory. On the other hand, the coupling of the fermions to the Higgs field is proportional to their mass, which can be tested experimentally.

Finally, an additional gauge boson, known as the Higgs boson, is also generated in the course of the spontaneous symmetry breaking. The Higgs boson is a scalar particle whose mass

is proportional to its self coupling parameter λ which, like the fermionic Yukawa couplings, is not specified by the theory. There are no strict limits from the theory on the Higgs mass other than it must be non-zero in order to undergo spontaneous symmetry breaking and it was generally thought to be below the TeV scale in order for the theory to be perturbative. However, once the mass is fixed, all other observable quantities associated with the Higgs field are specified.

It should also be noted that the Higgs mechanism provides a solution to another issue in addition to the generation of mass terms. In the SM, the longitudinally polarized $WW \to WW$ scattering amplitudes are proportional to the center of mass energy s, causing the cross section to diverge and violate unitarity at approximately the TeV scale. Introduction of the Higgs into the theory introduces diagrams which cancel the divergent terms, rendering the WW scattering probability finite.

2.2 Physics at Hadron Colliders

Particle scattering experiments have provided extensive testing grounds for the Standard Model. The parton model of the proton was developed in the 1960's by Feynman and Bjorken to explain the results of deep inelastic scattering experiments [11, 12]. The parton model treats the proton as a collection of point-like particles. For a high momentum transfer (Q^2) process such as a proton-proton collision, the individual components of the proton are predicted to interact independently due to a process known as Bjorken scaling. This greatly simplifies the calculation as one can consider the collision as a one-on-one parton scattering rather than a collection of particles colliding. This was observed to correctly predict the high energy interactions of the deep inelastic scattering experiments, but was also known to be insufficient to describe the low energy behavior of the proton.

The theory of quantum chromodynamics (QCD) was developed in the 1970s in order to describe the interactions of the quarks and gluons over a wider range of energies. QCD introduces the concepts of confinement and asymptotic freedom. Asymptotic freedom, first derived by Gross, Wilczek, and Politzer [13], is the ability of a renormalizable non-Abelian gauge theory to include interactions which decrease in strength as the energy increases. In the SM, the strong coupling constant, α_s, decreases with increasing energy, allowing perturbative calculations of QCD processes in orders of α_s for large Q^2 processes. At low energy, α_s becomes large and the perturbative calculations no longer are sufficient. The phenomenon of confinement, though as of yet not mathematically proven, is the observation that α_s is sufficiently large at low energies such that quarks can not be observed independently but always exist in colorless bound states of at least two quarks.

In perturbative QCD, the lowest order contributions in α_s correspond directly with the predictions of the parton model. Higher order terms in α_s are then considered as corrections to the lower order contributions. As in QED, the perturbative calculations include divergences which must be re-normalized in order to make meaningful predictions. The divergences are absorbed into a term known as the renormalization scale, μ_R, whose value is generally set by the Q^2 of the process. The actual value of this scale has no physical meaning, so variations of this parameter are considered when evaluating systematic uncertainties for QCD predictions (see Section 10.3.3).

In order to calculate cross sections for QCD processes, the contributions from both low and high energy processes must be considered. While the hard (high energy) processes are calculable using perturbative calculations, the low energy processes, also referred to as the long distance processes, are not and must be taken into account in other ways. The solution to this issue is the factorization theorem, which separates the high and low energy contributions to the cross section by absorbing the low energy processes into universal structure functions

known as parton distribution functions (PDFs). Specifically, the process $A + B \to C$ where A and B are hadrons consisting of partons a_i, b_j is written as:

$$\frac{d\sigma_{A+B\to C}}{dQ^2 dy} = \sum_{a_i} \sum_{b_j} \int_{x_A}^{1} d\xi_A \int_{x_B}^{1} d\xi_B \, f_{a/A}(\xi_A, \mu_F) \, f_{b/B}(\xi_B, \mu_F) \, \sigma_{a_i+b_j\to C}(Q^2, y) \tag{2.1}$$

where the $f_{A/B}$ are the PDFs which are parameterized in terms of the $\xi_{A/B}$ (which roughly correspond to the fraction of the hadron momentum carried by the parton), the hard scattering cross section σ, and the factorization scale μ_F. The PDFs are not predicted by theory but measured in previous experiments at lower energies. Extrapolation of the PDFs to higher energies is done using the Dokshitzer-Gribov-Lipatov-Altarelli-Parisi (DGLAP) evolution equations [14, 15, 16]. A number of proton PDF sets are available at the LHC energies from different collaborations, most notably the `CTEQ`[17], `MSTW`[18], and `NNPDF`[19] PDF sets. The unphysical scale parameter μ_F is needed in order to separate the low and high energy regimes and is usually chosen at a relevant scale in the question at hand, such as m_Z, and then varied in order to estimate a systematic uncertainty (see Section 10.3.3).

As already noted, the SM has had great success in making precise predictions for scattering experiments at particle colliders. For example, Figure 2.1 shows the predicted and measured production cross sections for a large number of SM processes using ATLAS data collected during LHC Run 1. The SM theory correctly predicts these phenomena over many orders of magnitude.

2.3 Search for the Higgs Boson

The experimental detection of a Higgs-like boson would provide strong evidence for the existence of the Higgs field and electroweak symmetry breaking. As of 2011, the Higgs boson had not yet been experimentally observed but limits had been placed on m_{H} (assuming the SM

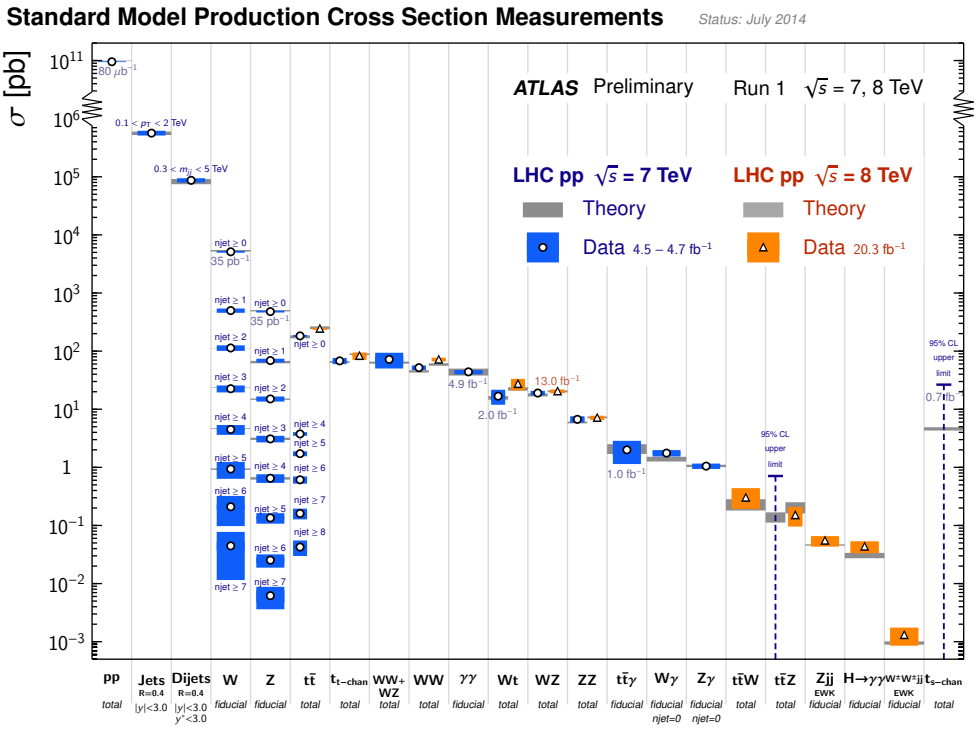

Figure 2.1: A summary of Standard Model total and fiducial production cross section measurements, corrected for leptonic branching fractions, compared to the corresponding SM theoretical predictions. The W and Z vector-boson inclusive cross sections were measured with 35 pb^{-1}of integrated luminosity from the 2010 dataset and all other measurements were performed using the 2011 dataset or the 2012 dataset.

couplings). A strong lower limit of $m_{\mathrm{H}} > 114.4$ GeV had been produced using the LEP-II data [20]. The Tevatron experiments, CDF and D0, also performed searches over a wide range of Higgs masses and had excluded the region $158 < m_{\mathrm{H}} < 175$ at 95% confidence level[21, 22, 23].

Indirect constraints on m_{H} were also possible through the precision measurements of electroweak observables. The Higgs, if it exists, makes corrections to a number of electroweak observables, most notably the W and top masses, through virtual loop diagrams. Results from a number of experiments, including LEP and the Tevatron, were combined in a global fit of electroweak parameters from which the preferred value of m_{H} could be determined [24]. The result of this fit is shown in Figure 2.2 and the best fit value of m_{H} is 87^{+35}_{-26} GeV, with

an upper limit of $m_{\mathrm{H}} < 157$ GeVat 95% confidence level.

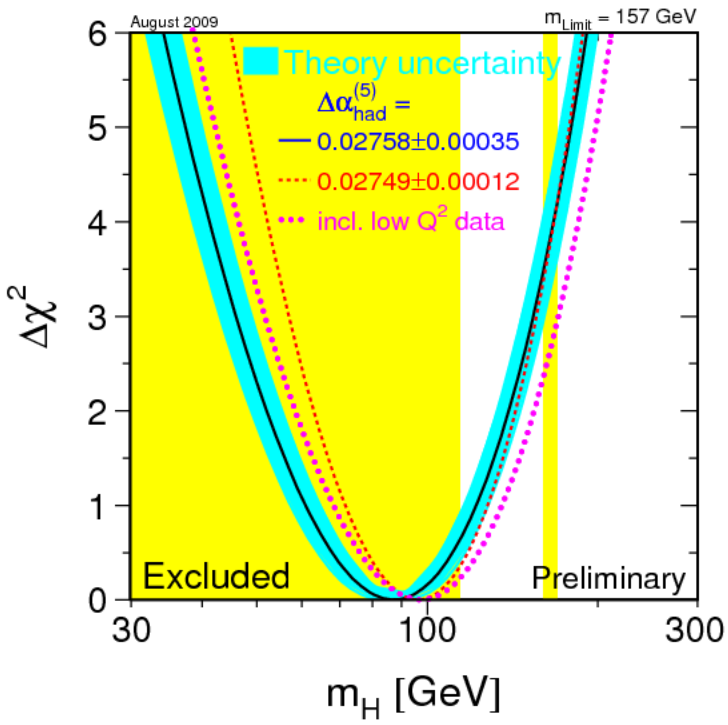

Figure 2.2: The black line with blue uncertainty band is the $\Delta\chi^2$ vs. m_{H} curve based on the results of a global fit of electroweak observables. The vertical yellow bands shows the 95% CL exclusion limit on m_{H} from the direct searches at LEP-II (up to 114 GeV) and the Tevatron (160 GeV to 170 GeV). [24]

Discovery of the Higgs boson was one of the major goals at the LHC. The dominant Feynman diagrams contributing to Higgs production at the LHC are shown in Figure 2.3 and the cross sections at $\sqrt{s} = 8$ TeV of the various production modes as a function of m_{H} are shown in Figure 2.4. The dominant production mode is gluon-gluon fusion (ggF), accounting for 87% of the total production cross section. The next largest production mode is vector boson fusion (VBF), which is notable because there is no color flow between the incoming quarks. This results in a final state with two forward jets and a central Higgs decay.

Associated production with a vector boson (VH) contributes $\sim 5\%$ to the total production cross section and associated production with a top pair ($t\bar{t}H$) is the smallest production mode considered with a cross section roughly 100x smaller than ggF.

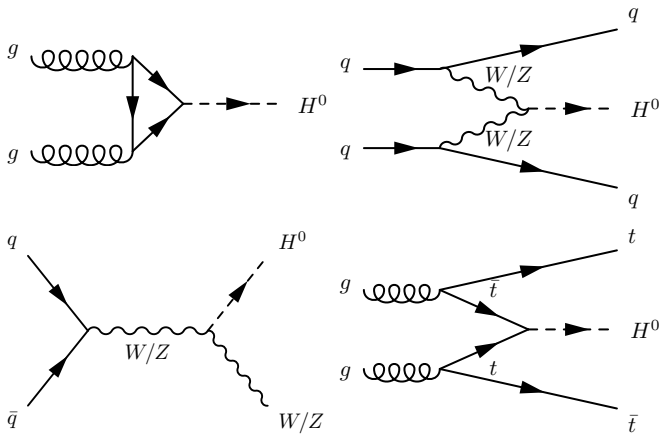

Figure 2.3: Leading order Feynman diagrams for the dominant Higgs production modes at the LHC, which from left to right are ggF, VBF(qqH), VH, and $t\bar{t}H$.

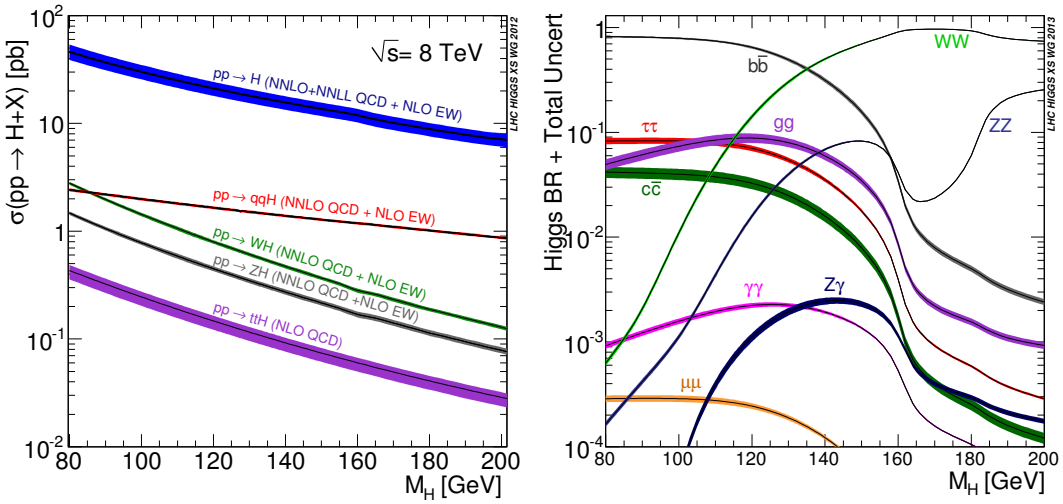

Figure 2.4: (left) Cross sections at $\sqrt{s} = 8$ TeV for the dominant Higgs production modes as a function of m_{H}, including ggF, VBF, WH, ZH, and $t\bar{t}H$. (right) Branching ratios for the Higgs decays to various final states as a function of m_{H}[25].

The branching ratios to various final states are also shown in Figure 2.4 as a function of m_{H}.

The LHC experiments have performed searches in all of these final states with varying search strategies depending on the final state. For $m_{\mathrm{H}} < 135$ GeV, the $b\bar{b}$ final state has the largest branching ratio, but the ggF production would be extremely challenging to separate from the SM di-jet backgrounds. Instead, searches are performed for $H \rightarrow b\bar{b}$ in association with a vector boson (VH production). The $H \rightarrow WW$ decay has one of the largest branching ratios over much of the m_{H} range and searches generally focus on the $\ell^+\ell^-\nu\nu$ final state. However, because of the energy lost to the neutrinos, this channel has reduced sensitivity to m_{H}. The $\gamma\gamma$ and ZZ final states both provide full reconstruction of the Higgs kinematics but are more statistically limited than the other final due to their smaller branching ratios. At $m_{\mathrm{H}} = 125$ GeV, the branching ratio of $H \rightarrow 4\ell$ ($\ell = e, \mu$) is 1.25×10^{-4}.

In July of 2012, the ATLAS and CMS collaborations simultaneously reported more than 5σ evidence of a new scalar particle with an approximate mass of 125 GeV, consistent with the SM predictions of the Higgs boson, using ~ 5 fb^{-1}each of $\sqrt{s} = 7$ TeV and $\sqrt{s} = 8$ TeV data [26, 27]. The observation was based primarily on the $\gamma\gamma$ and 4ℓ final states where a clear peak can be seen in the invariant mass distributions as shown in Figure 2.5, each with a significance greater than 3σ. The WW final state search also contributed with an observed 2.5σ excess. The local p_0 as a function of m_{H} from the combined search and the signal strength μ (the ratio of observed events to expected events from a SM Higgs boson) measured in the various final states is shown in Figure 2.6.

Since the discovery, numerous measurements have been performed in order to test whether the observed particle is consistent with the Higgs boson of the SM using the full Run 1 LHC dataset. First measurements of the bosonic and fermionic couplings have been performed by separating the candidate events into categories enriched in specific Higgs production modes [28, 29]. Measurements of the signal strength from the various production modes have been performed using a combination of the data from different final states and are shown in Fig-

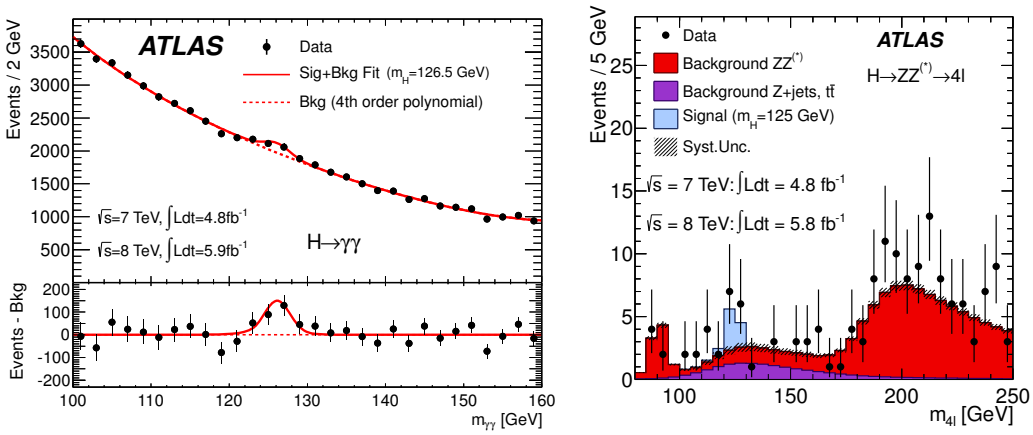

Figure 2.5: Invariant mass distributions in the ATLAS search for the Higgs boson in the (left) $H \to \gamma\gamma$ and (right) $H \to 4\ell$ final states using 4.8 fb^{-1}of $\sqrt{s} = 7$ TeV data and 5.9 fb^{-1}of $\sqrt{s} = 8$ TeV data [26].

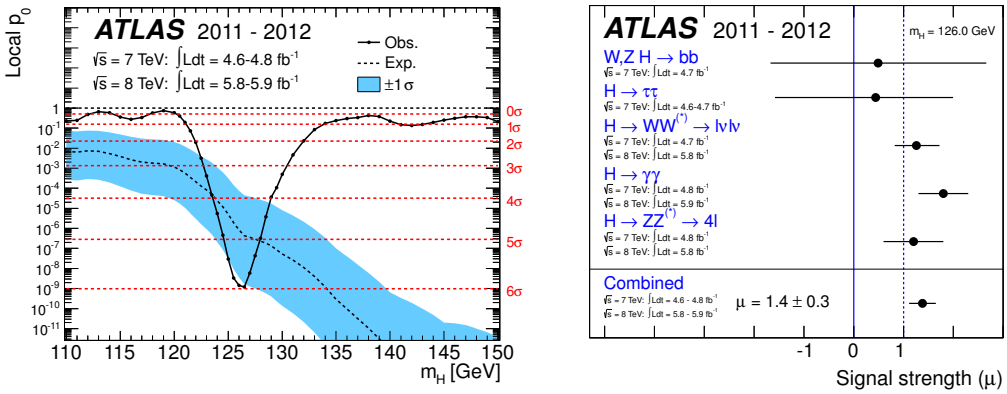

Figure 2.6: (left) Observed and expected local p_0 values as a function of m_{H} in the ATLAS search for the Higgs boson using 4.8 fb^{-1}of $\sqrt{s} = 7$ TeV data and 5.9 fb^{-1}of $\sqrt{s} = 8$ TeV data. A local p_0 of greater than 5σ is observed near $m_{\mathrm{H}} = 125$ GeV, consistent with the expectations for a SM Higgs boson. (right) Signal strength as measured in the various final states for a signal with $m_{\mathrm{H}} = 126$ GeV in the search for the Higgs boson at ATLAS using 4.8 fb^{-1}of $\sqrt{s} = 7$ TeV data and 5.9 fb^{-1}of $\sqrt{s} = 8$ TeV data [26].

ure 2.7. Spin/parity tests have also been performed to determine whether the particle is compatible with the SM prediction of $J^P = 0^+$. The $J = 1$ hypothesis can be ruled out immediately because a spin 1 particle cannot decay to two photons according to the Yang-Landau

theorem [30, 31], inconsistent with the observation of $H \to \gamma\gamma$. Analysis of the spin angles in the ZZ and WW final states favors the $J^P = 0^+$ hypothesis over alternative spin/parity hypotheses of 0^-, $1^\pm$, and 2^+ [32]. Finally, measurements of differential cross sections have been performed in the $\gamma\gamma$ final state which are complementary to the results presented in this thesis [33]. No significant deviations from the SM have been observed in any of these measurements.

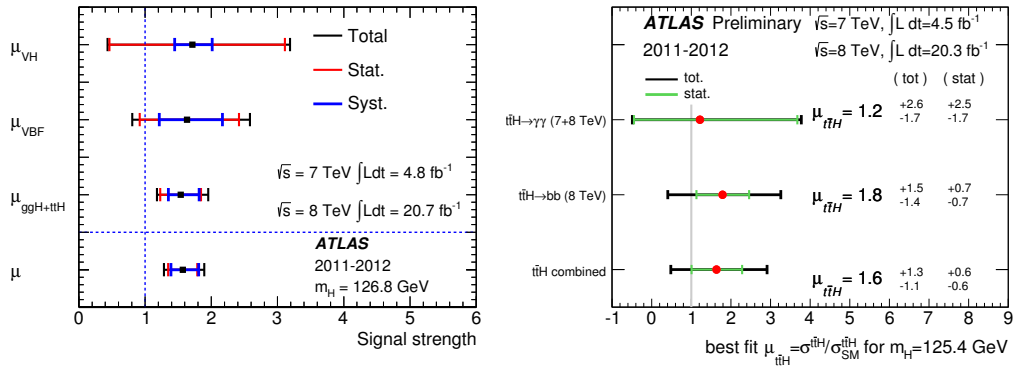

Figure 2.7: (left) Measured signal strength for the various Higgs production modes from a combination of the data in the $H \to \gamma\gamma$, $H \to 4\ell$, and $H \to WW$ final states using the full LHC Run 1 dataset [28]. (right) Measurement of the signal strength of the $t\bar{t}H$ production mode using the $H \to \gamma\gamma$ and $H \to b\bar{b}$ final states using the full LHC Run 1 dataset [34].

Searches continue for Higgs decays to other final state topologies. Preliminary results from ATLAS indicate a 4σ excess of events in the $\tau\tau$ final state consistent with the SM Higgs predictions, indicating that the observed particle couples to fermions [35]. A search has also been performed for $H \to b\bar{b}$ produced in association with a vector boson in which no excess over background is observed; a 95% confidence level limit on the cross section is set at $1.2\times$ the SM cross section [36]. The corresponding search from CMS finds a 2.1σ excess over background, consistent with the SM predictions [37]. Searches have also been conducted in final states for which the LHC experiments do not have sufficient statistics to observe a SM Higgs boson, such as $t\bar{t}H$ production, $H \to \mu\mu$, and di-Higgs production, and no significant

excesses have been observed [38, 39, 40, 41, 34].

2.3.1 Higgs Differential Cross Section Predictions

The differential cross section measurements in this thesis provide another test of the compatibility with the SM for this newly discovered scalar boson. The observed differential cross sections are compared to the results of several of the most recent theoretical calculations for Higgs production at the LHC. This section describes the tools used to make these theoretical predictions.

As shown in Figure 2.4, ggF accounts for the majority of SM Higgs production at the LHC. Therefore, the results of three different ggF calculations are combined with the results of a single set of calculations for the non-ggF modes in order to produce three sets of differential cross section predictions. All of the theoretical predictions are computed for a SM Higgs boson with $m_{\mathrm{H}} = 125.4$ GeV in $\sqrt{s} = 8$ TeV pp collisions and are normalized to the most precise SM inclusive cross section predictions currently available (See Section 6.2.1) and corrected for the fiducial acceptance derived from the Powheg simulation (see Chapter 8 for fiducial corrections).

Differential predictions for the ggF mode are provided by three calculations: Powheg [42], Powheg interfaced to Minlo [43], and HRes2 [44, 45] . Powheg provides event generation up to next-to-leading-order (NLO), with decay and showering performed by Pythia 8 [46]. FastJet [47] is used for jet reconstruction. Powheg with Minlo provides predictions for jet-related variables at NLO for Higgs boson production in association with one jet.

The HRes2 program computes fixed-order cross sections for ggF SM Higgs boson production up to next-to-next-to-leading-order (NNLO). All-order resummation of soft-gluon effects at small transverse momenta is consistently included up to next-to-next-to-leading-logarithm (NNLL), using dynamic factorization and resummation scales. The program implements top-

and bottom-quark mass dependence up to NLL+NLO. At NNLL+NNLO level only the top-quark contribution is considered. HRes2 does not perform showering and QED final-state radiation effects are not included.

The VBF differential cross sections are predicted up to NLO using Powheg [48]. The VH and $t\bar{t}H$ contributions are calculated using Pythia 8 [46].

2.4 Open Questions in the Standard Model

While the SM has proven very successful in describing a wide range of phenomena, there are questions which it has not yet answered. The following is an incomplete list of phenomena and theoretical issues which are not addressed by the SM in its current form. The following section on extensions of the SM will describe some possible solutions to these phenomena and other open issues.

2.4.1 Neutrino Masses

The neutrinos of the SM are massless because, unlike the charged leptons, there are no right handed neutrinos with which to generate Yukawa coupling terms with the Higgs field. It is generally accepted now that neutrinos do have mass based on observations of neutrino flavor oscillations [49]. For flavor oscillation to occur, the flavor eigenstates must be a mixture of unique mass eigenstates. Thus, the observation of neutrino oscillations provides strong evidence for non-zero (but small) neutrino masses.

The first indirect evidence for neutrino oscillation was discovered by the Homestake experiment, which found the solar neutrino flux to be roughly one third of the expected flux [50]. Kamiokande-II found similar evidence using atmospheric neutrinos [51]. Direct evidence of neutrino flavor oscillation was then established with atmospheric neutrinos at the Super

Kamiokande experiment [52] and later confirmed using solar neutrinos with the Sudbury Neutrino Observatory [53, 54]. Several mechanisms have been proposed to generate massive neutrinos in the SM, including the addition of sterile right handed neutrinos or Majorana neutrinos, but none have been confirmed experimentally.

2.4.2 Baryon Asymmetry

An open question in cosmology is based on the observation that only matter is observed in the universe and not anti-matter, while the observed laws of physics appear to be symmetric between both forms of matter [49]. Under the assumption that the universe began with equal parts matter and anti-matter, there must be a mechanism by which matter dominates over anti-matter in the beginnings of the Universe during a period known as baryogenesis. Sakharov proposed a set of conditions which must be satisfied in order for baryogenesis to occur, which include baryon number violation, CP violation, and C violation all occurring in a state which is not in thermal equilibrium[55]. CP violation has been observed experimentally and is included in the SM, but at rates which are too small in order to account for the observed baryon asymmetry in the universe.

2.4.3 Dark Matter/Energy

Based on observations of galactic rotational curves and gravitational lensing, there is now strong evidence for an additional form of non-luminous matter which is commonly referred to as dark matter. Furthermore, measurements of the rate of expansion of the universe also indicate an as of yet unaccounted for excess of energy, commonly referred to as dark energy. Current estimates indicate that the known matter of the SM only accounts for roughly 5% of the energy content of the universe - the rest consists of dark matter and dark energy [56]. Dark matter and energy are unaccounted for in the SM.

2.4.4 Hierarchy Problem

Unlike the other open questions of this section, the "hierarchy problem" is not based upon observation but instead is a theoretical contention. The hierarchy problem arises from the fact that there are extremely different scales needed in a theory to describe the strong, electroweak, and gravitational interactions. This gives rise to bare parameters of the theory whose values may differ from their renormalized counterparts or other parameters in the theory by many orders of magnitude. While mathematically consistent, the "fine-tuning" of these parameters may be considered unnatural and therefore undesirable in the theory.

There is not a single hierarchy problem; rather, there are several instances of it in the SM. Specifically, there is a hierarchy problem associated with the Higgs mass [49]. Because the Higgs boson is a scalar particle, its mass contains virtual corrections which generally push it many orders of magnitude higher than the electroweak scale, much higher than the observed resonance at 125 GeV. Therefore, a fine-tuned cancellation of terms is needed in order for the renormalized Higgs mass to remain below the TeV scale.

2.5 Beyond the Standard Model

While there have not been any significant deviations from the SM Higgs boson predictions for the newly discovered scalar particle at the LHC, there are still extensions of the SM which both contain a SM-like Higgs boson and solve some of the questions in Section 2.4. The following sections describe two possible extensions of the SM.

2.5.1 Supersymmetry

A large class of theories propose an additional symmetry which links fermions and bosons and is generally known as Supersymmetry (SUSY) [57]. Each particle of the SM would then

be associated with a "superpartner" whose spin differs by 1/2. Clearly, the supersymmetry must be broken as the superpartners are not observed at the same energy scales as the regular matter already observed. The symmetry breaking mechanism defines the specific models of SUSY, but in many models, after symmetry breaking, the superpartner masses are at or above the TeV scale in order to be consistent with observation.

The Higgs sector will be modified as at least one additional $SU(2)$ doublet is needed in order for a SUSY theory to be consistent. For instance, in the Minimal Supersymmetric Standard Model, the Higgs sector contains a set of five Higgs particles, with the lightest one corresponding to the new observed resonance at the LHC. Additionally, SUSY solves the Higgs mass hierarchy problem because the superpartners will introduce additional loop corrections which exactly cancel the divergent terms. SUSY theories also often naturally provide a dark matter candidate in the form of the lightest superpartner, a stable neutral particle which cannot decay to SM particles. Many searches for signatures of SUSY have been performed at the LHC but no evidence of SUSY has been found.

2.5.2 Extra Dimensions

Another set of theories propose the existence of extra dimensions beyond the 3+1 space-time dimensions we directly observe in order to incorporate gravity into the SM [49]. The fields of the SM only couple weakly to the extra dimensions while gravity (via the graviton) couples strongly, reducing the strength of the gravitational force relative to the electroweak and strong forces and solving the hierarchy problem. In order for the extra dimensions to be hidden, they are proposed to be small and compact. The phenomenology of the various models with extra dimensions depends on the number and geometry of the additional dimensions but most models result in so called Kaluza-Klein particles. These additional resonances could potentially provide a dark matter candidate [58] or modify Higgs production at the LHC [59].

Chapter 3

The ATLAS Detector

The ATLAS experiment [60] is one of four large experiments located at the LHC. The ATLAS detector is a multi-purpose particle detector with roughly 4π coverage and consists of four main detector components: the Inner Detector (ID), the calorimeter system consisting of liquid Argon (LAr) and Tile calorimeters, the Muon Spectrometer (MS), and the magnet system consisting of both solenoidal and toroidal magnets. Furthermore, a triggering system, which is essential due to the high luminosity of the LHC, is integrated into the calorimeter and MS systems. A cut-away view of the ATLAS detector is shown in Figure 3.1. The full detector is roughly 44 m in length and 25 m in diameter, weighing nearly 7000 metric tons [60].

The ATLAS coordinate system is defined as follows: the nominal interaction point is defined as the origin of the coordinate system, while the anti-clockwise beam direction defines the z-axis and the x-y plane is transverse to the beam direction. The positive x-axis is defined as pointing from the interaction point to the center of the LHC ring and the positive y-axis is defined as pointing upwards. The azimuthal angle ϕ is measured around the beam axis and the polar angle θ is the angle from the beam axis. The pseudorapidity is defined as $\eta = -\ln(\tan(\theta/2))$. The positive z side of the detector is designated the A-side, while the negative z side of the detector is designated the C-side. The transverse momentum p_{T} and

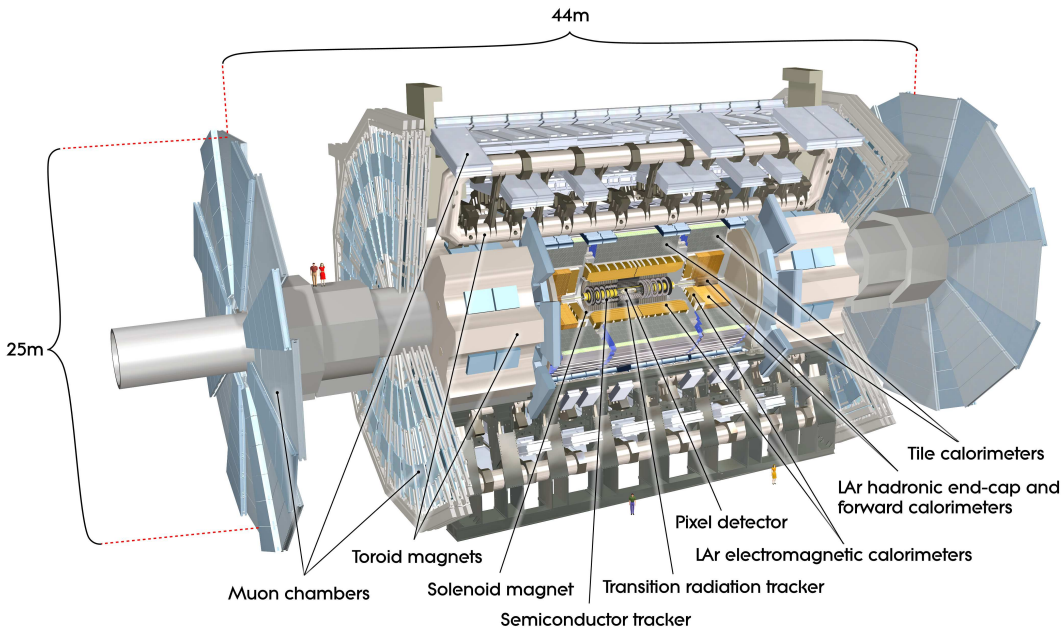

Figure 3.1: Cut-away view of the ATLAS detector [60].

transverse momentum E_{T} are the components of the momentum or energy in the x-y plane. The separation of two objects in angular space is defined as $\Delta R = \sqrt{\Delta\eta^2 + \Delta\phi^2}$.

The ID and its subdetectors are described in detail in Section 3.1 as the geometry is relevant in Chapter 4. A brief description of the calorimeters is given in Section 3.2 and the Muon Spectrometer is described in Section 3.3. The triggering scheme is described in Section 3.4.

3.1 Inner Detector

The ATLAS Inner detector (ID) is designed to measure the trajectories of charged particles with $p_{\mathrm{T}} > 500$ MeV within $|\eta| < 2.5$. The ID consists of three separate sub-detectors with an outer radius of 1.15 m, all contained within a 2 Tesla solenoid magnet. Each sub-detector is divided into barrel and end-cap elements and a cut-away view is shown in Figure 3.2. The

layout of the sensitive detector elements in both the barrel and end-caps of the ID with a $p_{\mathrm{T}} = 10$ GeV track passing through them can be seen in Figure 3.3 .

At the innermost radius is the Pixel detector, a silicon pixel tracker which provides high resolution position and vertexing measurements very close to the interaction point. The Semi-Conductor Tracker (SCT) is a silicon strip tracker located outside the Pixel detector which provides more precision position measurements of the track trajectory. Generally speaking, silicon sensors are composed of thin, high-purity doped silicon wafers. As a charged particle traverses the wafer, energy is deposited into the silicon and electron-hole pairs are created. A bias voltage is applied to the silicon and these electron-hole pairs are collected as currents read out by the front-end electronics on the surface of the silicon. Due to detector material and budgetary concerns, silicon trackers generally rely on a small number of very high precision measurements (usually at the micron level) to measure track trajectories.

At the outermost radius of the ID is the Transition Radiation Tracker (TRT), a straw-tube tracker which provides additional position measurements and particle identification capabilities. Each straw in the TRT is strung with a wire which is held at a positive electric potential with respect to the straw wall (see the diagram in Figure 4.1). As a charged particle traverses the straw, gas molecules within the straw are ionized. The ionization electrons accelerate towards the wire due to the electric field in the straw. As they gain energy, the electrons ionize additional gas molecules and an avalanche of electrons is created, which is read out as a current on the wire in the front-end electronics. Gas-based detectors generally provide a much less precise hit position measurement as compared to silicon trackers, but in the TRT this is compensated by the large number of recorded hits.

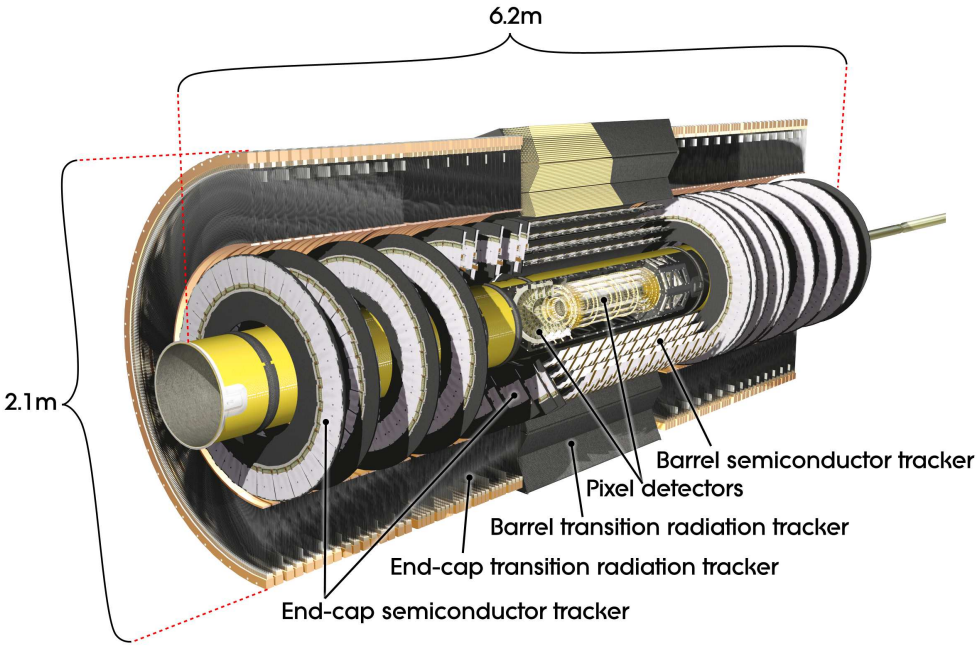

Figure 3.2: Cut-away view of the Inner Detector [60].

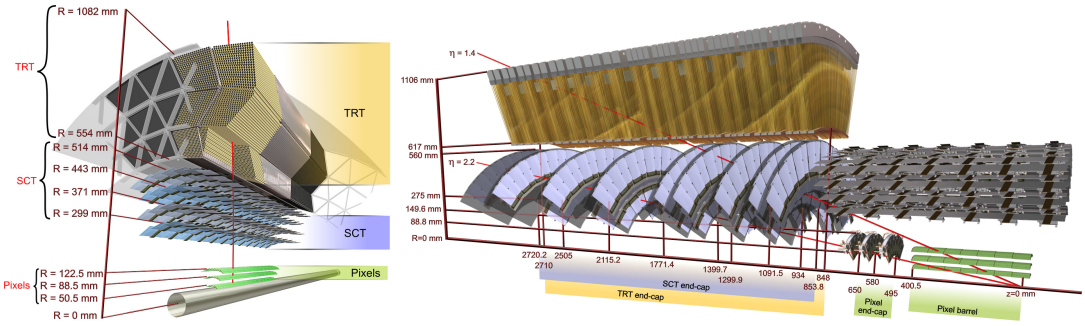

Figure 3.3: Schematic view of the Inner Detector active elements in the barrel on the left and the end-cap on the right [60].

3.1.1 Pixel Detector

The Pixel Detector consists of 1744 silicon sensors with dimension 19×63 mm^2, arranged in 3 barrel layers and in 3 end-cap rings on either side of the barrel (see Figure 3.3). The first layer in the barrel is referred to as the "B"-layer and is directly attached to the beam-pipe. The pixels have a nominal size of 50×400 μm^2 based on the readout pitch of the front end electronics. Roughly 10% of the pixels which are located near front-end chips are larger at 50×600 μm^2. Every sensor is identical and contains ∼46k readout channels, giving a total of ∼80 M readout channels [60].

The high-radiation environment near the collision point provides strict constraints on the design and operation of the silicon detectors. The pixel sensors are constructed using oxygenated n-type silicon wafers with a thickness of 250 μm and the readout pixels are located on the n^+-implanted side of the sensor. The sensors are designed to be operated with an initial bias voltage of $\sim$ 150 V, which will increase up to $\sim$ 600 V over the lifetime of the detector as the radiation dose accumulates. The pixels must be operated in the temperature range -5°C to -10°C in order to control noise levels after radiation damage [60].

The Pixel detector provides an average of 3 hits per track, covering $|\eta| < 2.5$. The intrinsic hit resolution is 10 (115) μm in the R-ϕ (z) plane for the barrel and 10 (115) μm in the z-ϕ (R) plane for the end-cap rings [60].

3.1.2 Semi-Conductor Tracker

The SCT consists of 15912 modules, arranged in 4 barrel layers and arranged in 9 end-cap rings on either side of the barrel (see Figure 3.3). Each module contains two back-to-back silicon sensors, each with a thickness of 285 μm and with 768 active silicon microstrips of length 12 cm. The strips in the rectangular barrel sensors are arranged parallel to z with a

pitch of 80 μm and the strips in the trapezoidal end-cap sensors are arranged radially with a mean pitch of ∼80 μm. The strips within each module are arranged with a stereo angle of ∼40 mrad in order to provide measurements in the coordinate parallel to the strips. The total number of readout channels is approximately 6.3 million [60].

A track has an average of 8 SCT hits giving 4 space points (2 hits per module) within the range $|\eta| < 2.5$. The intrinsic hit resolution is 17 (580) μm in the R-ϕ (z) plane in the barrel and 17 (580) μm in the z-ϕ (R) plane in the end-caps. The z (R) measurement in the barrel (end-caps) is much less precise as it is derived from the stereo angle between back to back sensors on each SCT module [60].

3.1.3 Transition Radiation Tracker

The TRT was designed to provide both charged particle tracking and particle identification capabilities. The TRT consists of a barrel and 2 end-cap segments composed of thin-walled straws made of polyimide and carbon fiber (diameter of 4 mm) filled with an active gas, a mixture of Xe (70%), CO_2 (27%), and O_2 (3%). Each straw is strung with a gold plated tungsten anode wire (diameter of 31 μm) and the straw wall is held at ∼ -1500 V with respect to the wire, creating a strong electric field within the gas. Charged particles ionize the gas, creating a detectable current on the wire. The TRT position measurement is much less precise than that of the silicon trackers, but this is compensated by the large number of measurements of the track trajectory which are made. The TRT additionally provides electron/hadron discrimination through the production and detection of transition radiation.

3.1.3.1 TRT Geometry

The 52,544 straws in the TRT barrel are 144 cm in length and are arranged parallel to the LHC beam in 96 modules ranging from $r = 554$ mm to $r = 1082$ mm. The modules are arranged

into 3 rings with 32 modules each. The modules are arranged such that no cracks are available for charged particles to pass through undetected (see Figure 3.3). The inter-straw space is filled with 19 μm-diameter polypropylene fibers for production of transition radiation.

The wire in each barrel straw is split electrically using a glass joint in the center such that both ends of the wire can be read out independently, giving a total of 105,088 readout channels. The nine straw layers closest to the beam line are split twice in order to reduce the occupancy expected at the nominal LHC luminosity. These straws have a shorter active region of $\sim$32 cm and are therefore referred to as "short straws".

The TRT has two end-caps (one on either side of the barrel), each consisting of 122,880 straws with length of 37 cm. The end-cap straws are arranged radially with uniform azimuthal spacing in end-cap wheels. Each wheel consists of 8 layers of straws (768 straws per layer) interleaved with layers of 15 μm thick polypropylene radiator foils. Each end-cap consists of 12 type-A wheels in which the straw layers are separated by 8 mm and 8 type-B wheels in which the straw layers are separated by 15 mm. The A-type wheels are located at smaller $|z|$ and have smaller straw spacing in order to maintain the roughly constant number of straws that a particle will traverse.

The TRT was originally designed to cover the range $|\eta| < 2.5$ but, due to constraints from detector powering and cooling services, the end-caps were shortened to cover the range $|\eta| < 2.0$. A track will traverse at least 36 TRT straws, with the exception of the barrel-to-end-cap transition region $0.8 < |\eta| < 1.0$ where this decreases to 22 straws. The expected hit position resolution is 130 μm.

3.1.3.2 Calibration of the Drift Time Measurement

As described previously, an avalanche of ionized electrons is created in the active gas of the straw whenever a charged particle crosses a straw. The primary ionizations drift to to

the anode wire with a drift velocity of approximately 50 μm/s and create a current with a typical gain of 2.5×10^4. This current travels down the wire and is read out by the front-end electronics. A charged particle creates 5-6 primary ionizations per mm on average and the primary ionization closest to the wire will arrive first at the front end electronics. Therefore, the measurement of the arrival time of the signal current is used to determine the distance of closest approach of the track trajectory and is known as the drift time measurement. The maximum drift time for a TRT straw is $\sim$ 50 ns.

The drift time measurement is performed by the front-end electronics located at the end of each straw, consisting of two custom ASIC components: the Amplifier, Shaper, Discriminator, and Baseline Restoration (ASDBLR) and the Drift Time Measuring ReadOut Chip (DTMROC). The ASDBLR is responsible for amplifying and shaping the signal from the wire and quickly restoring the wire current to its baseline. Additionally, it has two discriminators which for data-taking are set at a low threshold ($\sim$ 250 eV) for tracking of minimally ionizing particles and at a high threshold ($\sim$ 6 keV) for detection of transition radiation. The DTMROC performs the drift time measurement by digitizing the discriminator outputs into 3.12 ns bins for the low threshold and 25 ns bins for the high threshold. Each ASDBLR receives input from up to 8 straws and each DTMROC digitizes the output of 2 ASDBLRs.

The DTMROC stores the digitized output into a buffer and upon receiving a trigger sends three bunch crossings (75 ns) of digitized output to the TRT ReadOut Driver (ROD), corresponding to 24 (3) bits of low (high) threshold data. The ROD collects, compresses, and packages the output of up to 120 DTMROCs and sends the data fragment to the central ATLAS DAQ system.

Calibration of the drift time measurement is necessary in order to provide the best estimate of the track-to-wire distance, r_{track}. The first 0$\rightarrow$1 transition in the digitized output of the DTMROC is defined as the leading edge of the signal, t_{LE}. Initial coarse timing adjustments

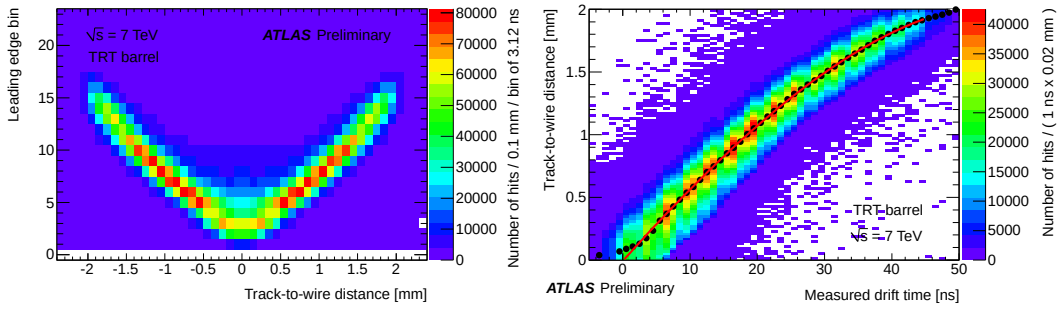

Figure 3.4: Measured leading edge time bin as a function of the track-to-wire distance in $\sqrt{s} = 7$ TeV collision data in the TRT barrel on the left. The calibrated r-t relation is shown on the right.

with 25 ns granularity (1 bunch crossing) were performed using cosmic data, synchronizing the 75 ns readout window throughout the detector. Figure 3.4 shows the leading edge time bin versus r_{track} for hits used in the reconstructed track fit using collision data in the TRT barrel, showing that the signals throughout the detector are synchronized.

The primary goal of the calibration is to characterize the the r-t relation, the relation between the drift time t and r_{track}, which is shown in Figure 3.4. The leading edge t_{LE} of the signal depends on a time offset T_0 and the drift time t. T_0 accounts for the timing of the particle collision, the time of flight of the particle to the straw, and the signal propagation time along the wire and in the front-end electronics. At the granularity of the DTMROC, these three time offsets have been shown to not vary significantly so they are absorbed into a single calibration constant T_0 [61].

The r-t relation has been characterized using a third order polynomial as shown in Equation 3.1, which was chosen because it is a simple function that describes the r-t dependence reasonably well. The four coefficients of the polynomial function are fit to the data separately for the barrel and end-caps because the r-t relation is expected to be slightly different due to the differing orientation of the straws with respect to the magnetic field. Furthermore, the A-side and C-side of the detector are calibrated separately even though they are not expected

to differ as a cross check.

$$
\begin{aligned}
f(t) &= a_0 + a_1 t + a_2 t^2 + a_3 t^3 \\
r(t) &= \begin{cases} 0 & : f(t) < 0 \\ f(t) & : 0 < f(t) < R_0 \qquad (R_0 = 2\text{mm}) \\ R_0 & : f(t) > R_0 \end{cases}
\end{aligned}
\tag{3.1}
$$

Therefore, the calibration procedure must determine the T_0 constants (one per DTMROC) and the 16 parameters of the r-t relations (4 per detector region). As the T_0 and r-t parameters are correlated, the parameters are determined in an iterative procedure in which the r-t parameters are derived using fixed T_0 parameters in each iteration and vice versa. This procedure is iterated until the parameters have converged.

To determine the r-t parameters, the hits from reconstructed tracks are divided into 1 ns wide bins of measured t. In each bin, the distribution of r_{track} for these hits is fit using a Gaussian function $G(\mu, \sigma)$ in order to determine the peak position μ of the distribution (shown as the black points in Figure 3.4). The measured μ as a function of t is then fit using the function in Equation 3.1. There is an ambiguity in that the a_0 term of the polynomial is degenerate with a constant shift in T_0. Therefore, one point of the r-t relation is fixed by definition to be $r(t = 18\text{ns}) = 1$ mm, which is in the middle of straw and produces $r(t = 0) \approx 0$ mm.

An example of the derived r-t relation is shown in Figure 3.4 for $\sqrt{s} = 7$ TeV collision data in the TRT barrel region. The fitted function describes the r-t relation well, with the exception of the points near $t \approx 0$, where the track-to-wire distance is strictly positive. The calibration procedure is performed for every ATLAS run and the calibration constants are updated only when significant changes in the calibration constants occur. The constants were observed to be stable but were updated several times over the course of data-taking during

2010-2012, most frequently due to changes in the arrival time of the LHC clock signal. The calibration directly affects the hit position resolution and thus the tracking performance, which is described in more detail in Section 4.3.

3.1.3.3 Transition Radiation

The production and detection of transition radiation (TR) is one of the unique features of the TRT detector. Transition radiation may be produced whenever a highly relativistic charged particle crosses a boundary between materials with differing dielectric constants. The TR photons are generally soft X-rays (energy of 1-30 keV for the TRT) and are emitted with a rate proportional to γ and an angle $1/\gamma$ with respect to the particle trajectory. Because electrons have a mass which is roughly 250 times smaller than pions, electrons will have a much higher rate of TR emission than pions of the same energy. Therefore, the detection of these TR photons allows for electron/pion discrimination.

However, the probability of emitting a TR photon at each boundary is small, so many transitions are needed in order to produce a detectable signal. Therefore, the space between the TRT straws is filled with radiator materials which have been optimized for production of transition radiation. In the straw, xenon was chosen as the primary active gas due to its large absorption cross section for TR photons (the carbon dioxide and oxygen are added for stability). Absorption of these TR photon results in a large number of primary electrons and consequently produces a much larger signal than that of a minimally ionizing particle, passing the high threshold of the ASDBLR. Therefore, the presence of high threshold hits on a track are evidence of transition radiation.

The fraction of high threshold (HT) hits on track is the primary TRT observable used for electron/pion discrimination.[1] The HT hit probability, measured as the ratio of HT hits to all hits in a given track sample, has been studied using both electron and pion candidates

in order to validate the modeling of transition radiation production and detection. This is important as mismodeling of the HT probability would lead to mismodeling of the electron selection efficiency because the HT fraction is used in the electron selection criteria later in this analysis.

A high purity sample of electron candidates ($> 95\%$ in simulation) is selected from $Z \to ee$ decays and photon conversions, covering the range $\gamma \sim 10^3 - 10^5$, using a tag and probe technique. In the tag and probe technique, a tag electron is selected using strict selection criteria and the probe, which is selected using looser criteria, is used to measure HT probability such that the measurement is unbiased by the candidate selection. If both electrons in an event pass the tag criteria, then both are used as probe candidates. For this measurement, the both tag and probe electrons are required to to pass the calorimeter based "medium" [62].

Pion candidates are selected from a minimum bias selection of tracks. A veto is applied to tracks coming from photon conversion candidates to suppress electrons and a requirement of $\mathrm{d}E/\mathrm{dx} > 1.6$ MeVg^{-1}cm^{-2} as measured in the Pixel detector is applied in order to suppress protons (and to a lesser extent kaons). The main background sources in the pion sample are protons and kaons and the purity of the pion sample varies from 95% at $\gamma \sim 10^0$ down to 60% at $\gamma \sim 10^3$ as estimated in the simulation [62].

The high threshold probability as a function of γ in the TRT barrel region is shown in Figure 3.5 for both the data and simulation using these selected samples of electron and pion candidates. For the pion candidates at low γ, the average HT hit probability is roughly 0.05, which arises due to large energy deposits from the tails of the Landau $\mathrm{d}E/\mathrm{dx}$ distribution which produce HT hits. A small increase in HT probability with γ is also observed for the pions, which is due to the increasing average $\mathrm{d}E/\mathrm{dx}$ with γ. A clear turn-on is observed in

[1] One may also use the Time over Threshold (ToT) for particle identification purposes, particularly at low momentum, but this is beyond the scope of this thesis.

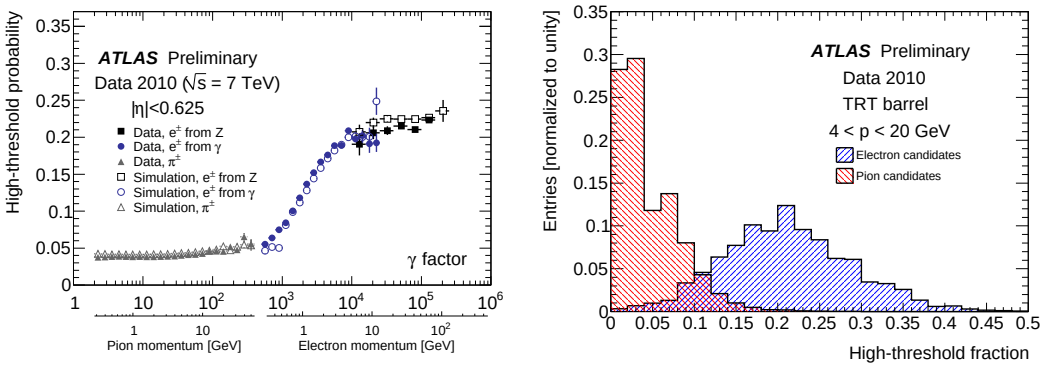

Figure 3.5: The plot on the left shows the probability to observe a high threshold hit as a function of the particle's Lorentz factor γ for electron and pion candidates in the TRT barrel region using $\sqrt{s} = 7$ TeV collision data and simulation. The plot on the right shows the distribution of the fraction of high threshold hits on track for the same candidates, showing good separation between electrons and pions [62].

the range $\gamma \sim 10^3 - 10^4$, where the HT probability rapidly increases from 0.05 to 0.2. Above $\gamma \sim 10^4$, the HT probability plateaus due to detector saturation effects. Figure 3.5 also shows the HT fraction for the electron and pion candidates, showing good separation [62].

3.2 Calorimetery

The primary purpose of the calorimetery system in ATLAS is to contain and measure particles which interact electromagnetically (photons and light charged particles such as electrons) and strongly (protons, kaons, pions, etc.). In an electromagnetic calorimeter, photons interact with the strong electric field of the heavy atomic nuclei and consequently decay via pair-production into electron-positron pairs. The electrons and positrons then proceed to lose energy primarily via bremsstrahlung photons (which in turn decay into $e^{\pm}$ pairs and so forth), creating a "shower" of electromagnetic energy which is sampled by the calorimeter. The typical distance in a material for which an electron will lose 1/e of its energy is defined as the radiation length X_0. Similarly, strongly interacting particles lose energy in the hadronic calorimeters

via strong interactions with the atomic nuclei, creating showers of hadronic particles whose energy is sampled by the calorimeter. The typical length over which 1/e of the hadronic energy is absorbed is defined as the absorption length λ.

The ATLAS calorimetery system uses two technologies: (1) high granularity liquid-argon (LAr) sampling calorimeters and (2) steel/scintillating tile sampling calorimeters. The LAr detectors are placed outside of the ID solenoid and consist of a barrel segment, two end-cap segments (each containing an electromagnetic and a hadronic sampling calorimeter) and two forward calorimeters (FCal). The tile calorimeter is consists of a barrel segment and two extended barrel segments. The entire calorimeter system provides ϕ-symmetric coverage up to $|\eta| < 4.9$ [60].

The precision electromagnetic (EM) calorimeters are LAr calorimeters using accordion-shaped lead and steel plate absorbers, with three readout layers in the barrel ($|\eta| < 2.5$) and two layers in the outer η regions. The precision position measurement in the barrel is achieved using a fine η segmentation of the first layer of the calorimeter. A pre-sampler is located in front of the barrel calorimeter ($|\eta| < 1.8$) which provides a complementary energy measurement before a portion of the detector services. Additionally, a copper/LAr calorimeter is placed in the forward region ($3.1 < |\eta| < 4.9$) to provide full η coverage. The EM calorimeters consist of between 23 and 39 radiation lengths X_0 of material depending on η [60].

The hadronic calorimeters are located outside of the EM calorimeters. In the barrel region ($|\eta| < 1.7$), tile hadronic calorimeters, composed of steel absorber plates with scintillating tiles, are sufficiently deep with 9.7 absorption lengths (λ) of active detector material to both provide good jet energy resolution and reduce calorimeter punch-through due to jets to levels well below the irreducible level of prompt or decay muons. The end-cap hadronic calorimeter is a copper/LAr sampling calorimeter covering the range $1.5 < |\eta| < 3.2$ and the forward

region ($3.1 < |\eta| < 4.9$) is covered by the forward hadronic calorimeter, using a combination of copper and tungsten absorbers with LAr. The full hadronic calorimeter system provides at least 10 absorption lengths of material over the entire η range [60].

3.3 Muon Spectrometer

Muons, though charged, interact minimally with the calorimeters because the probability of emission of bremmstrahlung, the primary energy loss mechanism for electrons in the calorimeter, is proportional to $1/m^2$. Therefore, the muon spectrometer (MS) is designed to track the trajectories of charged particles which are not stopped in the calorimeters, which are almost exclusively muons. The MS uses a combination of monitored drift tube (MDT) and cathode strip chamber (CSC) technologies for the precision tracking measurements and a combination of resistive plate chambers (RPC) and thin gap chambers (TGC) for triggering capabilities. Additionally, a system of three large air-core toroids provides a magnetic field for bending of the muon trajectories, allowing measurement of the muon momenta.

A schematic of the muon spectrometer geometry is shown in Figure 3.6. The precision tracking measurement is performed primarily using MDTs mounted in chambers, each consisting of 3 to 8 layers of MDTs. The MDT consists of a pressurized drift tube (diameter = 29.97 mm) of variable length depending on detector placement operating at 3 bar with Ar/CO_2 as the active gas. The barrel MDT chambers are arranged in three concentric cylindrical layers around the beam line, covering the range $|\eta| < 1.05$. The end-cap MDT chambers are arranged in four wheels aligned in the $|z|$ plane at distances from 7 m up to 20 m from the interaction point, allowing measurements up to $|\eta| < 2.7$. In the wheel closest to the interaction point, the innermost chambers covering the range $2.0 < |\eta| < 2.7$ have been designed with CSCs in order to handle the large particle fluxes expected in this forward region [60].

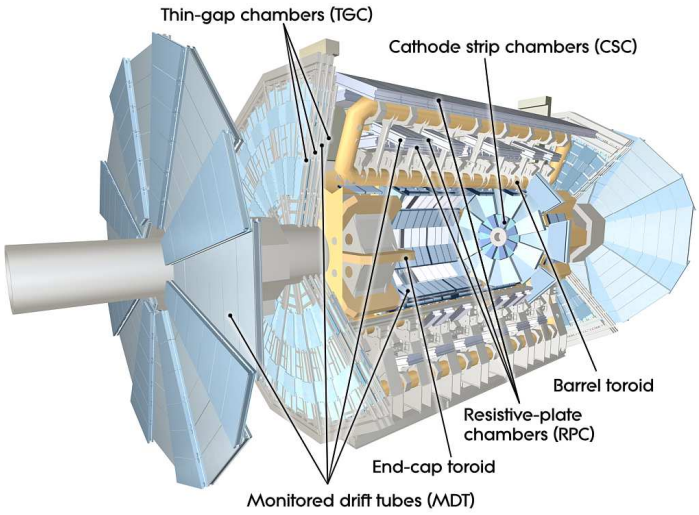

Figure 3.6: Schematic of the muon system layout [60].

The muon triggering system is composed of RPCs and TGCs and allows triggering of muons with full ϕ coverage up to $|\eta| < 2.4$. The barrel region is outfitted with three layers of RPCs arranged in concentric cylindrical layers attached to the MDT chambers, allowing a rough measurement of the muon momentum at the trigger level. The end-cap regions are instrumented with TGCs in four layers mounted on the end-cap wheels. The additional layer is needed in the end-caps in order to reduce the backgrounds due to combinatorics in the more forward regions [60].

3.4 Trigger

A trigger system is required in order cope with the expected design instantaneous luminosity of $1 \cdot 10^3 4\text{cm}^{-2}\text{s}^{-1}$ delivered by the LHC, reducing the event rate from the maximum rate of ∼40 MHz (the LHC bunch crossing rate) to 400 Hz for offline processing and storage[2]. A triggering system consisting of three levels, known as L1, L2, and event filter (EF), has been implemented in ATLAS to trigger on a wide range of final states including muons,

electrons, photons, jets, hadronically decaying τs and large missing transverse energy. Each level receives events as input from the previous level and refines the trigger decision using progressively larger sections of the detector readout.

The L1 trigger uses a small subset of detector information to make a trigger decision within 2.5 μs, reducing the trigger rate to a design maximum of 100 kHz. The L1 trigger is implemented using various detector technologies throughout ATLAS in order to trigger on the various physics objects of interest. High transverse momentum muons are triggered using the RPC and TGC chambers in the Muon Spectrometer and reduced granularity information from the calorimeters is used to trigger on electrons, photons, and other particles stopped in the calorimeter.

The L1 information from the various detectors is gathered by the Central Trigger Processor (CTP) which is responsible for maintaining a "menu" of trigger items and controlling the trigger rate such that detector dead-time is not introduced during data-taking. The CTP does so by applying pre-scales to the various trigger menu items as necessary in order to stay within the detector bandwidth limits. Additionally, the L1 trigger system produces one or more Regions-of-Interest (RoI's) for the regions of the detector in η and ϕ where interesting features have been identified based on the L1 trigger information. The RoI contains information on both the feature type and and the criteria it passed, such as energy thresholds within the calorimeter for example.

Events passing the L1 trigger selection are passed to the L2 trigger system, including the RoI's. The L2 trigger uses full detector readout information within the RoI's (accounting for roughly 2% of the total event data) in order to make a trigger decision with an average event processing time of 40 ms. The L2 system maintains a its own menu of trigger items and is

[2]The maximum limit on the event recording rate is primarily limited by data processing and storage (and thus financial) reasons.

designed to reduce the trigger rate to 3.5 kHz. Events passing the L2 trigger are sent to the event filter, where the full event information is used to make a final trigger decision using reconstruction procedures similar to the offline reconstruction, reducing the trigger rate to 400 Hz.

Chapter 4

ID Alignment and Tracking Performance

The ATLAS physics program requires unbiased, high resolution measurements of all charged particle kinematic parameters in order to produce accurate invariant mass reconstruction, efficient track vertex finding, and other high quality track-related measurements. These measurements depend critically on the proper alignment of the detector elements within the tracking system. It is also essential that alignment related systematic effects be well understood in order to reduce systematic uncertainties which will be propagated to all analyses using tracking measurements. In particular, the $H \to 4\ell$ measurements depend critically on the muon ID momentum measurement because the muons from the Higgs decay are typically in a momentum regime where the ID tracking resolution is better than the MS tracking resolution.

This chapter describes studies performed in order to measure and improve the tracking performance of the ID through detector alignment. Section 4.1 begins with a basic description of the tracking algorithms used in ATLAS followed by a description of the baseline χ^2 alignment algorithm used to align the the detector elements in Section 4.2. Section 4.3 details the results of studies of the TRT tracking performance before and after the alignment was performed. Section 4.4 concludes this chapter with a description of alignment weak modes and the algorithms developed to detect and remove them.

4.1 Inner Detector Tracking

As a charged particle traverses the ID, it leaves deposits of energy in the various detector elements which are known as detector hits. These hits are combined together to form a track from which the particle's momentum can be inferred. The combination of hits and measurement of track parameters is called a tracking algorithm.

The goal of the ID tracking algorithm is to produce measurements of charged particle tracks within the ID acceptance with high efficiency while simultaneously suppressing fake tracks due to hit combinatorics. The track measurements are parameterized as follows:

$$\boldsymbol{\tau} = (z_0, d_0, \phi_0, \theta, q/p) \tag{4.1}$$

where z_0 and d_0 are the longitudinal and transverse impact parameters measured with respect to the nominal interaction point, respectively. ϕ_0 is the azimuthal angle of the track and θ is the polar angle. Finally, q/p is the charge of the track divided by its momentum.

The ID tracking algorithm begins by seeding tracks from the collection of silicon detector hits in an event. A track seed is defined as a collection of three 3-dimensional space-time points which are derived from hits within single detector modules[63]. These track seeds are used to define a loose search window from which hits are collected and a track candidate is built using a combinatorial Kalman filter[64]. An ambiguity resolver algorithm then scores and ranks the track candidates in order to remove fake tracks which come from hit combinatorics. The surviving track candidates are then extrapolated into the TRT in order to add hits to the track which improve the track parameter resolution. Back-tracking is also used to find additional tracks, in which tracks are seeded in the TRT and extrapolated back in to the silicon detectors. Validation of the tracking algorithm performance was performed on the early LHC data with low pile-up and good agreement was observed between the data and the

simulation[63].

For tracking and alignment studies, several quality criteria are applied to ID tracks in order to suppress the fake track backgrounds. Requirements on the number of hits on track are made: at least 1 Pixel hit, at least 6 SCT hits and at least 15 TRT hits. Tracks coming from the nominal interaction point are selected by requiring $|d_0| < 10$ mm and $|z_0| < 300$ mm. Finally, a transverse momentum requirement of $p_{\mathrm{T}} > 2$ GeV is applied to remove low p_{T} tracks which are subject to large multiple-scattering effects.

4.2 Inner Detector Alignment

After assembly and installation of the ID, the relative positions of the various detector elements were known with much less precision than the intrinsic resolution of those elements. To fully utilize the tracking potential of the ID, the position and orientation of the detector elements must be determined in-situ. Alignment procedures were developed during the course of the LHC Run 1 with the goal of determining these positions so as not to significantly degrade the hit position resolution by more than 20% with respect to the intrinsic detector resolution. For the silicon trackers, this corresponds to determining the location of detector elements to within 10 μm of their true positions. The following sections describe the alignment framework and the validation of the alignment results.

4.2.1 Alignment Algorithm

The track based alignment algorithm used in ATLAS is based upon the minimization of the track to hit residual vectors (henceforth referred to as hit residuals). The residual vector points from a measured detector hit to the nearest extrapolated track position within that detector element. For example, the TRT hit residual is depicted in Figure 4.1. To minimize

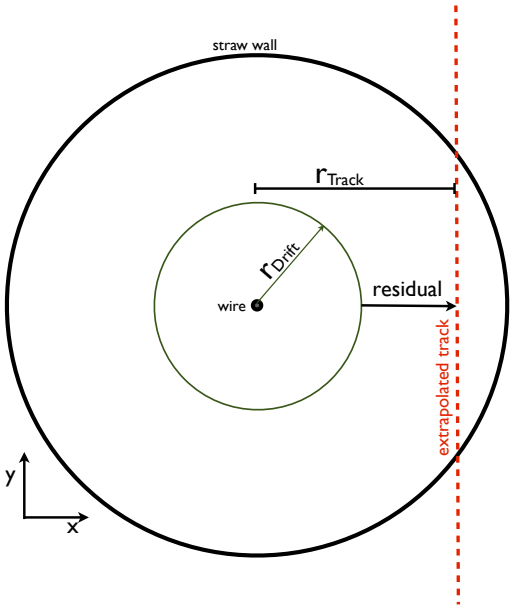

Figure 4.1: Idealized view of a track hit residual vector within a TRT straw.

the residuals, one constructs a χ^2 as in Equation 4.2, where $\mathbf{r}(\boldsymbol{\tau}, \mathbf{a})$ is the vector of hit residuals associated to a given track.

$$\chi^2 = \sum_{tracks} [\mathbf{r}^T(\boldsymbol{\tau}, \mathbf{a})\mathbf{V}^{-1}\mathbf{r}(\boldsymbol{\tau}, \mathbf{a})] \tag{4.2}$$

where $\boldsymbol{\tau}$ are the track parameters (as in Eqn. 4.1 and $\mathbf{a}$ are the alignment parameters of the detector elements. $\mathbf{V}$ is the covariance matrix of the hit residuals as measured in the tracking algorithm. One then minimizes the χ^2 with respect to the alignment parameters:

$$\frac{d\chi^2}{d\mathbf{a}} = 0 \Rightarrow \sum_{tracks} \left[\left(\frac{d\mathbf{r}}{d\mathbf{a}} \right)^T \mathbf{V}^{-1}\mathbf{r} \right] = 0 \tag{4.3}$$

This gives a unique solution for the alignment parameters $\mathbf{a}$ but would be computationally prohibitive to calculate. Instead, a Taylor expansion of $\mathbf{r}$ to first order around an initial residual $\mathbf{r}_0$ is performed, where $\delta\mathbf{a}$ are the first order corrections to the alignment parameters:

$$\mathbf{r} = \mathbf{r}_0 + \frac{d\mathbf{r}}{d\mathbf{a}}\delta\mathbf{a} \tag{4.4}$$

Substituting Equation 4.4 into Equation 4.3:

$$\sum_{tracks}\left[\left(\frac{d\mathbf{r}}{d\mathbf{a}}\right)^T \mathbf{V}^{-1}\left(\frac{d\mathbf{r}}{d\mathbf{a}}\right)\right]\delta\mathbf{a} + \sum_{tracks}\left(\frac{d\mathbf{r}}{d\mathbf{a}}\right)^T \mathbf{V}^{-1}\mathbf{r}_0 = 0 \tag{4.5}$$

Equation 4.5 shows that $\delta\mathbf{a}$ may be determined by solving a set of linear equations and thus requires an inversion of a square matrix with size equal to the number of degrees of freedom. Because this only accounts for first order effects in the Taylor expansion, this procedure is then iterated to correct any higher order misalignments[65].

This procedure is known as the Global χ^2 method because it aligns all detector elements with respect to each other simultaneously. When the number of degrees of freedom increases, as it will when aligning the large number of detector elements in the ID, this matrix inversion becomes computationally prohibitive and another solution is necessary A Local χ^2 method is used in which the correlations between alignable structures are discarded and the tracks are not refitted. Thus, the alignment matrix and vector become block diagonal, significantly reducing the computation time needed. Because the correlations are neglected when deriving the alignment corrections, the Local χ^2 procedure must be iterated until the alignment corrections converge.

4.2.2 Alignment Granularity

Alignment of the many detector elements in the three sub-detectors of the ID is very challenging due to the very large number of detector elements. To reduce the complexity of the problem, alignment of the detector has been broken into three levels of varying detector granularity which correspond to the various mechanical structures of each sub-detector.

Misalignments may have been introduced at all levels during assembly so it is necessary to perform the alignment at all levels.

The Level 1 alignment is responsible for aligning the largest detector structures, the barrel and end-cap segments, with respect to each other. This level has the largest expected alignment corrections, but it also has the fewest degrees of freedom to align, thus requiring the least statistics. The Level 2 alignment aligns the individual barrel layers and end-cap disks or wheels. This level has more structures to align than Level 1 and thus requires more track statistics for the alignment algorithm to converge. Finally, the Level 3 alignment aligns individual modules within the SCT and Pixels and individual wires within the TRT. This alignment requires the largest amount of track statistics due to the extremely large number of degrees of freedom involved. Table 4.1 gives an overview of the detector granularity of each level and the associated number of degrees of freedom. In total, the ID alignment contains over 700k degrees of freedom.

Constraints on the size of the misalignments come from mechanical surveys of the detector elements during manufacture and installation of the various detector elements. In-situ surveys suggest that the misalignments on the order of 1 mm can be expected between barrel and end-cap segments (Level 1) while misalignments of at the Levels 2 and 3 are expected to be much smaller.

4.3 TRT Tracking Performance

During ATLAS data-taking in 2010-2012, there was an ongoing campaign to refine the ID alignment. Initial alignment constants had been produced using cosmic data in 2010. These cosmic tracks were primarily triggered using the TRT FastOr Trigger [] which, due to the geometry of the TRT, triggers primarily on cosmic tracks which pass through the barrel

Table 4.1: Summary of the main alignment levels and the number of structures for each ATLAS ID subdetector, as well as the detail of the degrees of freedom being aligned and the total number of degrees of freedom aligned. All degrees of freedom are given in the local reference frame [65].

Alignment level	Detector	Structures	degrees of freedom used	number
Level 1	Pixel: whole detector	1	All	6
	SCT: barrel and 2 end-caps	3	All	18
	TRT: barrel	1	All (except T_z)	5
	TRT: 2 end-caps	2	All	12
	Total	7		41
Level 2	Pixel barrel: half shells	6	All	36
	Pixel end-caps: disks	6	$T_x,\ T_y,\ R_z$	18
	SCT barrel: layers	4	All	24
	SCT end-caps: disks	18	$T_x,\ T_y,\ R_z$	54
	TRT barrel: modules	96	All (except T_z)	480
	TRT end-caps: wheels	80	$T_x,\ T_y,\ R_z$	240
	Total	210		852
Level 3	Pixel: barrel modules	1456	All (except T_z)	7280
	Pixel: end-cap modules	288	$T_x,\ T_y,\ R_z$	864
	SCT: barrel modules	2112	$T_x,\ T_y,\ R_z$	6336
	SCT: end-cap modules	1976	$T_x,\ T_y,\ R_z$	5928
	TRT: barrel wires	105088	T_ϕ, R_r	210176
	TRT: end-cap wires	245760	T_ϕ, R_z	491520
	Total	356680		722104

region of the detector. This dataset allowed an initial Level 1 alignment of the barrel, but it was not possible to perform the end-cap alignment due to the lack of statistics. However, the first collision data in 2010 very quickly provided the statistics needed to align the end-caps at Level 1. As collision data became available in greater volumes, further refinements were performed at the various alignment levels. Concurrently, the first calibrations of the detector with collision data were ongoing.

Validation of both the TRT calibration and alignment was performed through an extensive study of the position residuals throughout the detector. The following paragraphs describe a sample of the studies performed on the TRT position residuals in order to validate both the alignment and calibration of the TRT.

As explained previously, the hit residual is the vector pointing from the reconstructed detector hit to the point of nearest approach of the reconstructed track. Because the hit contributes to the track, the track will be biased towards the hit locally which is undesirable for understanding the tracking performance. To make an unbiased measurement, the track is refit after removing the hit in question and the unbiased residual is defined using this refit track.

Because the TRT only measures the hit information in one dimension (the radius of the hit with respect to the wire), the residual vector is simplified to a 1-dimensional position residual defined as $r_{track} - r_{hit}$ (see Figure 4.1). Example residual distributions are shown in Figure 4.2, which shows the unbiased position residual distribution for TRT hits in the barrel and end-caps. The hit residual distribution is influenced by the calibration, the alignment, and the tracking. The mean of the distribution should be centered at zero and shifts from zero would indicate the presence of coherent misalignments. The width of the distribution defines the resolution of the hit position measurement, which receives contributions from both the TRT drift time resolution and the tracking resolution, though the former is expected to be the dominant contribution.

To characterize the mean and width of the position residual distribution over a large detector area, a fitting procedure was developed. First, a Gaussian function $\mathbf{G}(\mu, \sigma)$ is fit to the distribution. This initial fit is generally poor because the position residual distribution has significant non-Gaussian tails. To mediate this, the same fitting function is fit again but only over a restricted range from -2.5σ to +2.5σ, where σ is taken from the initial fit. This removes the contributions from the Gaussian tails and gives an estimate of the width of the core of the distribution. Because the fit range now depends on the fit parameters (and vice-versa), the fit is iterated several times in order for σ to converge to within 0.1%. This generally takes 2 to 5 iterations.

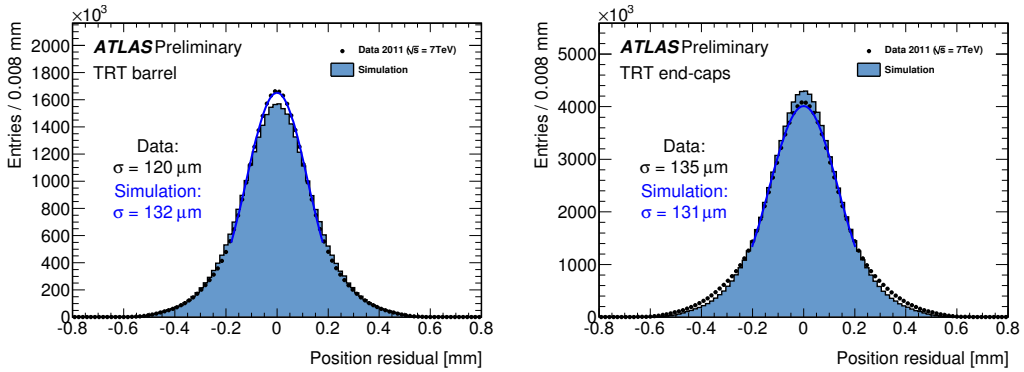

Figure 4.2: Distribution of the TRT position residuals for a sample of $\sqrt{(s)} = 7$ TeV data with a comparison to the simulation, which is normalized to the data, for hits in the barrel (end-caps) on the left (right). The core of the distribution is fit with a Gaussian function to estimate the position resolution, which is measured to be 120 (135) μm in the barrel (end-caps) in the data.

The results of this fitting procedure are included in Figure 4.2. The position resolution is estimated to be 120 (135) μm in the barrel (end-caps). There are discrepancies in the measured resolutions between the data and the simulation, most notably that the measured width of the residual distribution in the barrel is 12% larger in the simulation than in the data. There are many possible sources of mismodeling which could lead to this discrepancy, such as mismodeling of the TRT drift time resolution. However, this particular discrepancy cannot be attributed to detector misalignments because misalignments should decrease the resolution in data relative to the simulation (which uses a perfectly aligned geometry).

Measurements of σ and μ throughout the detector are performed by binning the data in the relevant variables (radius, ϕ, etc.) in order to check for anomalous behavior indicative of misalignments or calibration issues. Figures 4.3 and 4.4 shows example results of this procedure from the 2010 data-taking period after the Level 1 and 2 alignments had been performed. Figure 4.3 shows μ plotted as a function of the TRT end-cap 4-plane wheel (a collection of 4 straw layers in the end-cap) and radius both before and after the TRT level 3 alignment. Alternating large scale structure in the mean position residual both in ϕ and radius

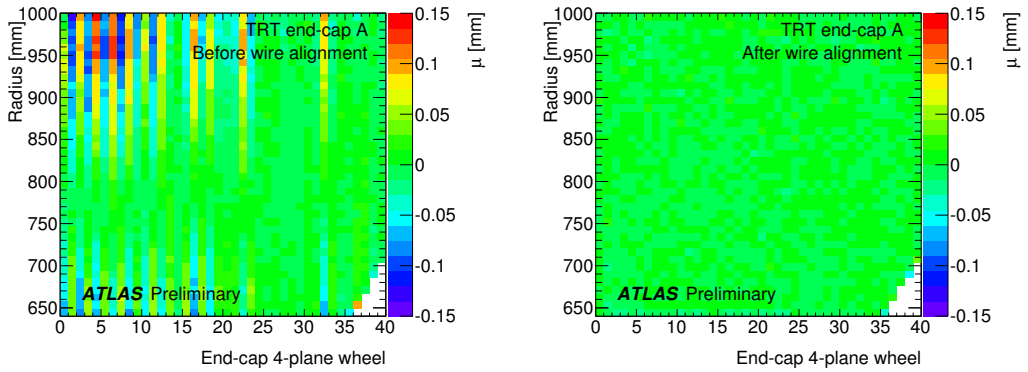

Figure 4.3: Mean of a Gaussian fit to position residuals vs detector radius and wheel before (left) and after (right) the Level 3 alignment in TRT end-cap A. The white bins are due to acceptance effects.

between consecutive 4-plane wheels is observed indicating the presence of misalignments. These specific patterns could be produced by coherent shifts in the 4-plane wheels with respect to each other. This is also supported by the observation that the 4-plane wheels were assembled independently and then stacked together, with every other wheel being flipped over to cancel any gravity induced deformations introduced during assembly. These misalignments would not be corrected by the Level 1 or 2 alignment because those levels do not have access to the degrees of freedom needed to correct these biases. After the Level 3 wire-by-wire alignment is performed for the TRT, these structures disappear, as shown in Figures 4.3 and 4.4, indicating that the misalignments have been removed.

Figure 4.5 shows the observed position resolution in the 2011 data as a function of radius and z with high granularity. The resolution varies from $\sim$100 μm in the short straws of the barrel up to $\sim$180 μm at the edges of the outer wheels of the end-caps. To understand the structure in Figure 4.5, recall that the position residual distribution is affected by both the intrinsic TRT hit resolution (which should not vary significantly from straw to straw) and the resolution in the track extrapolation. Figure 4.6 shows the average track position error as estimated by the ID tracking algorithm as function of radius and z throughout the TRT,

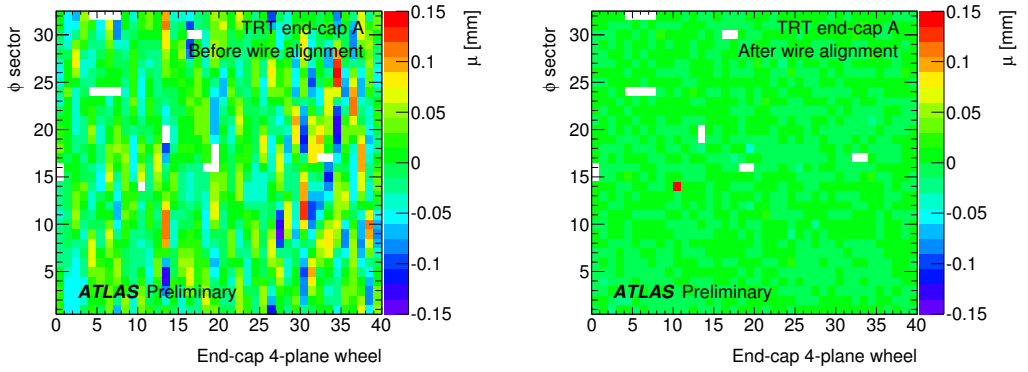

Figure 4.4: A 2D map of the mean from a Gaussian fit to the position residual distribution vs ϕ and TRT end-cap wheel before (left) and after (right) the Level 3 alignment in the TRT end-cap A. The white bins are due to missing channels.

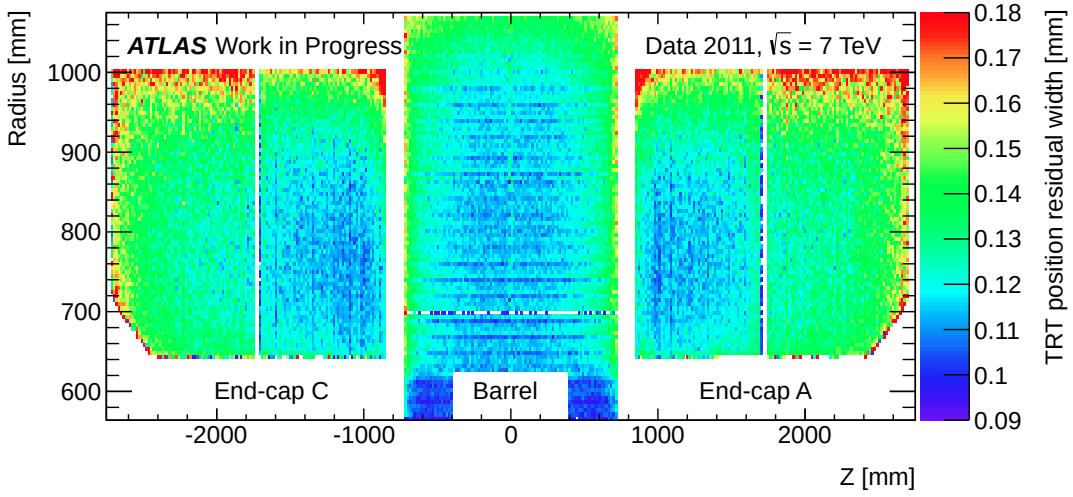

Figure 4.5: Hit position resolution as measured using a Gaussian fit to the core of the position residual distribution as a function of radius and z for $\sqrt{s} = 7$ TeV data taken during 2011. White regions are outside of the detector acceptance.

which varies from ∼30 μm in the middle of the barrel up to ∼80 μm at the edge of the detector. This clearly shows that the rapid increase in position residual width near the outer edges of the detector can be attributed to uncertainties in the track extrapolation rather than the intrinsic resolution.

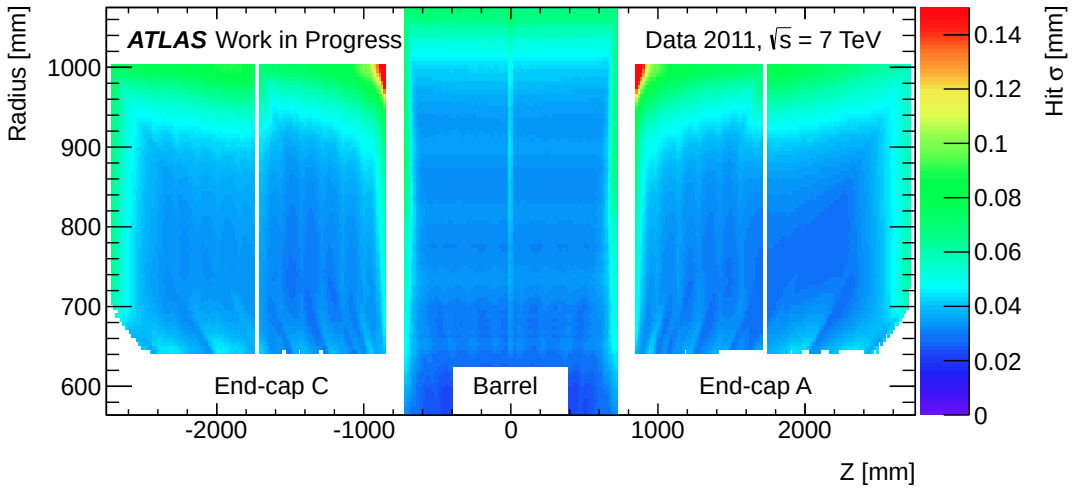

Figure 4.6: Average track error as a function of radius and z for $\sqrt{s} = 7$ TeV data taken during 2011. White regions are outside of the detector acceptance.

4.4 ID Weak Modes

The χ^2 alignment algorithms are not completely robust to all possible misalignments[66]. There exist classes of coherent misalignments, henceforth referred to as *weak modes*, which preserve the helical trajectory of the measured track while simultaneously leaving the χ^2 invariant. In other words, the solution to the matrix inversion is under-constrained and degenerate because coherent changes in the alignment parameters, $\mathbf{a}$, can be compensated by changes to the measured track parameters, $\boldsymbol{\tau}$, while preserving the χ^2. Several examples of weak modes are shown in Figure 4.7. For example, the "curl" weak mode results from a coherent shift in $\Delta\phi$ of the detector elements as a function of radius. This particular weak mode would result in charge dependent transverse momentum biases because the track curvature measurement would be biased asymmetrically depending on the charge of particle.

Weak modes are undesirable as they result in systematic biases in the measured track parameters and thus are one of the main sources of systematic effects in the ID tracking. Systematic biases in the track momentum will affect invariant mass reconstruction and charge

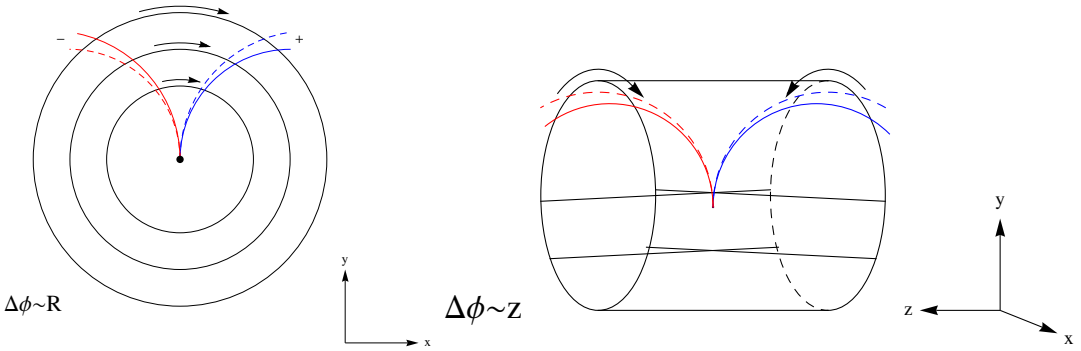

Figure 4.7: Examples of alignment weak modes, coherent misalignments for which the χ^2 alignment algorithms are not sensitive.

asymmetry measurements while biases on the impact parameter measurements can affect beam-spot reconstruction, track vertexing, and b-tagging performance. Therefore, it is important to both remove these biases in the alignment procedure and constrain the size of any remaining systematic effects.

To quantify the systematic momentum biases, consider a class of detector deformations known as sagitta distortions, consisting of detector movements which are orthogonal to the track trajectory, for which the "curl" seen in Figure 4.7 is the archetype example. These deformations will affect the reconstructed track curvature oppositely for positive and negatively charged particles and it can be shown that such a deformation introduces a shift into the reconstructed transverse momentum:

$$q/p_{\mathrm{T}} \rightarrow q/p_{\mathrm{T}} + \delta_{sagitta} \quad \textbf{or} \quad p_{\mathrm{T}} \rightarrow p_{\mathrm{T}}(1 + q \cdot p_{\mathrm{T}} \cdot \delta_{sagitta})^{-1} \tag{4.6}$$

In the case of a completely global detector deformation, the parameter $\delta_{sagitta}$ quantifies the bias for all measured momenta. This approximation will only hold for small detector deformations but serves as a good approximation in many cases in the alignment. Note that the absolute bias is proportional to the square of the transverse momentum, meaning that high p_{T} tracks will be more sensitive to these effects. Because the polar angle measurement

is unaffected, the momentum scales with the transverse component:

$$p \to p(1 + q \cdot p_{\mathrm{T}} \cdot \delta_{sagitta})^{-1} \tag{4.7}$$

Another class of detector deformation, known as radial distortions, affects the measured momentum in a charge symmetric way due to the expansion or contraction of the measured trajectory with the coherent radial shifts in the detector elements. These deformations can be parameterized as a direction dependent scaling of the radius:

$$r \to r(1 + \frac{1}{2} f(\eta, \phi)\delta_r) \tag{4.8}$$

The simplest case is a homogeneous expansion or contraction of all detector layers ($f(\eta, \phi) =$ constant) but does not usually occur due to physical constraints on the detector. However, for the sake of the example, this leads to scaling of both components of the transverse momentum, giving:

$$p_{\mathrm{T}} \to p_{\mathrm{T}}(1 + \frac{1}{2}\delta_r)^2 \approxeq p_{\mathrm{T}} \to p_{\mathrm{T}}(1 + \delta_r) \text{ for small } \delta_r \tag{4.9}$$

Charge-symmetric alignment biases are difficult to disentangle from other detector effects, such as absolute B-field scale and detector material mapping, so these will be estimated later but no action will be taken to remove these modes.

To demonstrate that weak modes will not be removed by the χ^2 alignment, simulated $Z \to \mu^+\mu^-$ events are reconstructed with three detector geometries: the nominal "perfect" alignment, a distorted alignment in which a "twist" had been introduced, and the alignment produced by the χ^2 algorithm when applied to the "twist" alignment. The results in Figure 4.8 show that the "twist" geometry introduces large biases into the transverse momentum relative to the nominal geometry while the impact parameter d_0 remains unchanged. Furthermore, the χ^2-aligned "twist" geometry shows that significant momentum biases in the end-caps remain after the alignment procedure.

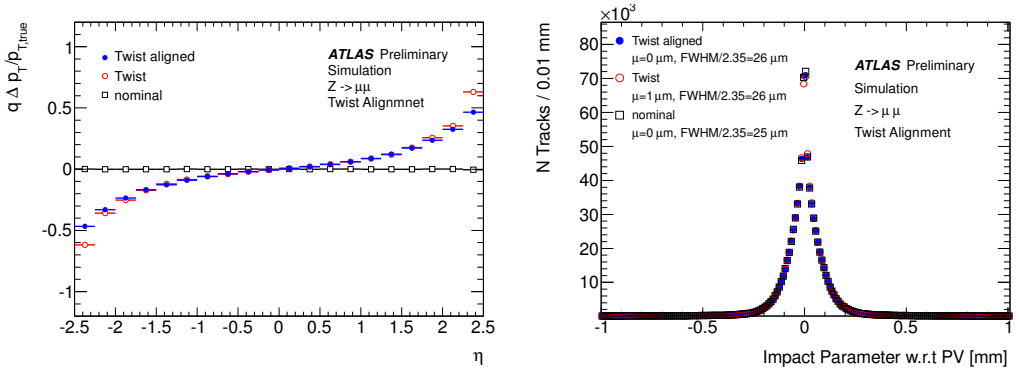

Figure 4.8: Effects of adding a "twist" weak mode into the alignment. The plot on the left shows a comparison of the bias in the transverse momentum for muons from $Z \to \mu^+\mu^-$ between the nominal geometry, the "twist" geometry, and the geometry produced by performing the χ^2 alignment on the "twist" geometry. The χ^2 alignment fails to remove the transverse momentum biases. The plot on the right shows the impact parameter distributions for the three geometries, which is not significantly affected by the "twist" distortion of the detector geometry.

One should note that the presence of weak mode misalignments can be a result of detector deformations but can also be introduced as an artifact of the χ^2 alignment itself. Therefore, the χ^2 alignment procedure must be modified to minimize the effects of weak modes. The next section will describe strategies to accomplish this.

4.4.1 Constraining Weak Modes

This section describes two general strategies which have been used to remove weak modes from the alignment: 1) the addition of different track topologies into the data sample and 2) the addition of constraints on the collision track parameters from independent measurements. Two independent constraints on the track parameters have been studied: a constraint on the momentum using the calorimeter energy measurement for electrons and using decays of known resonances (typically from $Z \to \mu^+\mu^-$, $J/\psi \to \mu^+\mu^-$, and $K^0_S \to \pi^+\pi^-$) to add constraints on the track momentum. All of these strategies will be described in more detail in the following sections.

4.4.2 Cosmic Tracks

As argued in the Section 4.4, weak modes are present due to degeneracies in the solutions of the χ^2 alignment procedure. For some modes, this is the direct result of the topology of the collision tracks used in the alignment. For example, the "curl" weak mode is only possible because collision tracks all originate at the interaction point, introducing a degeneracy between the ϕ position of the detector elements and the track momentum to which the χ^2 algorithm is insensitive. One can introduce other track topologies to break this degeneracy.

Cosmic-ray tracks provide one sample of tracks with significantly different topology than collision tracks. Cosmic-ray tracks do not originate at the beam interaction point and traverse the entire ID, correlating the alignment of the detector elements on opposite sides of the interaction point. Additionally, the track parameters (such as momentum) are constrained by the fact that they should be consistent on both sides of the detector. Cosmic-ray events are triggered and recorded during normal data-taking using non-collision BCIDs. Therefore, these tracks are subject to exactly the same conditions as the collision track data. Because of geometrical concerns, cosmic-ray tracks mostly constrain weak modes in the barrel segments of the detector. Cosmic-ray tracks are added to all data samples used in the alignment procedure (cite?). Indeed, the momentum biases were already well constrained in the barrel region ($|\eta|$ <1.0) before any further constraints were added to the alignment procedure - see Figure 4.9.

4.4.3 E/p Method

The calorimeter energy measurement (E) is a completely independent measure of the electron energy which can be used as a probe for systematic biases in the track momentum (p). There are also uncertainties in the calorimeter energy scale which factor into the distribution of the

electron E/p. However, assuming that the calorimeter response is charge independent, one may assume that charge dependent effects may be attributed to biases in the track momentum measurement. As a result, this method is not sensitive to weak modes which produce charge symmetric biases, such as a radial expansion of the detector elements.

Using the formulation of Eqn. 4.7 for charge-dependent systematic biases, the measured $\langle E/p \rangle$ will scale as:

$$\langle E/p \rangle^{\pm} \rightarrow \langle E/p \rangle^{\pm} \pm \langle E_{\mathrm{T}} \rangle \cdot \delta_{sagitta} \tag{4.10}$$

Assuming that $\langle E/p \rangle^{+}_{true} = \langle E/p \rangle^{-}_{true}$ for a given sample of electrons, it can be shown that one may extract the bias $\delta_{sagitta}$ using:

$$\delta_{sagitta} = \frac{\langle E/p \rangle^{+}_{rec} - \langle E/p \rangle^{-}_{rec}}{2 \langle E_{\mathrm{T}} \rangle} \tag{4.11}$$

It is important to select a sample of electrons and positrons for which the assumption $\langle E/p \rangle^{+}_{true} = \langle E/p \rangle^{-}_{true}$ holds such that the numerator of Eqn. 4.11 does not receive contributions from the calorimeter energy scale systematic uncertainties. In order to select a high-purity collection of electrons, $W \rightarrow e\nu$ and $Z \rightarrow ee$ decays are selected. The denominator of Eqn. 4.11, which is solely a scaling factor, is affected by the calorimeter energy scale which is known to $<= 1\%$ [67].

To select W boson decays, events with exactly one electron with $p_{\mathrm{T}} > 20$ GeV passing the tight electron identification criteria are selected. Events with more than one electron with $p_{\mathrm{T}} > 20$ GeV passing the medium electron identification are also excluded. Kinematic requirements on the missing transverse energy, $E_{\mathrm{T}}^{\mathrm{miss}} > 25$ GeV, and the missing transverse mass of the electron-neutrino system, $m_{\mathrm{T}} > 40$ GeV, are imposed in order to further suppress

backgrounds. The transverse mass is defined as:

$$m_{\mathrm{T}} = \sqrt{2p_{\mathrm{T}}^{\ell}p_{\mathrm{T}}^{\nu}(1 - cos(\phi^{\ell} - \phi^{\nu}))} \tag{4.12}$$

This selection is chosen in order to suppress the electron fake backgrounds, where a jet is misidentified as an electron. The most significant of these backgrounds, generically termed QCD background, is from multijet production. The QCD contribution is estimated to be 2.6% and 4.3% for the W^+ and W^- channels respectively [68]. As these backgrounds are small, they are considered to be negligible and no correction is made.

To select Z decays, events are required to have two opposite sign electrons passing the medium electron identification cuts with $p_{\mathrm{T}} > 20$ GeV. Within the the dielectron invariant mass window from 66 GeV to 116 GeV, the backgrounds are estimated to be 1.8% and are again considered negligible for this measurement[68].

An unbinned maximum likelihood fit with a Crystal-Ball function is used in order to extract the $\langle E/p \rangle$, or mean/most probable value, from the distribution of electron E/p. This function reduces the effects of background contamination (which may be different for electrons and positrons) and allows an accurate fit of the non-Gaussian bremsstrahlung tail of the distribution. The initial parameter values and range of the fit is determined using a series of Gaussian fits to the E/p distribution, giving rough measurements of the mean μ and width σ of the distribution. The final Crystal-Ball fit is performed over the range $\mu - \sigma < E/p < 2.5$. The strict lower limit removes the lower tail of the distribution where the background contamination is more significant while the upper limit includes the non-Gaussian tail which is modeled by the Crystal-Ball function. The electron and positron distributions are fitted simultaneously such that the resolution and tail parameters, which rely on material and detector resolution effects and should not be affected by the particle charge, are shared between the

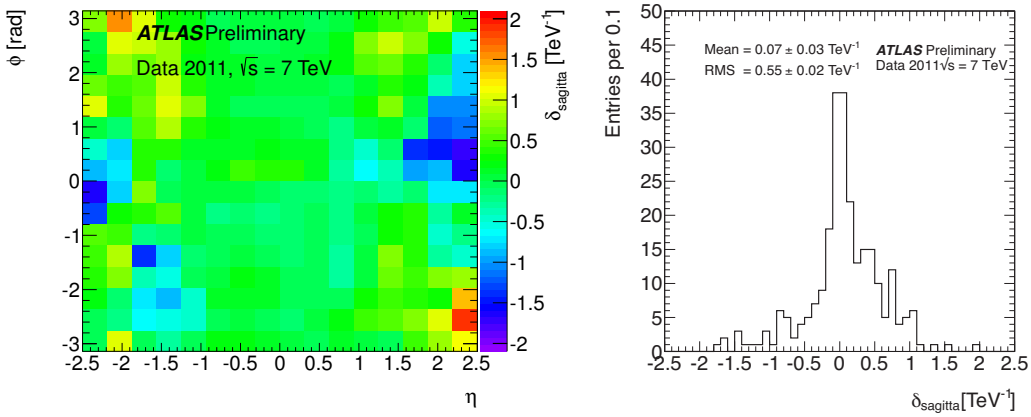

Figure 4.9: Momentum biases ($\delta_{sagitta}$) as measured using the E/p method using ∼1 fb^{-1}of $\sqrt{s} = 7$ TeV data collected during 2011. The plot on the left shows the 2D map of the measured $\delta_{sagitta}$ and the plot on the right shows the 1D projection of these values.

two distributions while the mean parameters are fitted separately for each distribution.

Because the systematic biases are expected to vary across the detector, the sample of electrons and positrons is binned into 16 × 16 bins in η/ϕ and each bin is fit separately. This procedure was performed upon ∼1 fb^{-1}of $\sqrt{s} = 7$ TeV data collected during 2011 (corresponding to ∼3.5 M electrons) before any attempt to remove weak modes in the alignment procedure and the results are shown in Figure 4.9. Negligible biases are observed in the central η region but significant biases are measured in the forward regions of the detector, up to 2 TeV^{-1}, corresponding to a momentum bias of ∼8% for a track with $p_{\mathrm{T}} = 40$ GeV.

4.4.4 $Z \to \mu^+\mu^-$ Method

Standard Model resonances such as $Z \to \mu^+\mu^-$, $J/\psi \to \mu^+\mu^-$, and $K^0_{\mathrm{S}} \to \pi^+\pi^-$can also be used to measure systematic momentum biases with high precision due to their relatively large cross sections at the LHC and their precisely known masses. In this study, $Z \to \mu^+\mu^-$ decays have been studied to provide a precise measurement of both charge symmetric (δ_{r}) and

charge anti-symmetric ($\delta_{sagitta}$) momentum biases. $Z \to \mu^+\mu^-$ decays are studied because they provide a large sample of high momentum muons with relatively small backgrounds. Additionally, high p_{T} muons are less sensitive to detector material effects.

The invariant mass m of two low mass and highly relativistic particles is given approximately by:

$$m^2 = 2p_1p_2(1 - \cos\theta) \tag{4.13}$$

where p_1 and p_2 are the magnitude of the momenta of the two particles and θ is the angle between them. Assuming a charge anti-symmetric type momentum bias as in Eqn. 4.7, then the reconstructed mass at leading order in $\delta_{sagitta}$ reduces to:

$$m^2 \to m^2_{rec} \approx m^2(1 + q_1 \cdot p_{\mathrm{T},1} \cdot \delta_{sagitta,1} + q_2 \cdot p_{\mathrm{T},2} \cdot \delta_{sagitta,2}) \tag{4.14}$$

One can see that the bias in the squared mass is linear in $\delta_{sagitta}$. Note that for neutral resonances with $q_1 = -1 * q_2$ and $p_{\mathrm{T},1} \approx p_{\mathrm{T},2}$, the two terms cancel and the invariant mass is unbiased on average. Therefore, the method is not sensitive to global charge anti-symmetric biases. However, if the momentum biases vary across the detector ($\delta_{sagitta} \to \delta_{sagitta}(\eta, \phi)$), then the two terms do not cancel and the mass will be sensitive to the relative momentum biases. In order to extract the function $\delta_{sagitta}(\eta, \phi)$ from the data, the average value of the difference between the reconstructed mass and the known resonance mass is used to extract the momentum bias:

$$\Delta(m^2) = \frac{m^2_{rec} - m^2_Z}{m^2_Z} \approx q_1 \cdot p_{\mathrm{T},1} \cdot \delta_{sagitta}(\eta_1, \phi_1) + q_2 \cdot p_{\mathrm{T},2} \cdot \delta_{sagitta}(\eta_2, \phi_2) \tag{4.15}$$

However, it is not known *a priori* what fraction of the mass bias comes from particle 1 and particle 2. Thus, an iterative procedure is used to determine $\delta_{sagitta}(\eta, \phi)$. In the first iteration, half of the mass bias is assigned to each muon from the Z boson decay:

$$\delta_{sagitta} = \frac{1}{2}\frac{\Delta(m^2)}{q \cdot p_{\mathrm{T}}} \tag{4.16}$$

The distribution of $\delta_{sagitta}$ is a convolution of the mass line-shape of the particle resonance with detector resolution effects. For $Z \to \mu^+\mu^-$ decays, the intrinsic width of the Z boson is comparable to the ID momentum resolution and the line-shape is expected to follow a Breit-Wigner function, which is approximately Gaussian in the peak of the distribution. The muons are binned using η and ϕ and a central value is extracted from the $\delta_{sagitta}$ distribution in each bin using an iterative fitting procedure. The distribution is initially fit with a Gaussian function $G(\mu, \sigma)$ over the entire range. This fit is then repeated in the range -1.5σ to +1.5σ in order to remove contributions from the tails, which will have larger background contamination. The fitted μ is assigned as $\delta_{sagitta}$ for that η/ϕ bin.

Because of the ambiguity in assigning the momentum bias to either muon, the entire procedure is then iterated in order to estimate the momentum biases correctly. At the beginning of each iteration, the measured biases from the previous iteration are used to correct the muon momenta before calculating the reconstructed mass. This procedure is iterated until the $\delta_{sagitta}$ parameters have converged.

$Z \to \mu^+\mu^-$events are selected by requiring pairs of oppositely charged muons with high quality ID tracks. Events are triggered using a single-muon trigger ($p_{\mathrm{T}} > 18$ GeV threshold) and are required to have a primary vertex with at least 5 tracks with $p_{\mathrm{T}} > 0.4$ GeV. Muon candidates are reconstructed using the Muon Spectrometer as described in Section 7.1.2 and a number of requirements are imposed in order to select candidates with high quality tracks:

- Hit requirements:
  - B-layer hit in Pixel detector except when muon passes through inactive module
  - Number of Pixel (SCT) hits + number of dead sensors crossed >1 (>5)
  - Number of Pixel + SCT holes <3
  - Successful TRT track extension within acceptance

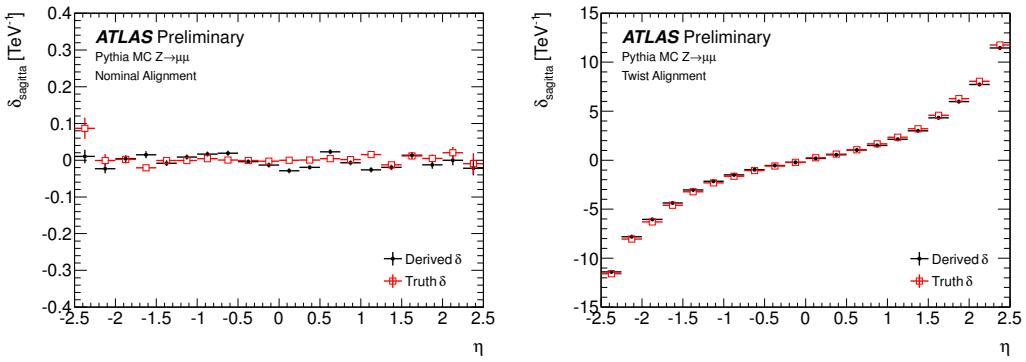

Figure 4.10: Validation of the $Z \to \mu^+\mu^-$ method on simulated $Z \to \mu^+\mu^-$ events. The left plot shows the measured null biases using the nominal geometry which shows that the lower limit on the method sensitivity is 0.04 TeV^{-1}. The plot on the right shows the measured biases after a "twist" deformation has been introduced into the simulation. The measured biases reproduce the true biases to within 5% with a small systematic under-estimation due to the iterative nature of the method.

- $p_{\mathrm{T}} > 20$ GeV
- isolation[3]: $\Sigma p_{\mathrm{T}}^{\mathrm{iso}}/p_{\mathrm{T}} < 0.2$
- $|d_0| < 0.2$ mm
- $|z_0| < 1.0$ mm

This procedure was performed on simulated $Z \to \mu^+\mu^-$ events reconstructed both with the nominal "perfect" geometry and also with the "twist" geometry in order to validate the algorithm. The results, shown in Figure 4.10, show that the procedure reproduces the null biases to within 0.04 TeV^{-1} and also reproduces the "twist" geometry biases to within 5%. There is a small systematic under-estimation of the momentum biases in the "twist" geometry which is due to the iterative nature of the algorithm.

Unlike the E/p method, the same procedure can also be used for charge symmetric momentum biases, as parameterized in Eqn. 4.8. It is trivial to show that the mass difference

[3]See Section 7.2 for definition of lepton isolation.

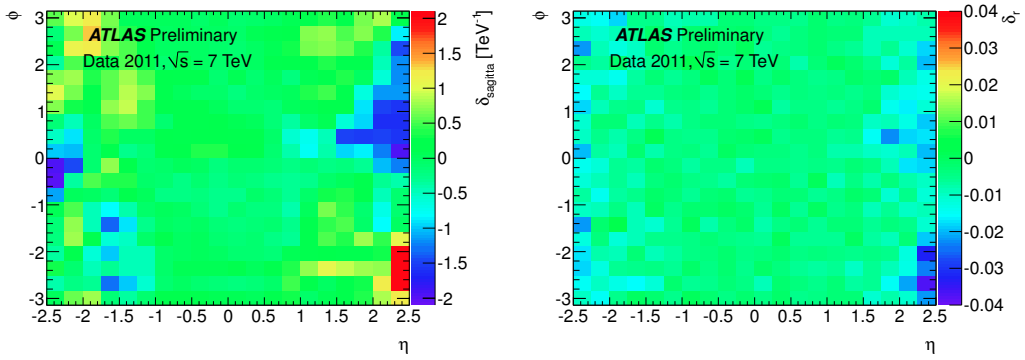

Figure 4.11: Momentum biases as measured using the $Z \to \mu^+\mu^-$ method using ~1 fb^{-1}of $\sqrt{s} = 7$ TeV data collected during 2011. The plot on the left shows the 2D map of the charge anti-symmetric momentum biases ($\delta_{sagitta}$) and the plot on the right shows the 2D map of the charge symmetric momentum biases ($\delta_{sagitta}$).

due to charge symmetric momentum biases is:

$$\Delta(m^2) = \frac{m^2_{rec} - m^2_Z}{m^2_Z} \approx \delta_r(\eta_1, \phi_1) + \delta_r(\eta_2, \phi_2) \tag{4.17}$$

The rest of the method proceeds identically to the charge anti-symmetric case.

The $Z \to \mu^+\mu^-$ method was used to estimate both $\delta_{sagitta}$ and δ_r in collision data. Figure 4.11 show the results for both measurements using ~1 fb^{-1}of $\sqrt{s} = 7$ TeV data collected during 2011 (the same data-taking period as used for the E/p results in Section 4.4.3). The charge anti-symmetric results confirm the E/p results: negligible biases in the central η region with larger biases up to 2 TeV^{-1} in the forward regions. Furthermore, the observed η/ϕ dependence is very well reproduced between the E/p and $Z \to \mu^+\mu^-$ methods. The charge symmetric biases are measured to be <0.005 in the central η region and up to 0.03 at the edges of the detector.

4.4.5 After Alignment

Clearly the momentum biases measured in the previous section are undesirable due to their negative impact on physics analyses. As argued previously, the χ^2 alignment procedure may produce biases in the track parameters because of the degeneracy between the track parameters and the alignment parameters. The degeneracy is broken by imposing tight constraints on the input track momenta. This was achieved by adding a term to the χ^2 in Eqn. 4.2 which constrains the the track momentum to its corrected momentum:

$$q/p_{Corrected} = q/p_{Reconstructed}(1 - q \cdot p_{\mathrm{T}}\delta_{sagitta}) \tag{4.18}$$

where $\delta_{sagitta}$ is taken from the E/p method for estimating momentum biases. This allows the $Z \to \mu^+\mu^-$ results to act as an independent cross-check on the final alignment results. The alignment procedure including the track momentum constraint was iterated many times at the various alignment levels. The momentum biases were evaluated after each iteration using the E/p method and fed back in as a constraint in order to remove the weak mode detector deformations.

The results of the both the E/p method and the $Z \to \mu^+\mu^-$ method for the final ID alignment can be seen in Figure 4.12. The largest biases in the forward regions have clearly been removed by the alignment procedure using the constrained momentum. Because there is no significant ϕ dependence observed in the remaining momentum biases, the final estimate of the momentum biases is measured as a function of η only and the results are shown in Figure 4.13. Some residual structure is observed as a function of η but the observed biases are constrained to $|\delta_{sagitta}| < 0.04$ TeV^{-1} with the exception of a few bins in the forward regions, a significant improvement with respect to the previous alignment. A conservative upper limit of $|\delta_{sagitta}| < 0.03$ TeV^{-1} is inferred from the observed biases, corresponding to a momentum bias of less than 0.12% for tracks with $p_{\mathrm{T}} = 40$ GeV.

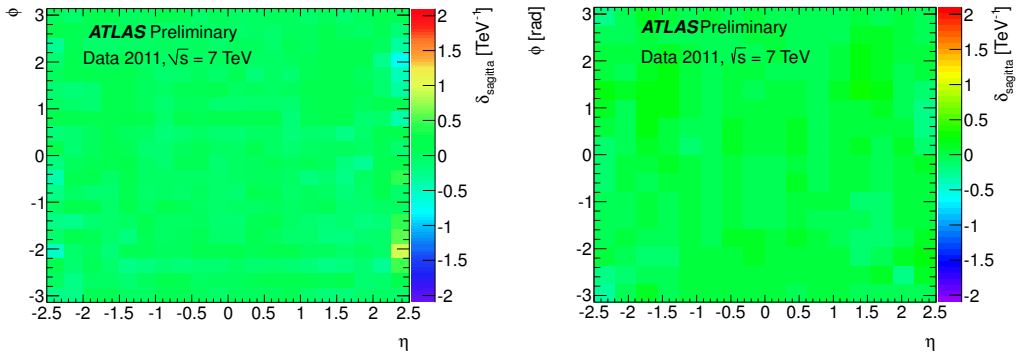

Figure 4.12: Observed charge anti-symmetric momentum biases using ∼1 fb^{-1}of $\sqrt{s} = 7$ TeV data collected during 2011 after the alignment was performed using constraints on the track momentum. The plots shows the 2D map of the measured $\delta_{sagitta}$ using the $Z \to \mu^+\mu^-$ method on the left and using using the E/p method on the right.

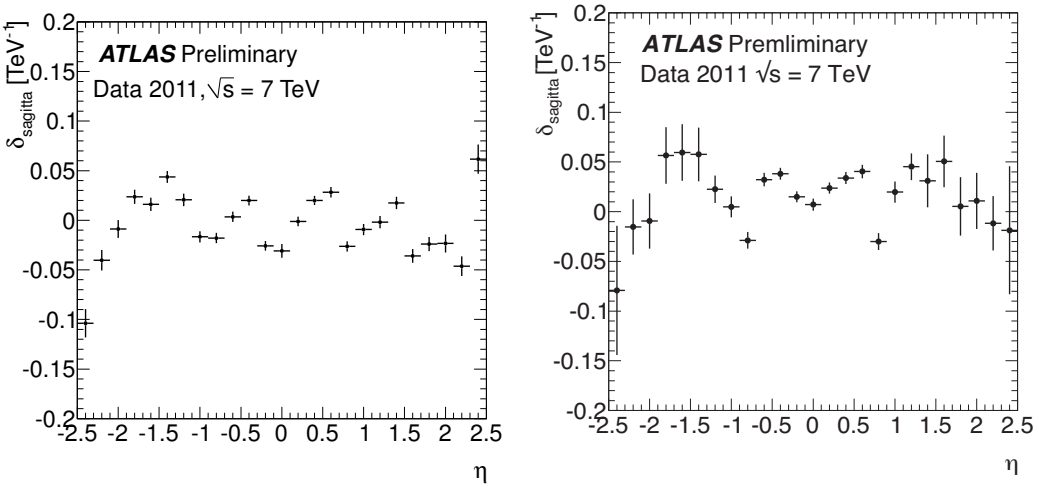

Figure 4.13: Observed charge anti-symmetric momentum biases using ∼1 fb^{-1}of $\sqrt{s} = 7$ TeV data collected during 2011 after the alignment was performed using constraints on the track momentum. The plots shows the measured $\delta_{sagitta}$ as a function of η using the $Z \to \mu^+\mu^-$ method on the left and using the E/p method on the right. Errors are statistical only.

Chapter 5

Analysis Overview

This thesis presents measurements of the Higgs boson in the $H \to 4\ell$ decay channel using the full LHC Run 1 dataset. These measurements provide initial tests of the SM Higgs boson predictions for the newly discovered scalar particle. Specifically, measurements of the mass, signal strength, and differential cross sections in a number of variables of interest are presented. Measurements of the spin/CP nature of the particle and the fermionic and bosonic couplings in the $H \to 4\ell$ decay channel have also been performed but are beyond the scope of this thesis; see References [28] and [32] for details and results of those analyses.

A common event selection is used for all of the $H \to 4\ell$ measurements and is described in Chapter 7. This chapter also includes the description of the final discriminating variables used in the mass and signal strength measurements ($m_{4\ell}$ and BDT_{ZZ}) as well as the variables chosen for the differential cross section measurements.

The backgrounds in this analysis are broadly categorized into reducible and irreducible backgrounds. The irreducible backgrounds consist of processes which produce four isolated leptons in the final state making them nearly indistinguishable from the signal. The reducible backgrounds are comprised of processes in which leptons originate from semi-leptonic decays of heavy flavor hadrons or from misidentification of jets as leptons. The presence of these "fake" leptons allows reduction of these backgrounds by imposing strict selection criteria. The

background estimation methods and results for both categories of backgrounds are described in Chapter 9.

The sources and estimates of systematic uncertainties for all measurements are described in Chapter 10. Systematic uncertainties associated with lepton selection efficiency most strongly affect the signal strength and cross section measurements while uncertainties in the lepton momentum resolution and scale affect the mass measurement. Jet-related uncertainties are also described as they affect the jet-related differential cross sections.

Measurements of the mass and signal strength are performed using an unbinned maximum likelihood fit of the invariant mass ($m_{4\ell}$) and multivariate discriminant (BDT_{ZZ}) distributions. The derivation of $m_{4\ell}$ and BDT_{ZZ} templates are described in Chapter 11. The results of the mass and signal strength measurements are presented in Chapter 11

Differential cross section measurements are performed using an event counting method after isolating the signal peak from the backgrounds using invariant mass cuts (a "mass window"). Optimization of the mass window is described in Chapter 7. The cross sections are extrapolated to a fiducial region based on the detector acceptance and analysis selection criteria using a simple unfolding method as described in Chapter 8. The observed cross sections are compared to several SM calculations and their compatibility is quantified in Chapter 12. The results of these measurements have been documented in Ref. [69].

Chapter 6

Data and Simulation

The measurements in the $H \to 4\ell$ decay channel presented in the following chapters are performed using collision data collected by the ATLAS detector during Run 1 at the LHC during 2011 and 2012. This chapter describes the data and simulation samples used in this analysis.

6.1 Data

Data were collected using the ATLAS detector (see Section 3) over the course of the LHC Run 1 in 2011 and 2012, corresponding to 4.5 fb^{-1}of $\sqrt{s} = 7$ TeV data and 20.3 fb^{-1}of $\sqrt{s} = 8$ TeV data respectively. The rate of data collection is shown in Figure 6.1, which shows both the integrated luminosity and the peak instantaneous luminosity as a function of time during Run 1 at the LHC. The instantaneous luminosity increased over the course of Run 1 and at its peak reached $0.75 \times 10^{34}\text{cm}^{-2}\text{s}^{-1}$, very nearly the LHC design goal of $1 \times 10^{34}\text{cm}^{-2}\text{s}^{-1}$. A Good-Runs-List (GRL) is used to record when the detector is fully operational at the granularity of individual luminosity blocks (which correspond to roughly 5 minutes of data-taking). For this analysis, the standard ATLAS "All Good" GRL is required for all events.

One side effect of the large instantaneous luminosity is the "pile-up" of many overlapping

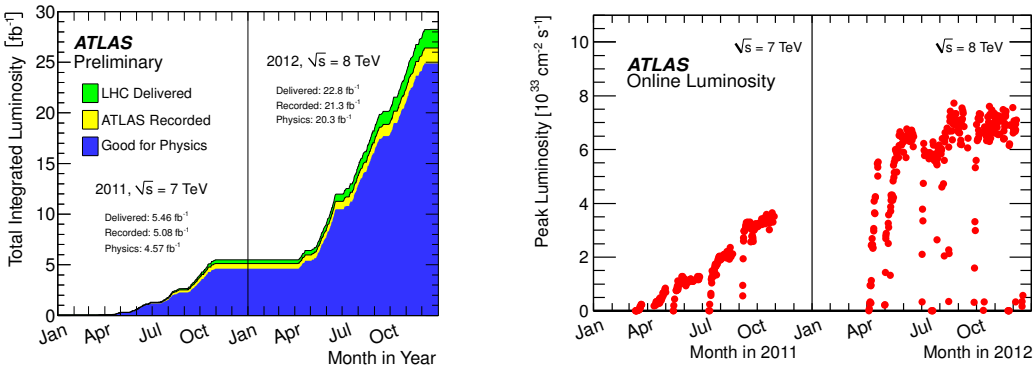

Figure 6.1: (left) The total integrated luminosity delivered by the LHC (green), recorded by ATLAS (yellow), and passing quality requirements (blue) is shown as a function of time during 2011 and 2012. (right) The peak instantaneous luminosity as a function of time during 2011 and 2012.

pp interactions in the detector, which is of major concern for the LHC experiments for several reasons. Increasing pile-up results in more hits in the detector per event, requiring a larger detector readout bandwidth. Pile-up can significantly increase computational costs if algorithms are not optimized to handle high occupancy events. For instance, the complexity of the pattern recognition in the tracking algorithm scales quadratically with the number of hits in the detector. Finally, pile-up introduces additional energy into the detector which distorts measurements of of the objects of interest, thus degrading the detector performance. Figure 6.2 shows the mean number of *pp* interactions per bunch crossing, which is determined by the LHC beam parameters.

Pile-up may be categorized into two types: "in-time" and "out-of-time". In-time pile-up results from additional *pp* interactions in the same LHC bunch as the interaction of interest. The main impact of in-time pile-up is degradation of the detector performance, particularly for jet energy and missing energy measurements. Out-of-time pile-up results from interactions which occur in nearby LHC bunches whose signals are still present in the detector. Out-of-time pile-up primarily affects the calorimeter measurements as their electronics response time

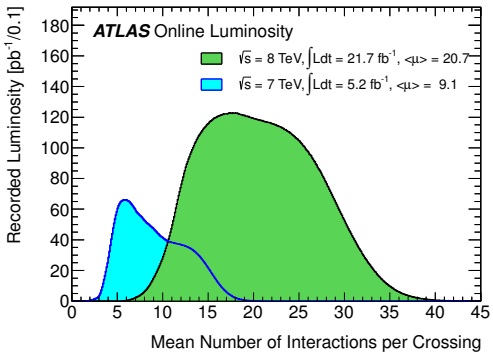

Figure 6.2: The mean number of interactions per LHC bunch crossing shown separately for the 7 and 8 TeV data sets.

is typically longer than the LHC bunch spacing of 50 ns used during Run 1.

In the 7 TeV data, candidate events are triggered using a selection of single lepton and dilepton triggers. The single electron (muon) triggers have a lower p_{T} threshold of 20 (18) GeV. During the latter portion of the 2011 data-taking, the p_{T} threshold for the electron trigger was raised to 22 GeV and a veto on hadronic energy near the electron cluster was applied due to the ramp-up of the instantaneous luminosity. Two dilepton triggers are used with a symmetric p_{T} threshold of 12 (10) GeV for electrons (muons). Finally, a mixed dilepton trigger requires an electron with $p_{\mathrm{T}} > 10$ GeV and a muon with $p_{\mathrm{T}} > 6$ GeV.

For the 8 TeV data, the trigger selection was modified in order to maintain reasonable trigger rates as the instantaneous luminosity further increased. The single lepton triggers have a lower p_{T} threshold of 24 GeV and isolation requirements[4] in order to reduce the trigger rate from fake lepton backgrounds. The single electron trigger has an additional veto on hadronic energy near the trigger electron. For single electrons (muons) with $p_{\mathrm{T}} > 60$ (36) GeV, the isolation and hadronic energy criteria are removed. One dielectron trigger is used with a symmetric p_{T} threshold of 12 GeV. Two dimuon triggers are used, one with a symmetric p_{T} threshold of 13 GeV and one with an asymmetric threshold of 18 GeV and 8 GeV. Finally, the

mixed dilepton trigger requires an electron with $p_{\mathrm{T}} > 12$ GeV and a muon with $p_{\mathrm{T}} > 8$ GeV.

6.2 Simulation

Simulation of signal and background processes is used in many key places of this analysis. The irreducible background estimation is performed entirely using the simulation. Reducible background processes, such as Z+jets and $t\bar{t}$, are also simulated in order to determine efficiency factors for extrapolation from control regions to the signal region and to provide shapes of variables for the mass, couplings, and differential measurements (see Chapter 9). The signal simulation is used for optimization of the analysis selection criteria (see Chapter 7) and the reconstructed signal yield predictions are used in the signal strength measurement. For the differential measurements, the signal unfolding factors (see Section 8.5) are taken from the simulated detector response.

This following sections describe the various generators used in the analysis, all of which use Monte Carlo (MC) methods for event generation. The detector response for all generated events is determined using the ATLAS detector simulation [70] within the `GEANT4` framework [71]. Addition of pile-up is done in a separate step by overlaying simulated minimum bias events over the signal and background events. A number of data-based corrections are applied to the simulation which are described in Section 6.2.3.

6.2.1 Signal samples and cross sections

Event generation for the $H \to ZZ^{(*)} \to \ell\ell\ell\ell$ process is performed using Powheg [42, 48], which calculates separately the ggF and the VBF production mechanisms with matrix elements up to NLO. The `CTEQ` CT10 Parton Distribution Functions (PDF)[17] are used. Powheg is interfaced with Pythia 8.1 [46] for showering, hadronization and modeling of

[4] See Section 7.2 for definition of lepton isolation.

the underlying event and PHOTOS [72] for quantum electrodynamics (QED) radiative corrections in the final state. Additionally, the ggF events have been reweighted in order to match the Higgs p_{T} predictions of Ref.[73], which includes QCD corrections up to NLO and takes into account soft gluon resummations at NNLL. Pythia is used to generate events for the VH and $t\bar{t}H$ production modes. Signal samples are produced for a selection of Higgs masses ranging from 110 GeV up to 400 GeV.

The Higgs boson production cross-sections, decay branching ratios, and their uncertainties have all been taken from Refs. [25, 74, 75]. The largest contribution to the total production cross section at the LHC comes from the ggF production mode, for which the production cross section has been calculated to NLO [76, 77, 78] and NNLO in QCD [79, 80, 81]. Corrections based on QCD soft-gluon resummations calculated in the NNLL approximation are applied for the gluon-fusion process. Electroweak radiative corrections at NLO are also applied [82, 83].

The production cross section for the VBF process has been calculated with full NLO QCD and EW corrections [84, 85, 86]. The cross sections for VH production have been calculated at NLO[87] and NNLO[88] in QCD and NLO EW corrections have been applied [89]. The cross section for associated production with top quark pairs via $gg/q\bar{q} \to t\bar{t}H$ is calculated up to NLO in QCD [90, 91, 92, 93, 94].

The partial width for the Higgs decay into four leptons has been calculated using PROPHECY4F[95, 96, 97] which takes into account NLO QCD and EW corrections plus the dominant two-loop contributions in the heavy Higgs mass limit [98, 99]. PROPHECY4F also includes interference effects among the diagrams containing identical final-state leptons. The partial widths of the other Higgs decay channels is calculated using HDECAY[100, 101] and the branching ratios are derived by combining these results as in Ref. [25].

The production cross sections, branching ratios, and their uncertainties for several Higgs masses are summarized in Table 6.1. Mass-dependent uncertainties are provided by Ref. [25]

accounting for systematic uncertainties associated with QCD scales and choice of PDF. Near $m_{\mathrm{H}} = 125$ GeV, QCD scale uncertainties are estimated to be $^{+7\%}_{-8\%}$ for the gluon fusion process and $\pm 0.2 - 1\%$ for the VBF, WH and ZH processes. Uncertainties in the production cross section due to uncertainties in PDFs and α_s are evaluated using the procedure in [102] using the `CTEQ`[17], `MSTW`[18], and `NNPDF`[19] PDF sets and found to be $\pm 7 - 8\%$ for gluon-initiated processes and $\pm 2 - 4\%$ for quark-initiated processes.

Table 6.1: Higgs boson production cross sections for ggF, VBF, VH, and $t\bar{t}H$ production modes for selected m_{H} in pp collisions at $\sqrt{s}$ of 7 TeV and 8 TeV. The quoted uncertainties correspond to the total theoretical systematic uncertainties using a quadratic sum of QCD scale and PDF+α_s uncertainties. The decay branching ratio for $H \to 4\ell$, with $\ell = e$ or μ, is reported in the last column [25].

m_H [GeV]	$\sigma(gg \to H)$ [pb]	$\sigma(qq' \to Hqq')$ [pb]	$\sigma(q\bar{q} \to WH)$ [pb]	$\sigma(q\bar{q} \to ZH)$ [pb]	$\sigma(gg \to Htt')$ [pb]	$\mathrm{BR}\left(H \to ZZ^{(*)} \to 4\ell\right)$ [10^{-3}]
$\sqrt{s} = 7$ TeV						
123	15.6 ± 1.6	1.25 ± 0.03	0.61 ± 0.02	0.35 ± 0.01	0.09 ± 0.01	0.103 ± 0.005
125	15.1 ± 1.6	1.22 ± 0.03	0.58 ± 0.02	0.34 ± 0.01	0.09 ± 0.01	0.125 ± 0.005
127	14.7 ± 1.5	1.20 ± 0.03	0.55 ± 0.02	0.32 ± 0.01	0.08 ± 0.01	0.148 ± 0.006
$\sqrt{s} = 8$ TeV						
123	19.9 ± 2.1	$1.61^{+0.04}_{-0.05}$	0.74 ± 0.02	0.44 ± 0.02	$0.14^{+0.01}_{-0.02}$	0.103 ± 0.005
125	19.3 ± 2.0	1.58 ± 0.04	0.70 ± 0.02	0.42 ± 0.02	$0.13^{+0.01}_{-0.02}$	0.125 ± 0.005
127	18.7 ± 1.9	1.55 ± 0.04	0.67 ± 0.02	0.40 ± 0.02	$0.13^{+0.01}_{-0.02}$	0.148 ± 0.006

6.2.2 Background samples

The Standard Model $ZZ^{(*)}$ background processes are simulated using `POWHEG`[103] for quark-antiquark annihilation and `GG2ZZ` [104] for gluon fusion processes. The uncertainties due to choice of PDF and α_{S} are evaluated using the mass-dependent parameterization used in Ref. [74], which is evaluated to be ± 3.4 (7.0)% for $q\bar{q}$ (gg) processes at $m_{4\ell} \sim 125$ GeV. Likewise, the mass-dependent QCD scale uncertainties are also taken from Ref. [74] and amount to $\pm$ 2.8 (24.3)% for $q\bar{q}$ (gg) processes at $m_{4\ell} \sim 125$ GeV. The interference between the $gg \to ZZ^*$ and the ggF signal is expected to be below 1% in the signal mass window [105] and is neglected

in this analysis.

The Z+jets background processes are generated using ALPGEN[106] which is then interfaced to PYTHIAfor showering and hadronization. The events are split into two samples: Z+light jets, which includes $Zc\bar{c}$ in the massless c-quark approximation and $Zb\bar{b}$ coming from parton showers, and $Zb\bar{b}$ as determined using matrix element calculations which include b-quark mass effects. The MLM [107] matching algorithm is used to remove double counting of identical light jets due to the overlap in phase space between the matrix element and parton showering models. However, this matching technique is not implemented for b-quarks so an alternative method is applied in which $b\bar{b}$ pairs with $\Delta\mathrm{R} > 0.4$ are taken from the matrix element calculations and $b\bar{b}$ pairs with $\Delta\mathrm{R} < 0.4$ are taken from the parton shower. The cross sections are calculated at NNLO in QCD using FEWZ [108, 109] for inclusive Z production and at NLO using MCFM [110] for $Zb\bar{b}$ production.

The $t\bar{t}$ background is modeled using POWHEG interfaced to PYTHIA for showering and hadronization, to PHOTOS for QED radiative corrections, and to TAUOLA[111, 112] for the simulation of the τ lepton decays. Simulation of Standard Model WZ production is performed using SHERPA[113].

6.2.3 Data-based Corrections

Several corrections are applied to the simulated events in order to better reproduce the running conditions under which the data were recorded. Simulated events are re-weighted to reproduce the distribution of the mean number of interactions observed in the data (Figure 6.2). Similarly, the LHC beam spot width is different in data and simulation, so another weight is applied to reproduce the beam spot size observed in the data.

Further corrections are made to the simulation in order to compensate for mismodeling of observables which are used in the event selection. Generally speaking, mismodeling of such

observables can result in biased measurements as the efficiencies in data and simulation will be different. Specifically, corrections for the lepton reconstruction and identification efficiencies have been applied based on studies of $Z \to \ell\ell$ and other SM processes [114, 115]. Furthermore, corrections to the lepton four-momentum are also made to reproduce the energy scale and resolution observed in the data [67, 116].

6.2.4 Differential Cross Section Predictions

The observed differential cross section measurements are compared to several theory predictions in order to quantify the compatibility of the data with the SM. Three different calculations of the ggF cross sections are used: Powheg Powheg+Minlo, and HRes2. As noted above, Powheg calculates the cross section at NLO. Minlo is accurate to NLO for Higgs+1 jet events. Finally, HRes2 provides NNLO calculations of ggF with a soft-gluon resummation at small transverse momenta up to NNLL. Additional contributions from VBF (simulated with Powheg+Pythia), VH and $t\bar{t}H$ (Pythia) processes are added to the estimate. Because the differential cross section measurement intends to test the shapes of the observables, all predictions are normalized to the best estimate of the cross sections for a SM Higgs boson with $m_{\mathrm{H}} = 125.4$ GeV [25]. Uncertainties associated with these predictions are described in Section 10.3.3 and the results of these calculations are shown in Section 12.4.

Chapter 7

Event Selection

The event selection in the $H \to 4\ell$ decay channel has been optimized for discovery significance over a wide range of Higgs masses in Run 1 at the LHC. The event selection criteria can be roughly broken into two steps: 1) the selection of the $H \to 4\ell$ final state in Section 7.1 and 2) additional cuts to further reduce backgrounds in Section 7.2. An optimization study of an invariant mass window has been performed for the differential cross section measurements in Section 7.3. Finally, the observables needed for the mass, signal strength, and differential cross section measurements are described in Section 7.4.

This chapter describes the details of the event selection for the $\sqrt{s} = 8$ TeV data. The $\sqrt{s} = 7$ TeV event selection closely follows the selection of the 8 TeV analysis and as such is omitted for brevity. Interested readers can find the details of the $\sqrt{s} = 7$ TeV event selection in Reference [28].

7.1 Four Lepton Final State

The presence of four isolated, relatively high p_{T} leptons in the final state provides a distinctive signature which is used to reject the large majority of SM backgrounds at the LHC. Conversely, the sensitivity of the search for, and measurements of, the $H \to 4\ell$ decay crucially depends

on the lepton selection. In order to maintain high signal efficiency, good reconstruction and identification efficiency is essential, especially in the low p_{T} regime. The following sections describe the reconstruction and identification criteria for electrons and muons.

7.1.1 Electron Selection

Construction of electron candidates in ATLAS is performed in two steps. First, electron candidates are *reconstructed* with very loose criteria in order to maintain high efficiency for real electrons. Second, further selection criteria are applied to the candidates to reduce the non-electron backgrounds using a number of high-level observables, referred to as *identification*.

Electron *reconstruction* begins with the selection of well-measured ID tracks which point to electromagnetic clusters in the calorimeter. A cluster will be identified as an electron candidate if at least one track falls within $\Delta\eta < 0.05$ and $\Delta\phi < 0.05(0.1)$ of the centroid of the reconstructed cluster for tracks bending towards (away from) the centroid of the cluster. The cluster must also satisfy a set of identification criteria that require the longitudinal and transverse shower profiles to be consistent with those expected for electromagnetic showers. Tracks associated with electromagnetic clusters are re-fitted using a Gaussian-Sum Filter tracking algorithm [117], which allows for energy losses along the track due to bremsstrahlung. Figure 7.1 shows the electron reconstruction efficiency as a function of E_{T} and η. Because of the loose criteria applied at this stage, the reconstructed electron candidates contain large contamination from hadronic decays and electrons from photon conversions.

The electron *identification* in ATLAS is based on variables that provide good separation between isolated electrons and hadronic jets faking electrons. Variables describing the longitudinal and transverse shapes of the electromagnetic showers in the calorimeters, the properties of the tracks in the Inner Detector (e.g. number of b-layer and silicon hits, high threshold ratio in TRT, or change in the momentum from the beginning to the end of the track from

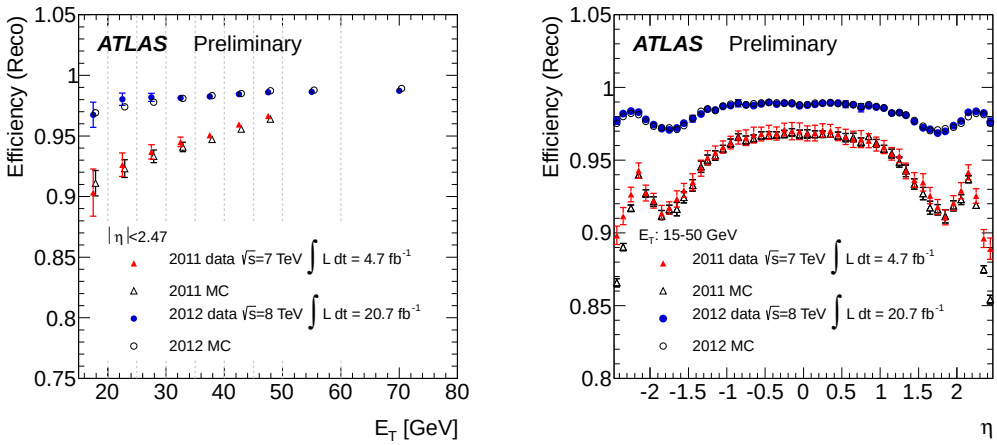

Figure 7.1: Measured electron reconstruction efficiencies as a function of E_{T} integrated over the full pseudorapidity range (left) and as a function of η for 15 GeV$< E_{\mathrm{T}} <$50 GeV (right) for the 2011 (triangles) and the 2012 (circles) datasets[114].

bremsstrahlung) as well as the matching between tracks and energy clusters are used to discriminate against the different background sources. Because many of these variables depend on calorimeter measurements, electron candidates are required to be within $|\eta| < 2.47$ in order to have a high quality calorimeter measurement. Furthermore, electrons are required to have $p_{\mathrm{T}} > 7$ GeV in order to control the backgrounds from jets.

A multivariate analysis (MVA) technique is employed to define the electron identification because it can provide better discrimination than a strictly cuts-based identification algorithm. Furthermore, variables can be used whose overlap between signal and background is too large for explicit cuts, but nonetheless have significant discriminating power.

A Likelihood ratio (LH) approach has been chosen for electron identification because of its simple construction. The electron LH makes use of signal and background probability density

functions (*pdf*) of the discriminating variables. Based on these *pdf*s, an overall probability is calculated for the object to be signal or background. The signal and background probabilities for a given electron are combined into a discriminant $d_{\mathcal{L}}$ on which a cut is applied:

$$d_{\mathcal{L}} = \frac{\mathcal{L}_S}{\mathcal{L}_S + \mathcal{L}_B}, \qquad \mathcal{L}_{S/B}(\vec{x}) = \prod_{i=1}^{n} P_{s/b,i}(x_i) \tag{7.1}$$

where $\vec{x}$ is the vector of variable values and $P_{s/b,i}(x_i)$ is the value of the signal/background probability density function of the i^{th} variable evaluated at x_i. The choice of the cut value on the discriminant determines the signal efficiency and background rejection of the LH working point.

Signal and background *pdf*s used in the electron LH particle identification (PID) are obtained from data as described in Ref. [114], using $Z \to ee$ decays for the signal *pdf*s and background enriched samples for the background *pdf*s. The variables counting the hits on the track are not used as *pdf*s in the LH, but are left as simple cuts, as every electron should have a high quality track to allow for a robust 4-vector measurement. The measured electron identification efficiency is shown as a function of E_{T} and η in Figure 7.2 for different operating points. The LooseLH operating point has been chosen for this analysis in order to maintain a high signal efficiency.

An additional calibration procedure is employed which improves the electron energy measurement by performing a combination of the electron track momentum and cluster energy. This results in significant improvement for electrons which pass through regions of the calorimeter where the energy resolution is poor, such as the calorimeter crack region ($1.37 < |\eta| < 1.52$). For electrons with $p_{\text{T}} < 30$ GeV and $|\eta| < 1.52$, a maximum likelihood fit of the track and cluster momentum measurements is performed. For all other electrons, the calorimeter cluster energy is used for the electron energy measurement. This procedure improves the mass resolution by roughly 4 (3.5)% in the $4e$ ($2\mu 2e$) channels compared to using

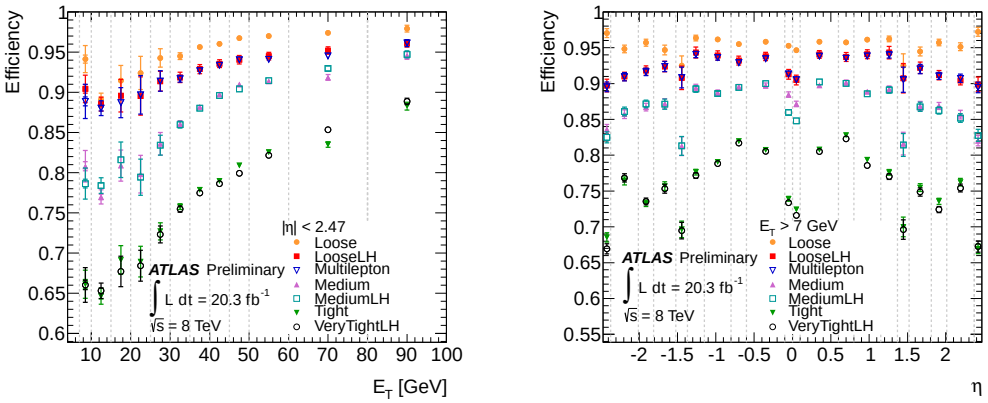

Figure 7.2: Measured electron identification efficiency for various cut-based and LH selections as a function of E_{T} and η. The uncertainties are statistical (inner error bars) and statistical+systematic (outer error bars). The last bin in E_{T} includes the overflow. The dashed lines indicate the bins in which the efficiencies are calculated [114].

the cluster energy alone.

7.1.2 Muon Selection

Four kinds of muon candidates are distinguished depending on the way they are reconstructed: *combined muons, stand-alone muons, segment tagged muons,* and *calorimeter tagged muons* [115]:

- *Combined muons* (CB): Identified using a combination of well-reconstructed tracks in both the MS and ID. A statistical combination of the momentum measurements is performed using the covariance matrices from the individual MS and ID track measurements.

- *Stand-alone muons* (SA): Tracks found only in the MS which are extrapolated to the interaction point, taking into account the effects from multiple scattering and energy

loss in the traversed material. The SA reconstructed muon candidates are used only in the $2.5 < |\eta| < 2.7$ region, outside the ID acceptance.

- *Segment tagged muons* (ST): An ID track which can be associated with track segments in the MS precision muon chambers. The ID track parameters are used for the muon momentum measurement.

- *Calorimeter tagged muons*: An ID track which points to energy depositions in the calorimeters which are compatible with the hypothesis of a minimum ionizing particle. These candidates are used to recover acceptance in the region $|\eta| < 0.1$ which is not equipped with muon chambers.

A number of additional selection criteria are applied to the muon candidates in order to ensure a good measurement of the muon trajectory. The list of track requirements for combined muons is given in Table 7.1. The muon reconstruction efficiency as measured in $Z \to \mu^+\mu^-$ events is shown in Figure 7.3 as a function of p_{T} and η. Finally, muons are required to have $p_{\mathrm{T}} > 6$ GeV and $|\eta| < 2.7$.

Table 7.1: List of Inner Detector hit requirements for the muons for 2011 and 2012 data.

ID Hit requirements 2011	
Silicon hit requirement	$N_{\mathrm{B-layer}} \geq 1$ if expect B-layer hit
	$N_{\mathrm{pixel}} + N_{\mathrm{pixel}}^{\mathrm{inactive}} > 1$
	$N_{\mathrm{SCT}} + N_{\mathrm{SCT}}^{\mathrm{inactive}} > 5$
	$N_{\mathrm{pixel}}^{\mathrm{holes}} + N_{\mathrm{SCT}}^{\mathrm{holes}} < 3$
TRT hit requirements: $\lvert\eta\rvert < 1.9$	$N_{\mathrm{TRT}} + N_{\mathrm{TRT}}^{\mathrm{outliers}} > 5$ & $\frac{N_{\mathrm{TRT}}^{\mathrm{outliers}}}{N_{\mathrm{TRT}}+N_{\mathrm{TRT}}^{\mathrm{outliers}}} < 0.9$
TRT hit requirements: $\lvert\eta\rvert \geq 1.9$	if $(N_{\mathrm{TRT}} + N_{\mathrm{TRT}}^{\mathrm{outliers}} > 5)$: $\frac{N_{\mathrm{TRT}}^{\mathrm{outliers}}}{N_{\mathrm{TRT}}+N_{\mathrm{TRT}}^{\mathrm{outliers}}} < 0.9$
ID Hit requirements 2012	
ID Si hit requirement	$N_{\mathrm{pixel}} + N_{\mathrm{pixel}}^{\mathrm{inactive}} > 0$
	$N_{\mathrm{SCT}} + N_{\mathrm{SCT}}^{\mathrm{inactive}} > 4$
	$N_{\mathrm{pixel}}^{\mathrm{holes}} + N_{\mathrm{SCT}}^{\mathrm{holes}} < 3$
TRT hit requirements: $\lvert\eta\rvert < 1.9$	$N_{\mathrm{TRT}} + N_{\mathrm{TRT}}^{\mathrm{outliers}} > 5$ & $\frac{N_{\mathrm{TRT}}^{\mathrm{outliers}}}{N_{\mathrm{TRT}}+N_{\mathrm{TRT}}^{\mathrm{outliers}}} < 0.9$

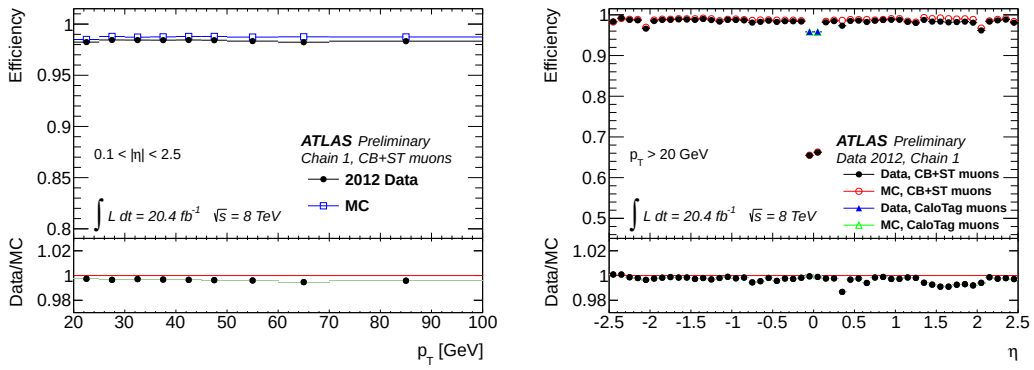

Figure 7.3: Reconstruction efficiency for combined and segment tagged muons as a function of the p_{T} (left) and η (right) of the muon. The panel at the bottom shows the ratio between the measured and predicted efficiencies[115].

7.1.3 Quadruplet Formation

All possible quadruplets consisting of two pairs of same flavor, opposite sign leptons are formed from the leptons passing the criteria above. Additional requirements are imposed on these quadruplets:

- Maximum of one stand-alone or calorimeter tagged muon
- p_{T} thresholds on the three leading leptons of 20, 15, and 10 GeV
- Match between the reconstructed leptons and triggered lepton objects

For each quadruplet, the pair of leptons with invariant mass closest to the Z boson PDG mass is denoted as the leading pair with invariant mass m_{12}; the remaining lepton pair is denoted the sub-leading pair with invariant mass m_{34}. The invariant mass of the four lepton system is denoted as $m_{4\ell}$. The quadruplets are then divided into four channels depending on the flavors of the leading and sub-leading pairs: 4μ, $2\mu 2e$, $2e2\mu$, and $4e$. If a channel contains more than one quadruplet passing the above requirements, the quadruplet with m_{12} closest to the Z boson PDG mass and the largest m_{34} is kept and the others are discarded.

7.2 Analysis Cuts

Additional kinematic cuts are imposed on the quadruplets in each channel separately. Each quadruplet is required to have $50 < m_{12} < 106$ GeV and $m_{\text{thresh}} < m_{34} < 115$ GeV. The value of m_{thresh} varies as a function of $m_{4\ell}$, starting at 12 GeV for $m_{4\ell} \leq 140$ GeV and rising linearly to 50 GeV at $m_{4\ell} \geq 190$ GeV. The leptons within the quadruplet are required to be well separated from each other by requiring $\Delta R(\ell, \ell') > 0.1$ for all same flavor lepton pairs and $\Delta R(\ell, \ell') > 0.2$ for opposite flavor lepton pairs. A requirement of $m_{\ell\ell} > 5$ GeV is applied for all same flavor lepton pairs in order to reject events containing J/Ψ.

To further reduce backgrounds containing leptons within jets or jets faking leptons, isolation and impact parameter requirements are imposed on all leptons within the quadruplet. Requirements are made on two different isolation variables, one based on track information, $\Sigma p_{\text{T}}^{\text{iso}}$, and one based on calorimeter information, $\Sigma E_{\text{T}}^{\text{iso}}$.

The track isolation variable $\Sigma p_{\text{T}}^{\text{iso}}$ is defined as the sum of the transverse momenta of all tracks which fall within a cone of $\Delta R < 0.2$ around the lepton, excluding tracks from any lepton within the quadruplet. The tracks entering this calculation are required to be of good quality by requiring at least four hits in the silicon detectors and $p_{\text{T}} > 1$ GeV for muons; and at least nine TRT hits, one B-layer hit, and $p_{\text{T}} > 0.4$ GeV for electrons. All leptons in a quadruplet are required to satisfy $\Sigma p_{\text{T}}^{\text{iso}}/p_{\text{T}} < 0.15$.

The calorimetric isolation variable $\Sigma E_{\text{T}}^{\text{iso}}$ is defined as the sum of transverse energy, ΣE_{T}, in the calorimeter cells within a cone of $\Delta R < 0.2$ around the lepton trajectory. For muons, a correction for the muon's energy deposition within the calorimeter is applied by subtracting the calorimeter energy found within a much smaller cone around the muon trajectory. For electrons, the electron cluster energy is subtracted from the ΣE_{T}. For all leptons, the contributions from other electrons in the quadruplet within a ΔR cone of 0.18 is also sub-

tracted. Muons are required to have $\Sigma E_{\mathrm{T}}^{\mathrm{iso}}/p_{\mathrm{T}} < 0.3$ and electrons are required to have $\Sigma E_{\mathrm{T}}^{\mathrm{iso}}/E_{\mathrm{T}} < 0.2$.

The impact parameter significance is defined by dividing the impact parameter d_0 by its estimated uncertainty σ_{d0}. Requirements on the impact parameter significance reduce contributions from backgrounds with long decay lifetimes, such as heavy flavor decays. Muons are required to satisfy $d_0/\sigma_{d0} < 3.5$ and electrons are required to satisfy $d_0/\sigma_{d0} < 6.5$.

Finally, if more than one channel contains a quadruplet passing all of the above cuts, the quadruplet from the channel with the best expected mass resolution is chosen and the others are discarded. This gives preference to the decay channels in this order: 4μ, $2e2\mu$, $2\mu2e$, and $4e$.

7.3 Mass Window Optimization

This section describes the optimization of the mass window chosen for the differential cross section measurements in light of the knowledge of the observed resonance around 125 GeV. An additional selection is required in order isolate the signal peak from the backgrounds: a mass window cut in $m_{4\ell}$, the four-lepton invariant mass after FSR correction and Z mass constraint (see Section 7.4).

An optimization procedure has been implemented using the inclusive signal (S) and background (B) yields. Three figures of merit have been studied: (1) $S/\sqrt{S+B}$ a measure of the statistical significance, (2) $S/\sqrt{B}$, a measure of significance vs the null hypothesis and (3) Z_0, a more general formula for $S/\sqrt{B}$ which is applicable in a low stats regime [118]:

$$Z_0 = \sqrt{2((S+B)\cdot \ln(1+S/B) - S)} \tag{7.2}$$

Each is studied by simultaneously varying the lower and upper $m_{4\ell}$ cuts over the range [110, 140] GeV. The final mass window will be chosen using $S/\sqrt{S+B}$ because this will minimize

the cross-section uncertainty, which will be dominated by the statistical uncertainty.

The results of this procedure can be seen in Figure 7.4 for the signal sample with $M_H = 125$ GeV. The window of [121.4, 127.1] GeV maximizes $S/\sqrt{B}$ while the window [118.6, 128.2] GeV maximizes $S/\sqrt{S+B}$. Similarly, the window [120.7, 127.5] GeV maximizes Z_0. One should notice that the significance changes more rapidly with the lower cut than the upper cut. This is due to the longer tail on the low mass side of the signal peak.

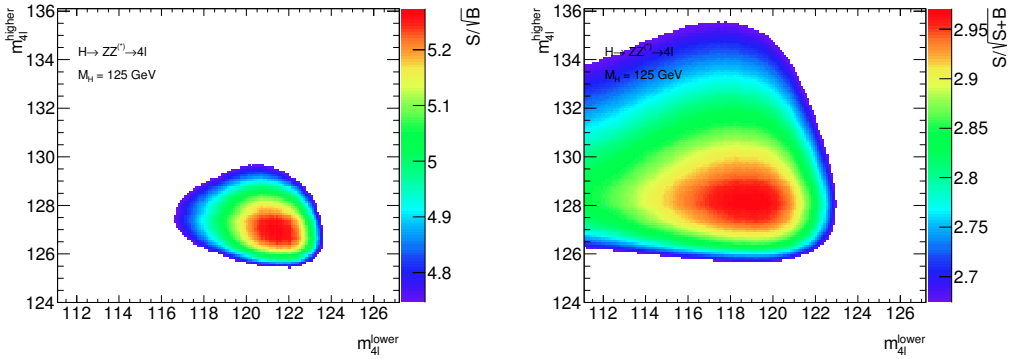

Figure 7.4: (a) $S/\sqrt{B}$ and (b) $S/\sqrt{S+B}$ as a function of lower and upper $m_{4\ell}$ cuts for the mass window optimization.

The optimal window was derived for Higgs masses from 123 GeV to 127 GeV in order to understand the impact of the Higgs mass on choice of mass window. The results are seen in Table 7.2 and show that the optimal mass window shifts directly with the Higgs mass. Figure 7.5 shows the best fit point and 97.5% contours of $S/\sqrt{S+B}$ and $S/\sqrt{B}$ for each of the Higgs mass samples. This shows that a single mass window can be chosen such that the expected error on the measurement is not severely affected by the uncertainty on the Higgs mass measurement (expected to be of the order of 500 MeV).

Table 7.2: Optimal mass window cuts for m_{H} from 123 GeV to 127 GeV based on three figures of merit: $S/\sqrt{B}$, $S/\sqrt{S+B}$, and Z_0.

m_{H} [GeV]	$S/\sqrt{B}$	Z_0	$S/\sqrt{S+B}$
123	[119.7, 124.9]	[118.9, 125.2]	[116.9, 126.0]
124	[120.5, 126.0]	[119.9, 126.5]	[117.8, 127.3]
125	[121.4, 127.1]	[120.7, 127.5]	[118.6, 128.2]
126	[122.5, 128.1]	[121.5, 128.4]	[119.7, 129.2]
127	[123.5, 128.8]	[122.5, 129.4]	[120.4, 130.4]

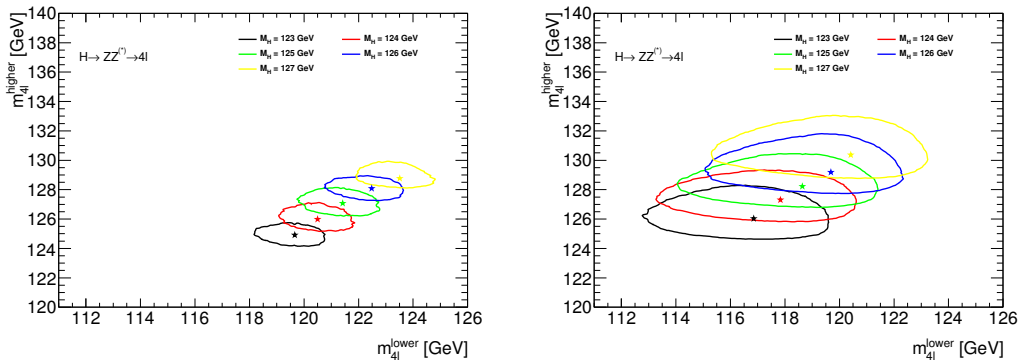

Figure 7.5: Optimal mass window cuts as determined by the metrics (a) $S/\sqrt{B}$ and (b) $S/\sqrt{S+B}$ for various Higgs mass scenarios from 123 to 127 GeV. The stars indicate the cuts which maximize the given metric and the contours indicate where the metric decreases to 97.5% of its maximum value for a given Higgs mass.

7.4 Observables

This section describes the final observables used for the measurements contained in this thesis. The mass and signal strength measurements rely on the two variables, $m_{4\ell}$ and BDT_{ZZ}, which are described in Sections 7.4.1 and 7.4.2. Furthermore, the differential cross section measurements are performed for the six observables described in Section 7.4.3.

7.4.1 Invariant Mass

The invariant mass of the four-lepton system, which forms a peak near m_{H}, is the most discriminating variable in this analysis. Two further corrections are implemented in order to improve the mass resolution and thus the sensitivity of the measurements.

7.4.1.1 Final State Radiation Recovery

A Final State Radiation (FSR) correction is performed in order to recover energy lost to low energy photons which are radiated from the leptons. Two strategies are employed to recover both collinear and non-collinear FSR photon candidates, from which one candidate will be chosen whose four-vector is added to the four-vector of the 4-lepton system.

A search for photons collinear to the selected muons is performed following the methods detailed in Ref. [119]. FSR photon candidates may be reconstructed from calorimeter clusters or the standard ATLAS reconstructed photons depending on the candidate energy. In the range 1.5 GeV $< E_{\mathrm{T}} <$ 3.5 GeV, FSR candidates are selected from calorimeter clusters which pass shower shape requirements and fall within $\Delta R < 0.08$ of a reconstructed muon. For $E_{\mathrm{T}} > 3.5$ GeV, FSR photon candidates are required to pass shower shape requirements and fall within $\Delta R < 0.15$ of the reconstructed muon. If more than one candidate is found, the candidate with the highest E_{T} is chosen as the final candidate.

Non-collinear FSR candidates may be selected from the ATLAS standard photon reconstruction for events with muons or electrons. A photon is considered to be a candidate if it passes the ATLAS *tight* photon identification requirements, has $E_{\mathrm{T}} > 10$ GeV, and does not fall within $\Delta R \leq 0.15$ of any lepton within the quadruplet. Furthermore, an isolation requirement of $\Sigma E_{\mathrm{T}}^{\mathrm{iso}} < 4$ GeV is applied in order to remove jets which may fake photons. If more than one candidate is found, the candidate with the highest E_{T} is chosen as the final candidate.

Finally, only one FSR photon candidate per event is chosen for the correction but several kinematic requirements are first applied. The collinear photon candidate is accepted only if $66 < m_{\mu\mu} < 89$ GeV and $m_{\mu\mu\gamma} < 100$ GeV for the leading Z only. If the collinear candidate search fails, the correction is applied using the non-collinear candidate provided it passes

certain kinematic criteria. The non-collinear FSR photon candidate may only be used to correct the leading Z for events with $m_{4\ell} < 190$ GeV but may be added to either the leading or sub-leading Z for $m_{4\ell} \geq 190$ GeV. The non-collinear photon will be accepted if $m_{\ell\ell} < 81$ GeV and $m_{\ell\ell\gamma} < 100$ GeV. If both Z's satisfy these requirements, then the correction is applied to the Z with $m_{\ell\ell\gamma}$ closest to the Z PDG mass.

7.4.1.2 Z-Mass Constraint

The second correction to $m_{4\ell}$ is the application of a Z-mass constraint. Because many of the lepton pairs are coming from the decay of an on-shell Z boson and the Z natural width is comparable to the detector mass resolution, one may use the knowledge of the Z mass line-shape to improve the 4-lepton mass resolution. The probability of observing a Z decaying to leptons with true mass m_{true} can be parameterized as:

$$L(\mathbf{p}_1^{\text{true}}, \mathbf{p}_2^{\text{true}}, \mathbf{p}_1^{\text{rec}}, \mathbf{p}_2^{\text{rec}}) = B(\mathbf{p}_1^{\text{true}}, \mathbf{p}_2^{\text{true}}) \cdot R_1(\mathbf{p}_1^{\text{true}}, \mathbf{p}_1^{\text{rec}}) \cdot R_2(\mathbf{p}_2^{\text{true}}, \mathbf{p}_2^{\text{rec}}) \tag{7.3}$$

where $\mathbf{p}_{1,2}^{\text{true}}$ are the true lepton momenta and $\mathbf{p}_{1,2}^{\text{rec}}$ are the reconstructed lepton momenta. The functions $R_{1,2}$ are response functions which model the detector resolution effects. Because the angular resolution (η/ϕ) is extremely good, the response functions can be simplified to only depend on the energy resolution:

$$R_{1,2}(\mathbf{p}_{1,2}^{\text{true}}, \mathbf{p}_{1,2}^{\text{rec}}) = R_{1,2}(E_{1,2}^{\text{true}} | \mathbf{p}_2^{\text{rec}}) \tag{7.4}$$

where $E_{1,2}^{\text{true}}$ are the true energies of the leptons.

The true mass line-shape of the Z boson is described the function B, which only depends on the invariant mass of the two leptons and can be written in terms of their energies in the relativistic limit:

$$m_{true}^2 = 2 \cdot E_1^{\text{true}} E_2^{\text{true}} (1 - \cos(\theta)) \tag{7.5}$$

where θ is the opening angle between the leptons. Therefore, all the terms in Eqn. 7.3 depend exclusively on the energies of the leptons. The Z-mass constraint is performed by maximizing this function with respect to the $E_{1,2}^{\text{true}}$ parameters, giving the most likely values of the true lepton energies.

The Z mass line-shape function B is modeled using a relativistic Breit-Wigner function with mean and width parameters set to the Z boson mass and Z natural width. This function was checked against the Z line-shape as determined using simulation and found to have negligible differences in performance. The response functions $R_{1,2}$ are approximated by Gaussian distributions with the mean set to the measured lepton energies $E_{1,2}^{\text{rec}}$ and variance set to the lepton energy resolution as obtained from the simulation. The actual lepton response functions receive enhanced tail contributions from reconstruction and photon radiation effects, but modeling of these effects is found to have a negligible effect on the performance of the method.

Finally, because the Z-mass constraint assumes on-shell Z production, the procedure is only applied to the leading lepton pair for events with $m_{4\ell} \leq 190$ GeV (the subleading lepton pair has a significantly different mass shape). For events with $m_{4\ell} > 190$ GeV, the Z-mass constraint is applied to both the leading and subleading lepton pairs. The results of this procedure are shown in Figure 7.6, where a clear improvement in the mass resolution is observed after applying the Z-mass constraint both in m_{12} and $m_{4\ell}$ using the $m_{\text{H}} = 125$ GeV signal samples.

7.4.2 Multivariate Discriminant

In order to improve the sensitivity of the mass and signal strength measurements, a multivariate discriminant against the irreducible background, BDT_{ZZ}, is created using the Boosted Decision Tree (BDT) technique. The discriminant is based upon three input variables: the p_{T}

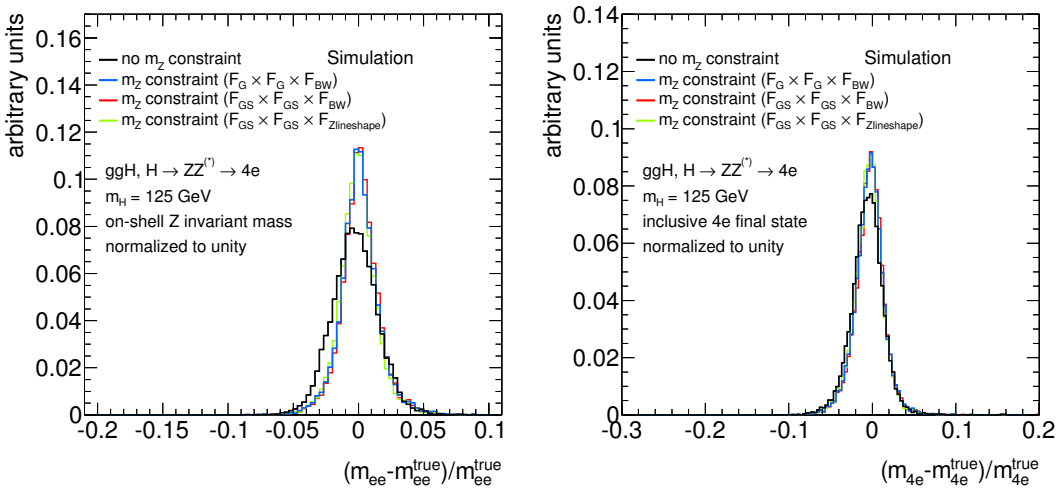

Figure 7.6: Distributions of the mass response, $\frac{m-m_{\text{true}}}{m_{\text{true}}}$, of the leading di-electron pair (a) and the 4-electron final state (b) in inclusive $H \to ZZ^* \to 4e$ events generated with $m_{\text{H}} = 125$ GeV. The mass response is shown without Z mass constraint (black), with the standard Z mass constraint using a Gaussian approximation of the electron energy response (blue), with a Z mass constraint using Gaussian sums for the response function (red) and with a Z mass constraint using the Gaussian-sum response functions and the actual generator m_{Z_1} distribution (green). The distributions are shown for events with $|m_{12} - m_Z| < 3$ GeV.

and η of the four-lepton system and a matrix-element based kinematic discriminant (D_{ZZ}). The distributions of these three variables for both the signal and the irreducible background are shown in Figure 7.7, showing separation between the signal and background.

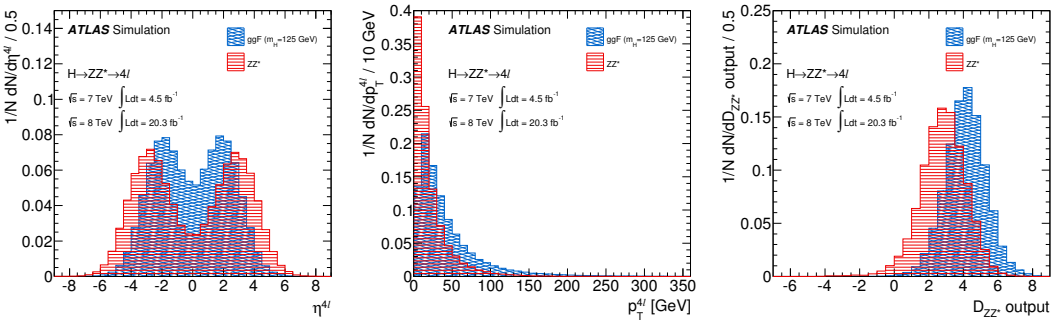

Figure 7.7: The η, p_{T} and D_{ZZ} distributions for the $m_{\text{H}} = 125$ GeV signal (blue) and ZZ background (red) samples in the mass range $115 < m_{4\ell} < 130$ GeV used for the training of the BDT discriminant.

The D_{ZZ} is based upon matrix element (ME) calculations which take as input the four-vectors of the four leptons in the final state. The square of the matrix element gives the probability of observing a particular kinematic configuration given a signal/background process hypothesis. The D_{ZZ} is the logarithm of the ratio of the Higgs signal probability over the ZZ background probability:

$$D_{ZZ} = \ln\left(\frac{|\mathcal{M}_{\text{sig}}|^2}{|\mathcal{M}_{ZZ}|^2}\right) \tag{7.6}$$

The ME are computed at LO using MadGraph [120] with the process $pp \to H \to ZZ \to 4\ell$ for the signal hypothesis ($\mathcal{M}_{\text{sig}}$) and $pp \to 4\ell$ for the ZZ background hypothesis ($\mathcal{M}_{ZZ}$). For the $\mathcal{M}_{\text{sig}}$ calculation, m_{H} is set to the reconstructed $m_{4\ell}$ for each event.

The BDT is trained separately for $4e/4\mu$ events and $2e2\mu$ events. The output of the BDT (BDT_{ZZ}) for the combined 7 and 8 TeV datasets is shown in Figure 7.8. Good separation is achieved between the signal and background processes.

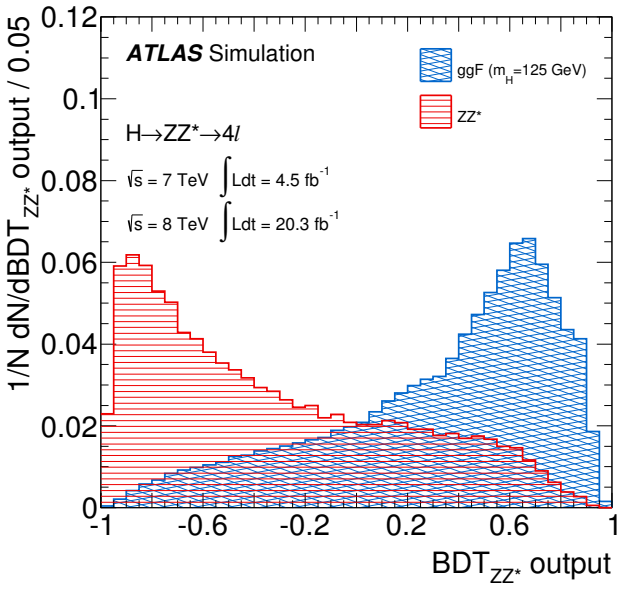

Figure 7.8: Shapes of the BDT output for the Higgs boson signal with $m_{\text{H}} = 125$ GeV (blue) and ZZ^* background (red) for the combined 7 and 8 TeV datasets.

7.4.3 Differential Variables

Differential cross section measurements are performed for a number of variables which describe event kinematics and properties of Higgs boson production. The following sections explain the choice of variables and their reconstruction. An overview is given in Table 7.3.

7.4.3.1 Higgs Kinematics

The kinematics of Higgs boson production and decay are of particular interest as deviations from the SM predictions could indicate non-SM properties of the Higgs itself or the presence of other particles being produced in association with the Higgs boson. The $H \to 4\ell$ decay channel is particularly interesting because the full Higgs kinematic information is accessible through the reconstruction of all of the Higgs decay products.

The kinematics of the Higgs particle in a pp collision can be described by the transverse momentum $p_{T,H}$, azimuthal direction Φ_H, and rapidity y_H. The decay to four leptons is described by the invariant mass of the leading lepton pair m_{12}, the invariant mass of the sub-leading lepton pair m_{34}, and five decay angles (Φ_H, Φ_1, θ^*, θ_1, θ_2) between the leptons as shown in Fig. 7.9. The dilepton masses and decay angles are sensitive to the spin and CP properties of the Higgs boson.

The Higgs boson differential transverse momentum cross section is of particular interest as the theoretical predictions have been studied extensively (see e.g. [73, 121, 122, 44, 45] and the References in [74]). In particular, the treatment of the top and bottom quark masses in the calculation of the ggF production mode cross section can lead to order 10% differences in the differential transverse momentum cross section [45].

This analysis makes the first differential cross section measurements of $p_{\mathrm{T,H}}$, $|y_H|$, m_{34}, and $|\cos\theta^*|$ in the $H \to 4\ell$ decay channel. The corresponding reconstructed variables are

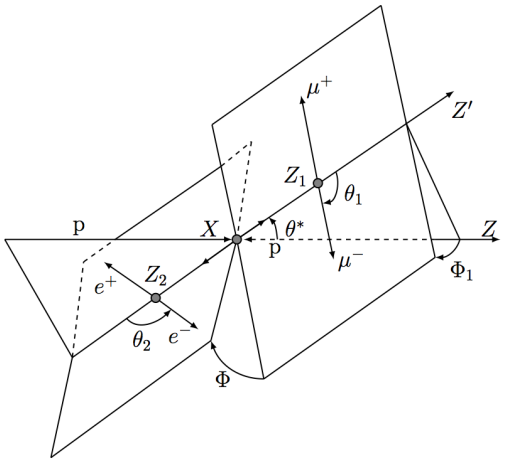

Figure 7.9: Diagram of decay angles for the $H \to 4\ell$ decay.

measured using the kinematics of the four reconstructed leptons are defined as $p_{\mathrm{T},H}^{\mathrm{reco}}$, $|y_H^{\mathrm{reco}}|$, m_{34}^{reco}, and $|\cos\theta^{*\mathrm{reco}}|$.

7.4.3.2 Jet variables

The measurement of the jet multiplicity and other jet properties probes both QCD radiation effects and contributions from the various production modes of the Higgs boson. The fraction of events coming from non-ggF production modes increases with jet multiplicity due to the presence of hadronic decays of the particles produced in association with the Higgs boson (see Fig. 12.7). This allows measurement of the relative strength between the ggH, VVH, and $t\bar{t}H$ couplings [28].

Jets are reconstructed from topological clusters in the calorimeters using an anti-k_{T} algorithm [123] with a distance parameter of $R = 0.4$. Jets are required to fall within the acceptance of the calorimeters ($|y| < 4.4$) with a p_{T} threshold of 30 GeV. Cleaning is applied to the jets using ATLAS standard procedures and a requirement on the jet vertex fraction (JVF) is applied in order reduce contributions from jets resulting from pile-up. The JVF

Table 7.3: Definition of variables used in the differential cross section measurement both at truth and reconstruction levels. For the definition of the truth particles see Sec. 8.2.

Variable	Truth Level Observable	Reconstruction Level Observable
$p_{\mathrm{T,H}}$	p_{T} of the intermediate Higgs particle	p_{T} of the reconstructed four-lepton system (no FSR correction)
$\lvert y_H \rvert$	rapidity of the intermediate Higgs particle	rapidity of the reconstructed four-lepton system (no FSR correction)
m_{34}	Invariant mass of the sub-leading lepton pair (includes mispairing)	Invariant mass of the sub-leading lepton pair (includes mispairing)
$\lvert\cos\theta^*\rvert$	θ^* is the production angle of Z_1, defined in the four lepton rest frame (includes mispairing)	θ^* is the production angle of Z_1, defined in the four lepton rest frame (includes mispairing)
n_{jets}	Number of truth jets	Number of reconstructed jets
$p_{\mathrm{T,jet}}$	p_{T} of the leading truth jet	p_{T} of the leading reconstructed jet

is defined as the fraction of track momentum associated with a jet that can be matched to the primary vertex. As it depends on ID tracking, it is only contributes within the ID acceptance. For jets with $|\eta| < 2.4$ and $p_{\mathrm{T}} > 50$ GeV, the jet must satisfy $|\mathrm{JVF}| > 0.25$. Furthermore, because electrons will also be reconstructed as jets, jets which overlap with an electron ($\Delta R < 0.2$) are removed in order to not double count these objects.

This analysis measures differential cross sections in jet multiplicity, n_{jets}, and the transverse momentum of the leading jet, $p_{\mathrm{T,jet}}$. As can be seen in Fig. 12.7, the 0-jet bin is dominated by ggF production while VH and VBF production modes contribute increasingly larger fractions in the 1-jet and 2-jet bins. The majority of $t\bar{t}H$ events have high jet multiplicity (≥ 3 jets). The leading jet transverse momentum directly probes quark and gluon radiation events inclusively and allows tests of fixed order QCD calculations of gluon-gluon fusion processes.

7.4.3.3 Differential Variable Binning

Binning is chosen for each variable of interest based on several criteria before looking into the data signal region ($118 < m_{4\ell} < 129$ GeV) in order to remain unbiased. First, the range of each variable is chosen. For fixed range variables, such as $|\cos\theta^*|$, this is trivial, while for variables with unbound ranges (such as $p_{\mathrm{T,H}}$), the range is chosen to cover approximately

95% of the events from the expected SM signal. Next, the number of bins is chosen in order to achieve an expected significance of roughly 1.5 σ in each bin. Within the signal region, $S/\sqrt{S+B}$ is expected to be approximately 3 in the SM with the current dataset, and, assuming that significances add in quadrature, a rough approximation gives $3^2/1.5^2 = 4$ bins for each variable. Finally, the bin edges are chosen based on individual considerations for each variable (see below) while also trying to maintain similar $S/\sqrt{S+B}$ in the various bins. Table 7.4 lists the chosen binning for all of the variables.

- $p_{\mathrm{T,H}}$: Bin edges are suggested by theoretical concerns. For $p_{\mathrm{T,H}} > 100$ GeV, the calculation of the ggF cross-section can be accomplished using a fixed order calculation, but below 100 GeV, the calculation requires resummation of leading order logarithms. Furthermore, the treatment of the finite top and bottom quark mass creates additional scales, one at twice the bottom quark mass.

- $|y_H|$: The rapidity distribution is fairly flat and thus allows for five bins.

- m_{34}: The lower edge of the distribution is bounded by the $m_{34} > 12$ GeV cut which is applied in the event selection. The bin edges are then placed at multiples of 10 GeV from 20 GeV to 60 GeV. The last two bins (40-50,50-60 GeV) are combined in order to improve the statistical significance.

- $|\cos\theta^*|$: This distribution is flat in the SM; therefore, a fixed width binning is chosen with a width of 0.2.

- n_{jets}: Trivial binning, except for the highest bin which is inclusive in order to decrease the effects of bin-to-bin migrations at high n_{jets} where there are large theoretical uncertainties in the modeling due to the use of perturbative calculations.

- $p_{\mathrm{T,jet}}$: Three bins are possible above the jet p_{T} threshold of 30 GeV.

Table 7.4: Binning chosen for the variables of interest. Overflow events are reported but do not contribute to the measurement.

Variable	Bin Edges	N_{bins}
$p_{\text{T,H}}$	0, 20, 50, 100, 200 GeV	4
$\lvert y_H \rvert$	0, 0.3, 0.65, 1.0, 1.4, 2.4	5
$\lvert \cos\theta^* \rvert$	0, 0.2, 0.4, 0.6, 0.8, 1.0	5
m_{34}	12.5, 20, 30, 40, 60 GeV	4
n_{jets}	0, 1, 2, $\geq$3	4
$p_{\text{T,jet}}$	0, 30, 50, 70, 140 GeV	4

Chapter 8

Analysis Fiducial Region

This chapter describes the fiducial region and unfolding methods used for the cross section measurements.

8.1 Definitions

The total production cross-section of a process σ_{total} is canonically expressed as:

$$\sigma_{\text{total}} \cdot BR = \frac{n_{\text{total}}^{\text{signal}}}{\mathcal{L}_{\text{int}}} = \frac{n_{\text{reco}}^{\text{signal}}}{\epsilon_{\text{total}} \cdot \mathcal{L}_{\text{int}}} \tag{8.1}$$

where BR is the branching ratio of a particular final state, $n_{\text{total}}^{\text{signal}}$ is the total number of signal events produced, $n_{\text{reco}}^{\text{signal}}$ is the number of reconstructed signal events in that final state, $\mathcal{L}_{\text{int}}$ is the integrated luminosity, and ϵ_{total} is the efficiency for detecting the signal process accounting for trigger, reconstruction and identification efficiencies (defined as $n_{\text{reco}}^{\text{signal}}/n_{\text{total}}^{\text{signal}}$).

The efficiency ϵ_{total} is typically model-dependent because it contains contributions from events which are outside of the detector acceptance. As a result, applying this efficiency to the observed signal yields extrapolates the measurement to regions of phase space to which the detector has no sensitivity. In order to remove this model-dependence, the efficiency is split into two terms:

$$\epsilon_{\text{total}} = A_{\text{fid}} \cdot \epsilon_{\text{fid}} \tag{8.2}$$

A_{fid} is the fiducial acceptance, the fraction of events that fall within the fiducial volume of the detector and ϵ_{fid} is the fiducial efficiency, the signal efficiency within the fiducial volume of the detector. These are defined as:

$$A_{\text{fid}} = \frac{n_{\text{fiducial}}^{\text{signal}}}{n_{\text{total}}^{\text{signal}}} \qquad \epsilon_{\text{fid}} = \frac{n_{\text{fiducial}}^{\text{signal}}}{n_{\text{reco}}^{\text{signal}}} \tag{8.3}$$

where $n_{\text{fiducial}}^{\text{signal}}$ is the number of events within the fiducial volume. Calculation of this number requires a fiducial volume definition - see Section 8.3.

By removing the acceptance term, one may measure a more model independent quantity, the *fiducial cross section*, σ_{fid}, defined as:

$$\sigma_{\text{fid}} \cdot BR = \frac{n_{\text{reco}}^{\text{signal}}}{\epsilon_{\text{fid}} \cdot \mathcal{L}_{\text{int}}} \tag{8.4}$$

8.2 Truth Object Definitions

Truth-level physics objects must be defined in order to choose a detector fiducial region and to provide truth-level "observables" to which to unfold. Truth-level electrons and muons are needed for the $H \to 4\ell$ fiducial selection and truth-level jets are defined for the jet-related differential cross section measurements.

When selecting truth leptons, one has a choice whether to include effects of initial and final state radiation in the truth lepton kinematics. The standard choices, commonly referred to as Born, bare, and dressed, are shown in Figure 8.2. Born level kinematics are specified by the matrix element before any QED corrections are applied. Bare kinematics take into account all radiative effects. Dressed kinematics are the same as bare except that nearby (collinear) photons are added back into the lepton four-vector.

The optimal choice of kinematics depends on the physics object in question. For example, the electron reconstructed kinematics are better approximated by the dressed electron

kinematics because the electron energy measurement is based on a localized cluster of energy in the calorimeter. However, for muons the bare kinematics provides a better description because the momentum measurement is based upon track curvature measurements. For this analysis, the Born kinematics are used for the leptons and the jets are formed using the bare particles. More detailed studies on the choice of the truth lepton kinematics can be found in Appendix A. The following additional criteria are applied to specific truth physics objects:

- **Electrons:** $p_{\mathrm{T}} > 7$ GeV, $|\eta| < 2.47$.

- **Muons:** $p_{\mathrm{T}} > 6$ GeV, $|\eta| < 2.7$

- **Jets:** Particle-level jets are reconstructed from all stable particles except muons and neutrinos using the anti-k_{t} algorithm [123] with distance parameter $R = 0.4$. Each jet is required to have $p_{\mathrm{T}} > 30$ GeV and $|y| < 4.4$ and must not be within $\Delta R < 0.2$ of any truth electron as selected above.

8.3 Fiducial Region Definition

Fiducial region cuts are chosen to replicate the reconstruction level cuts in order to minimize model-dependent acceptance effects on the measured fiducial cross section. At the same time it is important to make the fiducial region cuts easily reproducible with different event generators/matrix element calculators. The fiducial region for the $H \to 4\ell$ analysis is defined as follows:

- **Higgs candidate**:

  The Higgs candidate is composed of two pairs of same flavor, opposite charge truth leptons. The pairing is carried out the following way: The leading pair is defined as the

lepton pair with invariant mass closest to m_Z and the subleading pair is defined as the remaining lepton pair with invariant mass closest to m_Z.

- **Lepton kinematics**:

  $p_{\mathrm{T}} > 20, 15, 10$ GeV for leading leptons within the quadruplet

- **Mass-pair cuts**:

  $50 < m_{12} < 106$ GeV; $12 < m_{34} < 115$ GeV

- **Lepton separation**:

  $\Delta R(\ell_i, \ell_j) > 0.1(0.2)$ for same (opposite) flavor leptons

- **J/ψ veto**:

  $m(\ell_i, \ell_j) > 5$ GeV for same flavor opposite sign lepton pairs

- **Mass Window**:

  $118 < m_{4\ell} < 129$ GeV

Note that all leptons in an event are considered when pairing truth leptons into the Higgs candidate quadruplet. This allows leptons which are not direct decay products of the truth Higgs object to be chosen and is necessary in order to replicate the behavior of the reconstruction selection. This is particularly important when considering the VH production modes as the fraction of reconstructed events in which the pairing algorithm chooses a lepton coming from the associated vector boson can be as large as 20%.

In contrast to the reconstruction selection, there is no isolation cut applied in the fiducial selection. This allows the possibility to choose truth leptons coming from hadronic decays, which will introduce significant differences between the reconstruction and fiducial selections. Defining an isolation cut at truth-level is technically possible, but is considered to overly

complicate the fiducial region for this analysis. Instead, an alternative approach is to only select leptons coming form the decays of W and Z bosons.

Finally, the signal samples used to derive the correction factors include $H \to 2\tau 2\ell$ and $H \to 4\tau$ decays, which contribute $\sim 0.5\%$ of the reconstructed signal yield due to leptonic τ decays. The fiducial acceptance for the $H \to 2\tau 2\ell$ and $H \to 4\tau$ decays (given the above fiducial region definition) is similarly small. However, many theory predictions only consider direct $H \to 4\ell$ decays. Therefore, events containing $Z \to \tau\tau$ events are explicitly removed from the fiducial region in order to facilitate easier comparisons with theory predictions.

8.4 Fiducial Region Studies

In this section, several fiducial quantities are studied to validate the fiducial region definition defined in Sec. 8.3 and to understand the model-dependence of the measurement. These quantities have been studied as a function of the Higgs mass, production mode, and decay channel (4μ, $4e$, etc.). Comparisons are also made between the fiducial quantities with and without the mass window cut. Additionally, several models with non-SM spin/CP properties have been studied to demonstrate the model independence of the fiducial efficiency.

8.4.1 Fiducial Acceptance

Given an appropriate fiducial region definition, the fiducial acceptance (defined in Eqn. 8.3) describes the fraction of events which could possibly be reconstructed in the detector. Figure 8.1 shows the fiducial acceptance as a function of m_{H} for all Higgs production modes in the range from $m_{\mathrm{H}} = 120$ to $m_{\mathrm{H}} = 130$ GeV both with and without the mass window selection applied[5].

[5] Note that this measure of the acceptance contains the $H \to 2\tau 2\ell$ and $H \to 4\tau$ events for which the fiducial acceptance is zero because these events are excluded explicitly from the fiducial region.

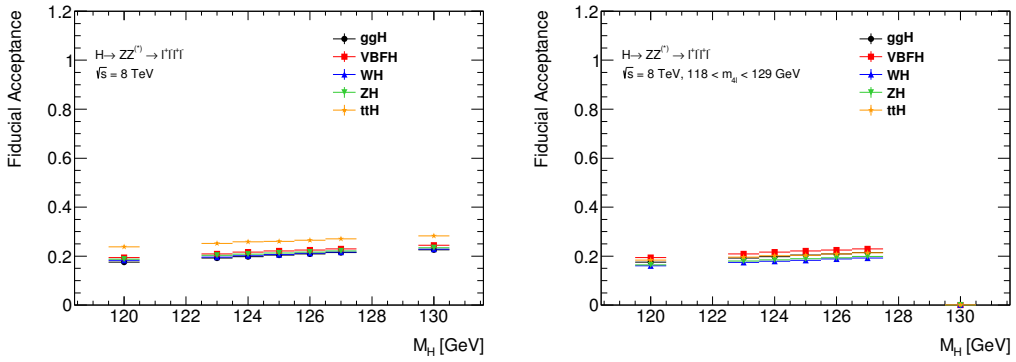

Figure 8.1: Fiducial acceptance as a function of the Higgs mass for all production modes (a) without a mass window cut and (b) with the mass window cut of $118 < m_{4\ell} < 129$ GeV.

The fiducial acceptance is within 10% for all Higgs production modes with the exception of $t\bar{t}H$ when no mass window cut is applied, as illustrated in Figure 8.4.1. The larger lepton multiplicity in the $t\bar{t}H$ production mode results in a combinatorially increasing number of possible pairings. This leads to a higher efficiency for the m_{12} and m_{34} requirements, resulting in a larger fiducial acceptance. The effects of this are also seen in the mispairing fraction. After applying the mass window cut, the mispairing fraction decreases in $t\bar{t}H$ and the fiducial acceptance is comparable to the other production modes.

The fiducial acceptance for each final state is shown in Figure 8.2 as a function of m_{H}. Note that here, because the acceptance is calculated in each channel, events containing $Z \to \tau\tau$ decays are not included. In the ggF mode, the 4μ channel has the largest fiducial acceptance and the $4e/2\mu 2e$ channels have a smaller acceptance due to the more strict kinematic requirements on electrons as compared to muons. In the $t\bar{t}H$ mode, one can again see the effect of the mispairing as the $4e$ channel has larger acceptance than the mixed channels.

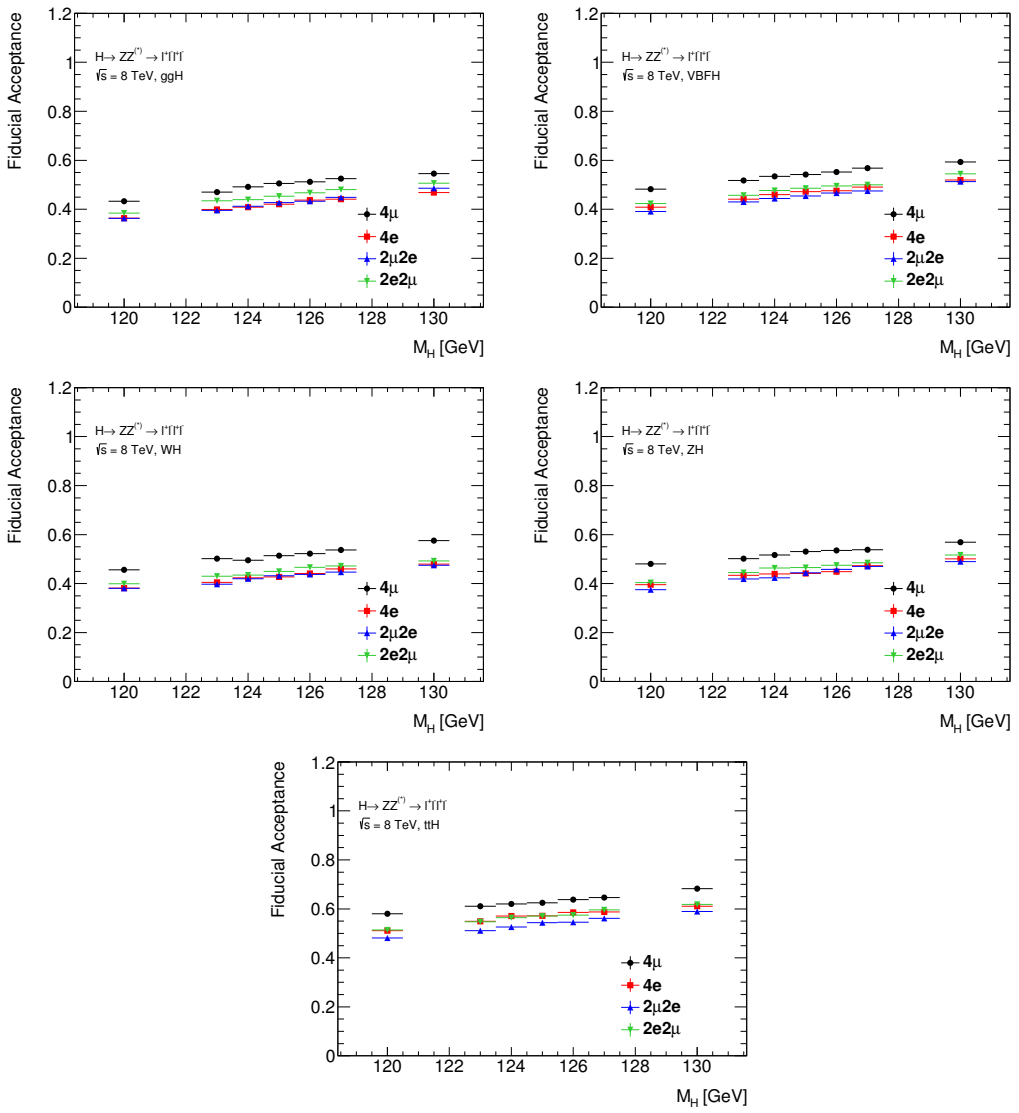

Figure 8.2: Fiducial acceptance as a function of the Higgs mass from $m_{\mathrm{H}} = 120$ to $m_{\mathrm{H}} = 130$ GeV, separately for each final state and production mode. Uncertainties are statistical only.

8.4.2 Fiducial Efficiency

The fiducial efficiency quantifies the signal efficiency within the fiducial volume of the detector and is defined in Eqn. 8.3 . In an ideal case, the fiducial efficiency will be independent of the underlying model and thus the fiducial cross-section measurement will be model-independent. Note that the fiducial efficiency is not an efficiency in the strictest sense as the reconstructed events are not a strict subset of the fiducial events (see Section 8.4.4).

The fiducial efficiency is presented in Figure 8.3 as a function of m_{H} for all Higgs production modes. The fiducial efficiency is similar for all production modes within 2-3% with the exception of the $t\bar{t}H$ mode, which has a reduced efficiency with respect to the other modes. The reduced fiducial efficiency in $t\bar{t}H$ is the result of a decreased reconstruction efficiency due to the lepton isolation requirements. The reconstructed leptons are less isolated because of the presence of the additional top decays within the event. The $t\bar{t}H$ fiducial efficiency is affected by this due to the lepton isolation cut being applied in the reconstructed selection but not in the fiducial selection.

Without the mass window requirement, the fiducial efficiency changes by $< 1\%$ over the range $120 < m_{\mathrm{H}} < 130$ GeV, as shown in Figure 8.3. This indicates that the choice of m_{H} used to derive the fiducial efficiency will introduce a small systematic uncertainty. The mass window requirement introduces a stronger dependence on m_{H} as shown in Figure 8.3 because the mass resolution is different between the truth-level and reconstruction-level observables. However, given that the uncertainties on the m_{H} are roughly 0.4 GeV, the relevant points to consider are from $m_{\mathrm{H}} = 124$ to $m_{\mathrm{H}} = 126$ GeV. Over this range, the fiducial efficiency within the mass window changes by $< 3\%$. A systematic uncertainty is applied to the correction factors to account for this dependence which is described in Section 8.5.3.

The combined fiducial efficiency for the signal is derived assuming the SM cross section

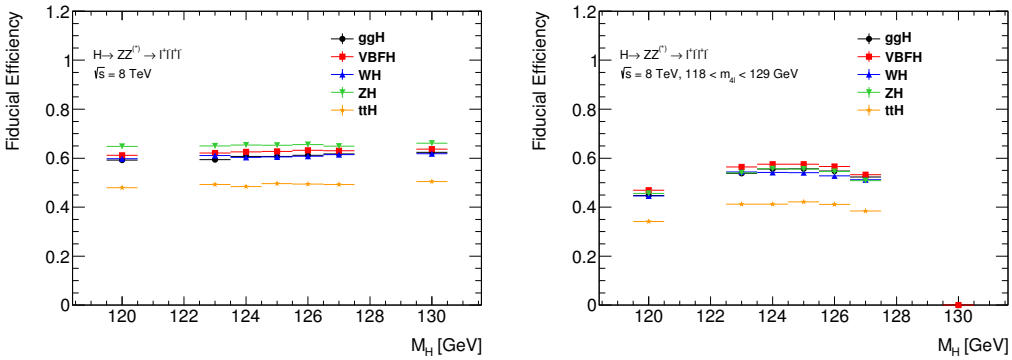

Figure 8.3: Fiducial efficiency as a function of the Higgs mass from $m_{\mathrm{H}} = 120$ to $m_{\mathrm{H}} = 130$ GeV for all production modes (a) without a mass window cut and (b) with the mass window cut of $118 < m_{4\ell} < 129$ GeV.

Table 8.1: Signal fiducial efficiency per production mode for signals from $m_{\mathrm{H}} = 124$ GeV to 126 GeV with the mass window [118,129] GeV applied. Errors are due to simulation statistics only.

	Fiducial Efficiency					
m_{H}[GeV]	ggF	VBF	WH	ZH	$t\bar{t}H$	Combined
124	0.556 ± 0.003	0.575 ± 0.003	0.542 ± 0.004	0.557 ± 0.004	0.412 ± 0.004	0.557 ± 0.002
125	0.557 ± 0.003	0.576 ± 0.003	0.541 ± 0.004	0.555 ± 0.005	0.395 ± 0.004	0.557 ± 0.002
126	0.548 ± 0.003	0.566 ± 0.003	0.528 ± 0.004	0.545 ± 0.004	0.411 ± 0.004	0.548 ± 0.002

predictions for the various production modes. Table 8.1 gives the fiducial efficiencies for all production modes and the combined fiducial efficiency for several signal mass points near $m_{\mathrm{H}} = 125$ GeV. This combination of fiducial efficiencies from different production modes introduces model dependence into the measurement because the cross sections of the individual Higgs production modes are not precisely measured experimentally. Therefore, a systematic uncertainty is introduced to account for a possible bias in this procedure which is evaluated by varying the contributions from the various SM production modes - see Section 8.5.3.

The final fiducial efficiency is evaluated at $m_{\mathrm{H}} = 125.4$ GeV, the best current estimate of m_{H} as reported by ATLAS [124]. This is done by performing a linear interpolation between the two nearest mass signal points (125 and 126 GeV). Tables 8.2 gives the final inclusive correction factor (which is equal to $1/\epsilon_{\mathrm{fid}}$) both with and without the mass window and for each mode separately.

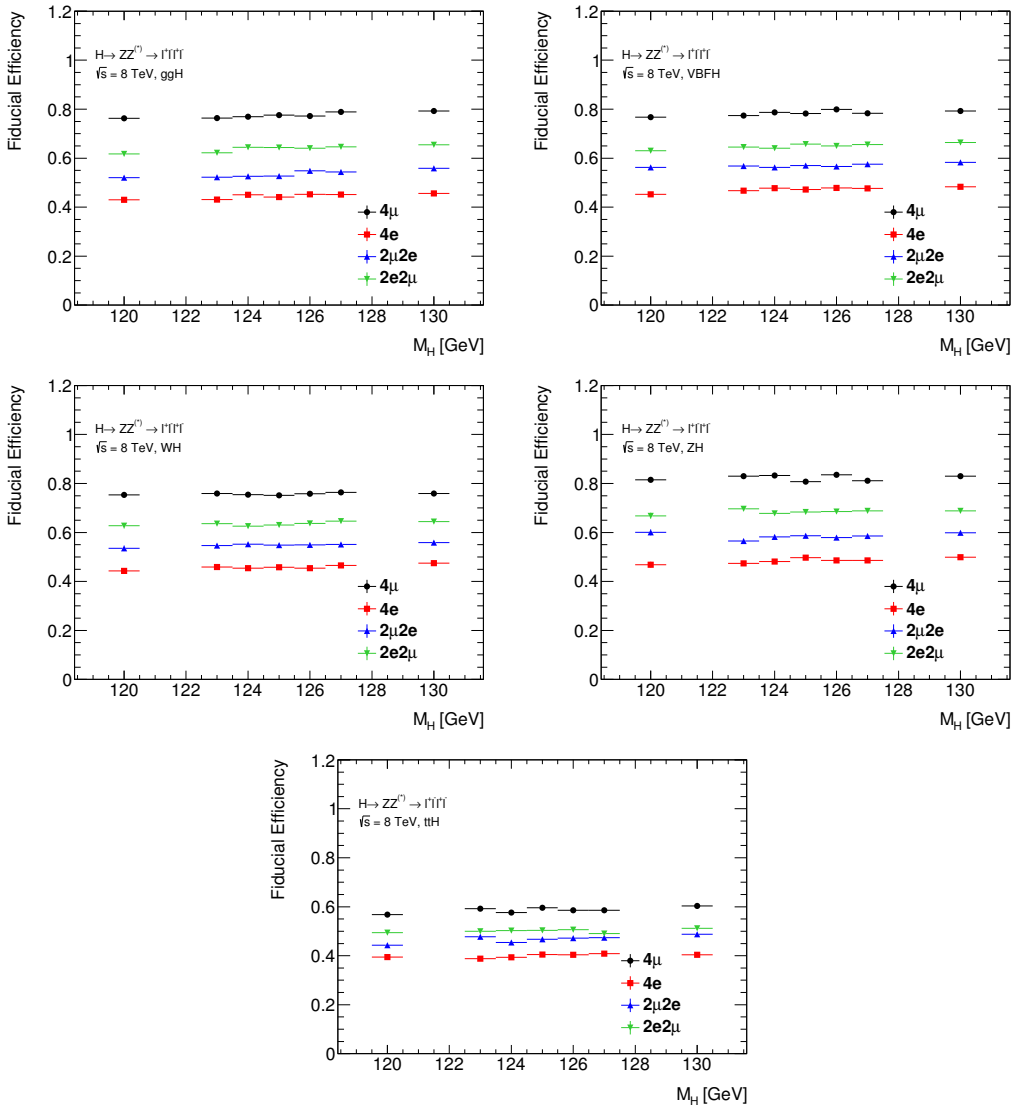

Figure 8.4: Fiducial efficiency as a function of m_{H} for all production modes and channels.

Table 8.2: Inclusive correction factors with and without the mass window cut evaluated at $m_{\mathrm{H}} = 125.4$ GeV. Uncertainties on the individual production modes are due to simulation statistics only.

	Inclusive Correction Factor	
Mode	Full $m_{4\ell}$ range	$118 < m_{4\ell} < 129$ GeV
ggF	1.643 ± 0.005	1.808 ± 0.007
VBF	1.589 ± 0.005	1.748 ± 0.006
WH	1.65 ± 0.007	1.868 ± 0.01
ZH	1.53 ± 0.007	1.814 ± 0.011
$t\bar{t}H$	2.018 ± 0.01	2.396 ± 0.016
Combined	1.639 ± 0.005 (stat) ± 0.044 (syst)	1.808 ± 0.006 (stat) ± 0.049 (syst)

8.4.3 Mispair Fraction

An event is considered to be mispaired if the truth leptons in the leading and/or sub-leading pair do not share the same mother truth particle. This can occur for two reasons: (1) incorrect lepton assignment to Z_1 and Z_2 in the same flavor channels (internal mispairing) and (2) selection of leptons which are not direct decay products of the Higgs but instead are present due to the decay of particles produced in association with the Higgs (external mispairing). Internal mispairing strongly affects variables related to the Higgs decay to four leptons (m_{34} and $cos(\theta^*)$, which depend on the definition of Z_1) and weakly affects $m_{4\ell}$ in the reconstruction due to the use of the Z mass constraint (which also relies on the definition of Z_1). External mispairing strongly affects $m_{4\ell}$, which causes events to move in and/or out of the $m_{4\ell}$ window.

Figure 8.5 shows the truth lepton multiplicity in the fiducial region for all production modes. The ggF and VBF modes have the lowest average multiplicity and similar distributions, while the VH modes have slightly higher average multiplicity due to the possibility of producing leptons from the decay of the associated vector boson. The $t\bar{t}H$ mode has the highest average multiplicity, which will lead to a higher mispairing fraction as compared to the other production modes.

Figure 8.6 shows the mispairing fraction for the fiducial events for each production mode both with and without the mass window cut. One immediately observes that the mispairing

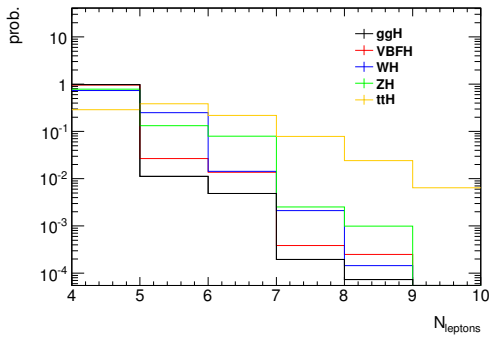

Figure 8.5: Truth lepton multiplicity distributions for fiducial events normalized to unity for all production modes assuming $m_{\mathrm{H}} = 125$ GeV.

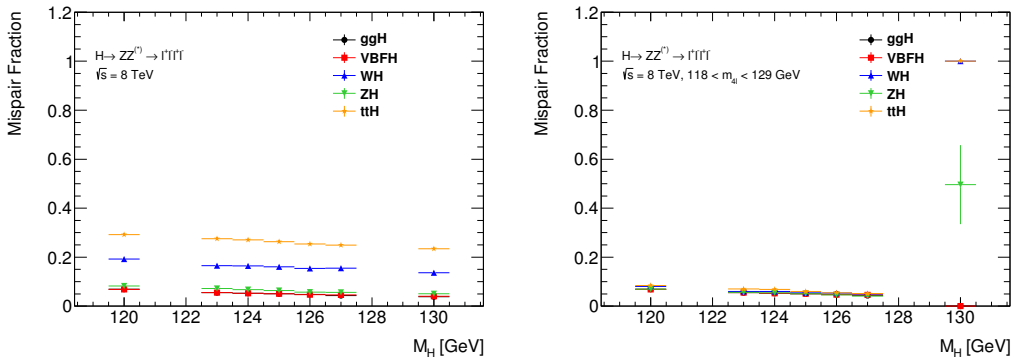

Figure 8.6: Fiducial mispair fraction as a function of m_{H} for all production modes (a) without a mass window cut and (b) with the mass window cut of $118 < m_{4\ell} < 129$ GeV.

fraction without the mass window cut is significantly higher in the VH and $t\bar{t}H$ production modes as compared to the ggF and VBF modes, as expected from the lepton multiplicity comparisons. Within the mass window, the mispairing fraction is greatly reduced for the VH and $t\bar{t}H$ production modes. This is expected as external mispairing will result in an $m_{4\ell}$ which is not correlated with m_{H} and thus will have a higher probability of falling outside of the mass window.

Figure 8.7 shows the mispairing fraction as a function of m_{H} for all production modes and channels separately. In the ggF and VBF modes, it is clear that the predominant effect

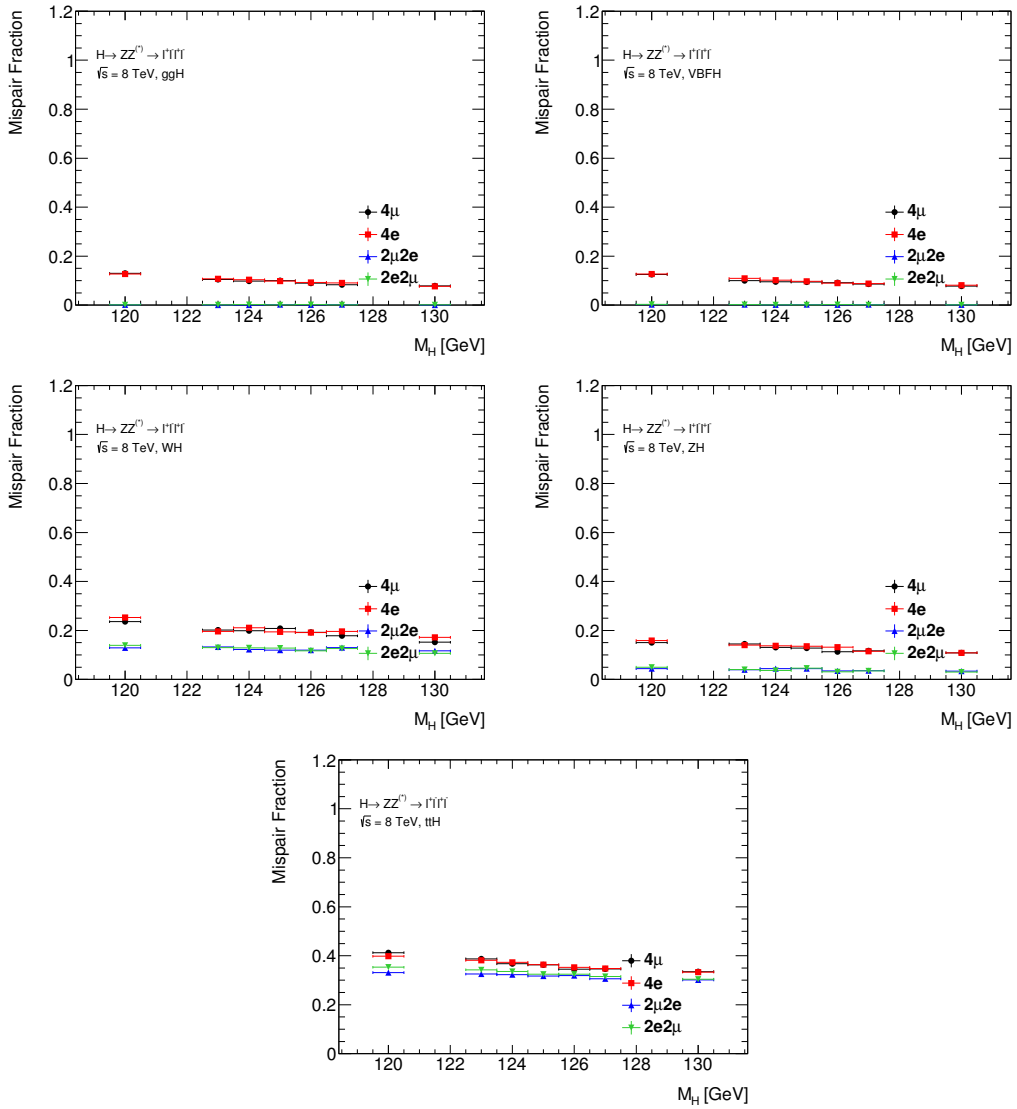

Figure 8.7: Fraction of fiducial events which are mispaired as a function of the Higgs mass for all production modes.

is internal mispairing as the mispairing fraction is nearly zero for the mixed flavor channels. However, in the VH and $t\bar{t}H$ modes, there is evidence of external mispairing as the mixed channels do have a non-zero mispairing fraction.

One can also compare the mispairing fraction between the fiducial selection and and the

reconstruction selection. Large differences would indicate differences in the pairing between the fiducial and reconstruction selection. To identify mispaired events in the reconstruction selection, the reconstructed leptons are truth matched by selecting the highest energy truth lepton of the same flavor within $\Delta\ R < 0.1$. The truth-matched leptons are then used to classify the event as mispaired following the same criterion as for the fiducial cutflow. A comparison of the reconstruction and fiducial mispairing fractions is shown in Table 8.3. The fiducial and reconstructed mispairing fractions are the same to within a few percent for all samples considered.

Table 8.3: Lepton mispairing fraction in the fiducial and reconstructed selections for the signal samples assuming $m_{\mathrm{H}} = 125$ GeV.

	Mispair Fraction - Full Mass Range				
	ggF	VBF	WH	ZH	$t\bar{t}H$
Fiducial	0.051 ± 0.001	0.051 ± 0.001	0.164 ± 0.003	0.090 ± 0.002	0.343 ± 0.003
Reconstructed	0.058 ± 0.001	0.054 ± 0.001	0.192 ± 0.003	0.086 ± 0.003	0.339 ± 0.005
	Mispair Fraction - 118-129 GeV				
	ggF	VBF	WH	ZH	$t\bar{t}H$
Fiducial	0.049 ± 0.001	0.049 ± 0.001	0.056 ± 0.002	0.054 ± 0.002	0.087 ± 0.003
Reconstructed	0.052 ± 0.001	0.048 ± 0.001	0.061 ± 0.003	0.051 ± 0.003	0.080 ± 0.003

8.4.4 Fiducial Leakage

The fiducial leakage, defined as the fraction of reconstructed signal events which do not pass the fiducial selection, is used to determine whether the fiducial region criteria are well defined. Large values of the fiducial leakage would indicate that the fiducial selection is not selecting the proper region of phase space. However, the fiducial leakage is expected to be non-zero due to detector and reconstruction effects, causing event migration at the edge of the fiducial region. Note that leakage events are being produced by signal processes but have the same effect on the measurement as background events because they are outside the fiducial region.

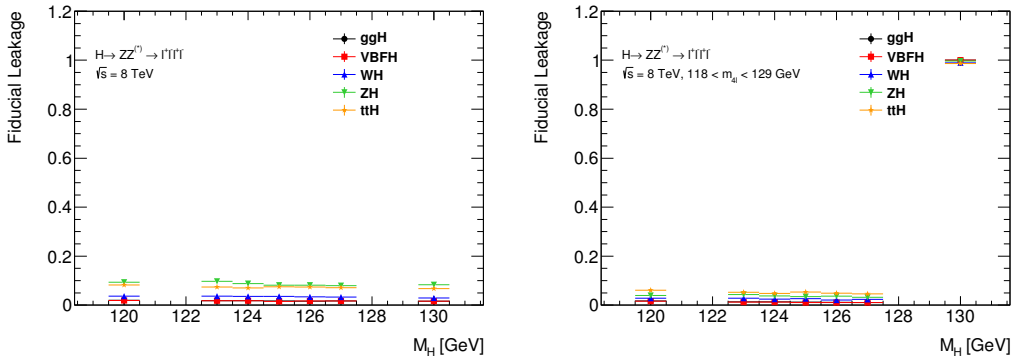

Figure 8.8: Fiducial leakage as a function of m_{H} for all production modes without a mass window cut on the left and with the mass window cut of $118 < m_{4\ell} < 129$ GeV on the right.

Therefore, reductions in the fiducial leakage are highly desirable as these events will be treated as signal rather than background.

The fiducial leakage for all production modes with and without the mass window cut is shown in Figure 8.8. Without the mass window cut, the leakage is found to be <10% for all samples, <5% for the ggF production mode, and is considered to be acceptable. Note that the ZH and $t\bar{t}H$ modes have roughly twice the fiducial leakage of the other modes. The ZH mode has higher leakage due to $ZH \to 4\ell 2\tau$ decays, in which the τs are decay products of the Higgs boson. These events are reconstructed due to the presence of the four leptons but fail the fiducial selection because $H \to 2\ell 2\tau$ events are removed explicitly from the fiducial region. Within the mass window, the effect is reduced because the $m_{4\ell}$ of these events does not correspond to m_{H}. Similarly, the increased lepton multiplicity in the $t\bar{t}H$ mode results in larger fiducial leakage as compared to the fiducial leakage in the ggF mode. No significant difference in fiducial leakage is observed among the $4e/2e2\mu/4\mu$ final states. With the mass window cut, the leakage is <5% for all production modes at $m_{\mathrm{H}} = 125$ GeV and is considered acceptable.

8.5 Unfolding Methods

This section describes the unfolding method used in the differential cross section measurements. The general idea of unfolding is to transform a "measured" distribution $f_{meas}(x)$ back to a "truth-level" distribution $f_{true}(y)$. Formally, the relation between these two distributions can be written:

$$f_{meas}(x) = \int R(x|y) f_{true}(y) dy \tag{8.5}$$

where $R(x|y)$ is known as the response function. The response function in particle physics is responsible for transforming truth-level observables to reconstructed variables, accounting for detector efficiency and resolution.

The ATLAS detector simulation acts as the response function, taking truth-level observables, the matrix element level truth particles, and producing reconstructed level observables, such as reconstructed leptons and jets. This transform is necessarily complex and information is lost in the transform, so inverting it is non-trivial and in some cases impossible. Thus, a number of unfolding methods have been developed to approximate this inversion.

8.5.1 Detector Response

For the differential cross section measurement, the observable distributions are measured using event counting in bins, so one first generalizes equation 8.5 to the discrete case:

$$\nu_i = \sum_{j=1}^{M} R_{ij} \mu_j \tag{8.6}$$

where ν_i is the expected number of measured events in bin i, R_{ij} is now a response matrix, μ_j is the true number of events in bin j, and M is the number of bins. The entries of R_{ij} are then the probability of an event which started in truth bin j to end up in measured bin i.

The response matrix is determined using the signal simulation and can be seen for all variables in Fig. 8.9. For the kinematic variables, the response matrix is nearly diagonal

because the detector resolution is much smaller than the bin width. Bin-to-bin migrations are of order 10% or less for these variables. For the jet variables, the bin-to-bin migrations are larger, up to 40% in some bins.

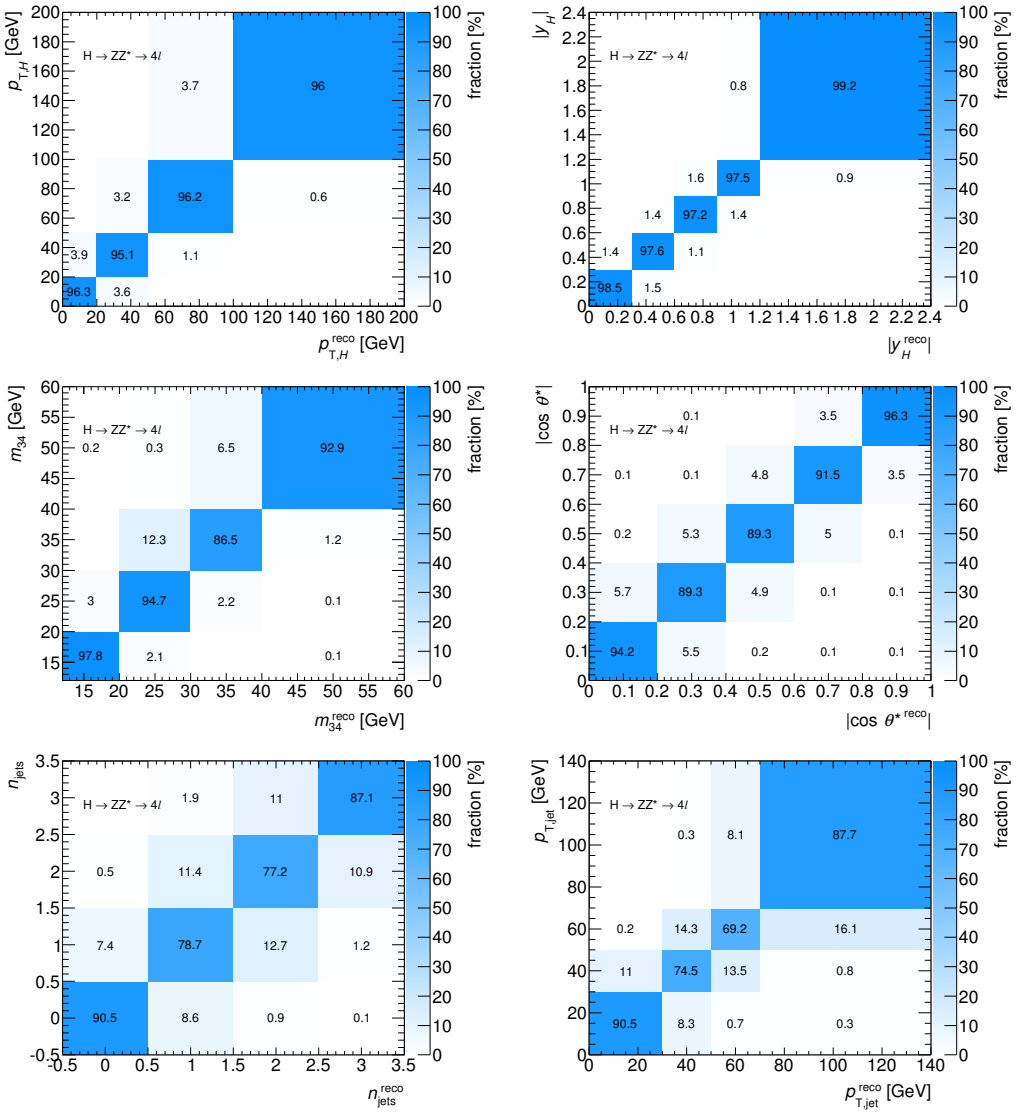

Figure 8.9: Response matrices for all observables of interest in the differential cross section measurement using the Higgs signal samples with $m_{\mathrm{H}} = 125$ GeV.

8.5.2 Correction Factors Method

The unfolding method employed in the differential measurements is the MC correction factors method. The correction factor in the i-th bin is calculated as:

$$C_i = \frac{N_i^{Fid}(x_{truth})}{N_i^{Reco}(x_{reco})} \tag{8.7}$$

where $N_i^{Fid}(x_{truth})$ is the number of fiducial events in the i-th bin of the truth distribution and $N_i^{Reco}(x_{reco})$ is the number of events in the i-th bin of the reconstructed distribution. Generally speaking, the correction factor method is known to introduce a bias into the measurement because the correction factors are derived from a signal model, which may not or may not reproduce the true underlying distributions. This bias can be quantified as [125]:

$$\langle \delta\mu_i \rangle = \nu_i \times \left[\left(\frac{\mu_i}{\nu_i} \right)_{\text{Model}} - \left(\frac{\mu_i}{\nu_i} \right)_{\text{Truth}} \right] \tag{8.8}$$

where $\langle \delta\mu_i \rangle$ is the average bias in the i-th bin. This bias can be difficult to estimate as it depends on the difference between the truth and the model, which is not known *a priori*. However, it can also be shown that the bias is proportional to the off-diagonal terms of the response matrix:

$$\langle \delta\mu_i \rangle = \nu_i \times \sum_{i \neq j} R_{ij}^{-1} \left[\left(\frac{\nu_j}{\nu_i} \right)_{\text{Model}} - \left(\frac{\nu_j}{\nu_i} \right)_{\text{Truth}} \right]. \tag{8.9}$$

The size of this bias goes to zero as the off-diagonal elements approach zero. Therefore, the use of this method is better justified for the unfolding of distributions in which the bin-to-bin migrations are small. This is true in the case of the kinematic variables for the differential cross section measurements as seen in Figure 8.9 in contrast to the jet related variables, which do have larger bin-to-bin migrations.

The correction factors account for both detector efficiencies and bin-to-bin migrations and are derived from the signal simulation using the SM prediction for the cross sections of the

various Higgs production modes. They are evaluated at $m_H = 125.4$ GeV using a linear interpolation between the two nearest mass point (125 and 126 GeV). The correction factors for all of the differential variables of interest are shown in Figure 8.10 separately for every production mode and the combined correction factors are shown in Figure 8.11. Systematic uncertainties are assigned to the correction factors to account for the assumptions about the Higgs mass and the signal model composition, as detailed in Sec. 8.5.3.

8.5.3 Correction Factor Systematic Uncertainties

As previously explained, the correction factors method can introduce biases depending on the model used to derive the correction factors. This section describes studies of systematic uncertainties associated with the model dependence of the correction factors, demonstrating that the uncertainties introduced by the choice of model are relatively small. Additional systematic uncertainties in the correction factors can be found in Section 10.3.

8.5.3.1 Signal Model Composition

As already seen in Figure 8.10, there is a non-trivial dependence on the signal production mode for the correction factors. Therefore, a systematic uncertainty is assigned in order to account for the lack of precise knowledge of the relative rates of the various production modes. To evaluate this uncertainty, the correction factors have been calculated for a number of signal models in which the signal production mode composition has been altered.

The current ATLAS constraints on the signal strengths in the various production modes are shown in Figure 2.7. Therefore, the following variations are chosen to estimate the signal composition systematic uncertainty:

- Vary the VBF and VH contributions by a factor of 0.5× and 2× the SM prediction.

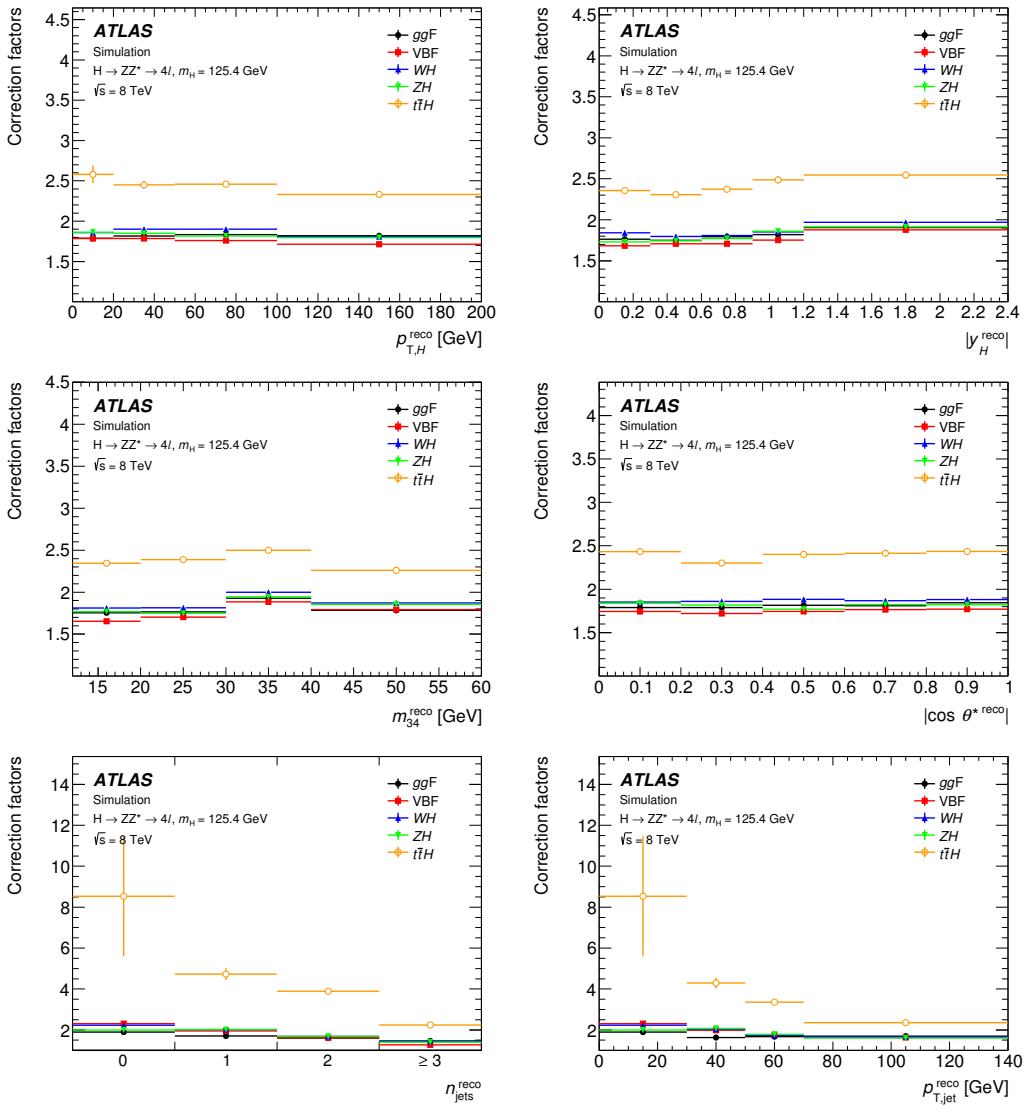

Figure 8.10: Correction factors for all Higgs production modes separately evaluated at $m_{\mathrm{H}} = 125.4$ GeV. Errors are statistical only, as the systematic uncertainties are only derived for the combined correction factor.

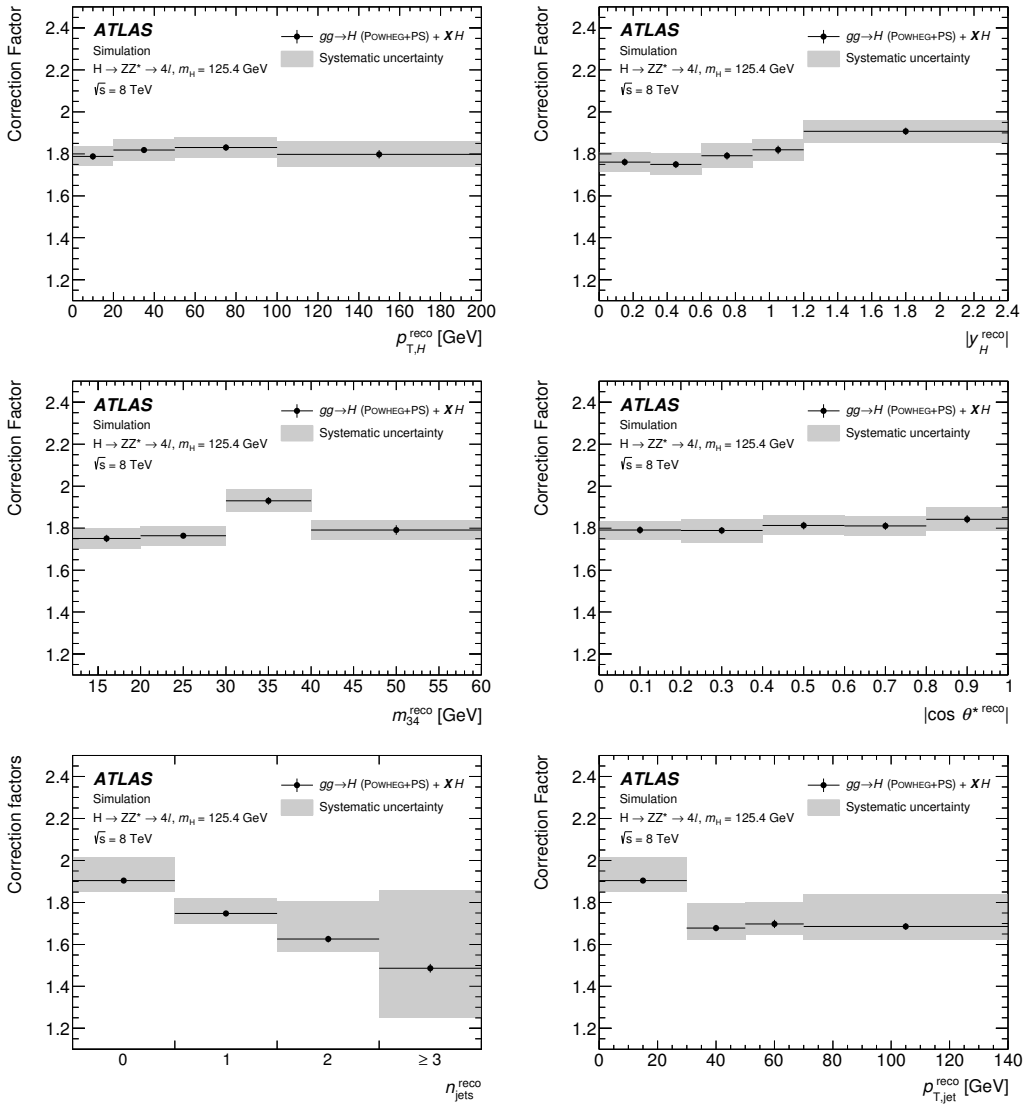

Figure 8.11: Combined correction factors evaluated at $M_H = 125.4$ GeV. All systematic uncertainties are included.

- Vary the $t\bar{t}H$ contribution by a factor of 0× and 5× the SM prediction.

For each bin, the largest variation in the correction factor from these variations is taken as the systematic uncertainty. The relative systematic uncertainty in the inclusive correction factor is 0.6% and the results of this procedure for all bins of the differential variables are seen in Table 8.4.

Table 8.4: Systematic uncertainties on the correction factors derived by varying the signal model composition by scaling the the VBF and VH contributions by factors of 0.5-2× and the $t\bar{t}H$ contribution by factors of 0-5× their SM prediction.

	Systematic Uncertainty (%)				
Variable	Bin 1	Bin 2	Bin 3	Bin 4	Bin 5
Inclusive	0.6	-	-	-	-
p_{T}	0.06	0.2	1.0	2.2	-
$\lvert y_H \rvert$	0.7	0.7	0.6	0.6	0.4
m_{34}	0.6	0.6	0.5	0.5	-
$\lvert \cos\theta^* \rvert$	0.6	0.5	0.6	0.6	0.6
n_{jets}	0.2	1.1	1.2	13.0	-
$p_{\mathrm{T,jet}}$	0.2	1.2	1.1	2.8	-

8.5.3.2 Higgs Mass Uncertainty

The experimental uncertainty in m_{H}, currently at the level of 0.5 GeV, results in an uncertainty on the correction factors because the correction factors are derived using a fixed value of $m_{\mathrm{H}} = 125.4$ GeV. As already seen in Sec. 8.4.2, the inclusive fiducial efficiency does not strongly depend on the Higgs mass in the range [123,127] GeV. Applying the mass window cut slightly increases this dependence, as seen in Figure 8.3.

To evaluate this uncertainty, the correction factors are derived using the signal samples with $m_{\mathrm{H}} = 125$ and 126 GeV and for each bin the largest variations are taken as the systematic uncertainty. The derived correction factors for the p_{T} cross sections are shown in Table 8.5 for the three relevant mass points. The results of this procedure for all variables are shown in

Table 8.6 and the relative systematic uncertainty on the inclusive correction factor is found to be 1.7%.

Table 8.5: Correction factors for the p_{T} distribution for signal models with $m_{\mathrm{H}} = 125$, 125.4 and 126 GeV. Uncertainties are from MC statistics only.

m_{H} [GeV]	Correction Factor			
	$0 < p_{\mathrm{T}} < 20$	$20 < p_{\mathrm{T}} < 50$	$50 < p_{\mathrm{T}} < 100$	$100 < p_{\mathrm{T}} < 200$
125	1.781 ± 0.015	1.801 ± 0.013	1.821 ± 0.015	1.782 ± 0.02
125.4	1.787 ± 0.015	1.817 ± 0.014	1.830 ± 0.015	1.797 ± 0.019
126	1.8 ± 0.015	1.842 ± 0.014	1.842 ± 0.016	1.824 ± 0.021

Table 8.6: Systematic uncertainties on the correction factors derived by varying m_{H} from 125 GeV to 126 GeV.

	Systematic Uncertainty (%)				
Variable	Bin 0	Bin 1	Bin 2	Bin 3	Bin 4
Inclusive	1.0	-	-	-	-
p_{T}	0.6	1.4	0.8	1.5	-
$\lvert y_H \rvert$	0.8	1.4	2.0	1.1	1.4
m_{34}	0.5	0.4	1.4	1.4	-
$\lvert \cos\theta^* \rvert$	0.4	1.8	0.5	0.6	1.7
n_{jets}	0.7	0.6	2.7	1.8	-
$p_{\mathrm{T,jet}}$	0.7	1.5	1.2	1.0	-

8.5.4 Non-SM Signal Models

Several alternative spin/CP hypotheses have been used to check the model dependency of the correction factors. These variations on the signal model do not contribute to the systematic uncertainty on the correction factors but are intended to demonstrate the model independence of the method. The JHU generator [126, 127] is used to produce signal samples with $J^P = 0^+$, 0^-, and 2^+ configurations. Two different generators have been used for comparison for the $J^P = 0^+$ hypotheses: Powheg, which is a NLO generator and JHU which is at LO. The ratio of the correction factor (CF) given from each model with respect to the JHU-0^+ hypothesis is shown in Figure 8.12 for the six differential variables of interest. No significant differences

are observed considering the statistical uncertainties of the different samples.

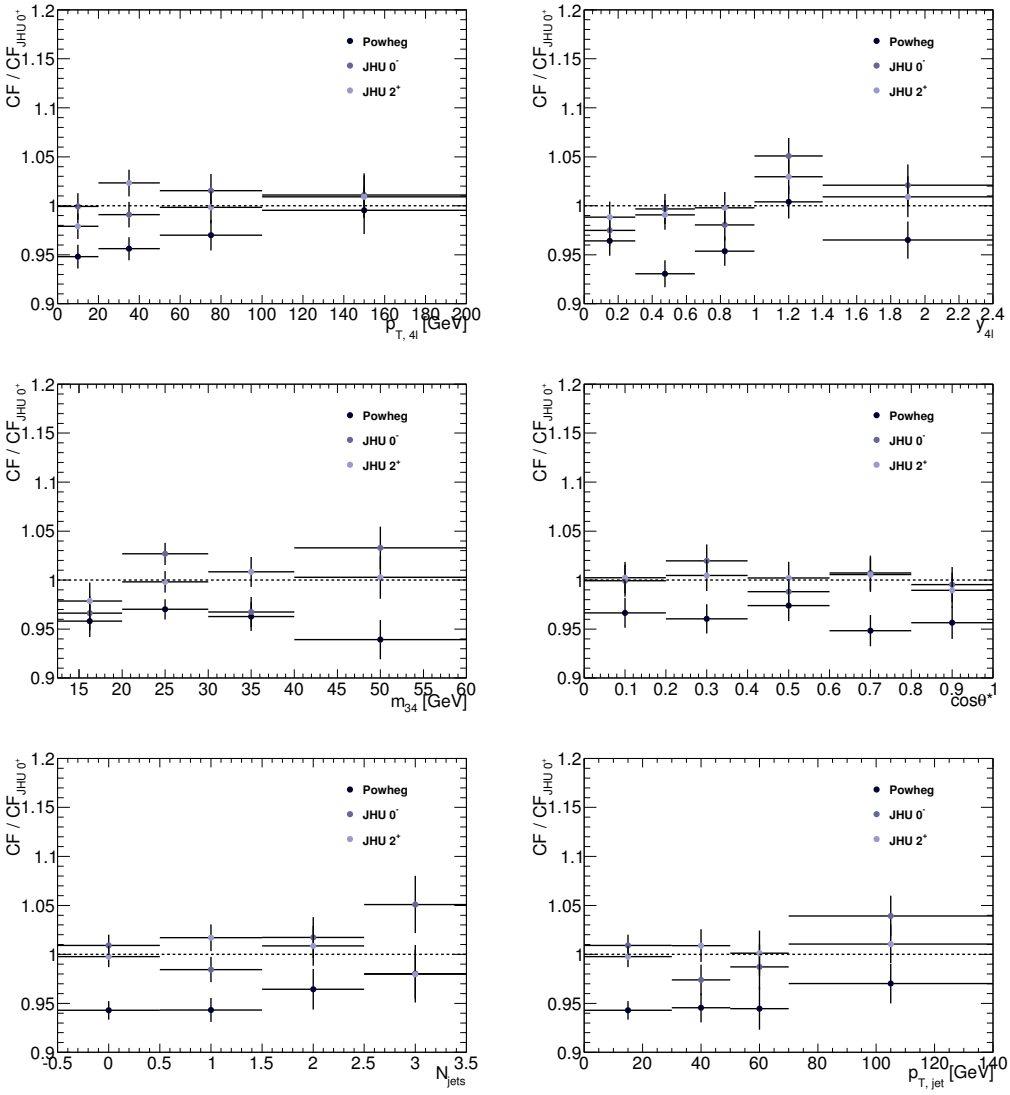

Figure 8.12: Ratio of Correction factors for different spin-parity hypotheses with respect to the JHU-0^+ sample for all of the differential variables.

Chapter 9

Background Estimation

This chapter describes the background estimation methods given the $H \to 4\ell$ event selection described in Chapter 6. The backgrounds are broadly categorized into irreducible and reducible backgrounds. Irreducible backgrounds consist of SM processes whose final states include four isolated leptons and are indistinguishable from that of the $H \to 4\ell$ process. Reducible backgrounds are present due to SM processes in which lepton candidates originate from semi-leptonic decays of heavy flavor hadrons or from misidentification of jets as leptons. The following sections describe the background estimation methods for both categories of backgrounds and show checks on the background predictions in suitable control regions.

9.1 Irreducible Background

The largest background in this analysis comes from the irreducible backgrounds. The primary contributions to the irreducible background come from SM $ZZ^{(*)}$ production. The leading order diagrams for the three dominant processes are shown in Figure 9.1 consisting of $q\bar{q} \to ZZ$ production, single resonant $Z \to 4\ell$, and $gg \to ZZ$. The interference between the $gg \to ZZ$ and the ggF signal is expected to be below 1% the near the signal peak [105] and is neglected in this analysis[6]. The background predictions for each of these processes are taken from the

simulation, as detailed in Section 6.2.2.

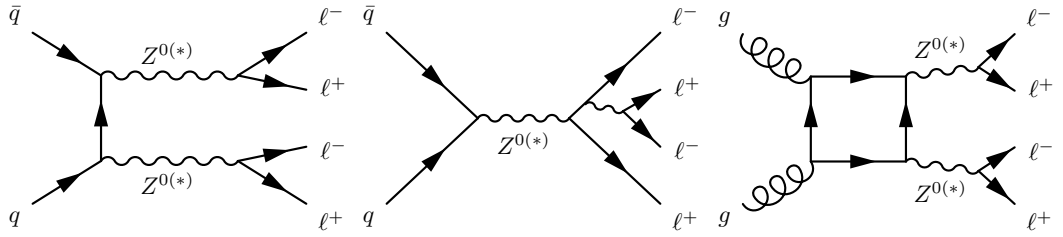

Figure 9.1: Leading-order Feynman diagrams for the SM processes giving contributions to the irreducible background, which from left to right are $q\bar{q} \to ZZ$, single resonant $Z \to 4\ell$, and $gg \to ZZ$.

A breakdown of the irreducible background estimates is shown in Table 9.1. The irreducible background is roughly 10× larger than the signal over the entire mass range but has a well-predicted shape in $m_{4\ell}$, shown in Figure 11.7. In the low mass region, the peak near 90 GeV comes from the single resonant production diagram. From 100 GeV up to 180 GeV, one of the Z's must be off-shell and is therefore suppressed. Above 180 GeV, both Z's are on-shell and the cross section falls off predictably.

Table 9.1: Irreducible background estimates for 20.3 fb^{-1} of $\sqrt{s} = 8$ TeV data over the full $m_{4\ell}$ range and within the mass window used in the differential measurements. Uncertainties are from simulation statistics only.

$ZZ*$ event yield estimates for 20.3 fb^{-1}at $\sqrt{s} = 8$ TeV		
Channel	Full $m_{4\ell}$ range	$118 < m_{4\ell} < 129$ GeV
4μ	122.6 ± 0.4	2.53 ± 0.01
$2\mu 2e$	84.8 ± 0.4	1.23 ± 0.01
$2e2\mu$	83.9 ± 0.4	1.79 ± 0.02
$4e$	67.6 ± 0.3	1.10 ± 0.01
Total	358.9 ± 0.7	6.65 ± 0.03

[6]Interference between $gg \to ZZ$ and $gg \to H \to ZZ$ does become significant for the off-peak cross sections and can be used to indirectly set a limit on the width of the Higgs boson.

9.2 Reducible Background

The reducible backgrounds consist of several SM processes with the dominant contributions coming from Z+jets and $t\bar{t}$ production and smaller contributions from WZ production. Example Feynman diagrams are shown for these processes in Figure 9.2. Because the selection efficiency for these backgrounds is not expected to be well-modeled, the reducible background yields are estimated using data-driven methods.

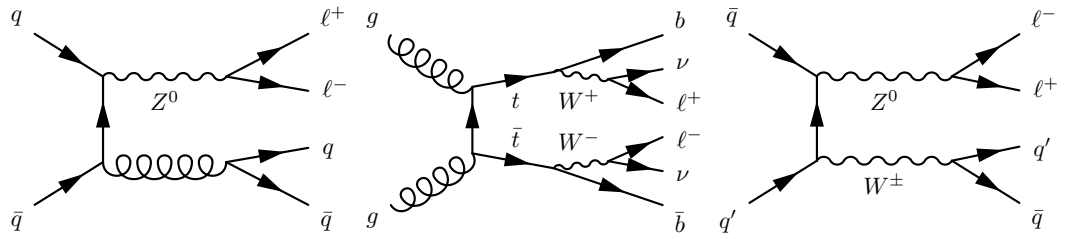

Figure 9.2: Leading-order Feynman diagrams for the SM processes giving contributions to the reducible background, which from left to right are Z+jets (both Zbb and Z+light), $t\bar{t}$ pair production, and WZ production.

The general strategy is as follows: the background composition and shapes are studied in special data control regions (CR) constructed by relaxing or inverting selection and/or lepton identification requirements. The larger statistics in the control regions permit several distributions to be compared between data and simulation. The expected background in the signal region (SR) is estimated by extrapolating from the control region using the so-called transfer factors. These factors are normally determined based on the efficiency of the relaxed or inverted selection criteria in the given control regions, but they can also be calculated by the ratio of the expected yields between the control and signal regions.

Because the composition of the reducible backgrounds depends strongly on the flavor of the low p_{T} leptons, separate extrapolations are done for events with subleading muons and subleading electrons. The following sections summarize the methods for both sets of final

states. For each background, three predictions are produced, from which one is used as the central value and the others are used to evaluate the systematic uncertainties. The methods to determine the central values for the background estimates are described here; the methods used for systematic variations are described in Ref. [28].

9.2.1 Reducible $\ell\ell + \mu\mu$ Background

There are three significant backgrounds which result in $\ell\ell + \mu\mu$ final states. The dominant contribution is from Z production in association with leptons from heavy quark meson semi-leptonic decays (heavy flavor), denoted as Zbb. A smaller contribution arises from Z production accompanied by π/K in-flight decays to muons from within light flavor jets, denoted as Z+light. The sum of the Zbb and Z+light contribution is denoted as Z+jets. Finally, $t\bar{t}$ production provides a small contribution when the top quarks decay semi-leptonically.

To estimate the $\ell\ell + \mu\mu$ backgrounds, four CRs are constructed and the background contributions in each are fit simultaneously. An unbinned maximum likelihood fit is performed on the m_{12} distribution, which allows discrimination between the Z+jets component, which peaks at the Z mass, from the $t\bar{t}$ component, which is relatively flat in m_{12}. Each CR is constructed to enhance certain backgrounds while remaining orthogonal to all other CRs as well as to the SR in order to gain sensitivity to each background separately and minimize signal contamination in the CR. The four CR are defined as follows:

(1) **Inverted d_0 CR:**

The standard four-lepton analysis selection is applied on the leading dilepton pair. At least one lepton in the subleading dilepton pair must fail the impact parameter significance requirement and the isolation requirements are not applied to either lepton. This CR is enhanced in $Zb\bar{b}$ and $t\bar{t}$ because leptons from b-quark meson decays are characterized by

large d_0 significance.

(2) **Inverted isolation CR:**

The standard four-lepton analysis selection is applied on the leading dilepton pair. The subleading dilepton pair has the standard impact parameter significance selection applied and at least one lepton must fail the isolation requirements. This control region enhances the Z+light jet component over the $Zb\bar{b}$ component by requiring the impact parameter significance selection. These two background processes are described by the same model and would be consequently highly correlated if the first two control regions were not separated.

(3) $e\mu + \mu\mu$ **CR:**

An opposite-charge different-flavor leading dilepton pair satisfying the standard four-lepton analysis selection is required. The subleading dilepton pair has neither the impact parameter significance nor the isolation selection applied and both same and opposite charge lepton pairs are accepted. This control region consists almost entirely of $t\bar{t}$ events.

(4) **Same Sign CR:**

The standard four-lepton analysis selection is applied on the leading dilepton pair. The subleading dilepton pair is required to have the same charge and neither the impact parameter significance nor the isolation requirements are applied. This same sign control region is not dominated by a specific background; all the reducible backgrounds have significant contributions.

A fifth CR, referred to as the relaxed OS CR, is more relaxed than the other four CRs, contains all background components as well as the signal region (and therefore is not used in the fit). Events in the relaxed OS CR are are required to pass the standard selection with the exception that the isolation and impact parameters significance cuts are not applied on the

subleading dilepton pair. The fit results are expressed in terms of number of events from the various background sources in the relaxed OS CR. The number of background events in the relaxed OS CR are then extrapolated to the SR using transfer factors from the simulation.

The shapes of the m_{12} distribution for the different backgrounds are parameterized based on the shapes from the simulation. The $Zb\bar{b}$ and Z+light shapes are approximated by a convolution of a Crystal Ball with a Breit-Wigner, which models well the peak and lower tail of the distribution. The $Zb\bar{b}$ and Z+light components are both modeled using the same function because both contain a real Z and thus share the same shape parameters. The $t\bar{t}$ background shape is modeled by a 2^{nd} order Chebychev polynomial. All shapes parameters are derived by fitting the functions to the simulation. A closure test in the simulation using these shapes was performed and no significant biases were found.

Despite the inverted selection, there are remaining contributions from WZ and $ZZ^{(*)}$ in the control regions. Because the contributions from these processes are small, their normalizations are fixed to their predicted values from the simulation in the simultaneous fit and their m_{12} shapes are modeled using the same functions as used for Z+jets.

The results of the simultaneous fit in the four control regions are shown in Figure 9.3. From the fit, the number of events in the relaxed OS CR is estimated and compared to the simulation prediction in Table 9.2. The simulation underestimates the Zbb and $t\bar{t}$ backgrounds by 32% and 17% respectively, while the Z+light prediction agrees with the estimated contribution in data. The transfer factors are also listed in Table 9.2 as estimated from simulation. The uncertainties in the transfer factors contain contributions from MC statistics as well as a 1.6% systematic uncertainty due to differences in the efficiency of the isolation/impact parameter selection criteria between the simulation and data as measured in a suitable control region. The final signal region estimates are shown in Table 9.3. The WZ prediction is taken from the simulation because its contribution is small relative to the other backgrounds and, unlike the

other reducible backgrounds, only one of the subleading leptons is expected to be background-like.

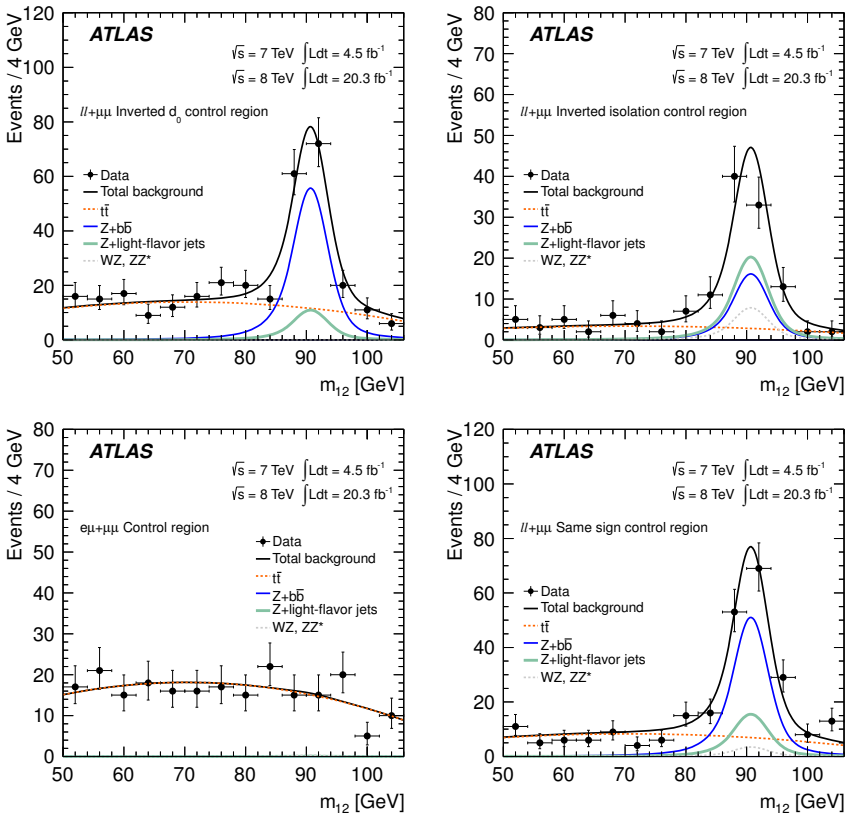

Figure 9.3: The data m_{12} distributions are shown after the unbinned simultaneous fit in the inverted d_0, inverted isolation, $e\mu + \mu\mu$, and same sign control regions. The WZ and ZZ^* contributions are estimated from the simulation and the remaining background normalizations are taken from the fit.

9.2.2 Reducible $\ell\ell + ee$ Background

The reducible $\ell\ell + ee$ background is primarily composed of events in which jets have been misidentified as electrons. Two control regions with relaxed identification electrons ("X") are constructed in order to enrich the fake electron background components:

Table 9.2: Estimation of the reducible $\ell\ell + \mu\mu$ background event yields in the relaxed OS CR as predicted from the simulation and estimated from the fit to the data control regions. The transfer factors to extrapolate from the relaxed OS CR to the SR are also listed.

Background	Simulation	Fit Estimation	Transfer Factor (%)
$Zb\bar{b}$	93.5 ± 0.7	139 ± 16	3.10 ± 0.19
Z+light	43 ± 5	46 ± 9	3.0 ± 1.8
$t\bar{t}$	150.6 ± 1.5	181 ± 11	0.55 ± 0.09

Table 9.3: Final predictions of the reducible $\ell\ell + \mu\mu$ background event yields in the signal region. The statistical uncertainties are derived from the fit to the data control regions and the systematic uncertainties are estimated from the transfer factor uncertainties.

Background	4μ	$2e2\mu$
Zbb	2.30 ± 0.26 (stat) ± 0.14 (syst)	2.01 ± 0.23 (stat) ± 0.13 (syst)
Z+light	0.81 ± 0.38 (stat) ± 0.41 (syst)	0.57 ± 0.31 (stat) ± 0.41 (syst)
$t\bar{t}$	0.511 ± 0.031(stat) ± 0.089(syst)	0.485 ± 0.029(stat) ± 0.084(syst)
WZ	0.42 ± 0.07	0.44 ± 0.06

(1) $3\ell + X$ **Control Region:**

Standard selection for the leading dilepton pair as well as the leading lepton in the subleading dilepton pair. Relaxed identification only for the low p_{T} electron in the subleading dielectron pair.

(2) $Z + XX$ **Control Region:**

Standard selection on leading dilepton pair. Relaxed identification for both electrons in the subleading pair.

The relaxed criteria on X are defined separately for each control region and method. Additionally, $Z+X$ control regions are defined in order to perform data-driven efficiency measurements for the relaxed electron selections.

For all methods, the composition of the control region must be well-understood because the efficiencies of the full identification criteria depend strongly on the origin of the fake electron (heavy flavor, light flavor, photon conversions, etc.). For the purpose of these studies,

electron candidates in the simulation have been categorized according to the truth information: isolated electrons (e), light jets faking an electron (f), photon conversions and the FSR (γ), and electrons from heavy quark semi-leptonic decays (q). Likewise, electron candidates may also be categorized as to whether they are more Electron-like (E) or Fake-like (F) based on discriminating reconstruction variables.

9.2.2.1 $3\ell + X$ Method

The $3\ell + X$ CR event selection is defined following the standard quadruplet selection with the exception that the lowest E_{T} electron has only the standard silicon hit requirements ($n_{\mathrm{silicon}} > 6$ and $n_{\mathrm{pixel}} > 1$) and the electron identification, isolation, and impact parameter significance requirements are not applied. Furthermore, same sign (SS) subleading dileptons are required in order to suppress the ZZ^* contribution and exclude the signal region. With this same-sign selection, 6% of the remaining events come from ZZ^* events with fake electron candidates and are subtracted from the final estimate. Finally, in the case that more than one quadruplet per event is built, all the quadruplets with the same m_{12} are considered.

A two dimensional fit of discriminating variables is used to obtain the yields of the different electron fake components in the data control region. The number of hits on track in the first layer of the pixel detector ($n_{\mathrm{hits}}^{\mathrm{B-layer}}$) is used to discriminate between photon conversions and light jets/electrons and the ratio of TRT high threshold hits to all hits on track (r_{TRT}) discriminates between light jets and electrons. Templates for these discriminating variables are derived from simulation of the $Z+X$ control region and are shown in Figure 9.4. Likewise, the expected yields in the $3\ell + X$ control region from the simulation for each background is also shown, with the dominant background coming from light jets faking electrons.

The fit is performed using the *sPlot* method [128], which assigns a weight w to each fitted event corresponding to the covariance-weighted probability of that event coming from a

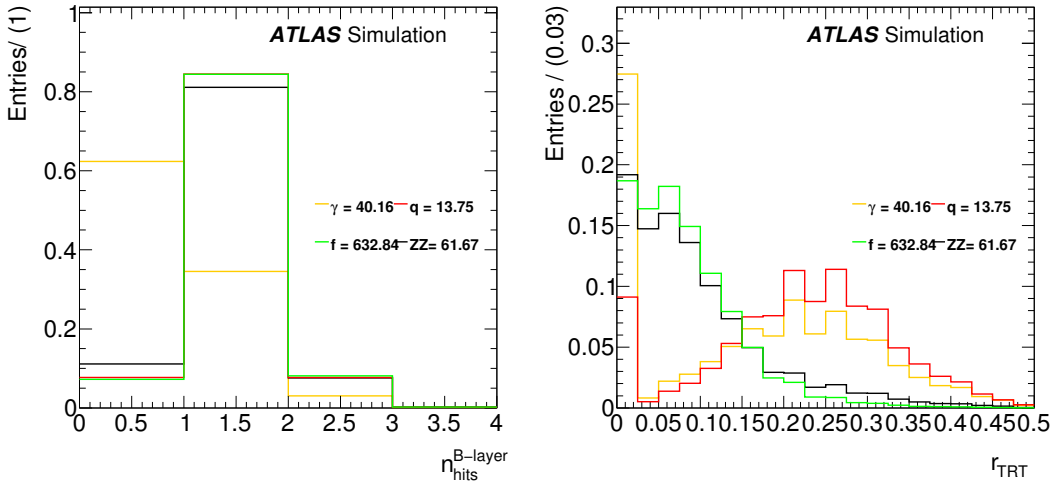

Figure 9.4: Templates of $n_{\text{hits}}^{\text{B-layer}}$ (a) and r_{TRT} (b) for the different sources of reducible backgrounds (γ,f,q) derived from simulation of the $Z + X$ control region. The templates for the ZZ^* background are obtained from the X in the simulated 3ℓ+X control region selection. The predicted yields for each background contribution in the $3\ell + X$ control region are also shown.

specific background. The sum of the weights gives the total background yield estimation. The $2\mu 2e$ and $4e$ channels are fit separately and the combined results of the fit are shown in Figure 9.5, including the fit yields in the control region. Because the heavy flavor background is small, its contribution in the fit is fixed to the prediction from the simulation with an allowed 20% variation using a Gaussian constraint.

The yields of the various background components are then extrapolated to the signal region by applying transfer factors derived from the efficiencies of the selection criteria which were relaxed (electron identification, isolation, and impact parameter significance). These efficiencies are measured in data using several different $Z + X$ control regions which have been enhanced in the different background components. The final efficiencies used for the extrapolation are measured in eight p_{T} bins for the different sources of the background.

For the efficiency measurements, $Z + X$ candidate events are selected by requiring an opposite-sign same-flavor lepton pair in which both leptons pass the standard analysis lepton

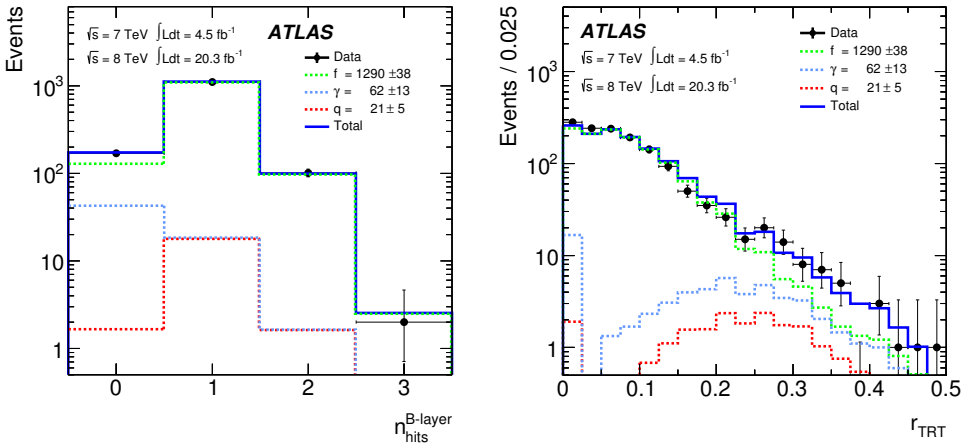

Figure 9.5: The results of a simultaneous fit to (left) $n_{\text{hits}}^{\text{B-layer}}$ and (right) r_{TRT} for the estimation of the $\ell\ell + ee$ background components. The $2\mu 2e$ and $4e$ channels are fit separately and the sum of both channels is shown here.

selection criteria with $p_{\text{T}} > 20$ GeV. An additional requirement on the transverse missing energy, $E_{\text{T}}^{\text{miss}} < 50$ GeV, is applied in order to suppress contributions from WZ events. The additional X leptons are required to be well separated from the leptons from the Z boson, satisfying $\Delta R > 0.2(0.1)$ for different (same) flavor leptons. The X is required to satisfy the standard silicon hit requirements as a baseline and then the various control regions are defined by imposing additional requirements on the X in order to enhance the different background components.

A control region enhanced in photon conversions is formed by requiring that X have no B-layer hits and $r_{\text{TRT}} > 0.15$. The truth composition in both the E and F categories is shown in Table 9.4 for this selection. The purity of photon conversions in this region is estimated to be about 86% integrated over the entire p_{T} spectrum, with 10% contamination coming from light jets and 3% from heavy flavor.

A fake-enriched $Z + X$ control region is constructed by requiring the X to have at least one B-layer hit, which reduces the contamination of the γ background. In this CR, the purity

Table 9.4: Truth composition of the X object for the combined sample and the E and F categories in the γ-enriched control regions for the $\ell\ell + ee$ reducible backgrounds.

$4e$	e	q	γ	f
E	0.01 ± 0.002	0.159 ± 0.007	0.469 ± 0.018	0.362 ± 0.015
F	0	0.07 ± 0.001	0.924 ± 0.012	0.068 ± 0.003
Combined	0.002 ± 0.001	0.027 ± 0.001	0.862 ± 0.011	0.108 ± 0.003
$2\mu 2e$	e	q	γ	f
E	0.01 ± 0.001	0.149 ± 0.006	0.464 ± 0.017	0.380 ± 0.014
F	0	0.07 ± 0.001	0.929 ± 0.011	0.064 ± 0.002
Combined	0.001 ± 0.001	0.025 ± 0.001	0.869 ± 0.010	0.105 ± 0.003

for the fake component is $> 90\%$ in the F-like category and approximately 70% in the E-like category as shown in Table 9.5.

Table 9.5: Truth composition of the X object for the combined sample and the E and F categories in the f-enhanced control regions for the $\ell\ell + ee$ reducible backgrounds.

$4e$	e	q	γ	f
E	0.01 ± 0.001	0.138 ± 0.010	0.193 ± 0.002	0.660 ± 0.005
F	0	0.013 ± 0.001	0.052 ± 0.001	0.934 ± 0.005
$2\mu 2e$	e	q	γ	f
E	0.01 ± 0.001	0.133 ± 0.010	0.200 ± 0.002	0.660 ± 0.005
F	0	0.013 ± 0.001	0.053 ± 0.001	0.934 ± 0.004

For both of these control regions, a scale factor (SF) is determined using:

$$SF_i = \frac{\epsilon^i_{\text{data}}}{\epsilon^i_{\text{MC}}} \tag{9.1}$$

where the $\epsilon^i_{\text{data/MC}}$ are the measured efficiencies in the data or simulation of the electron identification requirements in the ith p_{T} bin with respect to the $Z + X$ control region. The SFs are used to correct the simulation efficiencies before extrapolating the control region yields into the signal region. The SFs measured in the $Z + X$ CR are shown in Table 9.6 for both the γ and f components. The γ SFs are consistent with one for most p_{T} bins while the f SFs are as large as 2.3. A relative systematic uncertainty of 10 (30)% is assigned to account the residual mismodeling of the γ (f) background components. The e component SFs are taken

from the standard ATLAS evaluation and the heavy flavor SF is assumed to be consistent with one with an assigned uncertainty of 40%.

Table 9.6: Scale factors (SF) for the various background components. The values are averaged between the $Z \to ee + X$ and $Z \to \mu\mu + X$. The SF for the f component above 20 GeV is extrapolated from the values obtained in the lower p_{T} bins .

	Scale Factors	
p_{T} bin [GeV]	f	γ
< 8	1.40± 0.04	1.08 ± 0.04
$8 - 9$	1.41 ± 0.04	0.99± 0.04
$9 - 10$	1.36 ± 0.05	1.02 ± 0.04
$10 - 11$	1.81 ± 0.08	1.01± 0.05
$11 - 12$	2.32± 0.11	0.89 ± 0.05
$12 - 15$	1.88± 0.07	0.93 ± 0.03
$15 - 20$	2.20± 0.10	1.02 ± 0.04
> 20	–	1.05 ± 0.03

The background estimate in the signal region is calculated using the transfer function for the γ and f components:

$$SR^i = \epsilon^i_{\mathrm{MC}}(p_{\mathrm{T}}) \cdot SF^i(p_{\mathrm{T}}) \cdot w^i \tag{9.2}$$

where SR^i is the extrapolated background yield in the signal region for control region event i with weight w_i from the fit. Because multiple quadruplets are allowed in a single control region event (accounting for ∼10% of the CR events), the transfer function must be modified in order not to double count these contributions. Assuming multiple quadruplets within an event are uncorrelated, the transfer function for events with multiple quadruplets is:

$$SR^i = 1 - \prod_{\mathrm{j}=1}^{N_{\mathrm{quad}}} (1 - \epsilon^j_{\mathrm{MC}}(p_{\mathrm{T}}) \cdot SF^j(p_{\mathrm{T}}) \cdot w^j) \tag{9.3}$$

Because the heavy flavor component is small and the individual event weights are subject to large statistical uncertainties from the fit of the control region, an inclusive transfer factor is used to extrapolate this component to the signal region, given simply by n_{SR}/n_{CR}. An additional correction to the heavy flavor component is added to account for the expected difference in yield between the OS and SS control regions, which is found to be $SS_q/OS_q \approx 0.6$.

The final results for the $3\ell+X$ method, including control region yields, average efficiencies, and signal region estimates, are shown in Table 9.7. For the final estimate, two main sources of systematic uncertainty are taken into account: the quality of the templates of the fit and the precision on the transfer factors. The latter component contains the statistical uncertainty on the MC efficiency ($\sim$ 4%) and the systematic uncertainties on the SF described earlier. After the subtraction of the remaining ZZ contribution, the signal region estimate is $2.88 \pm 0.28(\text{stat}) \pm 0.54(\text{syst})$ events for the $4e$ channel and $2.91 \pm 0.33(\text{stat}) \pm 0.60(\text{syst})$ for the $2\mu 2e$ channel in the full mass range.

Table 9.7: Table containing fit results for the event yields of each background component estimated from the fit of the data in the $Z+X$ control regions, the average efficiencies of the additional selection criteria for each component, and the extrapolated yield of each component in the signal region. Estimates are done separately for the $4e$ and $2\mu 2e$ channels.

$4e$			
Background	Data CR fit yield	<efficiency>	Estimated SR yield
f	$420.0\ ^{+21.50}_{-21.20}$	0.0034 ± 0.0004	$1.45\ ^{+0.07\ +0.47}_{-0.07\ -0.47}$
q	$7.60\ ^{+1.51}_{-1.52}$	0.11 ± 0.02	$0.83\ ^{+0.18\ +0.14}_{-0.18\ -0.14}$
γ	$29.36\ ^{+8.28}_{-7.75}$	0.024 ± 0.004	$0.68\ ^{+0.20\ +0.20}_{-0.20\ -0.20}$
Signal Region Estimate			
Extrapolation to SR			2.96±0.61
ZZ contribution			0.08±0.01
Final $4e$ estimate			2.88±0.61

$2\mu 2e$			
Background	Data CR fit yield	<efficiency>	Estimated SR yield
f	$473.7\ ^{+22.8}_{-22.4}$	0.0034 ± 0.0004	$1.65\ ^{+0.08\ +0.53}_{-0.08\ -0.53}$
q	$10.66\ ^{+2.13}_{-2.13}$	0.09 ± 0.02	$0.96\ ^{+0.26\ +0.16}_{-0.26\ -0.16}$
γ	$18.2\ ^{+7.80}_{-7.19}$	0.024 ± 0.004	$0.43\ ^{+0.19+0.21}_{-0.19-0.21}$
Signal Region Estimate			
Extrapolation to SR			3.04±0.69
ZZ contribution			0.13±0.01
Final $2\mu 2e$ estimate			2.91±0.69

9.3 Additional Background Control Regions

Validation of both the irreducible and reducible background predictions is performed in a control region dominated by background contributions. The control region is constructed by following the standard analysis selection except that the isolation and impact parameter significance criteria are removed for the subleading lepton pair. The m_{12} and m_{34} distributions for all candidates passing the selection criteria are shown in Figure 9.6 to validate both the normalization and shapes of these predictions. The mass shapes are derived using the methods described in Section 11.2. Good agreement is observed between the predictions and the data.

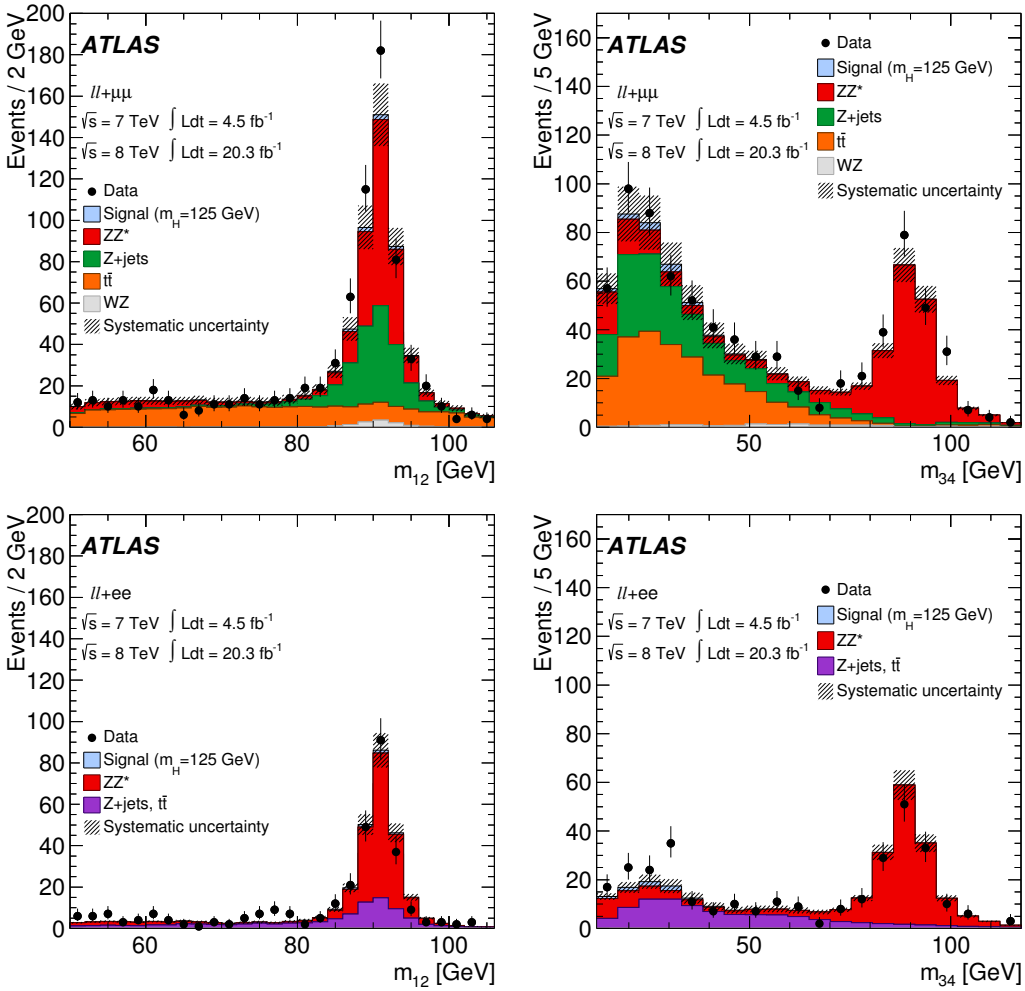

Figure 9.6: Invariant mass distributions of the lepton pairs in the control sample defined by a Z boson candidate and an additional same-flavor lepton pair over the full $m_{4\ell}$ distribution, for the $\sqrt{s} = 7$ and 8 TeV datasets . The kinematic selection of the analysis is applied and the isolation and impact parameter significance requirements are applied to the first lepton pair only. The sample is divided according to the flavor of the subleading lepton pair with the $\ell\ell + \mu\mu$ events shown in the top row and $\ell\ell + ee$ events in the bottom row. The simulation is normalized to the data driven background estimations.

Chapter 10

Systematic Uncertainties

This chapter describes the derivation of systematic uncertainties associated with the measurements in the $H \to 4\ell$ decay channel. The chapter begins with a general overview of the sources of systematic uncertainty in all of the measurements and the methods used to estimate their impact on the measurement in Section 10.1. Then, results from the specific studies for the mass and signal strength measurements are presented in Section 10.2 and the results specific to the differential cross section measurements are shown in Section 10.3.

10.1 Sources of Systematic Uncertainties

This section describes the sources of systematic uncertainty considered in the $H \to 4\ell$ measurements. These sources have been divided into two categories based on their impact on the analysis: those that primarily affect the predicted yields in Section 10.1.1 and those that primarily affect the shapes of the observables of interest in the signal region in Section 10.1.2.

10.1.1 Yield Systematics

Uncertainty in the signal and background event yield estimation can arise from a number of sources. For predictions from the simulation, mismodeling of reconstruction level observ-

ables used in the event selection generally leads to differing selection efficiencies between the simulation and the data, resulting in possible biases in the measurements. For data-driven predictions such as the reducible background estimation, uncertainties can arise from limited statistics and/or uncertainty in the composition of a data control region. This section describes the sources of systematic uncertainty affecting the signal and background yield estimation.

10.1.1.1 Luminosity

The overall uncertainty in the integrated luminosity is 1.8% and 2.8% for the 7 TeV and 8 TeV data, respectively, using the methods of Reference [129]. This uncertainty enters several places in the measurements. It is used to normalize both the irreducible background and the signal yield predictions because both are taken from the simulation. It also factors directly into the calculation of the observed cross sections.

10.1.1.2 Trigger Efficiency

Differences in the trigger efficiency between the data and simulation can arise due to mismodeling of the trigger-level observables. For this analysis, a trigger selection efficiency for the signal of over 99% is possible due to the presence of multiple high-p_{T} leptons in the final state. A conservative estimate of the systematic uncertainties associated with the trigger selection efficiency is evaluated by calculating the signal yield with and without the trigger requirements in the event selection. This results in a systematic uncertainty of 0.4% from muon triggers and 0.1% from electron triggers on the inclusive signal yield.

10.1.1.3 Electron Selection

Systematic uncertainties due to differences in the electron reconstruction and identification efficiencies between the data and the simulation are evaluated using the results of Refer-

ence [114]. The uncertainties in the electron reconstruction and identification efficiency range from less than 1% at high E_{T} up to a few percent at low E_{T} as shown in the data/MC ratio in Figure 10.1. The systematic uncertainties are divided into seven nuisance parameters according to the electron E_{T} and whether or not the systematic uncertainty is correlated between E_{T} bins, as shown in Table 10.2.

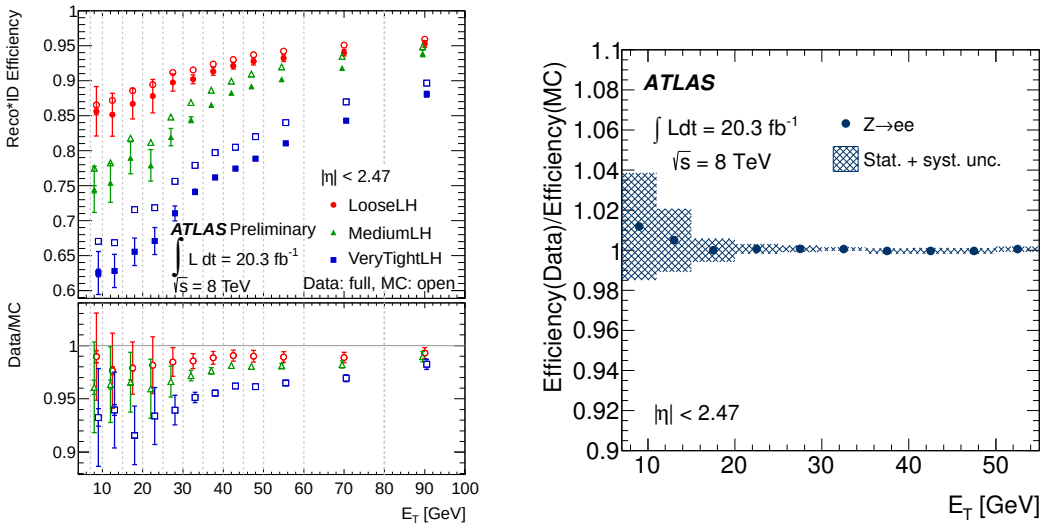

Figure 10.1: (left) Reconstruction and identification efficiency for electrons in the 8 TeV data and simulation as a function of E_{T} for several different operating points using the likelihood-based electron identification. The ratio between the data and the simulation (MC) is used to correct the efficiency in the simulation. (right) The ratio of the efficiencies in data and simulation for the additional impact parameter and isolation criteria required by the electron selection as a function of E_{T} for the 8 TeV data and simulation.

An additional systematic uncertainty is assigned to account for uncertainties in the modeling of the isolation and impact parameter significance as the requirements on these observables are not included in Reference [114]. The efficiencies of these additional cuts has been estimated using a dedicated tag and probe study of $Z \to ee$ events, the results of which are shown in Figure 10.1. The selection efficiency for electrons in the barrel ($|\eta| < 1.37$) is assigned a systematic uncertainty of 1.4% (0.7%) for $E_{\mathrm{T}} < 11$ GeV ($11 < E_{\mathrm{T}} < 15$ GeV) and the selec-

tion efficiency for electrons in the end-caps ($|\eta| > 1.37$) is assigned a systematic uncertainty of 2.5% (1.2%) for $E_{\mathrm{T}} < 11$ GeV ($11 < E_{\mathrm{T}} < 15$ GeV) per electron.

10.1.1.4 Muon Selection

Systematic uncertainties due to differences in the muon reconstruction efficiency between the data and the simulation are evaluated using the results of Reference [116]. The efficiency as a function of η for the different reconstructed muon types with $p_{\mathrm{T}} > 10$ GeV is shown in Figure 10.2. The ratio of the efficiency measured in data to the efficiency in the simulation shows that the uncertainties in the muon reconstruction efficiency are at the per-mille level.

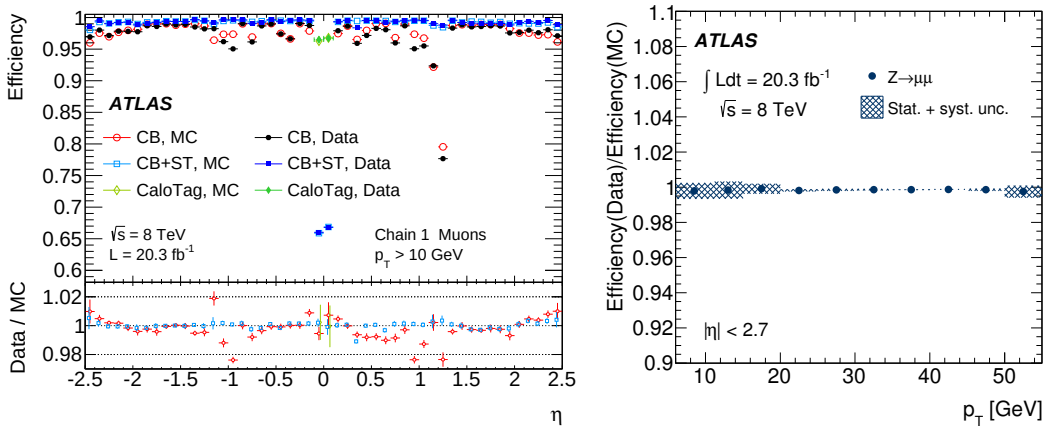

Figure 10.2: (left) Reconstruction efficiency for muons in the 8 TeV data and simulation as a function of η for the various muon reconstruction strategies. The ratio between the data and the simulation (MC) is used to correct the efficiency in the simulation. (right) The ratio of the efficiencies in data and simulation for the additional impact parameter and isolation criteria required by the muon selection as a function of p_{T} for the 8 TeV data and simulation.

The isolation and impact parameter significance selection efficiencies are also studied in $Z \to \mu^+\mu^-$ events and the results are shown in Figure 10.2. No significant differences between the data and simulation are observed so no systematic uncertainty is assigned.

10.1.1.5 Reducible Background Yield

The data-driven estimates for the reducible background are subject to uncertainties due to limited statistics in the various control regions as well as uncertainties in the composition of those control regions. The systematic uncertainties for the data-driven reducible background prediction are described in Section 9.2.

10.1.2 Shape Systematics

This section describes the sources of systematic uncertainty that primarily affect the shapes of the final observables in the signal region.

10.1.2.1 Lepton Energy/Momentum Scale and Resolution

Systematic uncertainties affecting the reconstructed energy/momentum scale or resolution for leptons have been evaluated. These are calculated by first modifying the energy/momentum of the reconstructed leptons by a scale factor prior to the event selection, allowing for changes in the event selection due to threshold effects. This can change the event yield due to events containing leptons near the p_{T} thresholds but this is a negligible effect. More importantly, the shape of the $m_{4\ell}$ distribution is modified, which directly affects the m_{H} measurement.

Systematic uncertainties associated with the electron/photon energy scales and resolution are evaluated following the results of Reference [67]. Sources of systematic uncertainty include the LAr calorimeter calibration procedure, detector high-voltage non-uniformity, ID and calorimeter material description, and uncertainties due to modeling of pile-up. The photon energy scale and resolution uncertainties are considered simultaneously with the electron systematic uncertainties because $m_{4\ell}$ can contain contributions from FSR photons and the uncertainties are highly correlated between electrons and photons due to the calorimeter EM

calibration procedures.

Detailed studies of the muon momentum scale and resolution in both the simulation and data have been performed using $Z \to \mu^+\mu^-$, $J/\psi \to \mu^+\mu^-$ and $\Upsilon \to \mu^+\mu^-$ events in Reference [116]. Because the MS and ID make independent measurements of the muon momenta, different sources of systematic uncertainty will affect these measurements, including but not limited to detector alignment (see Chapter 4), magnetic field description and hit reconstruction and calibration. These results show that the muon momentum scale is known with a precision of 0.05% to 0.2% depending on η.

10.1.2.2 Jet Systematic Uncertainties

Studies of systematic uncertainties in the jet energy scale and resolution have been performed in Reference [130, 131] for the 7 TeV data and preliminary results using the same methods are produced for the 8 TeV data. Sources of systematic uncertainty in the jet energy scale and resolution include detector material description, jet flavor/composition uncertainties and pile-up modeling. Figure 10.3 shows the jet energy scale uncertainties as a function of η and $p_{\mathrm{T}}^{\mathrm{jet}}$ for the 8 TeV data. Uncertainties in jet-related observables will not lead to uncertainties in the signal and background yield estimates because the event selection does not depend on the jets, but does result in uncertainties in the correction factors for the jet-related differential cross section measurements.

10.1.2.3 Theory Systematic Uncertainties

As explained in Section 2.2, there are inherent uncertainties in theoretical cross section calculations due to choice of factorization scale, renormalization scale, and PDFs. Uncertainties in the normalization of the background and signal predictions due to these choices are taken from Refs. [25, 74, 75] as described in Section 6.2. Additional shape uncertainties due to these

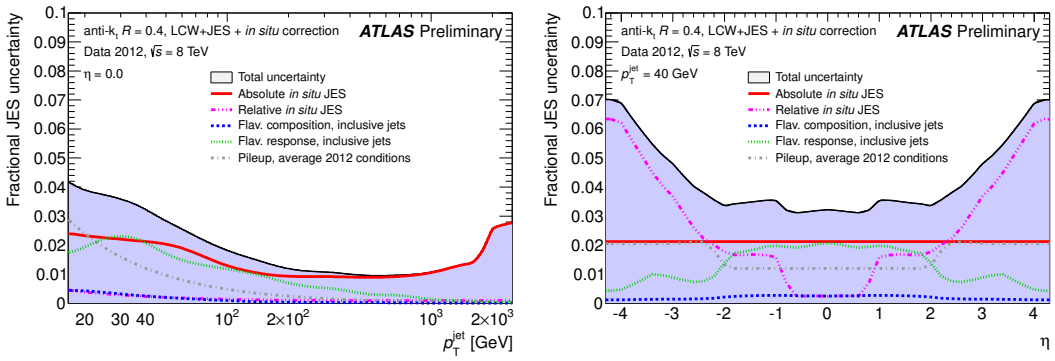

Figure 10.3: Jet energy scale uncertainties as a function of (left) jet p_{T} and (right) jet η in the 8 TeV data [130, 131].

choices for the irreducible background are also considered in the differential cross section measurements and are described in Section 10.3.1. Finally, uncertainties in the differential cross section theoretical predictions are evaluated as described in Section 10.3.3.

10.2 Mass and Signal Strength Systematic Uncertainties

The results of the systematic uncertainty studies for the mass and signal strength measurements are presented in this section. The methods and results of the individual studies are described and then a ranking of the nuisance parameters in the likelihood fit is shown in order to determine the dominant sources of uncertainty in the mass and signal strength measurements. A summary of the systematic uncertainties affecting the predicted signal yields is shown in Table 10.1.

10.2.1 Lepton Efficiency Uncertainties

Systematic uncertainties affecting the signal and background yields are evaluated by computing the difference between the nominal event yield and the event yield after applying a systematic variation to the simulated events. If Σ_{nom} is the nominal yield and Σ_{syst} is the

Table 10.1: The expected impact of the systematic uncertainties on the signal yield, derived from simulation, for $m_{\mathrm{H}} = 125$ GeV, are summarized for each of the four final states for the combined 4.5 fb^{-1} at $\sqrt{s} = 7$ TeV and 20.3 fb^{-1} at $\sqrt{s} = 8$ TeV. The symbol "–" signifies that the systematic uncertainty does not contribute to a particular final state. The last three systematic uncertainties apply equally to all final states. All uncertainties have been symmetrized.

Source of uncertainty	4μ	$2e2\mu$	$2\mu2e$	$4e$	combined
Electron reconstruction and identification efficiencies	–	1.7%	3.3%	4.4%	1.6%
Electron isolation and impact parameter selection	–	0.07%	1.1%	1.2%	0.5%
Electron trigger efficiency	–	0.21%	0.05%	0.21%	<0.2%
$\ell\ell + ee$ backgrounds	–	–	3.4%	3.4%	1.3%
Muon reconstruction and identification efficiencies	1.9%	1.1%	0.8%	–	1.5%
Muon trigger efficiency	0.6%	0.03%	0.6%	–	0.2%
$\ell\ell + \mu\mu$ backgrounds	1.6%	1.6%	–	–	1.2%
QCD scale uncertainty					6.5%
PDF, α_s uncertainty					6.0%
$H \to ZZ^*$ branching ratio uncertainty					4.0%

modified yield, then the relative systematic uncertainty is evaluated as $|\Sigma_{\mathrm{nom}} - \Sigma_{\mathrm{syst}}|/\Sigma_{\mathrm{nom}}$. For systematic variations which affect individual leptons in an event, the uncertainties between leptons are treated as correlated in order to produce more conservative systematic uncertainties.

The yield uncertainties have been derived for all signal samples over a large range of m_{H} and representative results are shown here for a SM Higgs boson with $m_{\mathrm{H}} = 125$ GeV. The evaluated systematic uncertainties in the signal yields of channels containing electrons are shown in Table 10.2. The total uncertainties in the electron reconstruction and identification efficiency of the signal yield at $m_H = 125$ GeV are 4.4%, 1.7% and 3.3% for $4e$, $2e2\mu$ and $2\mu2e$ final states, respectively. The muon selection related systematic uncertainties for the signal yield for channels containing muons are estimated to be 1.86%, 0.77% and 1.09% in the 4μ, $2\mu2e$ and $2e2\mu$ final states respectively. The electron trigger systematic uncertainties are evaluated to be 0.2%, 0.2%, and 0.05% in the $4e$, $2e2\mu$ and $2\mu2e$ final states respectively and the muon trigger systematic uncertainties are evaluated to be 0.7%, 0.6%, and 0.03% in the

4μ, $2\mu 2e$ and $2e2\mu$ final states respectively.

Table 10.2: Relative systematic uncertainties in the $4e/2e2\mu/2\mu2e$ channel yields for a SM Higgs signal with $m_{\mathrm{H}} = 125$ GeV resulting from uncertainties in the single electron reconstruction, identification, isolation, and impact parameter significance selection efficiencies. The reconstruction and identification uncertainties are divided into seven nuisance parameters based on electron E_{T} and the correlated nature of the systematic sources.

	Relative uncertainty in $4e/2e2\mu/2\mu2e$ signal yield			
Systematic Source	$7 < E_{\mathrm{T}} < 10$	$10 < E_{\mathrm{T}} < 15$	$15 < E_{\mathrm{T}} < 20$	$E_{\mathrm{T}} > 20$
ID+Reco, Uncorrelated	0.7/0.02/0.6%	0.9/0.1/0.9%	0.8/0.1/0.7%	2.6/1.6/1.0%
ID, Correlated	1.5/0.2/1.3%			
Reco, Correlated	2.6/0.2/2.5%		0.9/0.3/0.7%	
Isolation+IP	1.2/0.1/1.1%			

10.2.2 Mass Scale Uncertainties

Mass scales uncertainties arise due to uncertainties in the lepton energy/momentum scale as described in Section 10.1.2.1. The difference in the mean of the $m_{4\ell}$ distribution between the nominal and modified event selections ($\Delta m_{4\ell} = \langle m_{4\ell}^{\mathrm{modified}} \rangle - \langle m_{4\ell}^{\mathrm{nominal}} \rangle$) is taken as the mass scale systematic uncertainty. The mass scale uncertainties are then implemented using nuisance parameters which allow the $m_{4\ell}$ distribution of the signal model to shift proportionally to the derived systematic uncertainty as described in Section 11.1.

The mass scale uncertainty model for electron-related uncertainties is parameterized using 25 nuisance parameters which are correlated between electrons and photons, five nuisance parameters which affect only the photon energy scale, and one nuisance parameter for track momentum scale uncertainties for electrons only. Four nuisance parameters account for both the electron and photon energy resolution uncertainties.

The largest $\Delta m_{4\ell}$ for a SM Higgs with $m_{\mathrm{H}} = 125$ GeV after modification of the electron/photon energy scale and resolution are found to be 53, 34, and 20 MeV for the $4e$, $2e2\mu$ and $2\mu2e$ final states using the scale uncertainties as evaluated from $Z \to ee$ events. The

total combined mass scale uncertainties due to electron/photon energy scale and resolution uncertainties are estimated to be 0.06%, 0.03% and 0.04% for $4e$, $2e2\mu$ and $2\mu2e$ final states, respectively.

The muon momentum scale uncertainties are evaluated for the ID and MS components separately but ultimately combined into a single nuisance parameter which accounts for both components. The total mass scale systematic uncertainties for the $m_{\mathrm{H}} = 125$ GeV signal are 0.04%, 0.02% and 0.03% for the 4μ, $2e2\mu$ and $2\mu2e$ final states, respectively. The mass resolution systematic uncertainties are studied individually but found to have a negligible effect, primarily because the simulated momenta are smeared such that there are negligible differences in the individual muon momentum resolution between the simulation and data.

10.2.3 Systematic Ranking

Systematic uncertainties are implemented in the signal and background models for the m_{H} and μ measurements using nuisance parameters as described in Section 11.1, which allow study of the impact of the individual systematic uncertainties on the final fit. All of the nuisance parameters are ranked according to their impact on m_{H} and μ in fits of the Asimov data. The results of this ranking is shown in Figure 10.4 for the nuisance parameters having the largest post-fit impact on the uncertainties of the parameter of interest. The dominant uncertainties in the signal strength measurement are the QCD scale and PDF uncertainties in the ggF theoretical prediction. For the m_{H} measurement, the dominant systematic uncertainties are the experimental uncertainties in the lepton energy/momentum scales. Many of the nuisance parameters were found to have a negligible effect on the final fit result and therefore these uncertainties are removed from the final signal and background models.

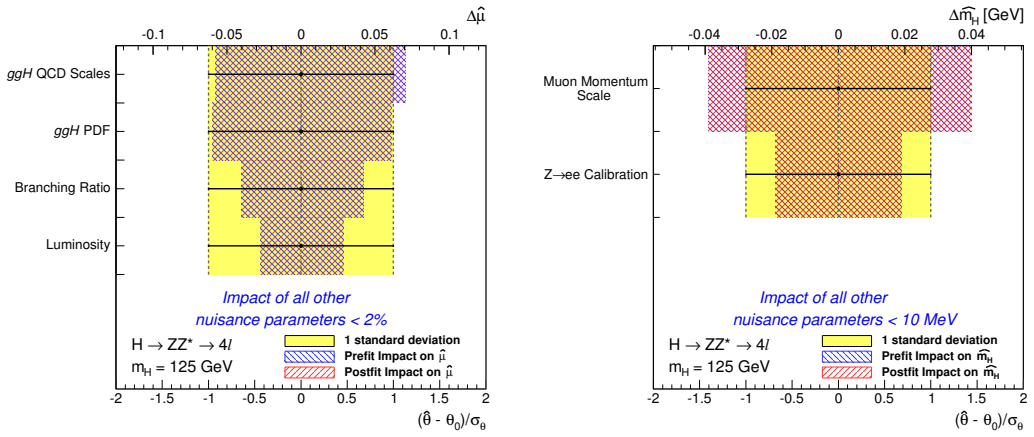

Figure 10.4: Ranking of the nuisance parameters in the 2D conditional fit according to their impact on the parameters of interest (left) μ and (right) m_{H} using the Asimov dataset for a Higgs boson with $m_{\mathrm{H}} = 125$ GeV. The black points indicate the post-fit pull of the nuisance parameters (with magnitude according to the lower axis) and the yellow boxes indicate the 1-σ variation of those nuisance parameters. The blue and red hatched areas indicate the impact of the nuisance parameter on the final parameter of interest according to the upper axis.

10.3 Uncertainties for the Differential Measurements

In this section, the results of studies of the systematic uncertainties for the differential cross-section analysis are presented. Systematic uncertainties can be categorized according to where they enter the cross section calculation:

1. Uncertainties in the observed number of signal events after background subtraction, $n_{\mathrm{reco}}^{\mathrm{sig}}$, which is directly related to uncertainties in the background predictions.

2. Uncertainties on the correction factors, consisting of experimental and model dependence uncertainties.

3. Uncertainties on the integrated luminosity $\mathcal{L}_{\mathrm{int}}$.

4. Uncertainties on the theoretical differential cross section predictions $(d\sigma/dx)_{\mathrm{theory}}$ (which do not affect the measured cross sections) .

Table 10.3 shows an overview of the systematic uncertainties considered in the differential cross section measurement, and Table 10.4 shows the resulting relative uncertainties. The ranges indicate the maximum and minimum relative uncertainty over all variables and bins.

Table 10.3: Overview of the systematic uncertainties considered in the fiducial cross section measurements.

Systematic source	$n_{\text{reco}}^{\text{sig}}$	CF	$\mathcal{L}_{\text{int}}$	$(d\sigma/dx)_{\text{theory}}$
Luminosity	✓		✓	
Experim. uncert. leptons/jet	✓	✓		
Irreducible background estimate (normalization)	✓			
Reducible background estimate (normalization/shape)	✓			
PDF/Scale+α_{S}	✓	✓		✓
Unfolding model dependence		✓		

Table 10.4: Summary of the systematic uncertainties. The ranges indicate the dependence on variables and bins.

Systematic Uncertainties (%)	
Background Estimate	
Luminosity	1.4 – 2.3
Reducible background	1.6 – 34
Experimental, leptons	1.3 – 2.3
PDF/scale	3.0 – 24
Correction factors	
Experimental, leptons	2.1 – 2.6
Experimental, jets	2.7 – 13
Production process	0.1 – 15
Higgs boson mass	0.4 – 2.7
Luminosity	2.8

The uncertainties on $n_{\text{reco}}^{\text{sig}}$ arise from several sources which affect the normalizations and shapes of the backgrounds. The systematic uncertainties associated with lepton reconstruction, identification, and trigger efficiencies for the irreducible background are evaluated using the same methods as in Section 10.2 but are done within the $m_{4\ell}$ window and for each differential bin separately, simultaneously accounting for both shape and normalization uncertainties. Additional shape uncertainties associated with theoretical uncertainties in the

irreducible background are described in Section 10.3.1. Normalization uncertainties in the reducible background have been described in Section 9.2 but additional shape uncertainties for the differential observables are presented here in Section 10.3.2.

Several sources of uncertainty are also considered for the correction factors. The experimental uncertainties are evaluated using the same method as done for the irreducible background. Uncertainties due to choice of QCD scale and PDF have also been evaluated but found to be negligible due to cancellation of the effect between the numerator and denominator of the correction factors. The model-dependence systematic uncertainties for the correction factors are described in Section 8.5.3. Finally, the systematic uncertainties for $(d\sigma/dx)_{\text{theory}}$ are described in Section 10.3.3.

10.3.1 Irreducible Background Shape Uncertainties

Because the irreducible background is estimated using simulation, it is subject to systematic uncertainties due to the choice of PDF and μ_F/μ_R scales, as described in Section 2.2. Uncertainties on the normalization for this background are described in Section 6.2.2 but there may be additional uncertainties in the shape predictions of the differential distributions, particularly the p_{T}. Furthermore, different treatment is required for the jet-related variables as the use of a fixed order calculation in the simulation will lead to poor modeling of high jet-multiplicity events.

For the kinematic variables only, shape uncertainties have been evaluated by repeating the background estimates with different choices of PDF and μ_F/μ_R scales using an event re-weighting procedure. For each kinematic variable, truth-level event weights are derived by taking the ratio between the nominal and a systematically varied differential distribution. The background yield is estimated after applying these weights to the reconstructed events using the truth level information and the systematic uncertainty for each bin is evaluated as the

maximum variation up/down with respect to the nominal value. The p_{T} is the most sensitive to these variations with relative uncertainties ranging from 3-8% for the choice of μ_F/μ_R and 2-4% for the choice of PDF. The uncertainties on the other kinematic variables are $\leq 1\%$ in all bins from both choice of PDF and μ_F/μ_R.

For the jet-related variables, a data-driven means of evaluating the shape systematic uncertainty has been implemented. The high mass control region ($m_{4\ell} > 190$ GeV, see Figure 12.3) provides a very pure sample of irreducible background events for evaluating the mismodeling of the jet distributions. The systematic uncertainty is evaluated as the larger of: (1) the data-MC difference and (2) the statistical uncertainty on the data in the control region after normalizing the MC estimate to the observed data yield. This systematic uncertainty accounts for both theory and experimental uncertainties in the mismodeling of the jet distributions. Table 10.5 shows the derived shape uncertainties for the jet variables.

Table 10.5: Systematic uncertainties on the irreducible background shape derived using the data-simulation comparison in the high mass control region ($m_{4\ell} > 190$ GeV).

Shape Systematic Uncertainty				
	Bin			
Variable	1	2	3	4
n_{jets}	8%	13%	25%	49%
$p_{\mathrm{T,jet}}$	8%	19%	22%	22%

10.3.2 Reducible Background Shape Uncertainties

Systematic uncertainties are assigned for both normalization and shape uncertainties in the reducible background. As done for the estimation of the reducible background yields, the associated shapes are obtained separately for channels with sub-leading muons and electrons.

For the $\ell\ell + \mu\mu$ reducible background, nominal shapes are taken from Z+jets and $t\bar{t}$ simulation in the signal region. Two systematic variations are assigned to these shapes,

obtained by modifying the track isolation and impact parameter significance requirements used in the selection of the sub-leading leptons. One variation is created by relaxing the selection to $\Sigma p_{\mathrm{T}}^{\mathrm{iso}}/p_{\mathrm{T}} < 0.3$ and $d_0/\sigma_{d0} < 4.5$ and another variation is created by tightening the requirements to $\Sigma p_{\mathrm{T}}^{\mathrm{iso}}/p_{\mathrm{T}} < 0.1$ and $d_0/\sigma_{d0} < 3$. All three predictions are normalized to the background estimate in Section 9.2.1 and are shown in Figure 10.5. The differences between the nominal and the variations are taken as the shape systematic uncertainty.

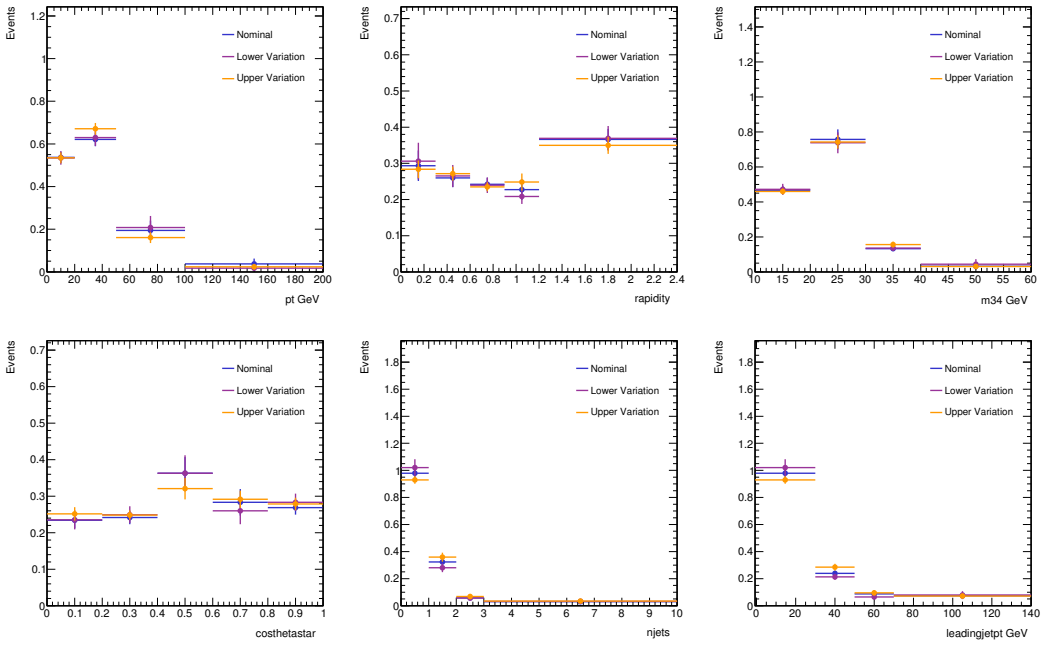

Figure 10.5: Reducible background shapes for the $\ell\ell + \mu\mu$ channels in the $m_{4\ell}$ window [118,129] GeV. All variables used in the differential cross section measurement are shown.

For the $\ell\ell + ee$ channels, the shapes are instead taken from control regions in the data and extrapolated to the signal regions by applying transfer factors. For the nominal shapes, the $3\ell + X$ method described in Section 9.2.2 is used. Two systematic variations are again assigned to these shapes, obtained by using different estimation methods. The lower variation is evaluated using the "truth-reco" method, while for the upper variation the "transfer factor

with b-enriched CR" method is used. All three shapes, shown in Figure 10.6, are normalized to the nominal background estimate from Section 12.2.2 and shape uncertainties are evaluated using the differences in the individual bins.

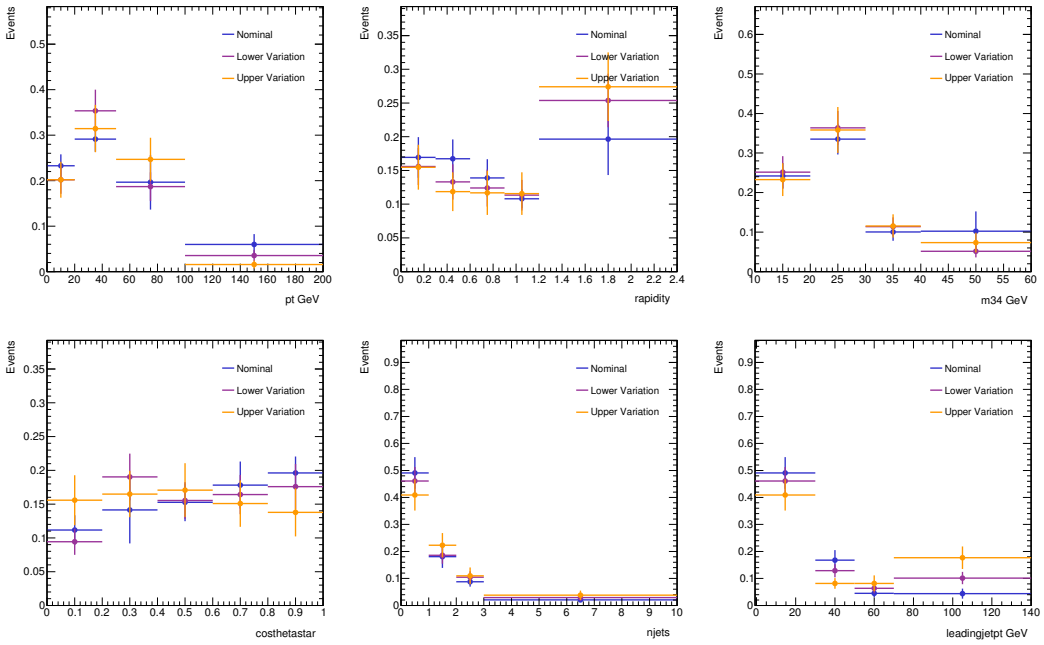

Figure 10.6: Reducible background shapes for the $\ell\ell + ee$ channels in the $m_{4\ell}$ range [118,129] GeV. All variables of interest used in the differential cross section measurement are shown.

10.3.3 Theoretical Prediction Uncertainties

The theoretical differential cross section predictions are subject to systematic uncertainties due to the choice of PDF and QCD renormalization and factorization scales. These uncertainties are evaluated by generating events with systematic variations in the PDF and scales.

Renormalization and factorization scale uncertainties are evaluated by varying μ_{R} and μ_{F} up ($\times 2$) and down ($\times 0.5$) from their nominal values, excluding $\mu_{\mathrm{R}}/\mu_{\mathrm{F}} = 4$ and 0.25. For the HRes2 calculation only, there are two additional resummation scales, $Q_1 = m_{\mathrm{H}}/2$ and

$Q_2 = m_b$ for the bottom quark contribution. These are varied up and down by factors of 2 while keeping μ_R/μ_Ffixed at their nominal values (and vice versa). The envelope of all variations is taken as the systematic uncertainty. The variations for the HRes2 prediction of the p_T and $|y|$ distributions are shown in Figure 10.7.

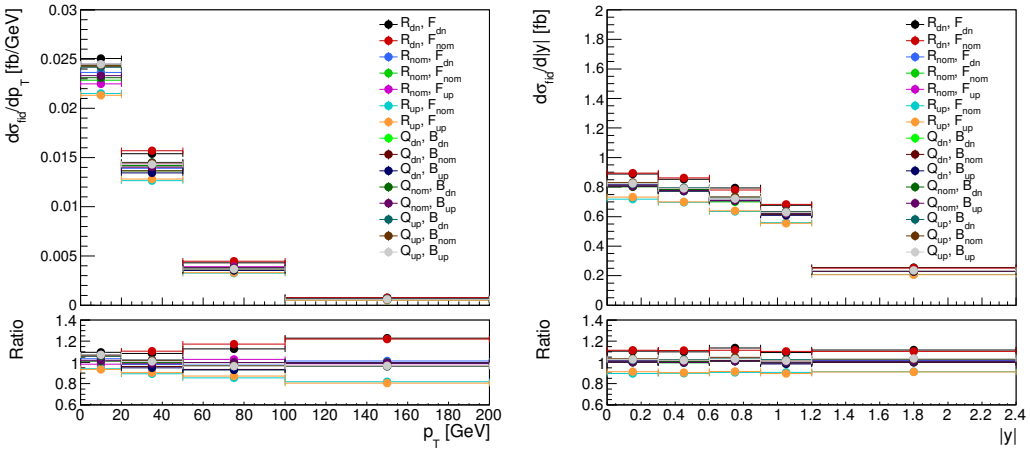

Figure 10.7: Comparisons of the 15 scale variations for a 125.4 GeV Higgs sample generated using HRes2. The ratio plots underneath are with respect to the nominal (R_{nom}, F_{nom}).

Two sets of variations are performed for the choice of the PDF (the nominal is the CT10 PDF set). First, the eigenvector sets included with the CT10 PDF set are used to derive one set of variations. The second set of variations is created by using the MSTW2008 PDF set and the NNPD 2.3 PDF set. The variations in the Powheg prediction after changing PDF sets for the p_T and $|y|$ is shown in Figure 10.8. For each set of variations, the systematic uncertainties are evaluated by taking the envelope of the difference between the variations and the nominal predictions. Finally, the uncertainties from the eigenvector and PDF set choice are added in quadrature.

To evaluate the QCD scale uncertainty in the n_{jets} distribution for Powheg and Minlo samples, the Stewart-Tackmann procedure is used to account for the additional perturbative

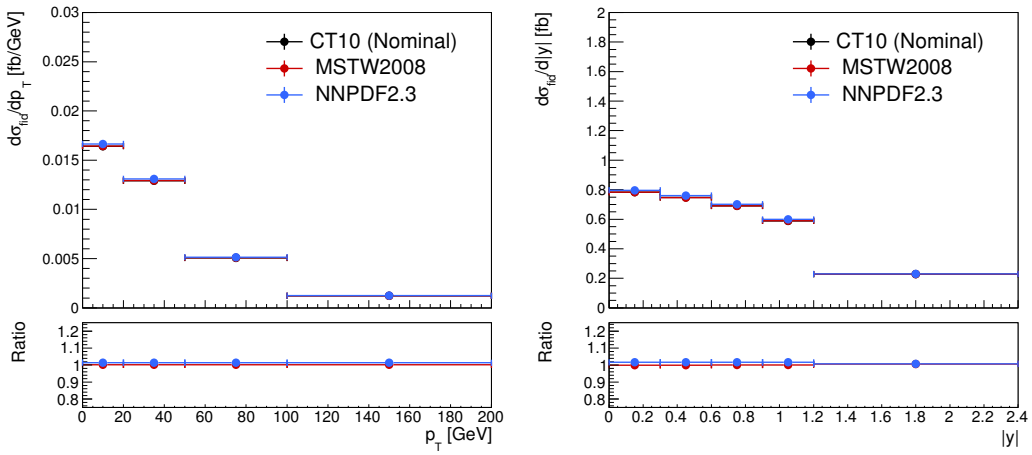

Figure 10.8: Comparisons of the cross section predictions for a 125.4 GeV Higgs sample generated using Powheg with the CT10, MSTW2008, and NNPDF PDF sets. The ratio plots underneath are with respect to the nominal (CT10).

uncertainty associated with a jet p_{T} cut [132]. The Stewart-Tackmann scale uncertainty is used in place of the QCD scale uncertainty, and added in quadrature with the other uncertainties.

Chapter 11

Mass and Signal Strength

The mass and signal strength μ measurements in the $H \to 4\ell$ channel are performed using a simultaneous unbinned fit of the $m_{4\ell}$ and BDT discriminant distributions in the signal region $110 < m_{4\ell} < 140$ GeV using both the $\sqrt{s} = 7$ and $\sqrt{s} = 8$ TeV data. This chapter describes the methods and results of these measurements.

11.1 Method

A simultaneous maximum likelihood fit is performed on the observed distributions of $m_{4\ell}$ and BDT_{ZZ} in eight data categories, including the four final states in the $\sqrt{s} = 7$ and $\sqrt{s} = 8$ TeV data. The fit model must necessarily describe both the shapes and normalization of the backgrounds and signal *pdf* continuously as a function of the parameters of interest m_{H} and signal strength μ while also including systematic uncertainties. The probability density function (*pdf*) of the model is parameterized as:

$$P(m_{4\ell}, \mathrm{BDT}_{ZZ}|m_{\mathrm{H}}) = P(m_{4\ell}|\mathrm{BDT}_{ZZ}, m_{\mathrm{H}}) \cdot P(\mathrm{BDT}_{ZZ}|m_{\mathrm{H}}) \tag{11.1}$$

$$\simeq \left(\sum_{n=1}^{4} P_n(m_{4\ell}|m_{\mathrm{H}}) \cdot \theta_n(\mathrm{BDT}_{ZZ}) \right) \cdot P(\mathrm{BDT}_{ZZ}|m_{\mathrm{H}}) \tag{11.2}$$

where $P(m_{4\ell}|\mathrm{BDT}_{ZZ}, m_{\mathrm{H}})$ has been approximated by a sum of *pdf*s in four BDT_{ZZ} bins with bin edges $[-1, -0.5, 0, 0.5, 1]$. The $\theta_n(\mathrm{BDT}_{ZZ})$ function is a step function which is equal to 1

when BDT_{ZZ} falls within bin n and 0 when BDT_{ZZ} is not. Using the binned conditional *pdf* greatly simplifies the treatment of the shape systematic uncertainties for $m_{4\ell}$, BDT_{ZZ}, and m_{H}. This approximation relies on the assumption that there is no significant variation in the $m_{4\ell}$ shape within a given BDT_{ZZ} bin, which has been validated in the simulation. Section 11.2 describes the derivation of the individual *pdf*s for both the signal and backgrounds.

11.2 Mass Templates

The 2-D fit of the $m_{4\ell}$ and BDT discriminant distributions requires templates for both signals and backgrounds. This section describes the derivation of these templates.

11.2.1 Signal Model

The simulated distributions for the two observables, $m_{4\ell}$ and BDT_{ZZ}, are directly used to derive shape templates for the signal *pdf*. Separate one-dimensional (1D) template *pdf*s are created for m_{4l} and BDT distributions. In order to reduce the impact of statistical fluctuations, larger statistics samples used for $H \to 4\ell$ for gluon-fusion ggF and VBF production mechanisms are generated without Higgs decay to τ-leptons. The missing τ decay events do not significantly affect the shape of the *pdf*s in the signal region because the reconstructed $m_{4\ell}$ from τ-leptons is typically below 120 GeV and the τ decay events contribute less than 0.5% to the total reconstructed event yield.

To further reduce the effects of statistical fluctuations, a kernel density estimation technique is used to provide smoothed templates of the observables. The goal of the kernel estimation technique is to produce a function which describes a smooth underlying parent distribution and is statistically consistent with the original sample. In this analysis, a *RooKeysPdf* [133] is used to perform the smoothing which uses a Gaussian kernel with an adjustable band-

width parameter ρ (the parameter that specifies the amount of smoothing to apply to the distribution). Many values of ρ were studied and the value $\rho = 2$ was chosen after validation. An example of the smoothing of the $m_{4\ell}$ distribution is shown in Figure 11.1 for the signal samples with $m_{\mathrm{H}} = 125$ GeV. Good agreement is observed between the original and smoothed distributions. Furthermore, the use of a the smoothed function allows one to continuously shift the peak in $m_{4\ell}$, as shown in Figure 11.1 where a +2 GeV shift has been applied. This technique is used to include uncertainties in the energy and momentum scales in the signal model, the effect of which will shift the $m_{4\ell}$ peak away from m_{H}.

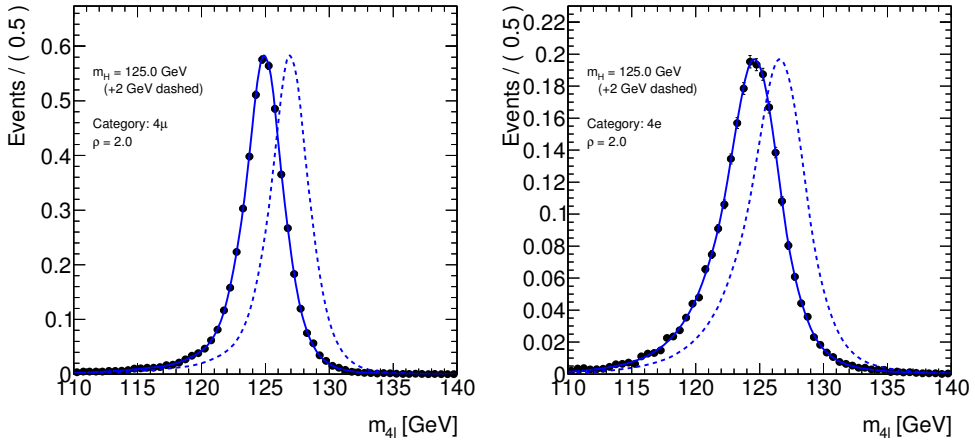

Figure 11.1: Invariant mass distribution for a simulated ggF signal sample with $m_{\mathrm{H}} = 125$ GeV in the 4μ channel on the left and the $4e$ channel on the right. The comparison between the histogram (black dots) and the smoothed distribution (solid blue line) is shown. A +2 GeV shift (dotted blue line) in m_{H} is shown for illustration.

Next, the signal model must be able to scan over m_{H} continuously, while the templates above are all generated with specific values of m_{H}. Because the $m_{4\ell}$ distribution shifts proportionally to m_{H}, templates for intermediate m_{H} values can be approximated by shifting the $m_{4\ell}$ distribution of the two nearest m_{H} sample points by an amount equal to the difference in m_{H} and then interpolating vertically between the two distributions. This technique is for-

mally implemented using B-splines [134], which produces a weighted combination of templates from different "control points" (points where a function is known; in this case the simulated m_{H} mass points). The weights as a function of m_{H} for each mass control point are specified by B-spline base functions. Linear and cubic base functions have been studied and the cubic interpolation was chosen in order to avoid discontinuities in the likelihood function when m_{H} is at or near a control point. The weighting functions and control points are shown in Figure 11.2 for the $\sqrt{s} = 8$ TeV simulation.

Similarly, the signal yield must also be interpolated as a function of m_{H}. The same strategy involving B-splines is employed to interpolate the signal yield between mass points. For higher order B-spline bases, the control points can be optimized to ensure that the resulting B-spline matches the signal yields obtained from the simulation at the control point masses by slightly scaling the signal yield at each control point. The optimization is carried out simultaneously on each control point in an iterative procedure until the B-spline matches the simulated yields to a given precision. The resulting function for the 4μ signal yield is shown in Figure 11.2 as an example.

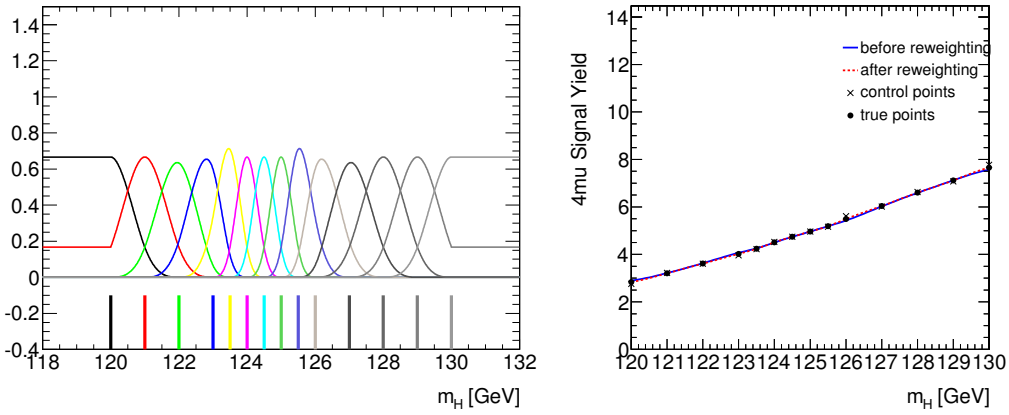

Figure 11.2: B-spline basis functions for each control point for $\sqrt{s} = 8$ TeV simulation using cubic interpolation on the left. The 4μ channel signal yield as a function of m_{H} as determined using B-splines is shown on the right.

Combining the shape and normalization B-spline functions, a representative sample of the resulting $m_{4\ell}$ signal distributions with m_{H} between 120 and 130 GeV are shown in Figure 11.3 for the 4μ and $4e$ decay channels.

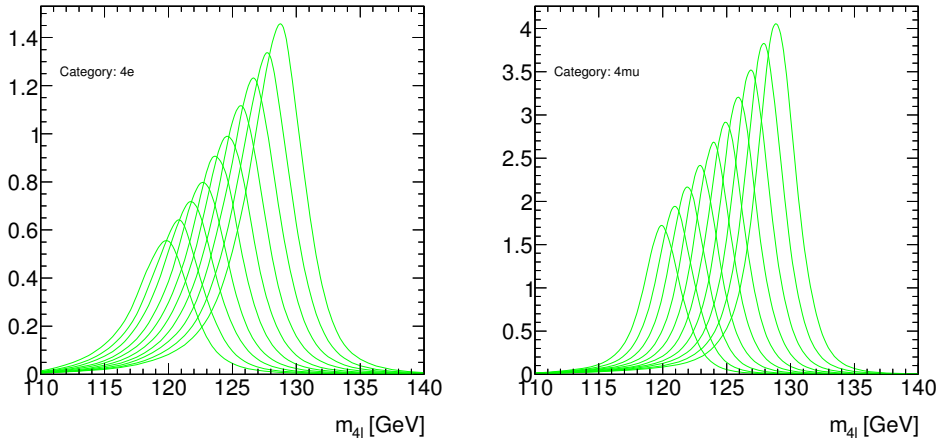

Figure 11.3: Predicted distributions of $m_{4\ell}$ from the signal *pdf* in the (left) $4e$ and (right) 4μ final states for selected m_{H} points between 120 and 130 GeV derived from the $\sqrt{s} = 8$ TeV simulation. The templates have been smoothed using kernel density estimation and continuously parameterized in m_{H} using B-splines.

11.2.2 Background Shapes

Full two-dimensional *pdf*s $P(m_{4\ell}, \mathrm{BDT}_{ZZ})$ are derived for both the irreducible and reducible backgrounds for use in the conditional 2D fit. The following sections describe the derivation of these *pdf*s.

11.2.2.1 Irreducible Background

The irreducible background ($q\bar{q} \to ZZ$ and $gg \to ZZ$) templates are derived directly from the simulation. Kernel density estimation is performed for both observables with smoothing parameters of $\rho = 0.25$ for the m_{4l} smoothing and $\rho = 0.15$ for the BDT_{ZZ} smoothing. A 2D histogram is derived from the kernel density estimate which is then projected onto $m_{4\ell}$ in the

BDT_{ZZ} bins to obtain the 1D shapes used for the conditional 2D fit. The template shape is obtained in this way to ensure consistency when comparing the various types of 2D fits that were used for studies comparing full 2D fits and BDT_{ZZ}-binned fits. Projections of the 2D smoothed shapes are compared with the original simulated histograms in Figure 11.4 for the $q\bar{q} \to ZZ$ and $gg \to ZZ$ backgrounds in the 4μ final state.

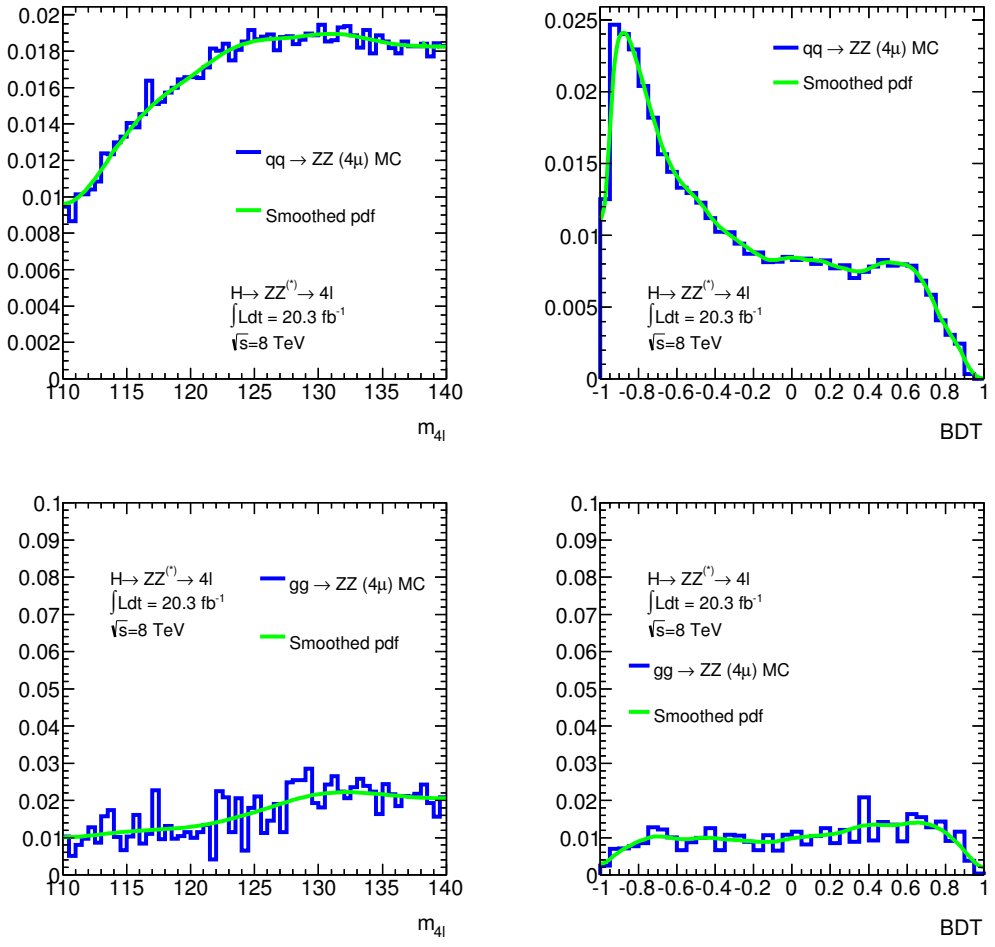

Figure 11.4: Comparison of the 2D smoothed $gg \to ZZ$ and $q\bar{q} \to ZZ$ background templates in $m_{4\ell}$ and BDT_{ZZ} with the original simulation for 8 TeV data in the 4μ final state.

11.2.2.2 Reducible Background

The reducible background shapes are obtained from the Z+jets and $t\bar{t}$ simulation for the $\ell\ell$+$\mu\mu$ channels and from the 3ℓ+X data control region for the $\ell\ell$+ee channels. For the $\ell\ell$+ee shape, the events in the $3\ell + X$ control region are weighted with their corresponding transfer factors to produce shape predictions in the signal region. The distributions are smoothed using kernel density estimation and a comparison between the original and the smoothed distributions over the entire $m_{4\ell}$ range is shown in Figure 11.5.

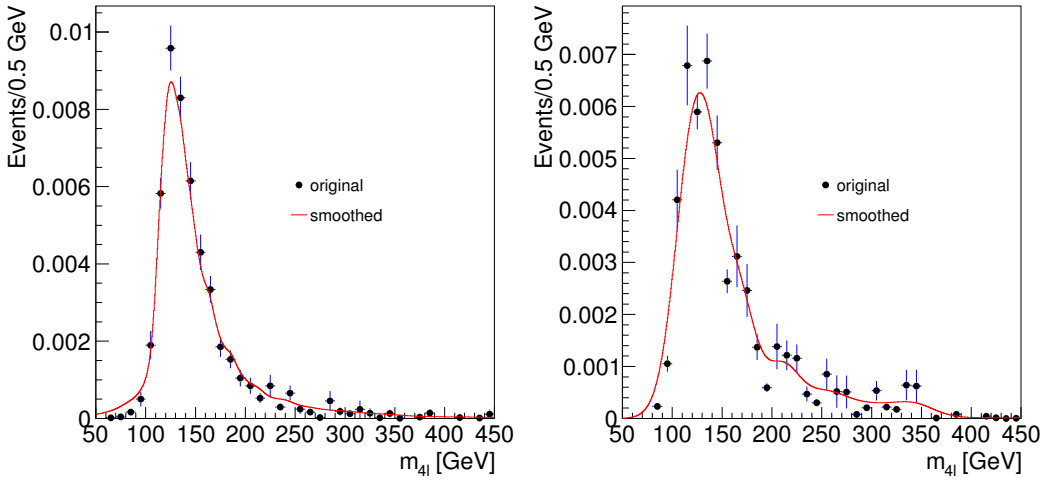

Figure 11.5: Original (blue) and smoothed (red) $m_{4\ell}$ distribution for the $\ell\ell + \mu\mu$ ($\ell\ell + ee$) reducible background on the left (right).

Two systematic variations on the shape used for the $\ell\ell + \mu\mu$ reducible background are derived by modifying the selection applied to the simulation. The nominal selection is applied with the exception that the track isolation and impact parameter significance criteria are modified on the subleading dilepton pair only. One variation is produced by tightening the selection criteria ($\Sigma p_{\mathrm{T}}^{\mathrm{iso}}/p_{\mathrm{T}} < 0.1$ and $d_0/\sigma_{d0} < 3.0$) while the other variation is produced by relaxing these criteria ($\Sigma p_{\mathrm{T}}^{\mathrm{iso}}/p_{\mathrm{T}} < 0.3$ and $d_0/\sigma_{d0} < 4.5$). The same smoothing procedure is applied to the nominal shape and systematic variations. Both the nominal shape and

variations for the $\ell\ell + \mu\mu$ reducible background are shown in Figure 11.6.

Two systematic variations on the shape used for the $\ell\ell + ee$ reducible background are derived from control regions which are orthogonal to the $3\ell + X$ control region. Both the nominal shape and variations for the $\ell\ell + ee$ reducible background are shown in Figure 11.6.

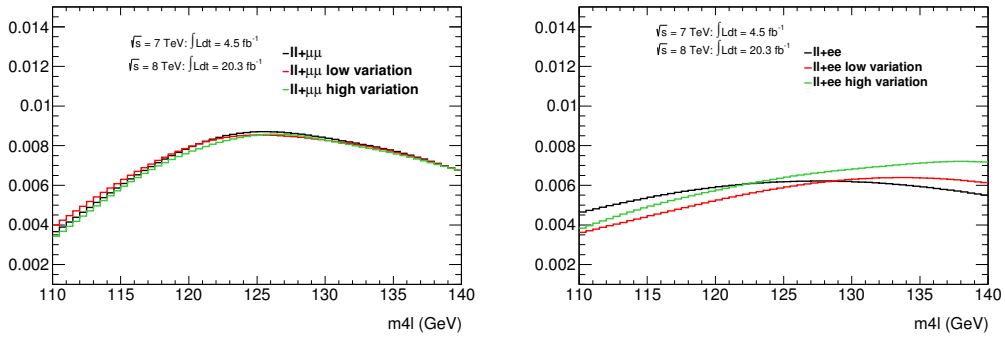

Figure 11.6: Shape templates for the reducible backgrounds in the signal region [110−140] GeV for the combined $\sqrt{s} = 7$ and $\sqrt{s} = 8$ TeV data. The reducible $\ell\ell$+$\mu\mu$ background shapes (left) are taken from the Z+jets and $t\bar{t}$ simulation while the reducible $\ell\ell + ee$ background shapes are derived from data control regions created by relaxing the selection criteria on the subleading di-electron pair.

11.3 Results

A total of 511 candidate events are selected from the combined 7 and 8 TeV data sets using the selection criteria described in Chapter 6. Categorization of the events by final state and high/low mass region are presented in Table 11.1. The $m_{4\ell}$ distribution of the observed candidates for the combined 7 and 8 TeV data as well as the background predictions are shown in Figure 11.7. A clear excess of events over the background expectation is observed near $m_{4\ell}$ of 125 GeV and good agreement with the background predictions is observed elsewhere. The BDT_{ZZ} distribution of the candidates near the observed excess ($120 < m_{4\ell} < 130$GeV) is shown in Figure 11.8.

Scans of $-2\ln\Lambda$ in the parameters of interest, m_{H} and μ, using the 2D conditional fit of the

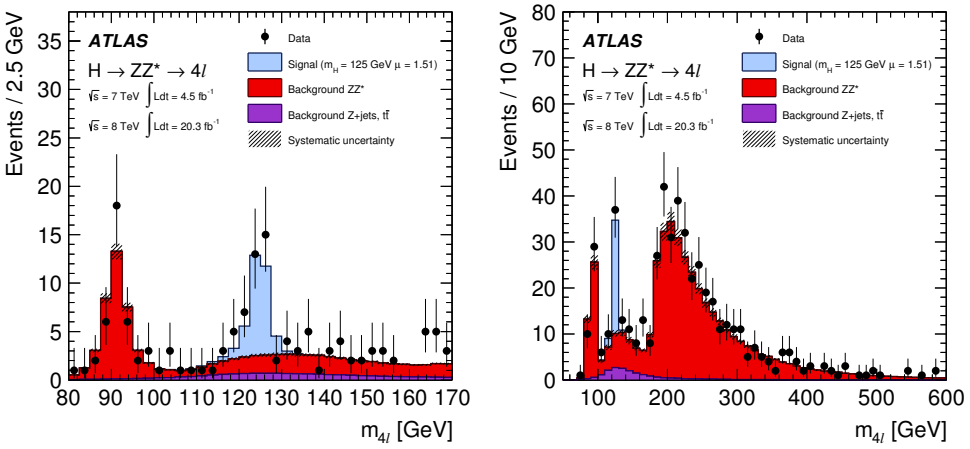

Figure 11.7: Distribution of $m_{4\ell}$ for the selected candidates for the $\sqrt{s} = 7 + 8$ TeV dataset, compared to the background expectation in the low mass region (left) and the entire mass spectrum (right). The contributions of the irreducible and reducible backgrounds are shown separately. The signal prediction for a Higgs boson with $m_{\mathrm{H}} = 125$ GeV is shown, normalized to the best fit value of μ for that m_{H}.

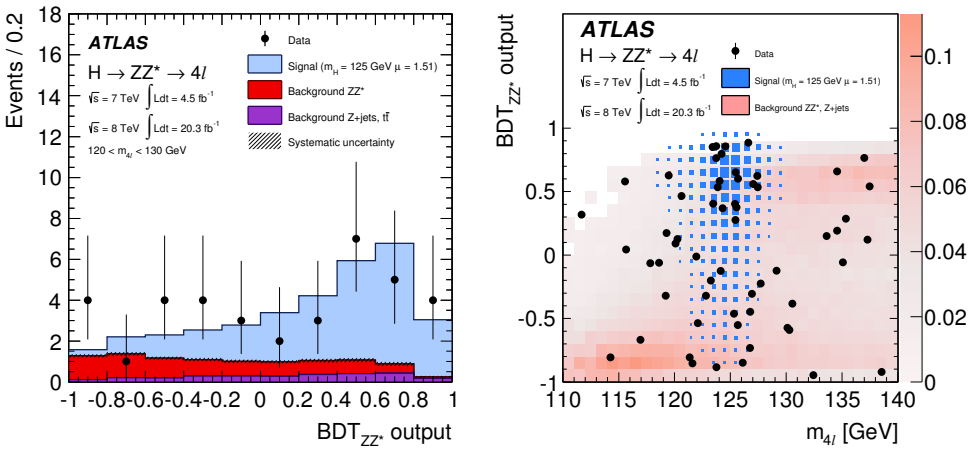

Figure 11.8: BDT$_{ZZ}$ distribution of the selected candidates in the $\sqrt{s} = 7+8$ TeV datasets in the $120 < m_{4\ell} < 130$ GeV region, compared to the background expectation. The signal prediction for a Higgs boson with $m_{\mathrm{H}} = 125$ GeV is shown, normalized to the best fit value of μ for that m_{H}.

Table 11.1: The observed number of events and the final estimate for the expected background, separated into "Low mass" ($m_{4\ell} < 160$ GeV) and "High mass" ($m_{4\ell} \geq 160$ GeV) regions, are presented for the $\sqrt{s} = 7$ TeV and $\sqrt{s} = 8$ TeV data. The expected number of signal events are also shown for various Higgs boson mass hypotheses. For signal and background estimates, the corresponding total systematic uncertainty is given.

$4.5\text{fb}^{-1}@\sqrt{s} = 7$ TeV						
	4μ		$2e2\mu$		$4e$	
	Low mass	High mass	Low mass	High mass	Low mass	High mass
$ZZ^{(*)}$	5.27±0.26	16.98±1.26	4.39±0.24	25.71±1.91	2.02±0.13	9.85±0.77
Z, $Zb\bar{b}$, and $t\bar{t}$	0.43±0.19	0.17±0.07	2.32±0.57	1.16±0.28	2.16±0.45	1.13±0.24
Total Background	5.70±0.32	17.15±1.26	6.71±0.64	26.87±1.94	4.18±0.47	10.98±0.81
Data	11.00	23.00	7.00	24.00	4.00	14.00
$m_H = 123$ GeV	0.80±0.08		0.93±0.09		0.35±0.04	
$m_H = 125$ GeV	1.00±0.10		1.16±0.11		0.46±0.05	
$m_H = 130$ GeV	1.55±0.14		1.89±0.18		0.72±0.07	

$20.3\text{fb}^{-1}@\sqrt{s} = 8$ TeV						
	4μ		$2e2\mu$		$4e$	
	Low mass	High mass	Low mass	High mass	Low mass	High mass
$ZZ^{(*)}$	27.58±1.37	95.00±7.06	23.43±1.28	145.25±10.85	11.20±0.74	56.42±4.44
Z, $Zb\bar{b}$, and $t\bar{t}$	2.90±0.53	1.14±0.21	4.44±0.87	1.98±0.40	1.89±0.40	0.99±0.21
Total Background	30.49±1.47	96.13±7.07	27.86±1.55	147.23±10.85	13.10±0.84	57.41±4.44
Data	42.00	95.00	38.00	174.00	23.00	56.00
$m_H = 123$ GeV	4.61±0.46		5.52±0.55		2.24±0.23	
$m_H = 125$ GeV	5.80±0.57		6.99±0.70		2.79±0.29	
$m_H = 130$ GeV	8.85±0.85		11.31±1.10		4.43±0.45	

$m_{4\ell}$ and BDT_{ZZ} distributions are shown in Figure 11.9 for each final state and the combined data. Consistent results are observed in all final states. Additionally, a scan which does not take into account systematic uncertainties is also performed (the dashed lines in Figure 11.9), showing that the measurement uncertainties are statistically dominated. A plot of the 68% and 95% confidence intervals in the μ-m_{H} plane is shown in Figure 11.10. The final estimates and 68% confidence levels of the parameters of interest are:

$$m_{\text{H}} = 124.51 \pm 0.52(\text{stat}) \pm 0.06(\text{syst}) \text{ GeV} \tag{11.3}$$

$$\mu = 1.64 \pm 0.38(\text{stat}) \pm 0.18(\text{syst}) \tag{11.4}$$

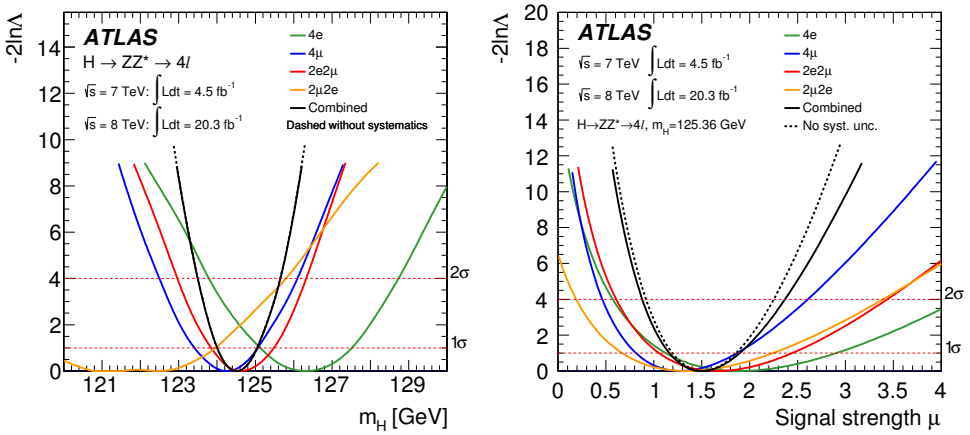

Figure 11.9: Scans of the $-2\ln\Lambda$ as a function of m_{H} (on left) and μ (on right) for the fit to the combined 7 and 8 TeV dataset using the 2D conditional method. Separate scans are shown for each final state as well as the combined scan (in black). The dashed line indicates the combined scan without taking into account any systematic uncertainties.

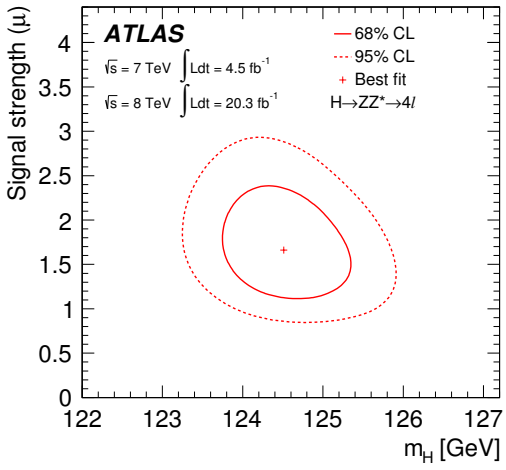

Figure 11.10: The 68% and 95% confidence interval contours in the μ-m_{H} plane for the 2D conditional fit of $m_{4\ell}$ and BDT_{ZZ}.

Chapter 12

Cross Section Measurements

This chapter describes the inclusive and differential fiducial cross section measurements performed in the $H \to 4\ell$ decay channel. Six differential fiducial cross section measurements are reported for variables of interest which describe the Higgs kinematics or are sensitive to the details of the Higgs boson production and decay.

In Chapter 11, a profile likelihood fit of the $m_{4\ell}$ distribution was developed to extract the signal strength and mass measurements. Performing the same technique in the differential analysis would require derivation of signal and background $m_{4\ell}$ templates in each bin of the variables of interest. Given the limited statistical significance expected in the measurement of the current dataset, a simpler counting method in a selected $m_{4\ell}$ window is employed for the differential cross section measurements.

For the inclusive cross section measurements, two methods are employed. The profile likelihood fit of the $m_{4\ell}$ distribution is modified to extract the number of signal events n_{signal} rather than μ, which is then used to compute an inclusive fiducial cross section using Equation 8.4. To facilitate a comparison between the inclusive and differential measurements, an inclusive measurement is also performed using the same counting method within a mass window as the differential measurement.

12.1 Event Counting Method

A likelihood to describe a binned counting experiment for Poisson distributed processes in N_{bins} bins with systematic uncertainties is constructed as follows:

$$\mathcal{L} = \prod_{\text{i}=0}^{N_{bins}} \text{Poisson}(n_{\text{i}}^{\text{obs}}; n_{\text{i}}^{\text{exp}}) \cdot \prod_{j=0}^{N_{\text{syst}}} \text{Gaussian}(\theta_{\text{j}}; 0, 1) \tag{12.1}$$

where $n_{\text{i}}^{\text{obs}}$ is the number of observed data events and the number of expected events, $n_{\text{i}}^{\text{exp}}$, is the sum of the signal (s_{i}) and background (b_{i}) events in the i-th bin:

$$n_{\text{i}}^{\text{exp}} = s_{\text{i}} + \sum_{\text{bkg}} b_{\text{i}} \tag{12.2}$$

The product of the Poisson *pdf*s from each bin is multiplied by Gaussian *pdf* constraints on the Nuisance Parameters (NP) θ_{j}, which are used to incorporate systematic uncertainties into the parameters of the likelihood. The backgrounds are constructed as:

$$b_{\text{i}} = b_{\text{i}}^{nom} \prod_{\text{j}=0}^{N_{\text{syst}}} (1 + \alpha_{\text{i,j}} \cdot \theta_{\text{j}}) \tag{12.3}$$

where b_{i}^{nom} is the nominal background prediction and $\alpha_{\text{i,j}}$ are the relative systematic variations up and down in the yield in i-th bin for the j-th systematic.

The likelihood defined in Eq. 12.1 can be used to extract the differential cross-sections using a profile likelihood ratio method. The profile likelihood ratio is defined as:

$$\Lambda(s_{\text{i}}) = \frac{\mathcal{L}\big(s_{\text{i}}\,,\,\hat{\hat{\vec{\theta}}}(s_{\text{i}})\big)}{\mathcal{L}(\hat{s}_{\text{i}}, \hat{\vec{\theta}})}\,. \tag{12.4}$$

where the single circumflex denotes the unconditional maximum likelihood estimate of a parameter and the double circumflex (*e*.g. $\hat{\hat{\vec{\theta}}}(s_{\text{i}})$) denotes the conditional maximum likelihood estimate (*e*.g. of $\vec{\theta}$) for given fixed values of s_{i}.

The number of signal events in the i-th bin, s_{i}, is formulated as a function of two Parameters Of Interest (POI):

- The observed differential cross section, $(d\sigma/dx)_{i,obs}$:

$$s_{\mathrm{i}} = (d\sigma/dx)_{\mathrm{i,obs}} \cdot \frac{\Delta x_{\mathrm{i}} \times \mathcal{L}_{\mathrm{int}}}{CF_{\mathrm{i}}} \tag{12.5}$$

- The signal strength, μ_{i}:

$$s_{\mathrm{i}} = \mu_{\mathrm{i}} \cdot \frac{(d\sigma/dx)_{\mathrm{i,theory}} \times \Delta x_{\mathrm{i}} \times \mathcal{L}_{\mathrm{int}}}{CF_{\mathrm{i}}} \tag{12.6}$$

where CF_{i} is the correction factor, Δx_{i} is the bin width, and $(d\sigma/dx)_{\mathrm{i,theory}}$ is the theory prediction in the i-th bin. Parameters for the correction factors and theory cross section predictions incorporate systematic uncertainties using the same parameterization as used for the background in Eqn. 12.3.

A `RooFit`[135] based work-space using `HistFactory` [136] is defined including all relevant NP's associated to the sources of systematic uncertainties of relevant parameters, namely the backgrounds, the integrated luminosity and the correction factors. The sources of the uncertainties are described in detail in Chapter 10. Some of the NP's are just normalization uncertainties, such as the uncertainty on the integrated luminosity, while others describe shape uncertainties that are correlated between bins. This approach properly accounts for correlations between systematic uncertainties that impact several components of the likelihood (signal and background, correlations between bins, etc.).

The extraction of a central value for each POI is obtained through minimization of the negative logarithm of the likelihood ratio, multiplied by a factor of 2 ($-2\ln\Lambda$). For each POI, a scan of the $-2\ln\Lambda$ is performed while profiling all other parameters, i.e. they are fitted to the value that minimizes the $-2\ln\Lambda$ for each value of the POI under study. This method is based on the assumption that the statistical observable $-2\ln\Lambda$ behaves as a χ^2 in the asymptotic limit [137]. This assumption may break down in bins with low statistics so a calibration of the uncertainties is performed using pseudo-experiments and the observed cross

sections, which is described in Section 12.4. Because one is only interested in changes in the value of the $-2\ln\Lambda$, one defines $-2\Delta\ln\Lambda$ as the difference in $-2\ln\Lambda$ between a given point and the global minimum of the $-2\ln\Lambda$. The region for which $-2\Delta\ln\Lambda \leq 1$ corresponds to the 68% Confidence Level (CL) interval (assuming one degree of freedom).

Using the Asimov dataset [137], example scans of $-2\Delta\ln\Lambda$ as a function of the μ_i for the p_T distribution are shown in Figure 12.1. The central values are unbiased in all bins and the 68% confidence level intervals are compatible with a simple estimate of the expected uncertainty in each bin based on $S/\sqrt{S+B}$. Furthermore, the scans are performed with and without systematic uncertainties included, showing that the measurements are expected to be systematically dominated.

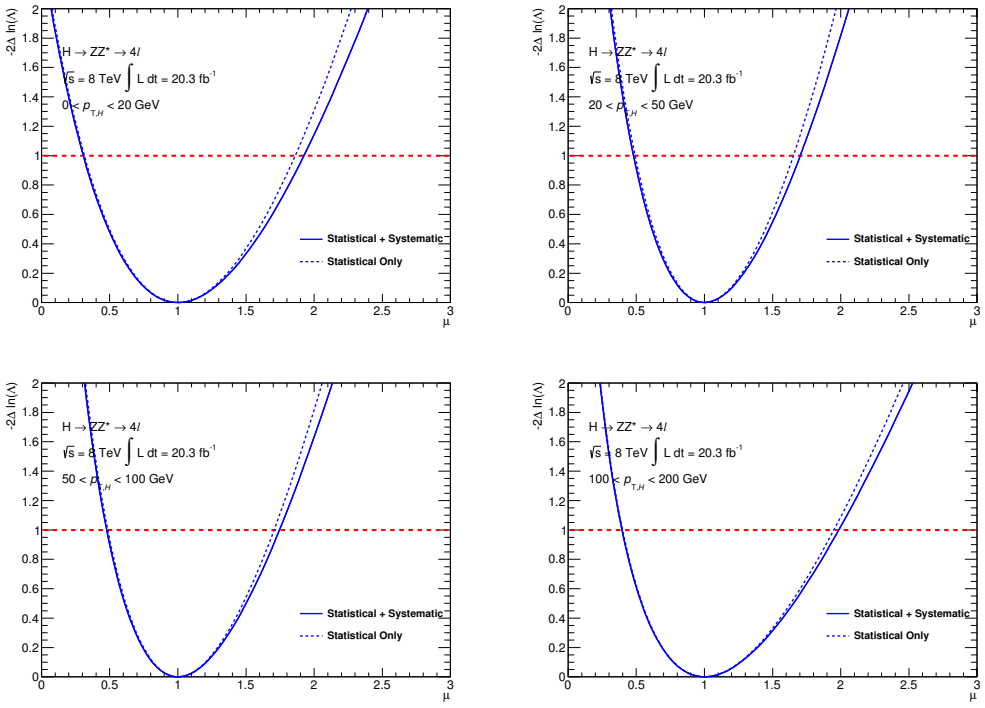

Figure 12.1: Scans of $-2\Delta\ln\Lambda$ as a function of μ_i in all four bins of the p_T distribution using the Asimov data set for a Higgs boson with $m_H = 125$ GeV. The solid line scan includes systematic and statistical uncertainties and the dashed line includes only statistical uncertainties.

Toy pseudo-experiment studies have been performed as an additional cross check. For each pseudo-experiment, the observed number of events in each bin is randomly drawn from a Poisson distribution with mean equal to the expected number of events for that bin. The $n^{\text{sig}}_{\text{i,reco}}$, $(d\sigma/dx)_{\text{i,obs}}$ and μ_{i} are fit using `MINUIT` to minimize the profile likelihood ratio.

A total of $100k$ pseudo-experiments are produced for the p_{T} distribution, injecting the SM expectation for a Higgs boson with $m_{\text{H}} = 125$ GeV. The results are shown separately for each p_{T} bin in Figure 12.2. A small fraction ($\sim 0.6\%$) having fit convergence failures is not included in the results. For all bins, the mean value of μ agrees with one within 0.6% (negligible with respect to the expected statistical error), indicating that the method is unbiased. In bins with a small number of total expected events, the measured values are clearly discretized due to the Poisson nature of the observed number of events. Smearing of these discrete values is observed due to the systematic constraints, which allow bin-to-bin correlations to modify the minimum of the $-2\ln\Lambda$.

The asymptotic assumption may not hold in all bins for the estimation of the 68% CL interval because the statistics may not be sufficient. Therefore, a comparison between the asymptotically derived uncertainties and uncertainties derived using pseudo-experiments is performed and the results are shown in Table 12.1 for the $d\sigma/dp_{\text{T}}$ measurements using the Asimov data set. The differences between the asymptotic uncertainties and the uncertainties derived using pseudo-experiments range from 8-45% depending on the bin. Because these differences are non-negligible, the pseudo-experiment based uncertainties are used to estimate the final uncertainty on the measured cross-sections when significantly different from the asymptotic result. This is done by injecting the observed cross sections from the data into pseudo-experiments and re-calculating the 68% confidence intervals.

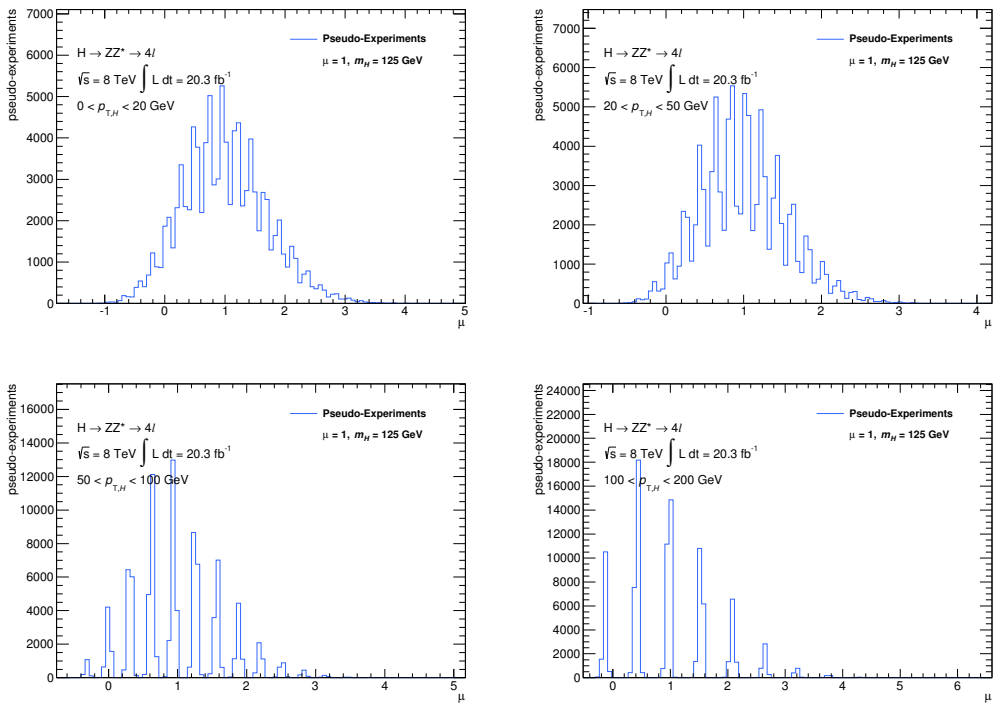

Figure 12.2: Distribution of fit signal strength ($\mu_{\rm i}$) for $100k$ pseudo-experiments with the SM signal injected assuming $m_{\rm H} = 125$ GeV. The individual peaks are due to the small number of expected events, such that discrete nature of the observed Poisson process is observed.

Table 12.1: Comparison of 68% confidence intervals calculated from the $-2\Delta\ln\Lambda$ scan and from the pseudo-experiments for the extraction of $d\sigma/dp_{\rm T}$ using the Asimov data set.

	68% CL Interval on $d\sigma/dp_{\rm T}$ [fb/GeV]	
Bin	$-2\Delta\ln\Lambda$ scan	pseudo-experiments
0	[0.0064, 0.0343]	[0.0055, 0.0322]
1	[0.0075 ,0.0243]	[0.0066, 0.0236]
2	[0.0029, 0.0099]	[0.0019, 0.0092]
3	[0.00081, 0.00296]	[0.00061, 0.00253]

12.2 Background Estimates

Background estimates for the cross section measurements employ the same methods used in the mass and signal strength analysis of Chapter 9. This section presents additional cross-checks evaluated for the specific variables of interest in the differential cross section measurement within the mass window [118,129] GeV.

12.2.1 Irreducible Background

The irreducible background for the differential measurements are estimated using the simulation as described in Section 9.1. To verify that the simulation correctly models the variables of interest, the simulation predictions are checked in a control region. The high mass region, $m_{4\ell} > 190$ GeV, provides a very pure sample of the irreducible backgrounds (less than 1% contamination from reducible backgrounds) and is expected to have around a few hundred events. This region therefore provides a good check of the simulation modeling of the variables of interest. Figure 12.3 shows the control region predictions and data in this control region. Compatibility of the data with the background prediction is quantified using the Kolmogorov-Smirnov Goodness-of-Fit test [138]. Good agreement is observed in all variables of interest.

12.2.2 Reducible Background

The data-driven methods of the reducible background estimates in Section 9.2 are used to estimate directly both the normalization and the shapes of the reducible background in the differential analysis. For the differential measurements, the background estimates are modified to account for the mass window and additional checks of the variables of interest are performed in various control regions. As in Section 9.2, the background estimates are calcu-

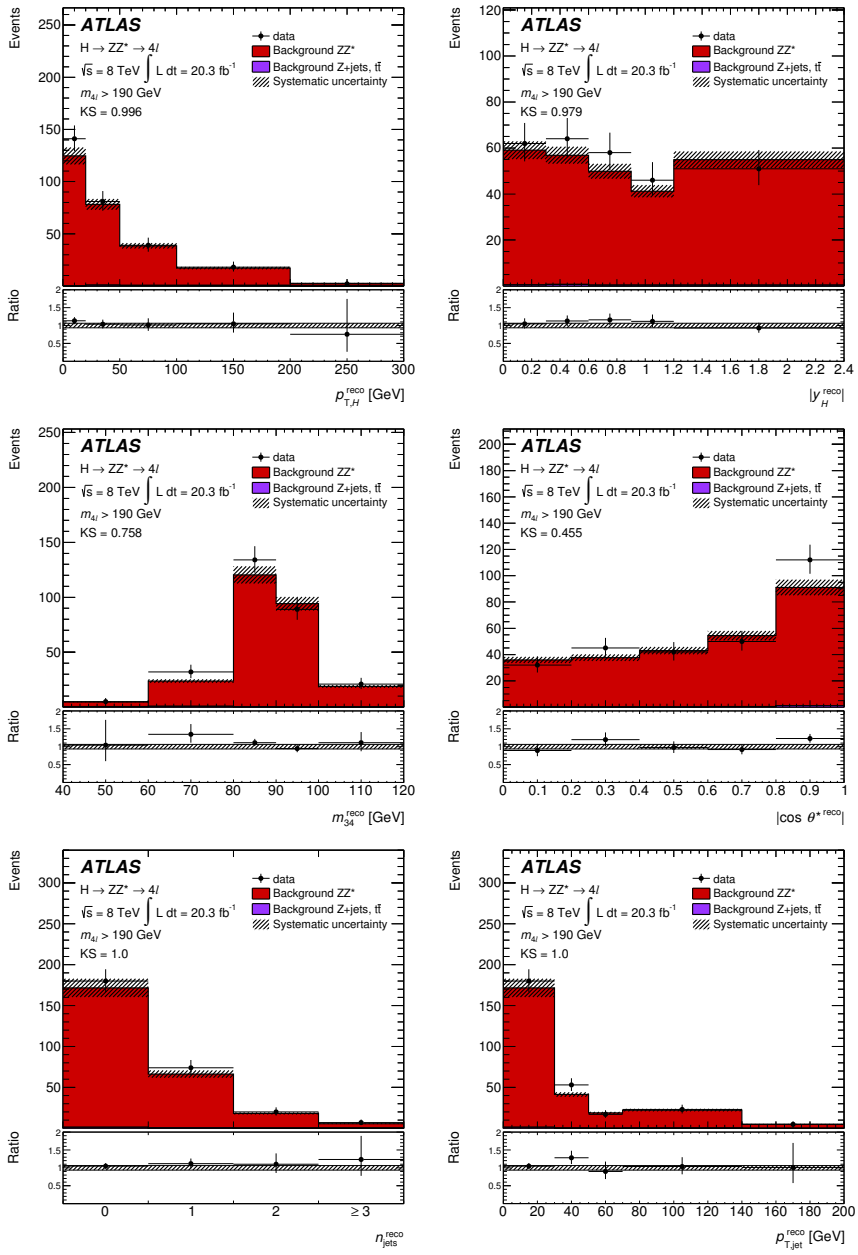

Figure 12.3: MC predictions and data yields in the high mass control region ($m_{4\ell} > 190$ GeV).

lated separately for the $\ell\ell + \mu\mu$ and $\ell\ell + ee$ backgrounds.

12.2.2.1 $\ell\ell + \mu\mu$ Backgrounds

The reducible $\ell\ell + \mu\mu$ backgrounds are estimated using the same methods as in Section 9.2. The normalization of this background is calculated by integrating the $m_{4\ell}$ template in the mass window [118,129] GeV and is found to be 1.39±0.16 events. The shapes of the variables of interest within the mass window are then taken from the simulation using the same methods to derive the $m_{4\ell}$ template. The final estimates and systematic variations are shown in Figure 10.5.

Because the variable shapes are taken from the simulation, a validation of the modeling of the variables of interest within a control region is performed. A comparison of the shapes in the inverted d_0 control region from Section 9.2 is shown in Figure 12.4. For this comparison, the individual background predictions from the simulation have been renormalized according to the scaling factors derived from the fit to the data. Then, both the data and total background prediction are renormalized to unity in order to perform a shape comparison. Good agreement is observed between the data and predicted shapes for all variables.

12.2.2.2 $\ell\ell + ee$ Backgrounds

The reducible $\ell\ell + ee$ backgrounds are estimated using the same methods as in Section 9.2. The normalization of this background is calculated by integrating the $m_{4\ell}$ template in the mass window [118,129] GeV and is found to be 0.78 ± 0.12 events. The nominal shapes of the variables of interest within the mass window are derived using the $3\ell + X$ method. Two systematic variations on this shape are taken using alternative methods. The nominal prediction and systematic variations are shown in Figure 10.6.

The variable shapes are completely data-driven for the $\ell\ell + ee$ reducible backgrounds but

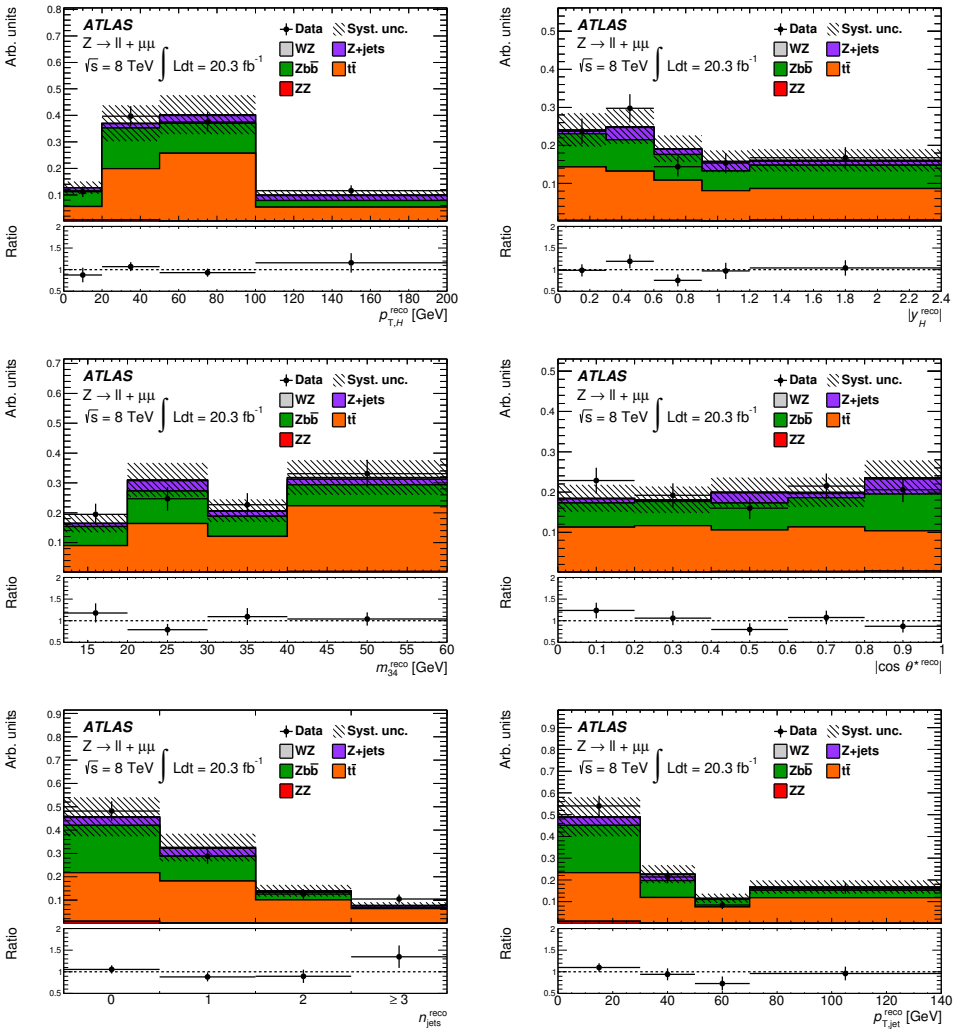

Figure 12.4: Comparison of reconstructed observable shapes in data and simulation for the inverted impact parameter significance control region for the $\ell\ell + \mu\mu$ background for all differential variables of interest. Data-driven normalization scaling factors are applied to the simulated Z+jets and $t\bar{t}$ samples. The shapes are normalized to unity.

a cross-check between the simulation and the data is still performed. A shape comparison is shown for the $3\ell + X$ control region in Figure 12.5. For this comparison, the sum of the background predictions and the observed data have been renormalized to unity for a shape comparison. Good agreement between the predictions and data are observed.

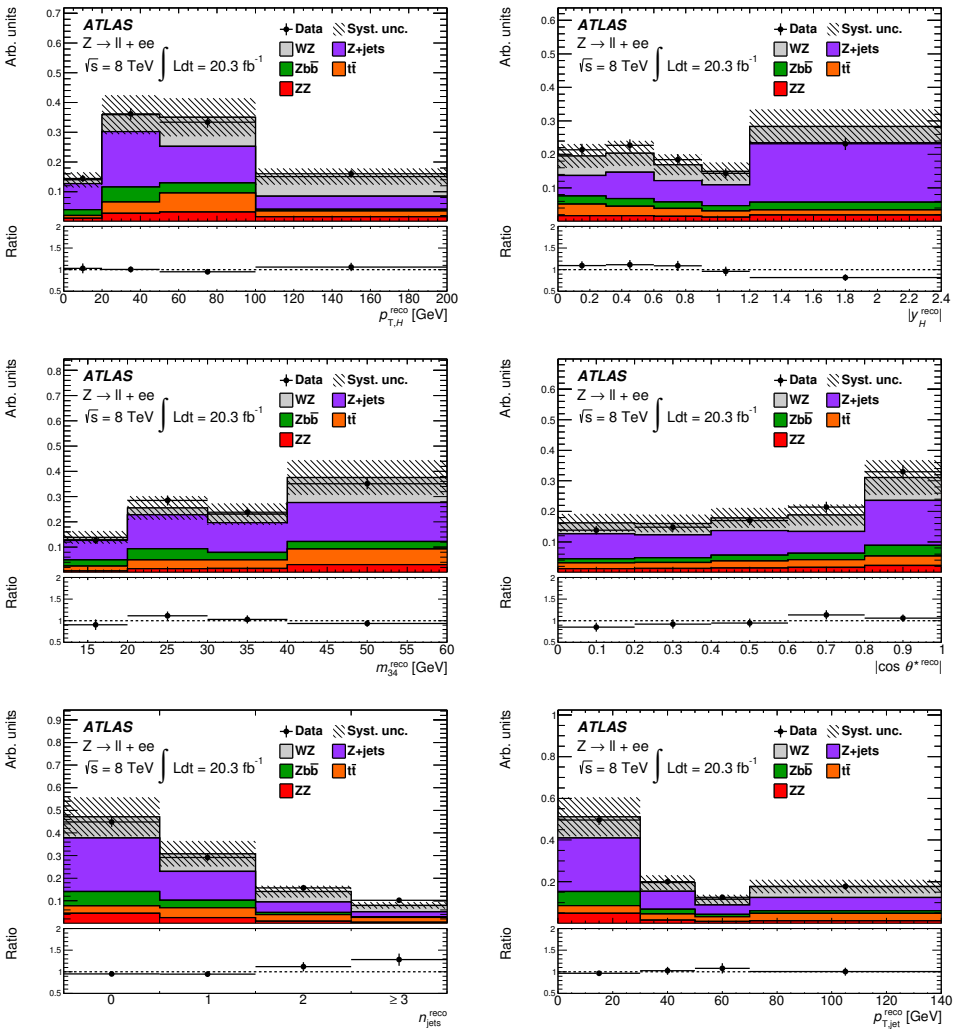

Figure 12.5: Comparison of reconstructed observable shapes in data and simulation for the $3\ell + X$ control region for the $\ell\ell + ee$ backgrounds for all differential variables of interest. The distributions are normalized to unity.

12.3 Signal Predictions

The expected reconstructed signal yields are derived using the Higgs signal samples and cross-sections described in Sec. 6.2.1. A total of 14.07 ± 0.09 (MC stat only) events are expected for a SM Higgs boson with $m_{\mathrm{H}} = 125$ GeV within the mass window for 20.3 fb^{-1} of $\sqrt{s} = 8$ TeV data and the expected contribution from each Higgs production mode is shown in Table 12.2.

Table 12.2: Number of expected reconstructed signal events for each Higgs production mode assuming $m_{\mathrm{H}} = 125$ GeV within the mass window [118, 129] GeV, as obtained with the samples and cross-sections described in Sec. 6.2.1. Errors are from simulation statistics only.

Signal Yield Prediction, $m_{\mathrm{H}} = 125$ GeV 20.3 fb^{-1}@$\sqrt{s} = 8$ TeV, $118 < m_{4\ell} < 129$ GeV	
ggF	12.26 ± 0.09
VBF	1.125 ± 0.008
WH	0.391 ± 0.004
ZH	0.245 ± 0.003
$t\bar{t}H$	0.0569 ± 0.0007
Total	14.07 ± 0.09

The expected distribution of signal events for each of the differential variables is shown in Figure 12.6. Figure 12.7 shows the composition of signal events by Higgs production mode in each differential bin for all variables of interest.

12.4 Results

This section describes the results of the inclusive and differential cross section measurements.

12.4.1 Inclusive Cross Section

The expected number of signal and background events and the observed number of events within the mass window are shown in Table 12.3. A significant excess with respect to the background prediction is observed. The measured number of events in the signal region is $25.1^{+6.3}_{-5.4}(\mathrm{stat})^{+0.6}_{-0.4}(\mathrm{syst})$ events and the correction factor within the mass window is $1.796 \pm 0.007(\mathrm{stat}) \pm 0.054(\mathrm{syst})$. The scan of $-2\Delta\ln\Lambda$ as a function of inclusive cross section is shown in Figure 12.8 using the cross-section extraction procedure described in Section 12.1. The observed fiducial cross section is:

$$\sigma_{\mathrm{fid}} \cdot \mathrm{BR} = 2.21^{+0.56}_{-0.48}(\mathrm{stat})^{+0.14}_{-0.10}(\mathrm{syst})\ \mathrm{fb}$$

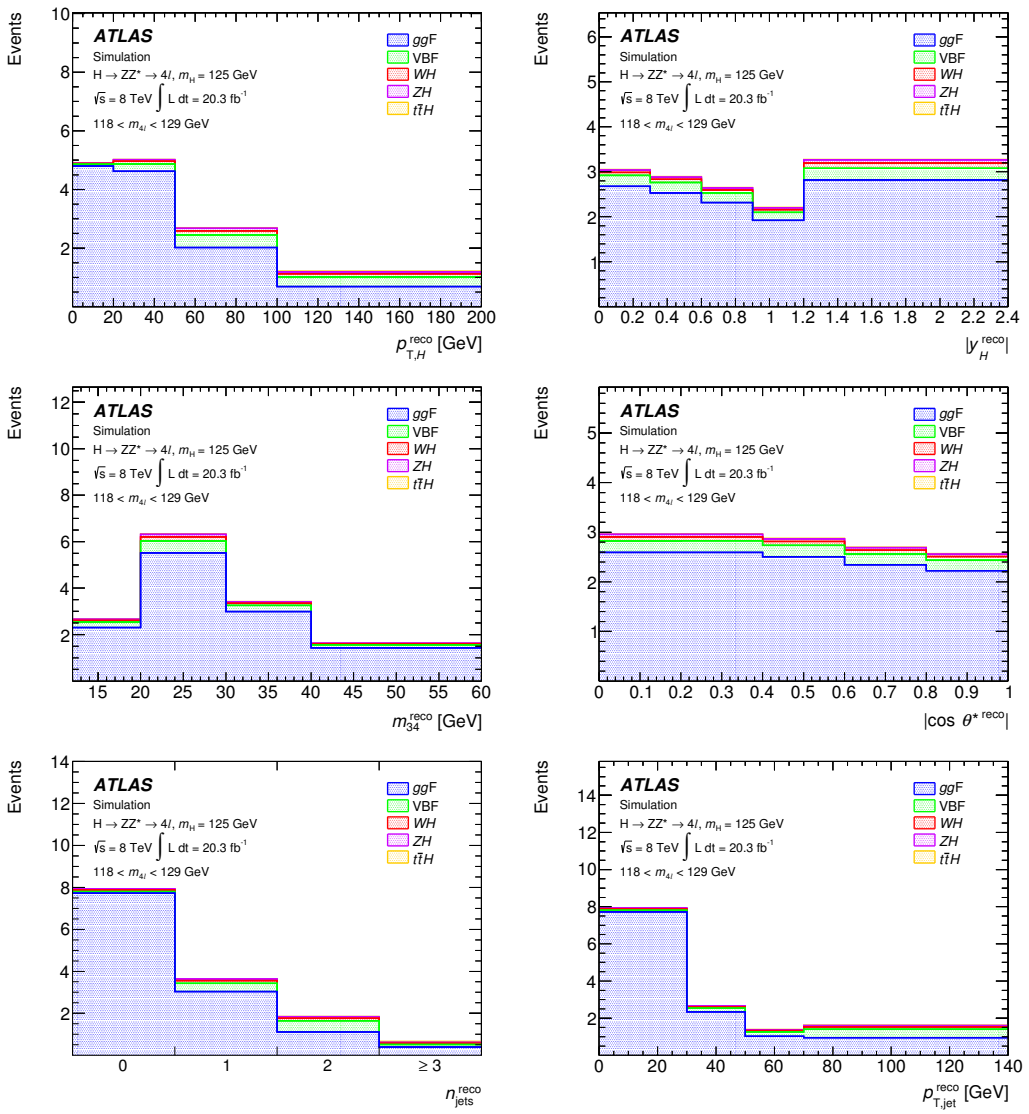

Figure 12.6: Predicted number of reconstructed signal events within the mass window [118,129] GeV in all variables of interest assuming a SM Higgs with $m_{\mathrm{H}} = 125$ GeV. The five production modes are plotted separately, with ggF as the dominant production mode.

Table 12.3: The predicted number of signal and background events and the observed number of events within the mass window [118, 129] GeV for 20.3 fb^{-1} of $\sqrt{s} = 8$ TeV data.

20.3 fb^{-1} at $\sqrt{s} = 8$ TeV, $118 < m_{4\ell} < 129$ GeV				
Signal	Irreducible	Reducible	Total Background	Observed
14.1	6.7	2.4	9.0	34

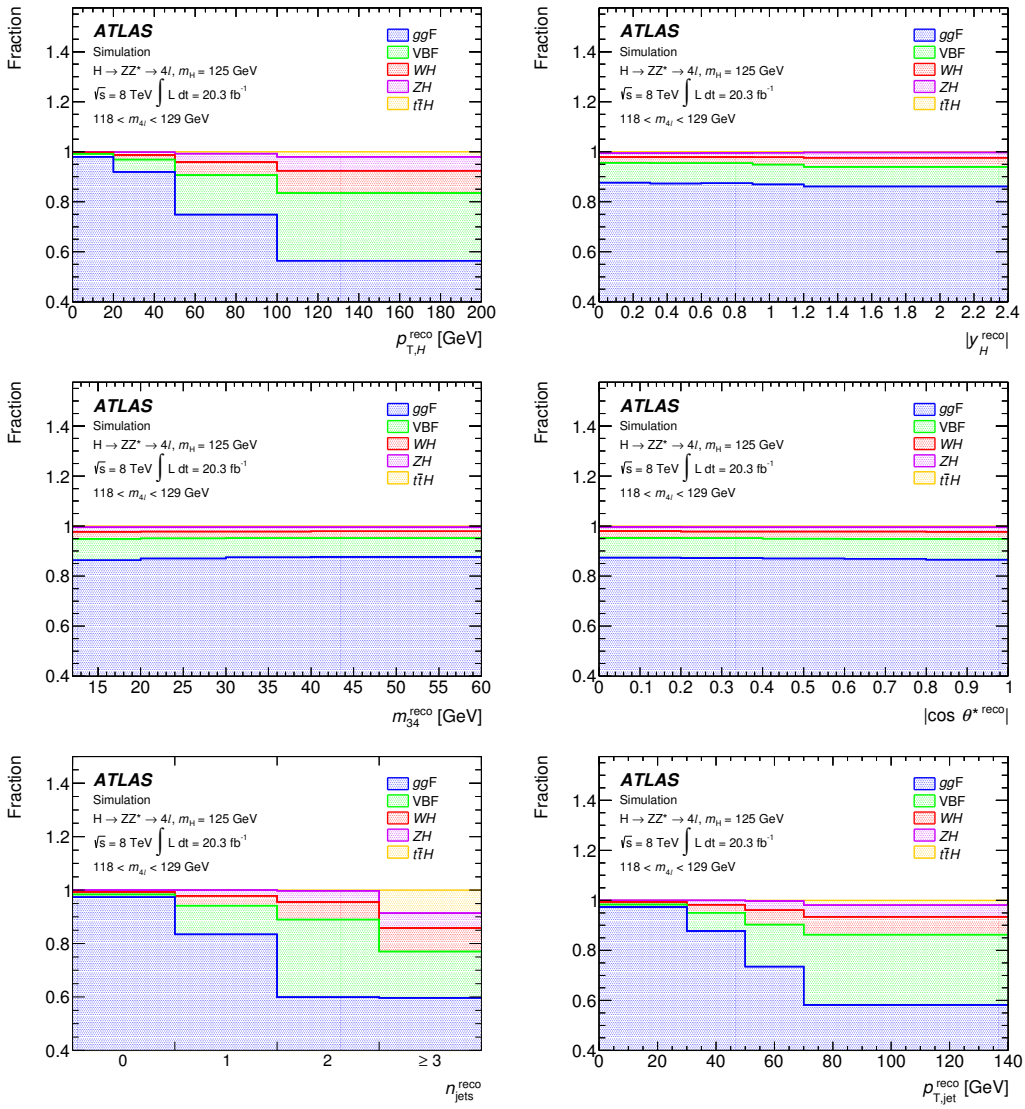

Figure 12.7: Composition of the predicted signal events by production mode within the mass window [118,129] GeV in all variables of interest assuming a SM Higgs with $m_{\mathrm{H}} = 125$ GeV.

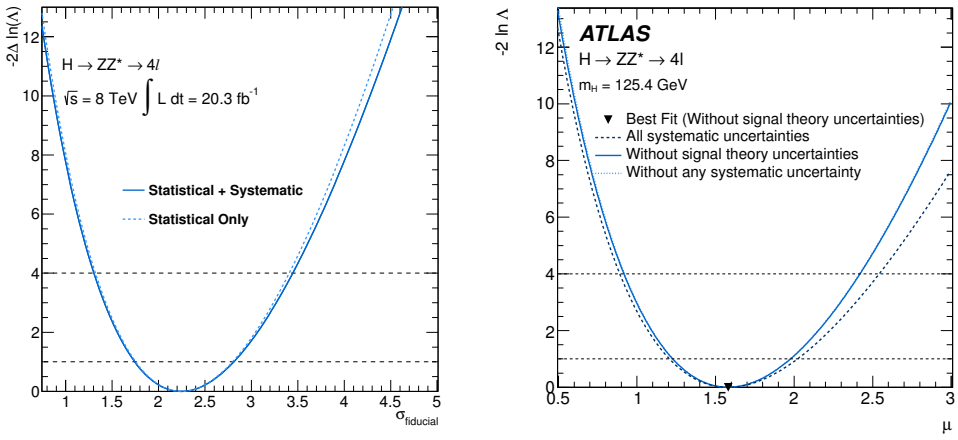

Figure 12.8: Scan of the $-2\Delta\ln\Lambda$ as a function of (left) the inclusive fiducial cross section using the event counting method and (right) the signal strength using the $m_{4\ell}$ fit at the global best estimate of m_{H}, 125.4 GeV.

Similarly, the scan of $-2\Delta\ln\Lambda$ as a function of the signal strength measurement resulting from the fit of the $m_{4\ell}$ distribution at the global best estimate of m_{H}, 125.4 GeV, is shown in Figure 12.8. Because the signal strength measurement includes the signal theory systematic uncertainties, these must be explicitly excluded for the inclusive cross section measurement by fixing the NP in the $m_{4\ell}$ fit (shown in Figure 12.8). Multiplying the measured signal strength by the number of expected signal events at the fitted mass, the number of observed signal events within the mass window [118, 129] GeV is $23.7^{+5.9(\mathrm{stat})+0.6(\mathrm{syst})}_{-5.3(\mathrm{stat})-0.6(\mathrm{syst})}$ events. The estimated correction factor is 1.81 ± 0.01 (stat) ± 0.05 (syst). Using Equation 8.4, the measured fiducial cross section times branching ratio is determined to be:

$$\sigma_{\mathrm{fid}} \cdot \mathrm{BR} = 2.11^{+0.53}_{-0.47}(\mathrm{stat})^{+0.08}_{-0.08}(\mathrm{syst})\ \mathrm{fb}$$

This value is compatible with the event counting method result and is used as the final measurement of the inclusive fiducial cross section.

Table 12.4: Observed differential cross sections for all observables in all bins. Both systematic and statistical uncertainties are included.

Obs.	Units	Bin 1	Bin 2	Bin 3	Bin 4	Bin 5
$p_{\mathrm{T,H}}$	[fb/GeV]	$0.018^{+0.015}_{-0.012}$	$0.034^{+0.013}_{-0.010}$	$0.0108^{+0.0054}_{-0.0043}$	$0.0025^{+0.0019}_{-0.0010}$	-
$\lvert y_H \rvert$	[fb]	$1.27^{+0.82}_{-0.61}$	$0.98^{+0.76}_{-0.54}$	$1.03^{+0.77}_{-0.56}$	$1.97^{+0.95}_{-0.76}$	$0.58^{+0.28}_{-0.23}$
m_{34}	[fb/GeV]	$0.059^{+0.037}_{-0.029}$	$0.105^{+0.038}_{-0.033}$	$0.048^{+0.027}_{-0.020}$	$0.0116^{+0.0092}_{-0.0050}$	-
$\lvert \cos\theta^* \rvert$	[fb]	$2.8^{+1.4}_{-1.1}$	$3.2^{+1.5}_{-1.2}$	$0.98^{+1.03}_{-0.75}$	$2.3^{+1.3}_{-1.0}$	$1.9^{+1.3}_{-1.0}$
n_{jets}	[fb]	$0.88^{+0.41}_{-0.36}$	$0.97^{+0.35}_{-0.28}$	$0.29^{+0.19}_{-0.13}$	$0.065^{+0.099}_{-0.064}$	-
$p_{\mathrm{T,jet}}$	[fb/GeV]	$0.029^{+0.014}_{-0.012}$	$0.028^{+0.014}_{-0.010}$	$0.0148^{+0.0100}_{-0.0069}$	$0.0055^{+0.0032}_{-0.0023}$	-

12.4.2 Differential Cross Sections

The observed distributions of reconstructed events for all differential variables of interest are shown in Figure 12.9. The observed unfolded fiducial cross sections and their 68% CL intervals are extracted as described in Section 12.1 and are shown in Table 12.4. Figure 12.10 shows the measured cross sections in comparison to the three theoretical predictions described in Section 6.2.4.

The compatibility between the measured cross sections and the theoretical predictions is evaluated by computing the difference between the value of $-2\Delta\ln\Lambda$ at the best-fit value and the value obtained by fixing the cross sections in all bins to the ones predicted by theory. Under the asymptotic assumption [137], this statistical observable behaves as a χ^2 with the number of degrees of freedom equal to the number of bins; it is used as a test statistic to compute the p-values quantifying the compatibility between the observed distributions and the predictions which are shown in Table 12.5. No significant deviations from the theoretical predictions is observed.

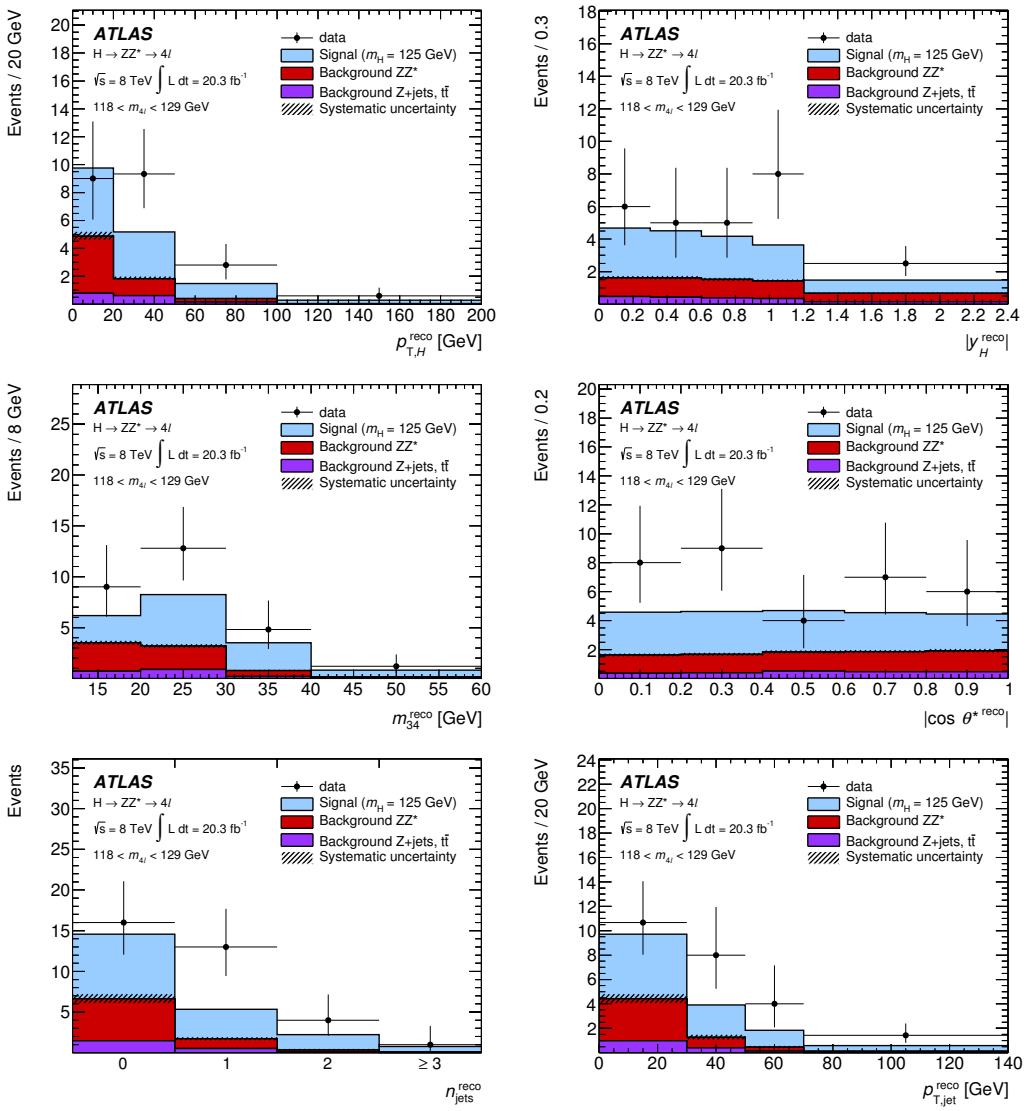

Figure 12.9: Background and signal predictions and data yields in the signal region ($118 < m_{4\ell} < 129$ GeV) for all differential variables of interest using 20.3 fb^{-1} of $\sqrt{s} = 8$ TeV data. The hashes indicate the systematic uncertainty on the total background prediction.

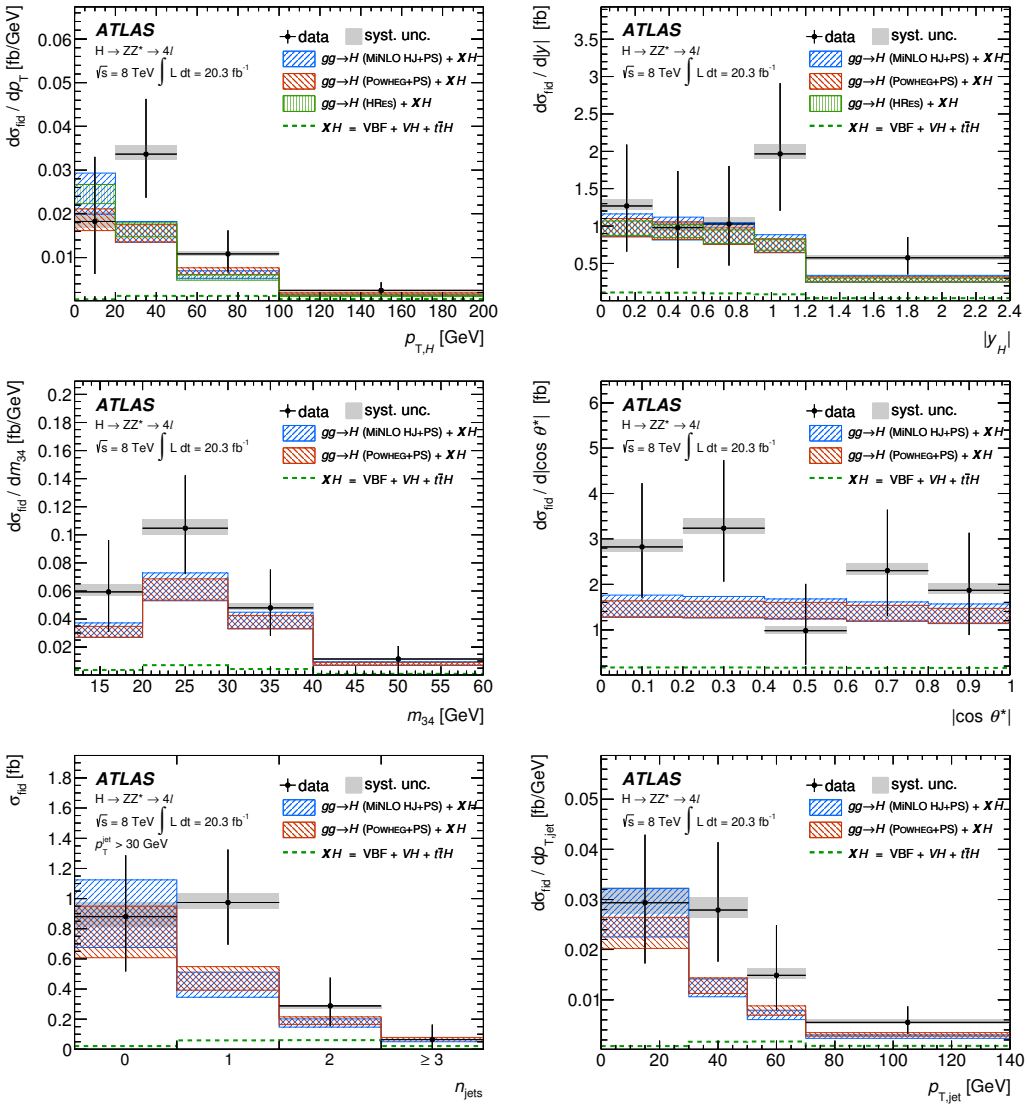

Figure 12.10: Measured differential cross sections ($d\sigma/dx$) in the 20.3 fb^{-1} of $\sqrt{s} = 8$ TeV dataset for all variables.

Table 12.5: Compatibility tests of data with Powheg, Minlo and HRes2 ggF calculations of SM Higgs boson production. The compatibility p-values are obtained, as explained in the text, from the difference between $-2\ln\Lambda$ at the best-fit value and $-2\ln\Lambda$ with the cross sections fixed to the theory computations.

	p-values		
Observable	Powheg	Minlo	HRes2
$p_{\mathrm{T,H}}$	0.30	0.23	0.16
$\lvert y_H \rvert$	0.37	0.45	0.36
m_{34}	0.48	0.60	-
$\lvert \cos\theta^* \rvert$	0.35	0.45	-
n_{jets}	0.37	0.28	-
$p_{\mathrm{T,jet}}$	0.33	0.26	-

Chapter 13

Conclusions

This thesis has described measurements of the mass and signal strength as well as the first differential cross section measurements of the Higgs boson in the $H \to ZZ^* \to 4\ell(\ell = e, \mu)$ decay channel. The measurements were performed using data from the ATLAS detector taken during Run 1 of the LHC, amounting to 20.3 fb^{-1} of $\sqrt{s} = 8$ TeV and 4.5 fb^{-1} of $\sqrt{s} = 7$ TeV proton-proton collisions. The measured value of m_{H} is 124.51$\pm$0.52 (stat)$\pm$0.06 (syst) GeV and the signal strength is measured to be $\mu = 1.64 \pm 0.38$ (stat) ± 0.18 (syst). The inclusive fiducial cross section is measured to be $\sigma_{\mathrm{fid}} \cdot \mathrm{BR} = 2.11^{+0.53}_{-0.47}$ (stat)$^{+0.08}_{-0.08}$ (syst) fb. Differential cross section measurements were performed in six variables of interest which are sensitive to various aspects of Higgs boson production and decay. No significant deviations from the Standard Model predictions were observed in any of these measurements. All of these measurements are currently statistically limited and will benefit from the larger datasets expected during future LHC runs.

Appendix A

Truth Object Selection Studies

To define the detector fiducial acceptance, one must define cuts based on MC truth information to determine the fiducial region. Ideally, these cuts should exclusively select events which could possibly be reconstructed in the detector, such that any difference between the fiducial yield and the reconstruced yield could be attributed to detector efficiency and resolution effects. Therefore, the fiducial cuts are chosen to replicate the lepton kinematic cuts at reconstruction level in order to determine the fiducial acceptance of the detector. Ideally, one chooses cuts based only on final state particles as the particles in the intermediate state are unobservable.

Truth lepton kinematics can be divided into two categories based on whether QED radiation effects are considered or not and are commonly referred to as bare and born, respectively. The bare kinematics are defined as the kinematics of the truth lepton after any QED corrections. The born level kinematics can be defined as the kinematics of the truth lepton at the generator level using the matrix element. One must choose at which truth level the kinematic cuts are applied when defining the fiducial region cuts.

The best description of the detector acceptance will be achieved if the truth lepton kinematics accurately reflect the reconstructed lepton kinematics. Figure A.1 shows the distribution of $p_{T,truth}/p_{T,reco}$ for both born and bare kinematics. The born level kinematics better describe the electron's reconstructed energy because FSR photons which are collinear with the

electron will be included in the electron's EM calorimeter cluster during reconstruction. However, reconstruction level muon momentum is better described by the bare level kinematics because the muon momentum measurement is based on track curvature rather than energy deposition. Because the born level kinematics are attributed to an intermediate state particle (which are technically unobservable), a third category of truth kinematics known as dressed is commonly defined as the sum of the bare truth lepton four-vector and the four-vectors of nearby final state photons. Using dressed kinematics allows one to make cuts using born-like kinematics without relying on the MC intermediate state truth record.

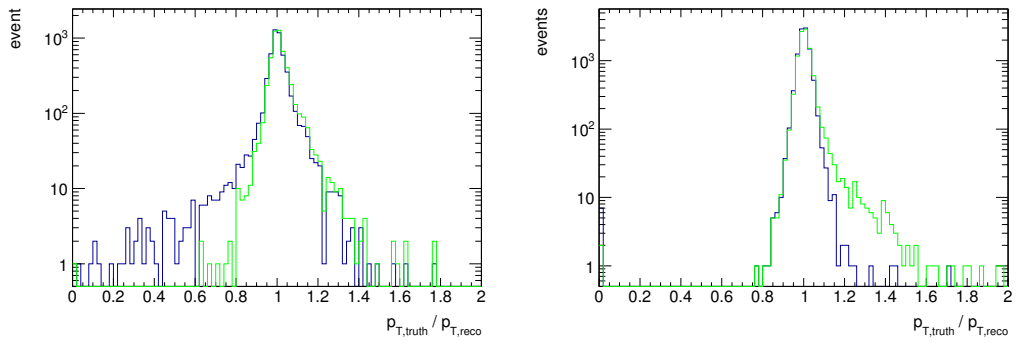

Figure A.1: Distributions of $p_{T,truth}/p_{T,reco}$ using the bare (blue) and born (green) kinematics for (a) electrons and (b) muons. Reconstructed leptons are matched to truth leptons using ΔR matching.

For this particular analysis, one must also decide which leptons to consider when pairing the leptons into a quadruplet. Ideally, one should consider using all final state leptons because this best reflects the pairing as it is done in the reconstruction selection. However, this introduces some model dependence into the measurement because there is no isolation cut applied at the truth level, which leads to the possibility of selecting leptons which are produced during hadronization. Another possibility considered was to select only leptons which are direct decay products of the Higgs in order to simplify the fiducial cuts. This also will introduce model dependence because the mismatch rate (the fraction of events with a selected lepton not from

the Higgs) differs significantly among the various production modes due to the presence or absence of additional prompt leptons in the event.

Three fiducial selections were considered for this analysis:

- **Mixed:** Kinematic cuts are applied at the bare level for muons and at the dressed level for electrons. All final state truth leptons are considered.

- **Born:** Kinematic cuts are applied at the born level for both muons and electrons. All born leptons are considered, but overlap removal is applied using ΔR matching to remove duplicate leptons from the truth record.

- **Higgs:** Kinematic cuts are applied at the born level for both muons and electrons. Only leptons which are direct decay products of the Higgs are considered.

The fiducial yields were evaluated for each of the three selections and are shown in Table A.1. By comparing the event yields before and after the mass window cut, one finds that the Mixed, Born, and Higgs selections have a combined mass window cut efficiency of 94.3%, 97.4%, and 99.8% respectively. This should be compared to the mass window cut efficiency for the reconstruction selection, which is 91.0%. One expects the mass window efficiency to be smaller in the reconstruction as compared to truth level because of detector resolution effects (the mass distribution will be more sharply peaked using the truth kinematics).

Furthermore, one also observes that there are significant differences in the mass window cut efficiency among the production modes for the Mixed and Born selections but not for the Higgs selection. This is expected as the mismatching of leptons (as allowed in the Mixed and Born selections) will move events from inside the mass window to outside the mass window. This difference in pairing causes the fiducial efficiency to be more mode-dependent, resulting in a larger systematic uncertainty on the correction factors from the signal composition systematic

	Selection	ggF	VBF	WH	ZH	$t\bar{t}H$	Combined
Full Mass Range	Mixed	22.19	1.96	0.83	0.50	0.21	25.69
	Born	22.35	1.97	0.83	0.50	0.20	25.85
	Higgs	22.81	2.01	0.81	0.48	0.18	26.29
	Reconstructed	13.76	1.25	0.51	0.33	0.09	15.94
Mass Window [118,129] GeV	Mixed	21.17	1.85	0.68	0.41	0.11	24.22
	Born	22.00	1.93	0.70	0.43	0.12	25.18
	Higgs	22.79	2.00	0.81	0.48	0.17	26.25
	Reconstructed	12.64	1.15	0.40	0.25	0.06	14.5

Table A.1: Fiducial event yields for 20.3 fb^{-1} of $\sqrt{s} = 8$ TeV data with and without the mass window cut.

variations. The Born selection results in a signal composition of 0.1% to 1% and moving from the Born to the Higgs selection increased the systematic uncertainty by a factor of 2x-10x depending on the bin. Similar systematic uncertainties were found with the Mixed selection as compared to the Born.

The Born selection was chosen for this analysis as it simplifies the truth lepton kinematic definition (no need to dress electrons, same selection on electrons and muons) but still retained mismatching effects which are clearly present in the reconstruction selection.

Bibliography

[1] F. Halzen and A. Martin, *Quarks & Leptons: An introductory course in modern particle physics*. John Wiley & Sons, New York, USA, 1984. 2.1

[2] F. Englert and R. Brout, *Broken symmetry and the mass of gauge vector mesons*, Phys. Rev. Lett. **13** (1964) 321–323. 2.1

[3] P. Higgs, *Broken symmetries, massless particles and gauge fields*, Physics Letters **12** (1964) 132–133. 2.1

[4] P. W. Higgs, *Broken symmetries and the masses of gauge bosons*, Phys. Rev. Lett. **13** (1964) 508–509. 2.1

[5] G. S. Guralnik, C. R. Hagen, and T. W. B. Kibble, *Global conservation laws and massless particles*, Phys. Rev. Lett. **13** (1964) 585–587. 2.1

[6] S. Glashow, *Partial symmetries of weak interactions*, Nucl.Phys. **22** (1961) 579–588. 2.1

[7] S. Weinberg, *A model of leptons*, Phys. Rev. Lett. **19** (1967) 1264–1266. 2.1

[8] A. Salam and J. C. Ward, *Electromagnetic and weak interactions*, Phys.Lett. **13** (1964) 168–171. 2.1

[9] A. Salam and J. C. Ward, *Gauge theory of elementary interactions*, Phys. Rev. **136** (1964) B763–B768. 2.1

[10] A. Salam, *Weak and electromagnetic interactions*, Svartholm: Elementary Particle Theory, Proceedings Of The Nobel Symposium Held 1968 At Lerum, Sweden, Stockholm (1968) 367–377. 2.1

[11] R. P. Feynman, *The Behavior of Hadron Collisions at Extreme Energies*, in *Special Relativity and Quantum Theory*, M. Noz and Y. Kim, eds., vol. 33 of *Fundamental Theories of Physics*, pp. 289–304. Springer Netherlands, 1988. 2.2

[12] J. D. Bjorken and E. A. Paschos, *Inelastic Electron-Proton and γ-Proton Scattering and the Structure of the Nucleon*, Phys. Rev. **185** (1969) 1975–1982. 2.2

[13] D. J. Gross and F. Wilczek, *Ultraviolet behavior of non-abelian gauge theories*, Phys. Rev. Lett. **30** (1973) 1343–1346. 2.2

[14] V. Gribov and L. Lipatov, *Deep inelastic e-p scattering in perturbation theory*, Sov.J.Nucl.Phys. **15** (1972) 438–450. 2.2

[15] G. Altarelli and G. Parisi, *Asymptotic freedom in parton language*, Nucl.Phys.B **126** (1977) 298. 2.2

[16] Y. L. Dokshitzer, *Calculation of the structure functions for deep inelastic scattering and e^+e^- annihilation by perturbation theory in quantum chromodynamics.*, Sov.Phys.JETP **46** (1977) 641–653. 2.2

[17] H.-L. Lai et al., *New parton distributions for collider physics*, Phys. Rev. **D** 82 (2010) 074024, arXiv:1007.2241 [hep-ph]. 2.2, 6.2.1

[18] A. D. Martin, W. J. Stirling, R. S. Thorne, and G. Watt, *Parton distributions for the LHC*, Eur. Phys. J. **C** 63 (2009) 189–285, arXiv:0901.0002 [hep-ph]. 2.2, 6.2.1

[19] R. D. Ball et al., *Impact of heavy quark masses on parton distributions and LHC phenomenology*, Nucl. Phys. **B** 849 (2011) 296–363, arXiv:1101.1300 [hep-ph]. 2.2, 6.2.1

[20] LEP Working Group for Higgs Boson Searches, ALEPH Collaboration, DELPHI Collaboration, L3 Collaboration, OPAL Collaboration, *Search for the standard model Higgs boson at LEP*, Phys.Lett.B **565** (2003) 61–75, arXiv:hep-ex/0306033 [hep-ex]. 2.3

[21] CDF Collaboration, T. Aaltonen et al., *Combined search for the standard model Higgs boson decaying to a bb pair using the full CDF data set*, Phys.Rev.Lett. **109** (2012) 111802, arXiv:1207.1707 [hep-ex]. 2.3

[22] D0 Collaboration, V. M. Abazov et al., *Combined search for the standard model Higgs boson decaying to $b\bar{b}$ using the D0 Run II data set*, Phys.Rev.Lett. **109** (2012) 121802, arXiv:1207.6631 [hep-ex]. 2.3

[23] CDF and D0 Collaboration, *Evidence for a particle produced in association with weak bosons and decaying to a bottom-antibottom quark pair in Higgs boson searches at the Tevatron*, Phys.Rev.Lett. **109** (2012) 071804, arXiv:1207.6436 [hep-ex]. 2.3

[24] ALEPH and CDF and D0 and DELPHI and L3 and OPAL and SLD Collaboration, J. Alcaraz, *Precision Electroweak Measurements and Constraints on the Standard Model*, arXiv:0911.2604 [hep-ex]. 2.3, 2.2

[25] LHC Higgs Cross Section Working Group, S. Dittmaier, C. Mariotti, G. Passarino, and R. Tanaka (Eds.), *Handbook of LHC Higgs Cross Sections: 1. Inclusive Observables*, CERN-2011-002 (CERN, Geneva, 2011) , arXiv:1101.0593 [hep-ph]. 2.4, 6.2.1, 6.1, 6.2.4, 10.1.2.3

[26] ATLAS Collaboration, *Observation of a new particle in the search for the Standard Model Higgs boson with the ATLAS detector at the LHC*, Physics Letters B **7**16 (2012) no. 1, 1 – 29. 2.3, 2.5, 2.6

[27] CMS Collaboration, *Observation of a new boson at a mass of 125 GeV with the CMS experiment at the LHC*, Physics Letters B **7**16 (2012) no. 1, 30 – 61. 2.3

[28] ATLAS Collaboration, *Measurements of Higgs boson production and couplings in diboson final states with the ATLAS detector at the LHC*, Phys.Lett. **B**726 (2013) 88–119, arXiv:1307.1427 [hep-ex]. 2.3, 2.7, 5, 7, 7.4.3.2, 9.2

[29] ATLAS Collaboration, *Measurement of Higgs boson production in the diphoton decay channel in pp collisions at center-of-mass energies of 7 and 8 TeV with the ATLAS detector*, arXiv:1408.7084 [hep-ex]. 2.3

[30] C. N. Yang, *Selection Rules for the Dematerialization of a Particle into Two Photons*, Phys. Rev. **77** (1950) 242–245. 2.3

[31] L. D. Landau, *On the angular momentum of a system of two photons*, Dokl. Akad. Nauk SSSR **6**0 (1948) 207. 2.3

[32] ATLAS Collaboration, *Evidence for the spin-0 nature of the Higgs boson using ATLAS data*, Phys.Lett. **B**726 (2013) 120–144, arXiv:1307.1432 [hep-ex]. 2.3, 5

[33] ATLAS Collaboration, *Measurements of fiducial and differential cross sections for Higgs boson production in the diphoton decay channel at* $\sqrt{s} = 8$ *TeV with ATLAS*, arXiv:1407.4222 [hep-ex]. 2.3

[34] ATLAS Collaboration Collaboration, G. Aad et al., *Search for* $H \to \gamma\gamma$ *produced in association with top quarks and constraints on the Yukawa coupling between the top quark and the Higgs boson using data taken at 7 TeV and 8 TeV with the ATLAS detector*, arXiv:1409.3122 [hep-ex]. 2.7, 2.3

[35] ATLAS Collaboration, *Evidence for Higgs Boson Decays to the* $\tau^+\tau^-$ *Final State with the ATLAS Detector*, ATLAS-CONF-2013-108, Nov, 2013. 2.3

[36] ATLAS Collaboration, *Search for the* $b\bar{b}$ *decay of the Standard Model Higgs boson in associated* $(W/Z)H$ *production with the ATLAS detector*, arXiv:1409.6212 [hep-ex]. 2.3

[37] CMS Collaboration, *Search for the standard model Higgs boson produced in association with a W or a Z boson and decaying to bottom quarks*, Phys. Rev. D **8**9 (2014) 012003. 2.3

[38] ATLAS Collaboration, *Search for the Standard Model Higgs boson decay to* $\mu^+\mu^-$ *with the ATLAS detector*, Physics Letters B **7**38 (2014) no. 0, 68 – 86, arXiv:1406.7663 [hep-ex]. 2.3

[39] ATLAS Collaboration, *Search For Higgs Boson Pair Production in the* $\gamma\gamma b\bar{b}$ *Final State using pp Collision Data at* $\sqrt{s} = 8$ *TeV from the ATLAS Detector*, arXiv:1406.5053 [hep-ex]. 2.3

[40] ATLAS Collaboration, *Search for Higgs boson decays to a photon and a Z boson in pp collisions at* $\sqrt{s}$*=7 and 8 TeV with the ATLAS detector*, Phys.Lett. **B**732 (2014) 8–27, arXiv:1402.3051 [hep-ex]. 2.3

[41] ATLAS Collaboration, *Search for Invisible Decays of a Higgs Boson Produced in Association with a Z Boson in ATLAS*, Phys.Rev.Lett. **1**12 (2014) 201802, arXiv:1402.3244 [hep-ex]. 2.3

[42] S. Alioli, P. Nason, C. Oleari, and E. Re, *NLO Higgs boson production via gluon fusion matched with shower in POWHEG*, JHEP **0**904 (2009) 002, arXiv:0812.0578 [hep-ph]. 2.3.1, 6.2.1

[43] K. Hamilton, P. Nason, and G. Zanderighi, *MINLO: Multi-Scale Improved NLO*, JHEP **1**210 (2012) 155, arXiv:1206.3572 [hep-ph]. 2.3.1

[44] D. de Florian, G. Ferrera, M. Grazzini, and D. Tommasini, *Higgs boson production at the LHC: transverse momentum resummation effects in the H->2gamma, H->WW->lnu lnu and H->ZZ->4l decay modes*, JHEP **1**206 (2012) 132, arXiv:1203.6321 [hep-ph]. 2.3.1, 7.4.3.1

[45] M. Grazzini and H. Sargsyan, *Heavy-quark mass effects in Higgs boson production at the LHC*, JHEP **1**309 (2013) 129, arXiv:1306.4581 [hep-ph]. 2.3.1, 7.4.3.1

[46] T. Sjostrand, S. Mrenna, and P. Skands, *PYTHIA 6.4 physics and manual*, JHEP **05** (2006) 026, arXiv:0603175 [hep-ph]. 2.3.1, 6.2.1

[47] M. Cacciari, G. P. Salam, and G. Soyez, *FastJet User Manual*, Eur.Phys.J. **C**72 (2012) 1896, arXiv:1111.6097 [hep-ph]. 2.3.1

[48] P. Nason and C. Oleari, *NLO Higgs boson production via vector-boson fusion matched with shower in POWHEG*, JHEP **0**2 (2010) 037, arXiv:0911.5299 [hep-ph]. 2.3.1, 6.2.1

[49] Particle Data Group Collaboration, J. Beringer et al., *Review of Particle Physics (RPP)*, Phys.Rev. **D**86 (2012) 010001. 2.4.1, 2.4.2, 2.4.4, 2.5.2

[50] R. Davis, D. S. Harmer, and K. C. Hoffman, *Search for Neutrinos from the Sun*, Phys. Rev. Lett. **2**0 (1968) 1205–1209. http://link.aps.org/doi/10.1103/PhysRevLett.20.1205. 2.4.1

[51] Kamiokande Collaboration, K. S. Hirata et al., *Experimental study of the atmospheric neutrino flux*, Phys. Lett. **B**205 (1988) 416. 2.4.1

[52] Super-Kamiokande Collaboration, *Evidence for oscillation of atmospheric neutrinos*, Phys. Rev. Lett. **81** (1998) 1562–1567. 2.4.1

[53] SNO Collaboration, *Measurement of the rate of $\nu_e + d \to p + p + e^-$ interactions produced by ^8B solar neutrinos at the Sudbury Neutrino Observatory*, Phys. Rev. Lett. **87** (2001) 071301. 2.4.1

[54] SNO Collaboration, *Direct evidence for neutrino flavor transformation from neutral current interactions in the Sudbury Neutrino Observatory*, Phys.Rev.Lett. **89** (2002) 011301, arXiv:nucl-ex/0204008 [nucl-ex]. 2.4.1

[55] A. Sakharov, *Violation of CP Invariance, c Asymmetry, and Baryon Asymmetry of the Universe*, Pisma Zh.Eksp.Teor.Fiz. **5** (1967) 32–35. 2.4.2

[56] Planck Collaboration Collaboration, P. Ade et al., *Planck 2013 results. I. Overview of products and scientific results*, arXiv:1303.5062 [astro-ph.CO]. 2.4.3

[57] S. P. Martin, *A Supersymmetry primer*, Adv.Ser.Direct.High Energy Phys. **2**1 (2010) 1–153, arXiv:hep-ph/9709356 [hep-ph]. 2.5.1

[58] G. Servant and T. M. Tait, *Is the lightest Kaluza-Klein particle a viable dark matter candidate?*, Nucl.Phys. **B**650 (2003) 391–419, arXiv:hep-ph/0206071 [hep-ph]. 2.5.2

[59] T. Kakuda, K. Nishiwaki, K.-y. Oda, and R. Watanabe, *Universal extra dimensions after Higgs discovery*, Phys.Rev. **D**88 (2013) 035007, arXiv:1305.1686 [hep-ph]. 2.5.2

[60] ATLAS Collaboration, *The ATLAS Experiment at the CERN Large Hadron Collider*, Journal of Instrumentation **3** (2008) no. 08, S08003. http://stacks.iop.org/1748-0221/3/i=08/a=S08003. 3, 3.1, 3.2, 3.3, 3.1.1, 3.1.2, 3.2, 3.3, 3.6, 3.3

[61] ATLAS TRT Collaboration, *Calibration of the ATLAS Transition Radiation Tracker*, ATLAS-CONF-2011-006, Feb, 2011. 3.1.3.2

[62] ATLAS TRT Collaboration, *Particle identification performance of the ATLAS Transition Radiation Tracker*, ATLAS-CONF-2011-128, Sep, 2011. 3.1.3.3, 3.5

[63] ATLAS Collaboration, *Performance of the ATLAS Silicon Pattern Recognition Algorithm in Data and Simulation at* $\sqrt{s} = 7$ *TeV*, ATLAS-CONF-2010-072, Jul, 2010. 4.1

[64] R. Fruhwirth, *Application of Kalman filtering to track and vertex fitting*, Nucl.Instrum.Meth. **A**262 (1987) 444–450. 4.1

[65] ATLAS Collaboration, *Alignment of the ATLAS Inner Detector Tracking System with 2010 LHC proton-proton collisions at* $\sqrt{s} = 7$ *TeV*, ATLAS-CONF-2011-012, Mar, 2011. 4.2.1, 4.1

[66] ATLAS Collaboration, *Study of alignment-related systematic effects on the ATLAS Inner Detector tracking*, ATLAS-CONF-2012-141, Oct, 2012. 4.4

[67] ATLAS Collaboration, *Electron and photon energy calibration with the ATLAS detector using LHC Run 1 data*, Eur.Phys.J. **C**74 (2014) no. 10, 3071, arXiv:1407.5063 [hep-ex]. 4.4.3, 6.2.3, 10.1.2.1

[68] ATLAS Collaboration, *A measurement of the total* $W^{\pm}$ *and* $Z/\gamma*$ *cross sections in the* e *and* μ *decay channels and of their ratios in pp collisions at* $\sqrt{s} = 7$ *TeV with the ATLAS detector*, ATLAS-CONF-2011-041, 2011. 4.4.3

[69] ATLAS Collaboration Collaboration, *Fiducial and differential cross sections of Higgs boson production measured in the four-lepton decay channel in pp collisions at* $\sqrt{s}$*=8 TeV with the ATLAS detector*, Phys.Lett. **B**738 (2014) 234–253, arXiv:1408.3226 [hep-ex]. 5

[70] ATLAS Collaboration, *The ATLAS Simulation Infrastructure*, Eur.Phys.J.C **70** (2010) , arXiv:1005.4568 [physics.ins-det]. 6.2

[71] GEANT4 Collaboration, S. Agostinelli et al., *GEANT4: A Simulation toolkit*, Nucl.Instrum.Meth. **A**506 (2003) 250–303. 6.2

[72] P. Golonka and Z. Was, *PHOTOS Monte Carlo: A Precision tool for QED corrections in Z and W decays*, Eur.Phys.J. C **45** (2006) 97–107, arXiv:hep-ph/0506026 [hep-ph]. 6.2.1

[73] G. Bozzi, S. Catani, D. de Florian, and M. Grazzini, *Transverse-momentum resummation and the spectrum of the Higgs boson at the LHC*, Nucl. Phys. **B** 737 (2006) 73–120. 6.2.1, 7.4.3.1

[74] LHC Higgs Cross Section Working Group, S. Dittmaier, C. Mariotti, G. Passarino, and R. Tanaka (Eds.), *Handbook of LHC Higgs Cross Sections: 2. Differential Distributions*, CERN-2012-002 (CERN, Geneva, 2012) , arXiv:1201.3084 [hep-ph]. 6.2.1, 6.2.2, 7.4.3.1, 10.1.2.3

[75] LHC Higgs Cross Section Working Group, S. Dittmaier, C. Mariotti, G. Passarino, and R. Tanaka (Eds.), *Handbook of LHC Higgs Cross Sections: 3. Higgs Properties*, arXiv:1307.1347 [hep-ph]. 6.2.1, 10.1.2.3

[76] A. Djouadi, M. Spira, and P. M. Zerwas, *Production of Higgs bosons in proton colliders: QCD corrections*, Phys. Lett. **B** 264 (1991) 440–446. 6.2.1

[77] S. Dawson, *Radiative corrections to Higgs boson production*, Nucl. Phys. **B** 359 (1991) 283–300. 6.2.1

[78] M. Spira, A. Djouadi, D. Graudenz, and P. M. Zerwas, *Higgs boson production at the LHC*, Nucl. Phys. **B** 453 (1995) 17–82, arXiv:hep-ph/9504378. 6.2.1

[79] R. V. Harlander and W. B. Kilgore, *Next-to-next-to-leading order Higgs production at hadron colliders*, Phys. Rev. Lett. **88** (2002) 201801, arXiv:hep-ph/0201206. 6.2.1

[80] C. Anastasiou and K. Melnikov, *Higgs boson production at hadron colliders in NNLO QCD*, Nucl. Phys. **B** 646 (2002) 220–256, arXiv:hep-ph/0207004. 6.2.1

[81] V. Ravindran, J. Smith, and W. L. van Neerven, *NNLO corrections to the total cross section for Higgs boson production in hadron hadron collisions*, Nucl. Phys. **B** 665 (2003) 325–366, arXiv:hep-ph/0302135. 6.2.1

[82] U. Aglietti, R. Bonciani, G. Degrassi, and A. Vicini, *Two-loop light fermion contribution to Higgs production and decays*, Phys. Lett. **B** 595 (2004) 432–441, arXiv:hep-ph/0404071. 6.2.1

[83] S. Actis, G. Passarino, C. Sturm, and S. Uccirati, *NLO Electroweak Corrections to Higgs Boson Production at Hadron Colliders*, Phys. Lett. **B** 670 (2008) 12–17, arXiv:0809.1301 [hep-ph]. 6.2.1

[84] M. Ciccolini, A. Denner, and S. Dittmaier, *Strong and electroweak corrections to the production of Higgs+2jets via weak interactions at the LHC*, Phys. Rev. Lett. **99** (2007) 161803, arXiv:0707.0381 [hep-ph]. 6.2.1

[85] M. Ciccolini, A. Denner, and S. Dittmaier, *Electroweak and QCD corrections to Higgs production via vector-boson fusion at the LHC*, Phys. Rev. **D** 77 (2008) 013002, arXiv:0710.4749 [hep-ph]. 6.2.1

[86] K. Arnold et al., *VBFNLO: A parton level Monte Carlo for processes with electroweak bosons*, Comput. Phys. Commun. **180** (2009) 1661–1670, arXiv:0811.4559 [hep-ph]. 6.2.1

[87] T. Han and S. Willenbrock, *QCD correction to the $p\ p \to W\ H$ and $Z\ H$ total cross-sections*, Phys. Lett. **B** 273 (1991) 167–172. 6.2.1

[88] O. Brein, A. Djouadi, and R. Harlander, *NNLO QCD corrections to the Higgs-strahlung processes at hadron colliders*, Phys. Lett. **B** 579 (2004) 149–156, arXiv:hep-ph/0307206. 6.2.1

[89] M. L. Ciccolini, S. Dittmaier, and M. Kramer, *Electroweak radiative corrections to associated WH and ZH production at hadron colliders*, Phys. Rev. **D** 68 (2003) 073003, arXiv:hep-ph/0306234. 6.2.1

[90] Z. Kunszt, *Associated production of heavy Higgs boson with top quarks*, Nucl. Phys. **B**247 (1984) 339. 6.2.1

[91] W. Beenakker et al., *Higgs Radiation Off Top Quarks at the Tevatron and the LHC*, Phys. Rev. Lett. **8**7 (2001) 201805. 6.2.1

[92] W. Beenakker et al., *NLO QCD corrections to t anti-t H production in hadron collisions.* , Nucl. Phys. **B** 653 (2003) 151–203, arXiv:hep-ph/0211352. 6.2.1

[93] S. Dawson, L. H. Orr, L. Reina, and D. Wackeroth, *Next-to-leading order QCD corrections to $pp \to t\bar{t}h$ at the CERN Large Hadron Collider*, Phys. Rev. **D**67 (2003) 071503. 6.2.1

[94] S. Dawson, C. Jackson, L. H. Orr, L. Reina, and D. Wackeroth, *Associated Higgs production with top quarks at the Large Hadron Collider: NLO QCD corrections*, Phys. Rev. **D** 68 (2003) 034022, arXiv:hep-ph/0305087. 6.2.1

[95] A. Bredenstein, A. Denner, S. Dittmaier, and M. M. Weber, *Precise predictions for the Higgs-boson decay $H \to WW/ZZ \to 4leptons$*, Phys. Rev. **D** 74 (2006) 013004, arXiv:hep-ph/0604011. 6.2.1

[96] A. Bredenstein, A. Denner, S. Dittmaier, and M. M. Weber, *Precision calculations for $H \to WW/ZZ \to 4$ fermions with PROPHECY4f*, arXiv:0708.4123 [hep-ph]. 6.2.1

[97] A. Bredenstein, A. Denner, S. Dittmaier, and M. M. Weber, *Radiative corrections to the semileptonic and hadronic Higgs-boson decays $H \to WW/ZZ \to 4$ fermions*, JHEP **0**2 (2007) 080, arXiv:hep-ph/0611234. 6.2.1

[98] A. Ghinculov, *Two loop heavy Higgs correction to Higgs decay into vector bosons*, Nucl.Phys. **B**455 (1995) 21–38, arXiv:hep-ph/9507240 [hep-ph]. 6.2.1

[99] A. Frink, B. A. Kniehl, D. Kreimer, and K. Riesselmann, *Heavy Higgs lifetime at two loops*, Phys.Rev. **D**54 (1996) 4548–4560, arXiv:hep-ph/9606310 [hep-ph]. 6.2.1

[100] A. Djouadi, J. Kalinowski, and M. Spira, *HDECAY: A Program for Higgs boson decays in the standard model and its supersymmetric extension*, Comput.Phys.Commun. **1**08 (1998) 56–74, arXiv:hep-ph/9704448 [hep-ph]. 6.2.1

[101] A. Djouadi, J. Kalinowski, M. Muhlleitner, and M. Spira, *An update of the program HDECAY, in The Les Houches 2009 workshop on TeV colliders: The Tools and Monte Carlo working group Summary Report*, arXiv:1003.1643 [hep-ph]. 6.2.1

[102] M. Botje et al., *The PDF4LHC working group interim recommendations*, 2011. arXiv:1101.0538 [hep-ph]. 6.2.1

[103] T. Melia, P. Nason, R. Rontsch, and G. Zanderighi, *W^+W^-, WZ and ZZ production in the POWHEG BOX*, JHEP **1**111 (2011) 078, arXiv:1107.5051 [hep-ph]. 6.2.2

[104] T. Binoth, N. Kauer, and P. Mertsch, *Gluon-induced QCD corrections to $pp \to ZZ \to \ell\bar{\ell}\ell'\bar{\ell}'$*, arXiv:0807.0024 [hep-ph]. 6.2.2

[105] N. Kauer and G. Passarino, *Inadequacy of zero-width approximation for a light Higgs boson signal*, JHEP **1**208 (2012) 116, arXiv:1206.4803 [hep-ph]. 6.2.2, 9.1

[106] M. L. Mangano, M. Moretti, F. Piccinini, R. Pittau, and A. D. Polosa, *ALPGEN, a generator for hard multiparton processes in hadronic collisions*, JHEP **0**307 (2003) 001, arXiv:hep-ph/0206293 [hep-ph]. 6.2.2

[107] M. L. Mangano, M. Moretti, F. Piccinini, and M. Treccani, *Matching matrix elements and shower evolution for top-quark production in hadronic collisions*, JHEP **0**1 (2007) 013, arXiv:hep-ph/0611129 [hep-ph]. 6.2.2

[108] K. Melnikov and F. Petriello, *Electroweak gauge boson production at hadron colliders through $O(\alpha_s^2)$*, Phys. Rev. **D** 74 (2006) 114017, arXiv:hep-ph/0609070. 6.2.2

[109] C. Anastasiou, L. J. Dixon, K. Melnikov, and F. Petriello, *High precision QCD at hadron colliders: Electroweak gauge boson rapidity distributions at NNLO*, Phys.Rev. **D**69 (2004) 094008, arXiv:hep-ph/0312266 [hep-ph]. 6.2.2

[110] J. M. Campbell, R. K. Ellis, and D. L. Rainwater, *Next-to-leading order QCD predictions for W + 2 jet and Z + 2 jet production at the CERN LHC*, Phys.Rev. **D**68 (2003) 094021, arXiv:hep-ph/0308195 [hep-ph]. 6.2.2

[111] S. Jadach, Z. Was, R. Decker, and J. H. Kuhn, *The tau decay library TAUOLA: Version 2.4*, Comput. Phys. Commun. **7**6 (1993) 361–380. 6.2.2

[112] P. Golonka et al., *The tauola-photos-F environment for the TAUOLA and PHOTOS packages, release II*, Comput. Phys. Commun. **1**74 (2006) 818–835. 6.2.2

[113] T. Gleisberg et al., *Event generation with SHERPA 1.1*, JHEP **0**2 (2009) 007, arXiv:0811.4622 [hep-ph]. 6.2.2

[114] ATLAS Collaboration, *Electron efficiency measurements with the ATLAS detector using the 2012 LHC proton-proton collision data*, ATLAS-CONF-2014-032, Jun, 2014. 6.2.3, 7.1, 7.1.1, 7.2, 10.1.1.3, 10.1.1.3

[115] ATLAS Collaboration, *Preliminary results on the muon reconstruction efficiency, momentum resolution, and momentum scale in ATLAS 2012 pp collision data*, ATLAS-CONF-2013-088, Aug, 2013. 6.2.3, 7.1.2, 7.3

[116] ATLAS Collaboration, *Measurement of the muon reconstruction performance of the ATLAS detector using 2011 and 2012 LHC proton-proton collision data*, Accepted for publication by EPJC (2014) , arXiv:1407.3935 [hep-ex]. 6.2.3, 10.1.1.4, 10.1.2.1

[117] ATLAS Collaboration, *Improved electron reconstruction in ATLAS using the Gaussian Sum Filter-based model for bremsstrahlung*, ATLAS-CONF-2012-047, May, 2012. 7.1.1

[118] G. Cowan, *Discovery sensitivity for a counting experiment with background uncertainty*, http://www.pp.rhul.ac.uk/ cowan/stat/notes/medsigNote.pdf. 7.3

[119] ATLAS Collaboration, *Reconstruction of collinear final-state-radiation photons in Z decays to muons in $\sqrt{s} = 7$ TeV proton-proton collisions*, ATLAS-CONF-2012-143, 2012. 7.4.1.1

[120] J. Alwall, M. Herquet, F. Maltoni, O. Mattelaer, and T. Stelzer, *MadGraph 5 : Going Beyond*, JHEP **1**106 (2011) 128, arXiv:1106.0522 [hep-ph]. 7.4.2

[121] D. de Florian, G. Ferrera, M. Grazzini, and D. Tommasini, *Transverse-momentum resummation: Higgs boson production at the Tevatron and the LHC*, JHEP **1**1 (2011) 064, arXiv:1109.2109 [hep-ph]. 7.4.3.1

[122] D. de Florian, G. Ferrera, M. Grazzini, and D. Tommasini, *Transverse-momentum resummation: Higgs boson production at the Tevatron and the LHC*, JHEP **1**111 (2011) 064, arXiv:1109.2109 [hep-ph]. 7.4.3.1

[123] M. Cacciari, G. P. Salam, and G. Soyez, *The anti-k_t jet clustering algorithm*, JHEP **0**4 (2008) 063, arXiv:0802.1189 [hep-ph]. 7.4.3.2, 8.2

[124] ATLAS Collaboration, *Measurement of the Higgs boson mass from the $H \to \gamma\gamma$ and $H \to ZZ^* \to 4\ell$ channels in pp collisions at center-of-mass energies of 7 and 8 TeV with the ATLAS detector*, Phys. Rev. D **9**0 (2014) 052004. 8.4.2

[125] G. Cowan, *A survey of unfolding methods for particle physics*, in *Prepared for Conference on Advanced Statistical Techniques in Particle Physics, Durham, England*, pp. 18–22. 2002. 8.5.2

[126] Y. Gao, A. V. Gritsan, Z. Guo, K. Melnikov, M. Schulze, et al., *Spin determination of single-produced resonances at hadron colliders*, Phys.Rev. **D**81 (2010) 075022, arXiv:1001.3396 [hep-ph]. 8.5.4

[127] S. Bolognesi, Y. Gao, A. V. Gritsan, K. Melnikov, M. Schulze, et al., *On the spin and parity of a single-produced resonance at the LHC*, Phys.Rev. **D**86 (2012) 095031, arXiv:1208.4018 [hep-ph]. 8.5.4

[128] Pivk, M. and Le Diberder, F. R., *sPlot: A statistical tool to unfold data distributions*, Nuclear Instruments and Methods in Physics Research A **5**55 (2005) 356–369, physics/0402083. 9.2.2.1

[129] ATLAS Collaboration, *Improved luminosity determination in pp collisions at $\sqrt{s} = 7$ TeV using the ATLAS detector at the LHC*, Eur.Phys.J. **C**73 (2013) 2518, arXiv:1302.4393 [hep-ex]. 10.1.1.1

[130] ATLAS Collaboration, *Jet energy measurement with the ATLAS detector in proton-proton collisions at $\sqrt{s} = 7$ TeV*, Eur.Phys.J. **C**73 (2013) 2304, arXiv:1112.6426 [hep-ex]. 10.1.2.2, 10.3

[131] ATLAS Collaboration, *Jet energy scale and its systematic uncertainty in proton-proton collisions at $\sqrt{s} = 7$ TeV with ATLAS 2011 data*, ATLAS-CONF-2013-004, Jan, 2013. 10.1.2.2, 10.3

[132] I. W. Stewart and F. J. Tackmann, *Theory Uncertainties for Higgs and Other Searches Using Jet Bins*, Phys.Rev. **D**85 (2012) 034011, arXiv:1107.2117 [hep-ph]. 10.3.3

[133] K. S. Cranmer, *Kernel estimation in high-energy physics*, Comput.Phys.Commun. **136** (2001) 198–207, arXiv:hep-ex/0011057 [hep-ex]. 11.2.1

[134] L. A. Piegl and W. Tiller, *The NURBS book: Monographs in visual communication*, ch. B-Spline Basis Function. Springer, 2nd ed., 1997. 11.2.1

[135] W. Verkerke *et* al., *The RooFit Toolkit for Data Modelling*, Available from http://roofit.sourceforge.net or with recent versions of the root framework available at http://root.cern.ch. 12.1

[136] ROOT Collaboration, K. Cranmer, G. Lewis, L. Moneta, A. Shibata, and W. Verkerke, *HistFactory: A tool for creating statistical models for use with RooFit and RooStats*, Tech. Rep. CERN-OPEN-2012-016, New York U., New York, Jan, 2012. 12.1

[137] G. Cowan, K. Cranmer, E. Gross, and O. Vitells, *Asymptotic formulae for likelihood-based tests of new physics*, Eur. Phys. J. **C** 71 (2011) 1554, arXiv:1007.1727 [physics.data-an]. 12.1, 12.4.2

[138] I. M. Chakravarti, R. G. Laha, and J. Roy, *Handbook of Methods of Applied Statistics*, vol. I. John Wiley and Sons, 1967. 12.2.1